

UNIVERSITY OF BIRMINGHAM

ELECTRICAL DISCHARGE MACHINING (EDM) OF CFRP COMPOSITES

by

RAMY MOHAMED ABDELNABY METWALLY ABDALLAH

A thesis submitted to

The University of Birmingham

for the degree of

DOCTOR OF PHILOSOPHY

Department of Mechanical Engineering

School of Engineering

University of Birmingham

June 2020

UNIVERSITY OF
BIRMINGHAM

University of Birmingham Research Archive

e-theses repository

This unpublished thesis/dissertation is copyright of the author and/or third parties. The intellectual property rights of the author or third parties in respect of this work are as defined by The Copyright Designs and Patents Act 1988 or as modified by any successor legislation.

Any use made of information contained in this thesis/dissertation must be in accordance with that legislation and must be properly acknowledged. Further distribution or reproduction in any format is prohibited without the permission of the copyright holder.

SYNOPSIS

The thesis details research to evaluate the feasibility of wire electrical discharge machining (WEDM) as an alternative to conventional cutting (milling/routing/slotting) of carbon fibre reinforced plastic (CFRP) composites. A comprehensive literature review of various non-conventional machining processes including laser beam machining, abrasive water jet machining, ultrasonic machining and electrical discharge machining revealed that there was comparatively limited work on WEDM of CFRP. In order to address this gap in knowledge, 3 primary phases of experimental work were undertaken to investigate the influence of operating parameters, electrode material, workpiece fibre orientation and stacking with metallic layers when WEDM of CFRP laminates.

Phase 1 trials were aimed at studying the effect of key process parameters (open gap voltage, ignition current as well as pulse on and off times) when WEDM unidirectional CFRP plates (all plies laid up in the same orientation) using a 0.25 mm diameter zinc coated brass wire (Topas plus D). The tests were divided into 2 sub-phases, both utilising a L18 Taguchi fractional factorial experimental design with Phase 1A and 1B involving machining parallel and perpendicular to the fibre direction respectively. The main results revealed that the maximum material removal rate (MRR) achieved was higher when cutting parallel to the fibre direction (2.41 mm^3/min) as opposed to the perpendicular orientation (1.94 mm^3/min), albeit at the expense of marginally wider (3.33%) kerf widths (Wa) and higher (38.6%) workpiece surface roughness (Sa). Ignition current and pulse off time were statistically significant factors with respect to MRR for both cutting directions in addition to open voltage when machining perpendicular to fibre orientation. Conversely, open voltage was the only major factor affecting roughness.

In Phase 2, similar experimental designs were utilised when machining parallel (Phase 2A) and perpendicular (Phase 2B) to the fibre directions, but performed using a dual coated (copper and β phase) steel core wire electrode (commercially named as Compeed). Considerably higher MRR of up to 4.7 mm^3/min was observed when operating parallel to the fibres compared to corresponding results in Phase 1, while no appreciable improvement was obtained when cutting in the perpendicular direction (maximum MRR of 1.68 mm^3/min). However, a marked increase in both kerf width (up to ~ 367 µm) and surface roughness (up to 26.29 µm Sa) was evident in Phase 2A trials. Despite no signs of major defects on the kerf edges, there was visible evidence of frayed fibres, areas of redeposited resin and matrix/fibre loss on the machined surface. Pulse

off time had a significant influence on workpiece roughness and recorded the highest percentage contribution ratio (PCR) of 40.55% according to the analysis of variance (ANOVA).

Preliminary trials to evaluate the influence of stacking UD-CFRP laminates between copper plates to improve workpiece conductivity and machining performance was undertaken in Phase 3A using both coated brass and steel cored wires. Surprisingly, a marginally higher MRR of 6.5 mm^3/min was obtained when machining with the Topas wire compared to 6.11 mm^3/min for the Compeed wire. This was possibly due to lower process stability when employing the Compeed wire as a result of greater resin debris in the spark gap. As wire breakage frequently occurred during the preliminary trials, the maximum values of voltage and pulse on time were reduced while pulse off time was increased in Phase 3B, where a response surface methodology (RSM) experiment was designed to study the effect of wire type, ignition current and pulse off time on MRR and surface roughness. While the Topas wire achieved a somewhat higher MRR of 5.89 mm^3/min compared to Compeed (5.35 mm^3/min), all of the factors were statistically significant at the 5% level with regard to MRR. In contrast, none of the variable parameters had a major influence on surface roughness. Notwithstanding the increased MRR, machining of the metallic-CFRP stacked configuration induced severe delamination on the top/bottom surfaces and kerf edges with frayed fibres. Results from a multi-objective optimisation analysis for MRR and roughness indicated that a current of 4 A and pulse off time of 8 µs were preferred when using the Topas wire.

In Phase 3C, multidirectional CFRP workpieces were machined using both wire electrodes, with MRR values ranging between 7.42 and 14.82 mm^3/min and from 5.29 to 13.31 mm^3/min for Topas and Compeed wires respectively. Pulse off time was the sole significant factor with a PCR of 67.76%, with a strong correlation observed between MRR, machining variables and their interactions based on a coefficient of determination (R^2) of 99.79%. The average kerf width (Wa) and Sa when machining with the Compeed wire was up to ~374 µm and 27.53 µm respectively, but which was marginally lower when using the Topas wire (~347 µm and 24.86 µm). Based on the ANOVA for kerf width (Wa), wire type and its interaction with pulse off time were significant terms, with the model for predicting Wa having a R^2 of 99.88%. Although none of the variables were significant with respect to surface roughness, the corresponding model demonstrated a strong correlation between predicated Sa and experimental data with a R^2 of 96.24%.

Generally, this study proved the feasibility/capability of WEDM in cutting thick CFRP composites in addition to identifying the preferred levels of key process variables and wire electrode types to achieve successful machining. While the stacking configuration of UD-CFRP using copper plates enhanced machining productivity, excessive damage was however observed. Machining parallel to workpiece fibre orientation resulted in higher MRR, Wa and Sa compared to perpendicular orientation, particularly when using the Compeed wire. However, the Topas wire revealed superior performance when machining UD-CFRP/Cu stacks and multidirectional CFRP workpieces.

ACKNOWLEDGEMENTS

The author would first like to extend his deepest thanks and appreciation to Dr. Sein Leung Soo (Reader in Manufacturing Science and Technology) and Dr. Richard Hood (Senior Lecturer in Advanced Manufacturing Technology), both in the Department of Mechanical Engineering, University of Birmingham for their continued supervision, guidance and support as well as for providing a conducive and stimulating environment to work during this scientific journey.

I wish to express my sincerest gratitude to Mr. Andrew Loat (Research and Development Technician in the Machining Research Group), Mr. Lee Gauntlett (Automotive Technician and Deputy Safety Co-ordinator), Mr. Peter Thornton (previously Engine Research and Development Engineer) and other members of the technical support team within the School of Engineering for their invaluable assistance during various stages of the experimental work.
I would like to thank Dr. Debajyoti Bhaduri and Dr. Alessandro Abena (both former Research Fellows in the Department) for their help with training on the Alicona InfiniteFocus and JEOL SEM microscopes. Similarly, thanks are due to Dr. Ali Abdelhafeez Hassan (Research Fellow/Technical Officer) for his guidance and assistance with experimental design techniques together with all my colleagues in the Machining Research Group for their support and friendship.

I am grateful to the Egyptian Government and Ministry of Higher Education and Scientific Research for financial support throughout the research project.

Last but not least, I would like to express my sincere love, gratitude and appreciation to my parents, my brother, my wife Wessam Saad and my sons Mohamed and Malik, for their motivation, support and encouragement throughout this long journey.

TABLE OF CONTENTS

SYNOPSIS ..... **i**
ACKNOWLEDGEMENTS ..... **iv**
TABLE OF CONTENTS ..... **v**
LIST OF FIGURES ..... **x**
LIST OF TABLES ..... **xvi**
NOMENCLATURE ..... **xviii**
1 INTRODUCTION **1**
1.1 Background to the project and motivation for the work 1
1.2 Aim and objectives of the research 2
1.3 Thesis structure 2
1.4 Summary 3
2 LITERATURE REVIEW **4**
2.1 Introduction 4
2.2 Fibre reinforced plastic (FRP) composites 6
2.2.1 Matrix materials 7
2.2.2 Fibre materials 11
2.2.2.1 Glass fibre 11
2.2.2.2 Aramid fibre 11
2.2.2.3 Carbon fibre 12
2.2.2.4 Other fibres 13
2.2.3 Fibre architecture in composites 14
2.2.3.1 Prepregs 17
2.2.3.2 Laminates 17
2.3 Carbon fibre reinforced plastic (CFRP) composites 20
2.3.1 Machinability of CFRP 22
2.3.1.1 Drilling of CFRP 22
2.3.1.2 Milling/trimming of CFRP 25
2.3.2 Challenges in conventional machining of CFRP 27
2.4 Non-conventional machining of CFRP 28
2.4.1 Water jet machining 28
2.4.1.1 Drilling operation 28

2.4.1.2 Milling operation....30
2.4.2 Laser beam machining....33
2.4.2.1 Drilling operation....34
2.4.2.2 Milling operation....36
2.4.3 Ultrasonic machining....38
2.4.3.1 Drilling operation....39
2.4.3.2 Milling operation....42
2.4.4 Electrical discharge machining (EDM)....44
2.4.4.1 Die- sink EDM....45
2.4.4.2 Wire EDM....49
2.5 Wire electrodes....50
2.5.1 Characteristics of wire electrodes....51
2.5.2 Types of wire electrodes....51
2.5.2.1 Plain wires....52
2.5.2.2 Coated wires....53
2.5.2.3 Diffusion annealed coated wires....53
2.5.2.4 Composite wires....54
2.6 Electrical resistivity measurement of CFRP....55
2.6.1 Two and four probe method....56
2.7 Summary....57
3 EXPERIMENTAL WORK....59
3.1 Workpiece materials....61
3.2 Wire electrodes....63
3.2.1 Zinc coated brass core wire electrode (Topas plus D)....64
3.2.2 Copper/brass coated steel core wire electrode (Compeed)....64
3.3 Equipment, experimental setup and measurement procedures....65
3.3.1 WEDM machine tool....65
3.3.2 Experimental setup....66
3.3.3 Material removal rate calculation....67
3.3.4 Kerf width measurement....68
3.3.5 Surface integrity evaluation....69
3.3.5.1 Surface roughness measurement....69
3.3.5.2 Surface damage and delamination....72
3.3.5.3 Surface topography and structure....72

3.3.6 Electrical resistivity measurement 73
3.4 Design of experiment and test arrays 74
3.4.1 Phase 1A: Effect of operating parameters when cutting UD-CFRP parallel to fibre direction using zinc coated brass core wire 75
3.4.2 Phase 1B: Effect of operating parameters when cutting UD-CFRP perpendicular to fibre direction using zinc coated brass core wire 77
3.4.3 Phases 2A/2B: Effect of operating parameters when cutting UD-CFRP parallel / perpendicular to fibre orientation using copper/brass coated steel core wire 77
3.4.4 Phase 3A: Preliminary investigation on cutting UD-CFRP/Cu stacks using zinc coated brass and copper/brass coated steel core wires 77
3.4.5 Phase 3B: Influence of operating parameters and wire electrode material when cutting UD-CFRP-metallic stacks 78
3.4.6 Phase 3C: Influence of wire electrode material and operating conditions on cutting performance of multidirectional CFRP laminates 80
3.5 Summary 81
4 RESULTS AND DISCUSSION 82
4.1 Phase 1A: Effect of operating parameters when cutting UD-CFRP parallel to fibre direction using zinc coated brass core wire 82
4.1.1 Material removal rate 82
4.1.2 Kerf width 84
4.1.3 Surface roughness 86
4.1.4 Surface damage 88
4.2 Phase 1B: Effect of operating parameters when cutting UD-CFRP perpendicular to fibre direction using zinc coated brass core wire. 90
4.2.1 Material removal rate 90
4.2.2 Kerf width 92
4.2.3 Surface roughness 93
4.2.4 Surface damage 95
4.2.5 Confirmation tests for Phase 1 experiments 98
4.3 Phase 2A: Effect of operating parameters when cutting UD-CFRP parallel to fibre orientation using copper/brass coated steel core wire 99
4.3.1 Material removal rate 99
4.3.2 Kerf width 100
4.3.3 Surface roughness 102
4.3.4 Surface damage 104

4.4 Phase 2B: Effect of operating parameters when cutting UD-CFRP perpendicular to fibre orientation using copper/brass coated steel core wire 106
4.4.1 Material removal rate 106
4.4.2 Kerf width 108
4.4.3 Surface roughness 110
4.4.4 Surface damage 112
4.4.5 Confirmation tests 114
4.5 Comparison between Phase 1 and 2 tests (effect of wire electrode) 115
4.5.1 Material removal rate 115
4.5.2 Average kerf width 117
4.5.3 Average surface roughness 118
4.6 Phase 3A: Preliminary investigation on cutting UD-CFRP/Cu stacks using zinc coated brass and copper/brass coated steel core wires 119
4.6.1 Material removal rate 119
4.7 Phase 3B: Influence of operating parameters and wire electrode material when cutting UD-CFRP-metallic stacks 120
4.7.1 Material removal rate 120
4.7.2 Surface roughness 123
4.7.3 Surface integrity and damage 127
4.7.4 Confirmation tests 130
4.8 Phase 3C: Influence of wire electrode material and operating conditions on cutting performance of multidirectional CFRP laminates 133
4.8.1 Material removal rate 133
4.8.2 Kerf width 136
4.8.3 Surface roughness 139
4.8.4 Surface integrity 142
4.9 Summary 145
5 CONCLUSIONS 147
5.1 Literature review 147
5.2 Experimental work 147
5.2.1 Phase 1A: Effect operating parameters when cutting UD-CFRP parallel to fibre direction using zinc coated brass core wire 147
5.2.2 Phase 1B: Effect of operating parameters when cutting UD-CFRP perpendicular to fibre direction using zinc coated brass core wire 148

5.2.3 Phase 2A: Effect of operating parameters when cutting UD-CFRP parallel to fibre orientation using copper/brass coated steel core wire 149

5.2.4 Phase 2B: Effect of operating parameters when cutting UD-CFRP perpendicular to fibre orientation using copper/brass coated steel core wire 149

5.2.5 Phase 3A: Preliminary investigation on cutting UD-CFRP/Cu stacks using zinc coated brass and copper/brass coated steel core wires 150

5.2.6 Phase 3B: Influence of operating parameters and wire electrode material when cutting UD-CFRP-metallic stacks 150

5.2.7 Phase 3C: Influence of wire electrode material and operating conditions on cutting performance of multidirectional CFRP laminates 151

5.3 Overall conclusions and recommended cutting conditions 152

5.3.1 Comparison between Phase 1 and 2 experiments 152

5.3.2 Phase 3A and 3B: Cutting of CFRP/Cu stacks 153

5.3.3 Phase 3C: Cutting of multidirectional CFRP 153

5.4 Summary 154

6 RECOMMENDATIONS FOR FUTURE WORK 155

REFERENCES 156

APPENDICES 169

Appendix-A: Carbon fibre data sheet 169

Appendix-B: Safety data sheet of carbon fibre prepreg 170

Appendix-C: Resistivity measurements for CFRP samples 171

Appendix-D: Micrographs of machined kerf for preliminary tests 172

Appendix-E: Surface topographical maps for areal roughness measurements 176

Appendix-F: Data tables for experimental phases 184

Appendix-G: List of publications 187

LIST OF FIGURES

Figure 2.1: Classification of manufactured composites according to reinforcement [7]. 5
Figure 2.2: Comparison of mechanical properties between steel, aluminium (Al) and composites (adapted from [4]).....5
Figure 2.3: Evolution of composite material utilisation in the aircraft industry since 1960 [6].6
Figure 2.4: Specific strength of composites at different temperatures [3]. 6
Figure 2.5: Schematic illustration of FRP composites utilisation in Boeing 787 Dreamliner [6]. 7
Figure 2.6: Schematic diagram comparing FRP composite properties and other materials [13]. 7
Figure 2.7: Cost ratio for different types of fibres [13].....13
Figure 2.8: Comparison of specific strength/modulus for different types of fibres (adapted from [3]). 14
Figure 2.9: Schematic representation for unidirectional and bidirectional fibre architecture [24, 25]. 15
Figure 2.10: Schematic representation for unidirectional and fabric prepreg tapes [11]. 15
Figure 2.11: Schematic illustration for different woven fabric styles (a) plain weave, (b) 5 harness stain weave and (c) 2 x 2 twill weave [11, 15].....16
Figure 2.12: Schematic representation for non-crimp fabrics [11]. 17
Figure 2.13: Fibre arrangements in lamina construction [14]. 18
Figure 2.14: Composite laminate anatomy [21].....19
Figure 2.15: Laminate code examples [31]. 19
Figure 2.16: Comparison between unidirectional and quasi-isotropic lay-up [33].....19
Figure 2.17: The main applications of monolithic CFRP in Airbus A380 [39]. 21
Figure 2.18: Relative efficiency of structural aerospace materials (adapted from [5]).....21
Figure 2.19: Schematic illustration for 2D and 3D delamination in drilling process [25].....23
Figure 2.20: Schematic showing calculation of delamination factor in (a) drilling, and (b) milling [25, 49].....23
Figure 2.21: Exit hole surface induced at same cutting conditions (*Vc* =75 m/min and *f*= 62 mm/min) and tool diameter (ϕ 6 mm) via (a) conventional drilling and (b) circular drilling [63]. 25
Figure 2.22: Common milling operations for CFRP; (a) End milling, and (b) Edge trimming [9]. 25
Figure 2.23: Effect of workpiece temperature on cutting force at different cutting speeds (adapted from [66]).....26
Figure 2.24: Comparison between circular saw and end milling via multidirectional CFRP machining (a) Flank wear and (b) Surface roughness [71]. 27
Figure 2.25: Morphology of machined surface at hole exit for various machining parameters and process types (adapted from [78]). 30
Figure 2.26: Morphology of CFRP delamination caused by abrasive particles [82]. 31
Figure 2.27: Mechanism of workpiece delamination in CFRP composite following AWJM; (a) crack initiation; (b) water indentation; (c) abrasive penetration [83]. 31
Figure 2.28: Kerf profile of Ti/CFRP and CFRP/Ti stacks at various traverse speeds [84]. ...32

Figure 2.29: Schematic illustration of solid state (Nd:YAG) laser cutting system (adapted from [86]). 33
Figure 2.30: Surface morphology of 2 mm hole obtained through fibre laser machining of CFRP (a) hole entry and (b) hole exit [92]. 34
Figure 2.31: Laser drilling of CFRP (a) multi rings strategy and (b) HAZ at various power and speed levels [99]. 35
Figure 2.32: Comparison between HAZ levels for different laser types (adapted from [112]). 37
Figure 2.33: Defects induced by laser cutting at different kerf zones [96]. 38
Figure 2.34: Schematic diagram illustrate the main components of USM [88]. 39
Figure 2.35: Schematic representation of RUM process [116]. 39
Figure 2.36: Comparison between CD and UAD of CFRP in terms of (a) surface roughness, (b) process temperature and (c) delamination factor [125]. 41
Figure 2.37: Chip removal at first and fifth holes (a) CD, (b) RUAD 5 μm and (c) RUAD 7.5 μm [131]. 42
Figure 2.38: Cutting orientations when edge trimming of CFRP using RUM [132]. 43
Figure 2.39: Comparative performance of UAM and CM for various response measures (adapted from [137]). 44
Figure 2.40: Schematic representation of main EDM process configurations, (a) die sink EDM, (b) wire EDM (adapted from [143, 144]). 45
Figure 2.41: Effect of pulse duration on removal rate and surface roughness for various tool/workpiece materials [142]. 46
Figure 2.42: Schematic illustration of machining in different fibre directions; (a) perpendicular CFRP2, (b) perpendicular CFRP1 and (c) parallel CFRP1 [151]. 47
Figure 2.43: Voltage and current waveforms during (a) short-circuiting and (b) normal discharge [156]. 48
Figure 2.44: Cross section of drilled holes at different machining times (a) 10 minutes and (b) 40 minutes [157]. 48
Figure 2.45: Effect of different factors on performance attributes [162]. 50
Figure 2.46: The main characteristics to consider in wire electrode selection (adapted from [163]). 51
Figure 2.47: Classification/categories of wire electrodes [166]. 52
Figure 2.48: Influence of wire core and coating on cutting speed and roughness (adapted from [162]). 53
Figure 2.49: Composition of different coated and diffusion annealed wires; (a) zinc coated brass, (b) X type, (c) D type, (d) Gamma brass, (e) Gamma X and (f) Gamma D [166]. 54
Figure 2.50: Schematic illustration for composite wires [166]. 55
Figure 2.51: Influence of skin effect on current density distribution for different wires [172]. 55
Figure 2.52: Comparison between the cutting speed of brass and performance wires [162]. 55
Figure 2.53: Schematic illustration for resistivity measurements using (a) two probe and (b) four probe methods (adapted from [176]). 56
Figure 2.54: Electrical resistance measurement [177]. 57
Figure 2.55: Illustration showing the gaps in knowledge relating to WEDM of CFRP. 58
Figure 3.1: Flow graph illustrating the different experimental work phases. 60

Figure 3.2: Unidirectional CFRP laminate with a micrograph of the cross section. 61
Figure 3.3: Unidirectional CFRP laminate covered with adhesive copper foil and machining damage after cutting on the (a) top and (b) bottom surfaces of the workpiece. 62
Figure 3.4: Schematic representation of CFRP/Cu stacks used in Phase 3A and 3B 62
Figure 3.5: Micrograph showing the cross section of the multidirectional CFRP laminate [184, 185]. 63
Figure 3.6: Topas plus D wire electrode and its composition. 64
Figure 3.7: Compeed wire electrode and its composition. 65
Figure 3.8: Comparison between tensile strength and different types of brass wire at various work zone temperatures [189]. 65
Figure 3.9: Robofil FL240CC wire EDM machine. 66
Figure 3.10: Schematic illustration for cutting to fibre orientations. 67
Figure 3.11: Experimental setup for tests involving; (a) individual CFRP and (b) metallic-CFRP stacked workpieces. 67
Figure 3.12: Precision digital scale for workpiece weight measurement. 68
Figure 3.13: Kerf width measurement using Alicona G5 InfiniteFocus 3D optical measurement device. 69
Figure 3.14: Standard reference sample for calibration of surface roughness. 69
Figure 3.15: Experimental set up for surface roughness measurements. 70
Figure 3.16: Optical micrographs captured using tool maker microscope. 72
Figure 3.17: Setup for SEM surface topography assessment. 73
Figure 3.18: Two probe resistivity measurements 74
Figure 3.19: Micrograph of kerf damage caused by flow of molten copper. 78
Figure 3.20: The key challenges and suggested solutions when WEDM of CFRP. 81
Figure 4.1: Material removal rate when machining parallel to fibre orientation using Topas wire. 83
Figure 4.2: Main effects plot for MRR when cutting parallel to fibre orientation using Topas wire. 84
Figure 4.3: Average kerf width when machining parallel to fibre direction using Topas wire. 84
Figure 4.4: Main effects plot for average kerf width through parallel cutting to fibre orientation. 85
Figure 4.5: Average surface roughness when cutting parallel to fibre orientation using Topas wire. 86
Figure 4.6: Surface topographical map of machined workpiece from Test 9 (highest MRR). 87
Figure 4.7: Main effects plot for surface roughness (Sa) when machining parallel cutting to fibre orientation. 87
Figure 4.8: Optical micrographs of machined kerf on the (a) top and (b) bottom surfaces of the workpiece from Test 9 (highest MRR). 88
Figure 4.9: Sample SEM micrographs of machined surfaces in (a) Test 2 – lowest MRR, (b) Test 6 - median MRR and (c) Test 9 - highest MRR. 89
Figure 4.10: Material removal rate when cutting perpendicular cutting to fibre orientation using Topas wire. 91
Figure 4.11: Main effects plot for MRR when machining perpendicular to fibre orientation. 91

Figure 4.12: Average kerf width measurements cutting perpendicular to fibre orientation using Topas wire. 92
Figure 4.13: Main effects plot for average kerf width when cutting perpendicular to fibre orientation. 93
Figure 4.14: Average surface roughness when cutting perpendicular to fibre orientation using Topas wire. 94
Figure 4.15: Surface topographical map of machined workpiece from Test 1 (highest Sa). 94
Figure 4.16: Main effects plot for surface roughness when cutting perpendicular to fibre orientation using Topas wire. 95
Figure 4.17: Optical micrographs of machined kerf on the (a) top and (b) bottom surfaces of the workpiece from Test 4 (highest MRR). 96
Figure 4.18: Sample SEM micrographs of surface delamination for Test 4 - highest MRR. 96
Figure 4.19: Sample SEM micrographs of machined surfaces in (a) Test 14 – lowest MRR, (b) Test 6 – median MRR and (c) Test 4 – highest MRR. 97
Figure 4.20: Sample SEM micrographs of machined surfaces from Phase 1B confirmation test. 98
Figure 4.21: Material removal rate when cutting parallel to fibre direction using Compeed wire. 99
Figure 4.22: Main effects plot for MRR when cutting parallel to fibre orientation using Compeed wire. 100
Figure 4.23: Average kerf width when cutting parallel to fibre orientation using Compeed wire. 101
Figure 4.24: Main effects plot for average kerf width when cutting parallel to fibre orientation using Compeed wire. 101
Figure 4.25: Bar chart illustrates average surface roughness during parallel cutting using Compeed wire. 103
Figure 4.26: Surface topographical map of machined workpiece from Test 4 (highest Sa). 103
Figure 4.27: Main effects plot for Sa when cutting parallel to fibre orientation. 104
Figure 4.28: Optical micrographs of machined kerf accomplished at highest MRR using Compeed wire (a) top surface and (b) bottom surface. 105
Figure 4.29: Sample SEM micrographs of machined surfaces in (a) Test 3 - lowest MRR, (b) Test 18 - median MRR and (c) Test 9 – highest MRR. 106
Figure 4.30: Material removal rate when cutting perpendicular to fibre direction using Compeed wire. 107
Figure 4.31: Main effects plot for MRR when cutting perpendicular to direction using Compeed wire. 108
Figure 4.32: Average kerf width when cutting perpendicular to direction using Compeed wire. 109
Figure 4.33: Main effects plot for average kerf width when cutting perpendicular to direction using Compeed wire. 109
Figure 4.34: Average surface roughness when cutting perpendicular to direction using Compeed wire. 110
Figure 4.35: Surface topographical map of machined workpiece from (a) Test 7 – highest MRR and (b) Test 11 – highest Sa. 111

Figure 4.36: Main effects plot for Sa when cutting perpendicular to direction using Compeed wire. 111
Figure 4.37: Optical micrographs of machined kerf on the; (a) top and (b) bottom surfaces from test at highest MRR using Compeed wire. 112
Figure 4.38: Sample SEM micrographs of machined surfaces in (a) Test 12 - lowest MRR, (b) Test 15 – median MRR and (c) Test 7 – highest MRR. 113
Figure 4.39: Sample SEM micrographs of machined surface from the confirmation test in Phase 2B. 114
Figure 4.40: Comparison between material removal rates for Phases 1 and 2 using Topas and Compeed wire electrodes at different cutting orientations. 116
Figure 4.41: Comparison of MRR performance achieved by Topas and Compeed wires when cutting parallel to fibre direction at equivalent cutting conditions and nozzle standoff distance. 116
Figure 4.42: SEM micrographs of cavities and reduction in wire cross section of the Topas wire; (a) front view, and (b) top view. 117
Figure 4.43: Comparison of average kerf widths obtained using Topas and Compeed wires when cutting parallel and perpendicular to fibre direction. 118
Figure 4.44: Comparison of average areal surface roughness obtained using Topas and Compeed wires when cutting parallel and perpendicular to fibre direction. 119
Figure 4.45: Comparison of MRR obtained when machining plain UD-CFRP and UD-CFRP/Cu stacks using Topas and Compeed wires. 120
Figure 4.46: Comparison of MRR obtained when machining CFRP/Cu stacks using Topas and Compeed at different operating parameters. 120
Figure 4.47: Comparison of MRR when machining CFRP/Cu stacks using Topas and Compeed wires. 121
Figure 4.48: Normal plot of standardised effects for MRR. 122
Figure 4.49: Contour and surface plots showing the relationship between machining variables and MRR for (a) Topas and (b) Compeed wires. 123
Figure 4.50: Average areal surface roughness when machining CFRP/Cu stacks for both wire electrodes. 124
Figure 4.51: Surface topographical map of machined workpiece from Test 2 (highest Sa) using Topas plus D wire. 124
Figure 4.52: Normal plot of standardised effects for Sa. 125
Figure 4.53: Contour and surface plots showing the influence of current and pulse off time on Sa for (a) Topas and (b) Compeed wires. 126
Figure 4.54: Optical micrographs of the top and bottom surfaces of the CFRP machined using Topas wire in Test 2 (highest MRR) at (a) front, (b) middle and (c) end kerf regions. 128
Figure 4.55: Optical micrographs of the top and bottom surfaces of the CFRP machined using Compeed wire in Test 2 (highest MRR) at (a) front, (b) middle and (c) end kerf regions. 128
Figure 4.56: Sample SEM micrographs of machined surfaces using Topas wire in (a) Test 12 - lowest MRR, (b) Test 4 - median MRR and (c) Test 2 - highest MRR. 129
Figure 4.57: Sample SEM micrographs of machined surfaces in using Compeed wire in (a) Test 12 – lowest MRR, (b) Test 6 - median MRR and (c) Test 2 - highest MRR 130
Figure 4.58: Optimisation plot of performance measurements. 131

Figure 4.59: Optical micrographs for different regions on the top/bottom surfaces gained at confirmation test (a) front, (b) middle and (c) end kerf regions. 132
Figure 4.60: Sample SEM micrographs of machined surfaces in confirmation test using Topas wire. 132
Figure 4.61: EDS spectra of the re-solidified layer in the confirmation test. 133
Figure 4.62: Material removal rate when machining multidirectional CFRP using Topas and Compeed wires. 134
Figure 4.63: Main effects plot for MRR following machining of multidirectional CFRP. 134
Figure 4.64: Interaction plot matrix for MRR following machining of multidirectional CFRP. 136
Figure 4.65: Average kerf width following machining of multidirectional CFRP with Topas and Compeed wire electrodes. 137
Figure 4.66: Main effects plot for average kerf width following machining of multidirectional CFRP. 137
Figure 4.67: Interaction matrix plot for average kerf width. 139
Figure 4.68: Average areal surface roughness following machining of multidirectional CFRP using Topas and Compeed wire electrodes. 140
Figure 4.69: Surface topographical map of machined workpiece from Test 2 (highest Sa / MRR) (a) Topas and (b) Compeed. 140
Figure 4.70: Main effects plot for average surface roughness. 141
Figure 4.71: Interaction matrix plot for average areal surface roughness. 142
Figure 4.72: Optical micrographs showing the machined kerf in Test 2 (highest MRR) using Topas wire at the (a) top and (b) bottom surface. 143
Figure 4.73: Optical micrographs showing the machined kerf in Test 2 (highest MRR) using Compeed wire at the (a) top and (b) bottom surface. 143
Figure 4.74: Sample SEM micrographs of machined surfaces using Topas wire in (a) Test 3 – lowest MRR and (b) Test 2 – highest MRR. 144
Figure 4.75: Sample SEM micrographs of machined surfaces using Compeed wire in (a) Test 3 – lowest MRR and (b) Test 2 – highest MRR. 145
Figure 4.76: Bar chart showing (a) MRR (b) Wa and (c) Sa for each wire type when cutting UD-CFRP. 146

LIST OF TABLES

Table 2.1: Physical and mechanical properties of various thermoset and thermoplastic polymer resins [3]. 10
Table 2.2: Physical and mechanical properties of various fibre types [9]. 13
Table 2.3: Classification of manufacturing processes [10]. 21
Table 3.1: Physical/mechanical properties of the carbon fibre used in the UD-CFRP laminates [28]. 61
Table 3.2: Key properties of the prepreg layers and multidirectional CFRP laminate [184, 185]. 63
Table 3.3: Technical specifications of Robofil FL240CC WEDM machine [191]. 66
Table 3.4: Comparison between surface roughness measured using Alicona and standard values. 70
Table 3.5: Technical specifications of the Alicona G5 InfiniteFocus microscope [192]. 71
Table 3.6: Technical specifications of JCM-6000 SEM equipment [193]. 73
Table 3.7: Constant and variable machining parameters used in preliminary tests. 75
Table 3.8: Full factorial test array for preliminary trials. 75
Table 3.9: Variable machining parameters and associated levels. 76
Table 3.10: Taguchi L18 orthogonal array. 76
Table 3.11: Experimental array for preliminary testing for WEDM of CFRP/Cu stacks. 77
Table 3.12: Variable machining parameters and their levels. 78
Table 3.13: Face centred response surface methodology test array. 79
Table 3.14: Machining parameters and levels of full factorial plan. 80
Table 3.15: Full factorial test array. 81
Table 4.1: ANOVA for MRR when cutting parallel to fibre direction using Topas wire. 83
Table 4.2: ANOVA for average kerf width when cutting parallel to fibre orientation. 85
Table 4.3: ANOVA for mean surface roughness (Sa) when cutting parallel to fibre orientation. 88
Table 4.4: ANOVA for MRR when cutting perpendicular to fibre direction. 91
Table 4.5: ANOVA for mean kerf width when cutting perpendicular to fibre orientation. 93
Table 4.6: ANOVA for areal surface roughness when cutting perpendicular to fibre direction. 95
Table 4.7: Predicted and experimental results from Phase 1 confirmation tests for various responses. 98
Table 4.8: ANOVA for MRR when cutting parallel to fibre direction using Compeed wire. 100
Table 4.9: ANOVA for average kerf width when cutting parallel to fibre direction using Compeed wire. 102
Table 4.10: ANOVA for Sa when cutting parallel to fibre orientation 104
Table 4.11: ANOVA for MRR when cutting perpendicular to direction using Compeed wire. 108
Table 4.12: ANOVA for average kerf width when cutting perpendicular to direction using Compeed wire. 109
Table 4.13: ANOVA for Sa when cutting perpendicular to direction using Compeed wire. . 112
Table 4.14: Predicted and experimental results from Phase 2 confirmation tests for various responses. 114

Table 4.15: ANOVA for material removal rate when machining CFRP/Cu stacks. 122
Table 4.16: Regression equations and model summary for MRR. 122
Table 4.17: ANOVA for areal roughness (Sa) when machining CFRP/Cu stacks. 125
Table 4.18: Regression equations and model summary for Sa. 126
Table 4.19: Confirmation tests for MRR and Sa. 131
Table 4.20: Elemental composition of recast/re-solidified material. 133
Table 4.21: ANOVA for MRR following machining of multidirectional CFRP. 135
Table 4.22: ANOVA for MRR including interactions following machining of multidirectional CFRP. 135
Table 4.23: ANOVA for average kerf width considering linear factors. 138
Table 4.24: ANOVA for average kerf width including interactions. 138
Table 4.25: ANOVA for average areal roughness. 141
Table 4.26: ANOVA for average areal roughness including interactions. 142
Table 5.1: Preferred cutting conditions for machining of UD-CFRP. 153
Table 5.2: Preferred cutting conditions for machining of multidirectional CFRP. 154

NOMENCLATURE

LIST OF ACRONYMS

Acronym	Description
ACG	Advanced Composite Group
ANOVA	Analysis of variance
AWJM	Abrasive water jet machining
BEI	Backscattered electron image
BMC	Bulk moulding compound
C	Compeed
C/SiC	Carbon fibre reinforced silicon carbide
CC	Clean cut
CCD	Central composite design
CD	Conventional drilling
C-FFRP	Carbon-flax fibre reinforced plastic
CFRP	Carbon fibre reinforced plastic
CM	Conventional milling
CO_2	Carbon dioxide
CT	Computed tomography
CTE	Coefficient of thermal expansion
Cu	Copper
CW	Continuous wave
EDM	Electrical discharge machining
EDS	Energy dispersive X-ray spectroscopy
E-glass	Electrical glass
EP	Epoxy
FFRP	Natural flax fibre reinforced plastic
FRP	Fibre reinforced plastic
GFRP	Glass fibre reinforced polymer
Gr	Graphite
HAZ	Heat affected zone
$HAZ_{ellipse}$	Elliptical HAZ

HHT	High heat treatment
HIE	High eagle
HIF	High falcon
HIH	High hawk
HIR	High real
HIS	High sonic
HM	High modulus
HRC	Rockwell hardness
HT	High tensile
HTS	High tensile strength
IACS	International Annealed Copper Standard
IHT	Intermediate heat treatment
IM	Intermediate modulus
LBM	Laser beam machining
LHT	Low heat treatment
NCF	Non-crimp fabric
Nd:YAG	Neodymium-doped yttrium aluminium garnet
Nd:YVO4	Neodymium-doped yttrium orthovanadate
PA	Polyamide
PAN	Polyacrylonitrile
PCD	Polycrystalline diamond
PCR	Percentage contribution ratio
PEEK	Polyether-ether ketone
PEI	Polyetherimide
PEKK	Polyether ketone ketone
PES	Polyether sulfone
PP	Polypropylene
PPS	Polyphenylene sulfide
PS	Picosecond
PSC	Point stress criterion
PWJM	Pure waterjet machining
Q-switched	Quality-switched

RIM	Reaction injection moulding
RSM	Response surface methodology
RTM	Resin transfer moulding
RUAD	Rotary ultrasonic assisted drilling
RUEM	Rotary ultrasonic elliptical machining
RUM	Rotary ultrasonic machining
RUSM	Rotary ultrasonic surface machining
S/S2-glass	High strength glass fibre
SCRIMP	Seemann composite resin infusion moulding process
SEI	Secondary electron image
SEM	Scanning electron microscope
SHT	Super high tensile
SKD11	Tool steel
SMC	Sheet moulding compound
SOD	Standoff distance
SRIM	Structural reaction injection moulding
T	Topas
TEA	Transversely excited atmospheric
Ti	Titanium
TWR	Tool wear rate
UAD	Ultrasonic assisted drilling
UAM	Ultrasonic assisted milling
UD	Unidirectional
UHM	Ultra-high modulus
USM	Ultrasonic machining
USV	Ultrasonic assisted vibration
UV DPSS	Ultraviolet diode-pumped solid-state
VE	Vinyl ester
W	Wire type
WC	Tungsten carbide
WEDM	Wire electrical discharge machining
WJM	Waterjet machining

WTD	Width to depth ratio
Yb:YAG	Ytterbium-doped yttrium aluminium garnet
Zn	Zinc

LIST OF SYMBOLS

Symbol	Description	Unit
$\bar{\eta}_i$	Optimal level mean value	
$\bar{\eta}_m$	Overall mean	
$\hat{\eta}$	The predicted value	
2D	Two dimensions	
3D	Three dimensions	
A	Pulse on time	µs
a_e	Depth of cut	mm
A_o	Cross sectional area	m^2
B	Pulse off time	µs
C_l	Chip length	µm
D	Gross/global desirability	
d_i	Desirability of the response	
E_l	Energy per unit length	J/mm
f	Feed rate	mm/min
F_a	Two dimensional	
F_d	Delamination factor	
F_{da}	Adjusted delamination factor	
F_{fa}	Force adjusted delamination factor	
$F_{resultant}$	Resultant force	N
F_x	Cutting force in feed direction	N
F_y	Cutting force perpendicular to feed direction	N
f_z	Feed per tooth	mm
F_z	Normal cutting force	N
$High_i$	Upper limit/acceptable value of the response	
IAL	Ignition current	A
L	Sample length	m
Low_i	Lower limits/acceptable value of the response	
m_a	Mass after machining	g
m_b	Mass before machining	g
MRR	Material removal rate	mm^3/min

n	Number of repeated trials	
R	Electrical resistance	Ω
Ra	Arithmetic average surface roughness	µm
r_i	Importance of response or variable	
R_r	Chip space radius	µm
Rz	Ten-point height	µm
Sa	Arithmetic 3D areal roughness	µm
T_g	Glass transition temperature	°C
t_m	Machining time	min
T_w	Workpiece temperature	°C
V_c	Cutting speed	m/min
V_f	Fibre volume fraction	
V_o	Open gap voltage	V
Wa	Average kerf width	µm
W_{max}	Maximum damage width	µm
wt	Weight or power	
Y_i	Response	
y_i	Individual observation	
η	Signal to noise ratio	
ρ	Electrical resistivity	Ω.m
ρ_o	Density	g/mm^3

1 INTRODUCTION

1.1 Background to the project and motivation for the work

Carbon fibre reinforced plastic (CFRP) composites are widely used in various industrial applications, particularly in the aerospace sector due to its excellent properties including high specific strength/stiffness coupled with lower weight that outperforms traditional metallic materials. This has a direct impact on reduced fuel consumption and improved operational efficiency for some of the latest civil aircraft manufactured by Airbus and Boeing, where CFRP constitutes up to 50% of their weight. However, the utilisation of CFRP in key airframe structural parts such as the fuselage, wing and empennage sections requires considerable assembly, which is facilitated primarily through mechanical joining techniques. Therefore, drilling for producing fasteners holes and milling/routing for component sizing/finishing are the two main processes typically employed for machining CFRP. Nonetheless, the abrasive nature of carbon fibres and inhomogeneity of the mechanical/physical characteristics of CFRP results in significant challenges when conventional machining such as rapid tool wear, workpiece delamination, matrix degradation and fibre pull out, leading to detrimental effects on assembly integrity, dimensional accuracy and material properties.

The use of non-conventional machining processes such as abrasive water jet, laser beam machining, ultrasonic assisted machining and electrical discharge machining (EDM) have been considered as potential alternatives for cutting CFRP to overcome the shortcomings of conventional processes. While abrasive water jet and laser beam machining provide comparatively high material removal rates, severe delamination remains prevalent with surface burn (matrix decomposition occurs at ~400°C) commonly observed in the case of the latter. Research publications involving EDM die-sinking/drilling of CFRP is relatively scarce, with even less devoted to wire EDM (WEDM), hence the motivation for the present work.

The research detailed in this thesis was conducted within the Machining Research Group at the University of Birmingham as part of a Doctor of Philosophy (PhD) degree programme. The project was performed with the assistance of GF Machining Solutions (GFMS) through the provision of a Robofil FL240CC wire EDM machine together with a fully funded PhD studentship awarded by the Egyptian Ministry of Higher Education and Scientific Research.

1.2 Aim and objectives of the research

The overall aim of the study is to investigate the feasibility of WEDM for cutting unidirectional and multidirectional CFRP composite laminates, with a focus on identifying the influence of cutting conditions on machining productivity and workpiece surface integrity. The key objectives of the project are to:

- Understand the current state-of-the art regarding the use of non-conventional machining processes for cutting CFRP through a detailed/comprehensive literature review, with emphasis on EDM technology.
- Evaluate the influence of operating parameters including open gap voltage, ignition current, and pulse on/off time on key response measures including material removal rate (MRR), average kerf width and surface integrity (surface roughness and damage) when WEDM of UD-CFRP plates both parallel and perpendicular to fibre direction.
- Investigate the performance of different wire electrode materials for WEDM of CFRP.
- Assess the effect of stacking UD-CFRP plates with metallic layers on overall bulk electrical conductivity and analyse the impact of ignition current, pulse off time and wire type on resulting WEDM productivity and workpiece surface integrity.
- Investigate the feasibility of cutting multidirectional CFRP using different wire electrodes in addition to assessing the influence of varying ignition current and pulse off time on MRR, average kerf width, surface roughness and workpiece damage.

1.3 Thesis structure

The thesis consists of 6 key chapters beginning with an introduction outlining the background as well as the aim and objectives of the project followed by a comprehensive literature review of the subject area in Chapter 2. This includes topics such as matrix/fibre types, problems associated with conventional drilling/milling, non-conventional machining of CFRP, wire electrode types and electrical resistivity measurement techniques. Chapter 3 describes the workpiece materials, equipment, test procedures and design of experiments used in the various tests phases while corresponding results from the experiments are presented and discussed in Chapter 4. Finally, the main conclusions are summarised in Chapter 5 with recommendations for future work outlined in Chapter 6.

1.4 Summary

This chapter outlines the importance of CFRP composites and its widespread use in different engineering/industrial applications in addition to the difficulties in conventional and non-conventional machining of this material. These limitations represented the principal motivation to explore an alternative solution such as wire EDM. Additionally, the chapter states the aim and objectives of the project, which formed the basis for the experimental work phases, together with an overview of the thesis structure.

2 LITERATURE REVIEW

2.1 Introduction

Over the past five decades, composite materials have played an increasingly vital role in various engineering applications, in particular the aerospace industry and more recently the automotive and power generation sectors. This is due to its favourable attributes such as high specific strength (~ 20 to 800 kN.m/kg)/stiffness (~2.85 to 123 MN.m/kg), low density (~1220 to 2050 kg/m^3), good corrosion and fatigue resistance as well as comparatively low assembly costs because of fewer fasteners/assembled parts [1-5]. Composites is a term used to describe materials that are made from a combination of two or more dissimilar and insoluble constituents that has superior properties/characteristics than the individual materials [1, 6-8]. The application of composites can be traced back to ancient times where the Japanese covered swords or blades made of soft iron with steel to improve its impact and flexural strength [3]. Other examples of composites include bricks that are formed by the combination of mud reinforced with straw, while wood and bone represent naturally occurring composites where the former has cellulose fibres impregnated in lignin, while the latter is comprised of a mineral matrix reinforced by soft/short collagen fibres [1, 4, 9].

Modern industrially manufactured composite materials typically consist of two phases, a matrix and the reinforcement. The matrix is used to contain the reinforcement elements together and maintains the shape/volume of composite part, while the reinforcement phase enhances the overall mechanical properties of the composite and bears the applied loads as it is stronger/stiffer than matrix material [5, 9, 10]. The classification of composites are typically according to their matrix material and shape/type of the reinforcement phase. In terms of the matrix, there are three primary types of materials employed, which are either ceramic, metallic or polymer based. As for the reinforcement phase, the principal configurations are in the form of particles, fibres or structures, as shown in Figure 2.1. Other types of composite materials include hybrid composites, which consist of a combination of two different types of fibres embedded in each layer as well as advanced composites such as FRP (fibre reinforced polymer), which are widely utilised in aerospace applications owing to its distinct high specific strength and stiffness [1, 4, 9].

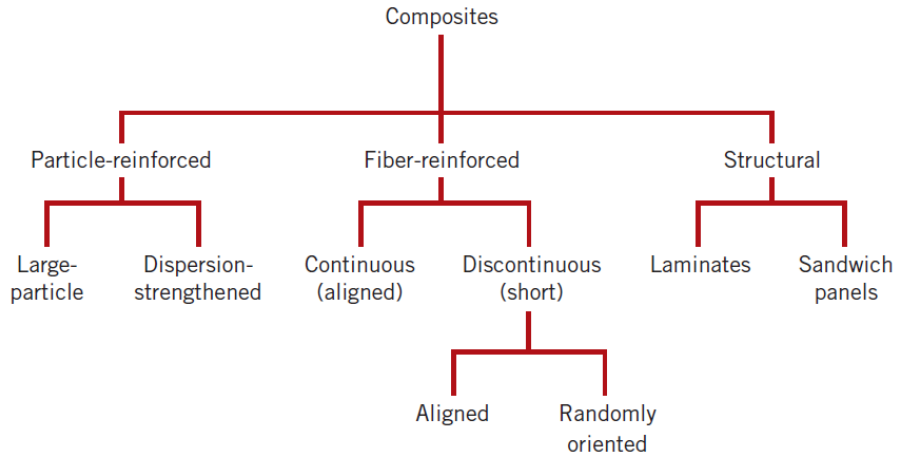


Figure 2.1: Classification of manufactured composites according to reinforcement [7].

Composite materials are increasingly replacing traditional metallic alloys such as steel and aluminium in various high-performance applications. This is not surprising, as illustrated by a comparison of key physical and mechanical properties of composites, aluminium and steel in Figure 2.2, which clearly shows composites generally having superior strength, stiffness and fatigue resistance but with lower weight, as opposed to steel and aluminium. The aircraft manufacturing industry in particular has seen a rapid rise in the use of composites over metallics in the past 15 years, as shown in Figure 2.3. However, for high temperature applications, ceramic matrix composites is the obvious choice as the strength of polymer based composites degrades significantly between 100-200°C, see Figure 2.4.

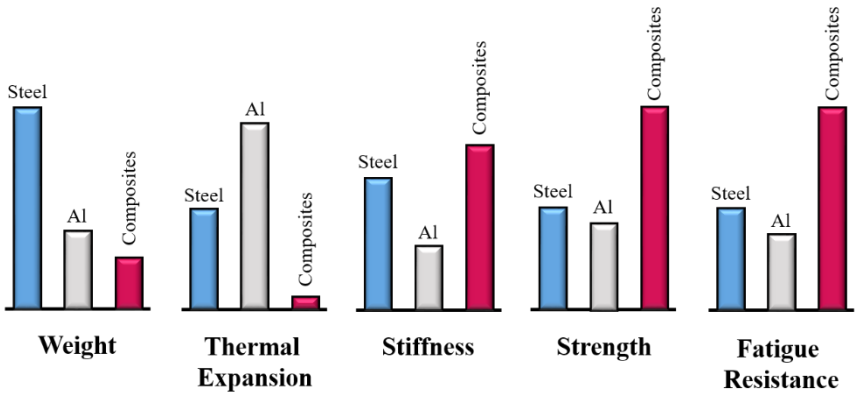


Figure 2.2: Comparison of mechanical properties between steel, aluminium (Al) and composites (adapted from [4]).

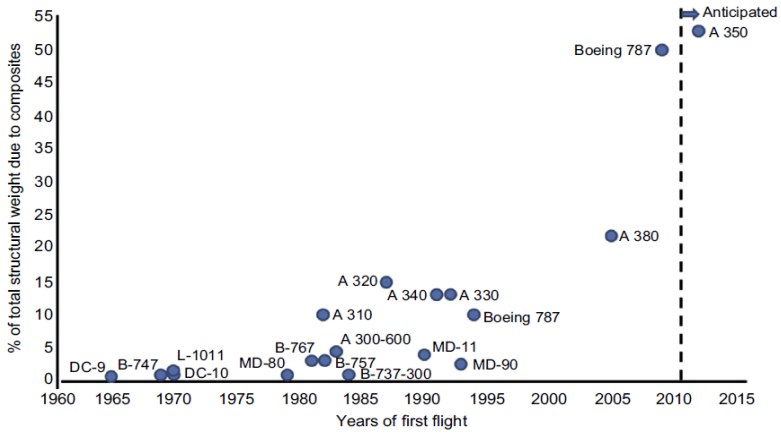


Figure 2.3: Evolution of composite material utilisation in the aircraft industry since 1960 [6].

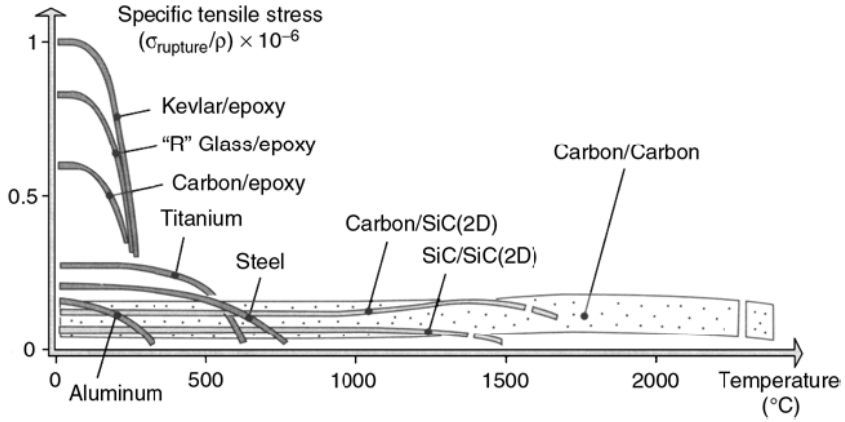


Figure 2.4: Specific strength of composites at different temperatures [3].

2.2 Fibre reinforced plastic (FRP) composites

Advanced composites is a term that is widely used to refer to fibre reinforced plastic (FRP) based materials, which are formulated by embedding the fibre reinforcement phase within a polymer resin matrix. Such composites are increasingly commonplace in applications for the aerospace (e.g. civilian/military aircraft, spacecraft and helicopters), automotive, sports equipment, construction (e.g. wind turbines, and bridges) and biomedical industries [1, 11, 12]. For instance, approximately 50% of the Boeing 787's airframe weight is comprised of FRP composites as illustrated in Figure 2.5, leading to benefits such as reduced fuel consumption when compared to traditional metallic dominant airframes [4, 6]. The range of density, tensile strength and tensile modulus values for FRP composites compared to other materials are shown in Figure 2.6. An overview of the polymer matrices and fibre types commonly employed in FRP's are discussed in the following sections.

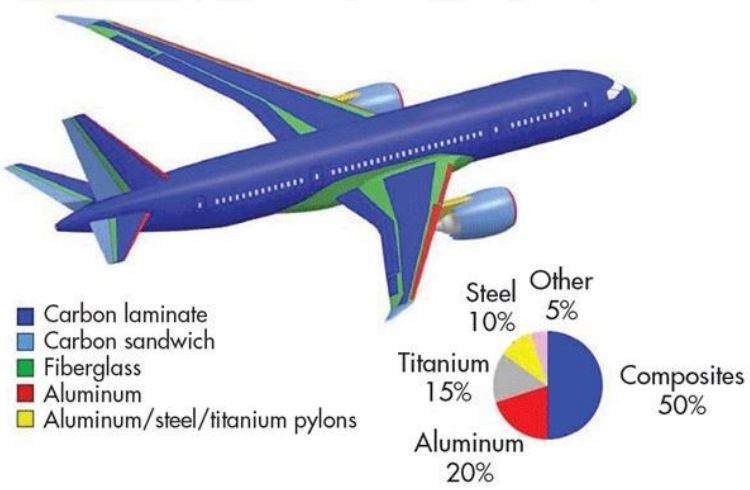


Figure 2.5: Schematic illustration of FRP composites utilisation in Boeing 787 Dreamliner [6].

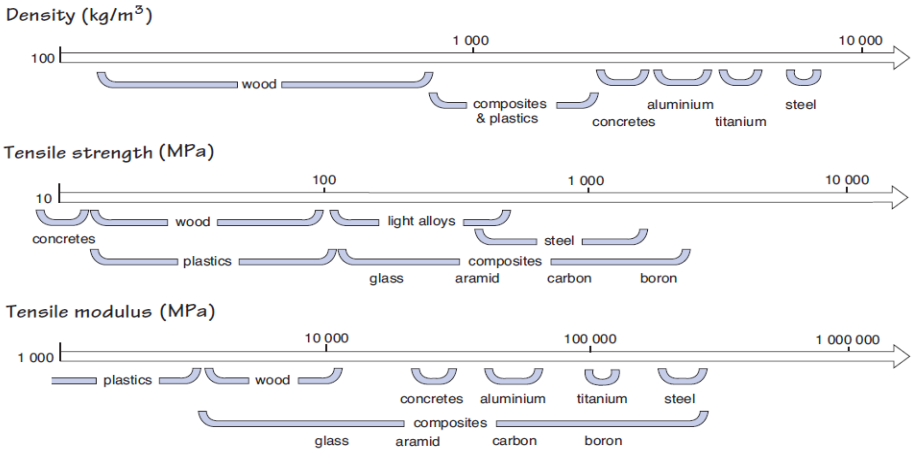


Figure 2.6: Schematic diagram comparing FRP composite properties and other materials [13].

2.2.1 Matrix materials

The matrix phase in a FRP composite plays a pivotal role in terms of protecting the fibres from chemical/mechanical/environmental damage, transferring the load to the fibres as well as maintaining appropriate direction of fibres and the spacing/alignment between them [2, 5]. The two most common types of polymers used in FRP as the matrix are thermoplastics and thermosets. The glass transition temperature (T_g) of a polymer is the point where it changes from being hard/rigid into a semi-flexible material, and is a key factor determining the selection of a matrix for elevated temperature applications [5].

In thermoplastic based polymers, the hydrocarbon molecules are joined together by covalent bonds forming chains, but weaker secondary bonds (Van der Waals) connect these chains together, which are easily broken with increasing temperature (165 to 345 °C) leading to melting of the thermoplastic [9, 14]. The absence of crosslinking and the relatively weak bonds between the chains allows for reforming/reheating/reprocessing of the thermoplastic when

heated beyond the processing/transition temperature followed by re-solidification after cooling. The arrangement of molecular patterns in thermoplastics are typically either amorphous or semi-crystalline, which relate to a random or regular order of the molecules respectively [5, 9-11]. The degree of crystallinity is significantly influenced by the cooling rate, with slower rates resulting in increased crystallinity [9]. The main advantages of thermoplastics is that the polymer matrix and fibres can be recycled/reused and has fast processing/consolidation speed (minutes or seconds) due to its high molecular weight [5]. Conversely, the high viscosity (10^4-10^7 poise) of thermoplastics restricts its wider usage in certain applications due to the lack of impregnation between the fibre and matrix, which increases the potential for formation of porosity and air bubbles in the material, resulting in poorer part quality. Furthermore, the high viscosity increases the difficulty of using manual lay-up or tape winding processes for manufacturing thermoplastics [2, 5, 10]. The most common types of thermoplastics include polypropylene (PP), polyphenylene sulfide (PPS), polyether-ether ketone (PEEK), polyether ketone ketone (PEKK), polyetherimide (PEI), nylon, polystyrene, polycarbonate and polyacetals [5, 10]. PEEK is characterised by lower absorption of water at room temperature (0.5%) compared with epoxy (4 to 5%), strong resistance to solvents and elevated service temperature up to 250°C, hence its substantial use in aerospace structures such as fuselage [10].

The molecules in thermoset polymers are primarily connected by strong covalent bonds with groups of 3D chains formed by crosslinking, which results in a strong/stiff structure. This however precludes it from being reshaped after heating/melting, unlike thermoplastic-based polymers, with material decomposition occurring with increasing heat. Thermosets generally have low viscosity (~20 poise) [5], which helps the control of impregnation duration between the fibre and matrix. However, thermosets have low recyclability, as fibre damage is likely to occur at temperatures required to separate the fibres from the matrix [2, 5, 9, 10, 14]. Polyester, vinyl ester, phenolic, cyanate esters, epoxy, bismaleimides, and polyimides are the most common types of thermosets. Polyester is relatively low cost with strong corrosion resistance and therefore employed for applications such as automotive and marine as well as internal sections of aircraft. The appearance and curing properties of vinyl ester is similar to polyester but has superior mechanical properties such as ductility and toughness compared to polyester/epoxy [10, 11, 14]. Phenolics are utilised substantially for internal parts of aircraft

and missiles due to low smoke/toxic emissions, in addition to having high resistance to fire/temperature [5, 10, 11, 13, 15].

Epoxy is extensively used in various applications due to its favourable mechanical/physical characteristics in terms of elevated strength/stiffness, low volatiles/shrinkage rate and outstanding adhesion characteristics as well as good chemical resistance. However, its relative brittleness and poor resistance to moisture are major drawbacks, in addition to its higher cost compared to polyester and vinyl ester [10, 11]. The curing temperature of epoxy ranges from 120 to 180°C depending on the application, with the maximum service temperature typically varying between 100 and 155°C respectively. Low curing temperature (120°C) epoxies are employed for aerospace, automotive and transport applications whereas high temperature (180°C) variants are used for military applications [13, 16].

The outstanding mechanical properties such as Young's modulus (3.2 – 5 and 4 – 19 GPa respectively) [3, 9] and toughness of bismaleimide and polyimide at elevated temperatures have contributed to their widespread use in missiles, aeroengines and circuit boards [10, 11, 13]. Their maximum service temperature of up to 260°C exceeds those of other thermosets [13, 15]. Table 2.1 displays the key physical and mechanical properties for the most common thermoplastic and thermoset-based polymers. Polymer based matrices however suffer from moisture absorption, which reduces the transition temperature. The rate of moisture absorption increases at high temperature, which reflects the deterioration of mechanical properties (compressive/tensile strength) of the matrix [5]. Additionally, moisture causes swelling of the matrix leading to the formation of cracks and delamination in the composite laminate.

Table 2.1: Physical and mechanical properties of various thermoset and thermoplastic polymer resins [3].

Resins	Density, ρ (kg/m^3)	Elastic Modulus, E (MPa)	Tensile Strength, σ_{Ult} (MPa)	Elongation E%	Coefficient of Thermal Expansion, α ($°C^{-1}$)	Coefficient of Thermal Conductivity, λ (W/m°C)	Heat Capacity, C (J/kg °C)	Useful Temperature Limit, T_{max} (°C)
				Polymers-Thermosets				
Epoxy, EP	1200	4500	130	2 (100°C) 6 (200°C)	$11x10^{-5}$	0.2	1000	90 - 200
Phenolic	1300	3000	70	2.5	1×10^{-5}	0.3	1000	120 - 200
Polyester	1200	4000	80	2.5	8×10^{-5}	0.2	1400	60-200
Polycarbonate	1200	2400	60		6×10^{-5}		1200	120
Vinylester, VE	1150	3300	75	4	5×10^{-5}			>100
Silicone	1100	2200	35					100 - 350
Urethane	1100	700 - 7000	30	100				100
Polyimide	1400	4000 - 19000	70	1	8×10^{-5}	0.2	1000	250-300
				Polymers-Thermoplastic				
Polypropylene, PP	900	1200	30	2 - 400	9×10^{-5}		330	70 - 140
Polyphenylene sulfone, (PPS)	1300	4000	65	100	5×10^{-5}			130 - 250
Polyamide, PA	1100	2000	70	200	8×10^{-5}		1200	170
Polyether sulfone, PES	1350	3000	85	60	6×10^{-5}			180
Polyetherimide, PEI	1250	3500	105	60	6×10^{-5}	0.2		200
Polyether-ether ketone, PEEK	1300	4000	90	50	5×10^{-5}	0.3		140 - 250

2.2.2 Fibre materials

Glass, aramid and carbon fibres are the 3 main types used as the reinforcement phase in FRP composites. These fibres are typically either continuous or discontinuous with varying lengths, but can also be supplied in the form of whiskers. Continuous fibres generally have high aspect ratios (L/D) compared to discontinuous fibres, which are normally in the region of 5-5000 [17]. The aspect ratio of whiskers varies from 10 to 1000 and is typically used for enhancing the properties of materials that are otherwise isotropic [9]. Unidirectional, bi-directional (woven), multidirectional and roving are the different arrangements for continuous aligned fibres, while discontinuous fibres are usually chopped and distributed randomly within the matrix. The type, length, volume fraction and orientation of fibres has a significant influence on the overall properties of the composite laminate, such as density, tensile/fatigue strength and thermal/electrical conductivities [2, 5, 14].

2.2.2.1 Glass fibre

The emergence of glass fibre reinforced polymer (GFRP) composites in the market and their utilisation in commercial and military aircraft date back to the 1940s [2, 14]. The cost of glass fibres are comparatively lower than other fibres and has exceptional corrosion resistance [2]. Electrical glass (E-glass) and high strength (S-glass and S2-glass) are the most common types of glass fibres while C-glass is normally used in applications where corrosion resistance is key. The good electrical resistivity/insulating properties of E-glass makes it suitable as an electrical insulator [10, 11, 14], while S-glass and S2-glass fibres have higher strength (4.38–4.59 GPa) and are more expensive than E-glass. Despite having comparatively low stiffness/service temperature (< 200°C), intermediate strength and high strain/elongation to failure, glass fibres are widely employed in marine, automotive, wind turbine blade and pipe manufacturing.

2.2.2.2 Aramid fibre

Since the 1970s, aramid fibres that are made of aromatic polyamides have been employed in several applications including aviation, sporting apparatus and preservative/protective clothes [7, 9]. Nomex and Kevlar are examples of well-known commercial names for aramid fibres, with the latter comprising a range of grades including 29, 49 and 149, each having varying mechanical properties. For instance, Kevlar 49 and 29 exhibit high (124-131 GPa) and low (62-83 GPa) stiffness respectively whereas Kevlar 149 has the top tensile modulus (186 GPa) [7, 11, 18, 19]. In general, aramid fibres have higher strength/stiffness but lower compressive strength compared to glass fibres, as well as the highest specific strength (2000 kN.m/kg)

amongst the 3 fibre types [3, 10, 14]. Water absorption of components made using aramid fibres can reach up to 8% of total part weight [11], although the moisture absorbed by Kevlar 149 is approximately 70% lower than Kevlar 49 under similar conditions [14].

2.2.2.3 Carbon fibre

Carbon fibres are mainly composed of carbon or graphite, with the difference primarily due to material purity and processing temperature. The carbon content in carbon fibres are typically up to 90%, and > 99% in graphite fibres [8, 9], while the fibre structure can be crystalline or amorphous [20]. Common trade names of carbon fibres include Celion and Thornel [8, 21]. The demand for carbon fibre has increased dramatically over the years, with up to 17500 and 9800 tons used for industrial and aerospace applications respectively in 2010 [20]. The manufacture of carbon fibres involves the pyrolysis of a precursor polymer resin such as PAN (polyacrylonitrile) or pitch. Typically, PAN based carbon fibres possess higher compressive strength but lower thermal/electrical conductivity compared to those made with pitch. The tensile modulus of carbon fibres can range from 207 to 1035 GPa [14] and exhibits superior strength/stiffness to weight ratio compared to other types of fibres [7]. Furthermore, carbon fibres have good rigidity, electrical/thermal conductivities, dimensional accuracy (zero CTE (coefficient of thermal expansion)) and corrosion/fatigue resistance, albeit being costlier to produce compared to other fibres, as detailed in Figure 2.7. Carbon fibres are typically classified according to their mechanical properties (modulus and strength) or heat treatment. There five main categories of carbon fibres when designated based on mechanical properties are; ultra-high modulus (UHM, E > 450GPa), high modulus (HM, 350-450 GPa), intermediate modulus (IM, 200-350GPa), low modulus (E < 100GPa)/high tensile (HT, σ > 3 GPa) and super high tensile (SHT, σ > 4.5 GPa) [12, 22]. Conversely, the classification based on heat treatment includes high (HHT, T > 2000ºC), intermediate (IHT, T ≥ 1500ºC) and low heat treatment (LHT, T < 1000ºC).

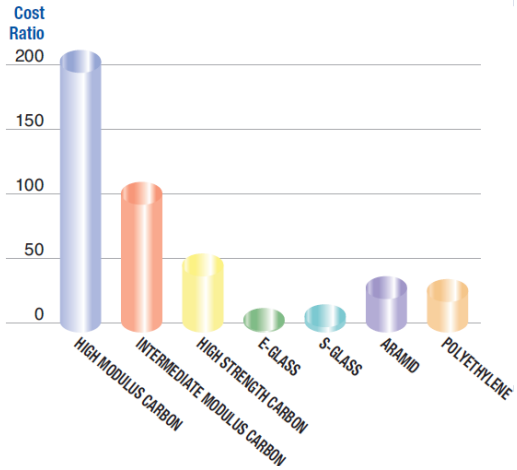


Figure 2.7: Cost ratio for different types of fibres [13].

A comparison of the mechanical and physical properties of selected carbon, aramid and glass fibres are detailed in Table 2.2.

Table 2.2: Physical and mechanical properties of various fibre types [9].

Characteristics	PAN-based carbon		Kevlar 49	E-glass	S-glass
	HM	HS			
Diameter (μm)	5-8	6-8	8-14	10-20	10-20
Density (kg/m^3)	1.81	1.78	1.44	2.62	2.46-2.49
Young's modulus (GPa)					
Parallel to fibre axis	400	230	131	80-81	88-91
Perpendicular to fibre axis	12	20	70	-	-
Tensile strength (GPa)	2.5-4.5	3.8-4.2	3.6-4.1	3.1-3.8	4.38-4.59
Strain to failure (%)	0.6	2.0	2.8	4.6	5.4-5.8
Coefficient of thermal expansion (10^{-6} K^{-1})					
Parallel to fibre axis	-0.5	-0.6	-4.3	6.0	2.9
Perpendicular to fibre axis	7.0	10.0	41	-	-
Thermal conductivity (W/m. K)	70	11	0.04-1.4	10-13	1.1-1.4
Specific heat (kJ/kg. K)	0.7-0.9		0.769	0.45	0.41

2.2.2.4 Other fibres

Alternative materials such as boron, silicon, polyethylene and ceramic fibres are also used as reinforcement in composites. Boron fibres impregnated in an epoxy matrix are employed primarily in the construction of military aircraft components including stabiliser skins and fins [11, 14]. Boron fibres have relatively high modulus values ranging from 379 to 414 GPa, see Figure 2.8 for comparison of specific modulus and strength to other fibre materials and Al alloy. However, the hazardous nature of boron fibres, which can fatally affect the stomach, kidney and brain even after brief exposure to boric acid (30 gram), as well as high costs are the main reasons preventing its wider use [11, 14, 23]. Ceramic fibres are typically employed for components operating in elevated temperature (up to 2200 °F) environments such as turbine

blades in gas engines [11]. Aluminium oxide (melting point of 2045 °C) and silicon carbide (melting point of 2830 °C) are the most common types of ceramic fibres, which can maintain their strength above 650°C and 1370°C respectively. Silicon carbide has superior electrical (0.1-10^{-4} S/m)/thermal (80-130 W/m.°C) conductivities than aluminium oxide (10^{-12}-10^{-14} S/m /18.7-32.4 W/m.°C), as well as a lower thermal expansion coefficient (4-4.8 10^{-6}/°C) [14]. Spectra fibre is the trade name of oriented polyethylene/extended chain polyethylene fibres, which has a higher strength/modulus to weight ratio compared to carbon fibre. It is widely used in marine applications (e.g. boat hulls) due to its exceptional abrasion resistance and low absorption of moisture. However, its limited use in structural applications is attributed to poor adhesion of the fibre and matrix materials and its low service temperature (80-90 °C) [9, 14].

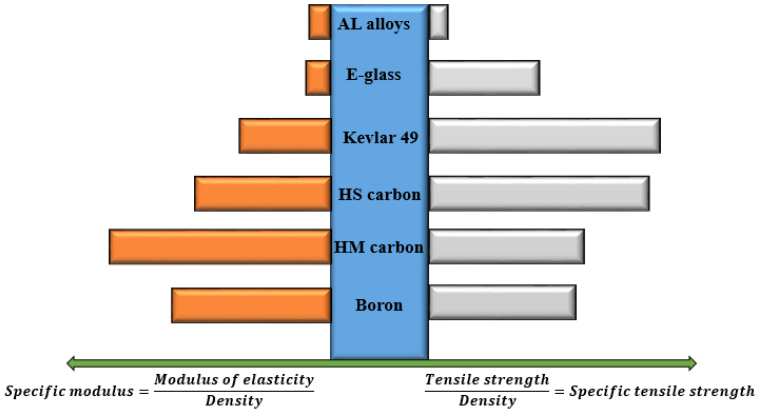


Figure 2.8: Comparison of specific strength/modulus for different types of fibres (adapted from [3]).

2.2.3 Fibre architecture in composites

Fibre architecture describes the arrangement of fibres in composite materials and is grouped into three main categories covering; (i) unidirectional (e.g. yarns, tows and roving tapes); (ii) woven or non-woven fabrics (e.g. mats), which are also denoted as bidirectional; and (iii) multidirectional fabrics where the fibres are aligned in more than two directions [3]. Figure 2.9 shows a schematic of unidirectional and bidirectional fibre arrangements. Unidirectional tape, prepregs and yarns/tows typically have fibres pre-impregnated and ordered in a single direction within a resin matrix (e.g. epoxy), where material strength is considerably higher along the fibre direction [11]. However, unidirectional composites are prone to delamination during machining [24].

Fabric based architectures such as woven and non–woven or non-crimp fabric (NCF) provides greater flexibility in manufacturing of intricate shapes due to ease of deformation than unidirectional configurations. This bidirectional form provides uniform strength in all

directions and overcomes the defects of unidirectional fibres. In woven fabric, the fibres are weaved in two mutually perpendicular directions where the longitudinal orientation is known as warp, while the transverse direction is referred to as weft/fill [3, 11, 14]. The fill yarn is passed over and then underneath the warp repeatedly to form the woven architecture. Woven fabric is also used in prepreg form similar to unidirectional tape as displayed in Figure 2.10. Fabric crimp describes the degree of yarn/fibre waviness or bending in the weave structure, where high crimp levels indicate increased stiffness but poor drapeability (extent of reinforcement conformity to the die shape during manufacturing). Conversely, low crimp values relates to straighter fibres, which leads to greater flexibility in the fabric, improved drapeability and superior mechanical attributes [9].

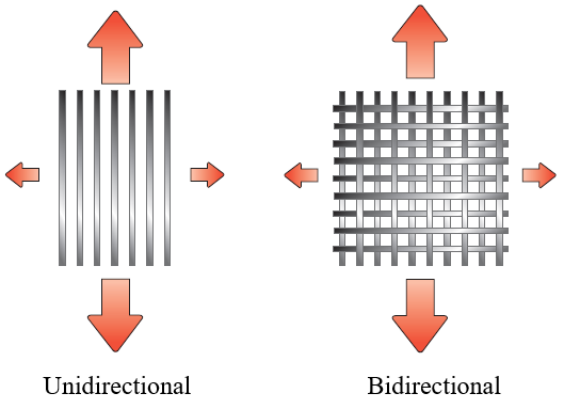


Figure 2.9: Schematic representation for unidirectional and bidirectional fibre architecture [24, 25].

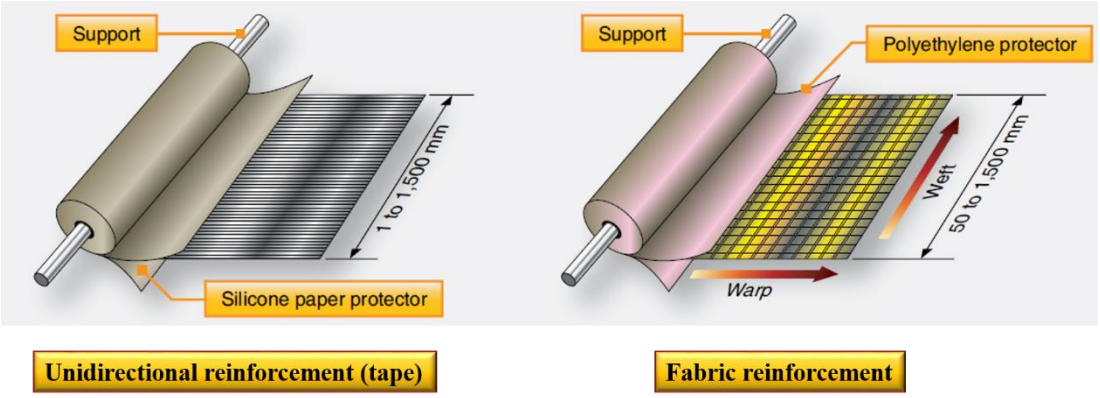


Figure 2.10: Schematic representation for unidirectional and fabric prepreg tapes [11].

Woven structures include different fibre patterns such as plain, basket, stain and twill weaves [26]. In a plain weave, the fill yarns alternatingly passes over one and then underneath the next warp [3, 11] as shown in Figure 2.11(a). Similarly, basket weaves have the same structure except that 2 yarns are utilised instead of one for each warp and weft [9]. As for stain weaves, the weft yarns overstep several warp bundles before moving underneath another warp. Stain

weaves have distinctly greater flexibility and drapeability compared to plain weaves, due to inherently lower crimp as a result of its structure [9, 15]. The most popular types of stain weaves are 3 and 5 harness. For example, a 5 harness stain weave means that a weft yarn is threaded above four consecutive warp yarns before going beneath the fifth as detailed in Figure 2.11(b). A twill weave configuration is formed by regular steps or offsets, resulting in a diagonal pattern. The example shown in Figure 2.11(c) is a 2 x 2 twill weave, where the weft yarn crosses on top of two warp bundles before moving below the next two warps in a repeating fashion. Low distortion and fabric stability are key advantages of plain weaves, however the high crimp adversely affects its mechanical properties as well as drapeability. In contrast, a 5 harness stain weave has higher density and superior mechanical properties compared to other weave patterns in addition to good drapeability, however it provides high distortion through its handling which attributed to its low number of interlaces per area [5].

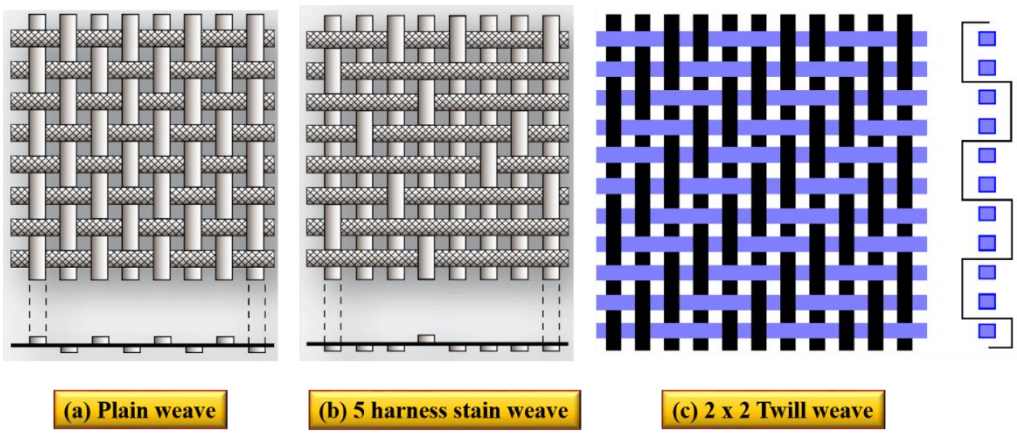


Figure 2.11: Schematic illustration for different woven fabric styles (a) plain weave, (b) 5 harness stain weave and (c) 2 x 2 twill weave [11, 15].

Non-crimp or multiaxial fabrics can be obtained by stitching unidirectional fibre layers together using threads (e.g. polyester) [15], see Figure 2.12. The non-crimp architecture provides higher strength compared to woven fabrics due to the straightness of fibres. The availability of rapidly producing high thickness of NCF eliminates the need additional manufacturing steps as single layer laminates can be produced [27]. Despite its relatively low cost, NCF often contain gaps with considerably higher waviness [28].

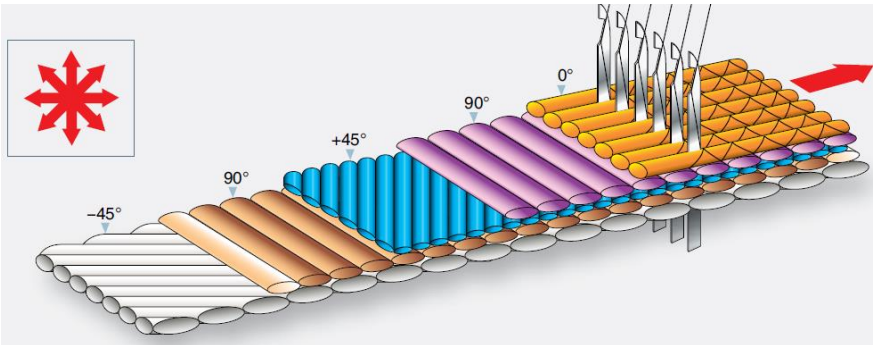


Figure 2.12: Schematic representation for non-crimp fabrics [11].

2.2.3.1 Prepregs

Prepreg (pre-impregnated fibres or fabrics) is a term used to describe thin composite sheets composed of fibres impregnated within a resin matrix. There are several forms of prepregs such as unidirectional tapes and fabric prepregs as shown previously in Figure 2.10, as well as rovings and chopped mat prepregs [10, 11]. Prepregs are generally stored at low temperatures (0 °F) prior to use/lay-up and before curing in an autoclave or oven for material consolidation. Prepregs are generally wound in rolls and covered with plastic film in order to protect the prepregs from damage and exposure to moisture as well as to facilitate storage and transportation. Thermoset based prepregs and in particular epoxy tapes, are used extensively in the aerospace sector [11] and various other industries have thicknesses ranging from 0.127 to 0.254 mm [10]. Thermoset prepregs have better drapeability and are used more widely compared to thermoplastic-based counterparts, however they have a restricted shelf life (~ 2 weeks for styrene at 25 °C) [29] as well as longer processing time of 1 to 8 hours compared to only several minutes for thermoplastics. Furthermore, aside from having higher toughness, thermoplastic prepregs have the advantage of being recyclable, flexibility for reshaping and an unlimited shelf life during absence of refrigeration/freezing conditions [10]. The principal benefits of prepregs include reducing damage of fibre through handling, good dispersion of short filament leading into enhancement of laminate attributes, reduced void formation and increased fibre wetting due to its ability for withstanding high curing pressure [28].

2.2.3.2 Laminates

The thickness of FRP composites vary depending on the application and are usually determined based on the load that has to be supported during service. This generally requires the stacking of multiple layers of fibres and consolidated to form a laminate. Each group of layers is called laminae (plural of lamina) [30]. A lamina or ply/lay-up is a thin layer of large number of incorporated fibres with a thickness ranged between 0.1 and 1 mm [5, 14]. They are composed

of fibres, matrix, fillers, coupling agent and other additives. The fibres within a lamina can be continuous or short and aligned in single or multiple directions as illustrated in Figure 2.13. Hybrid laminates are those that incorporate two or more types of fibres within their structures and mainly consists of two configurations; interply and intraply. The different fibres in interply hybrid laminates are placed in separate laminas while the varying fibres are mixed within the same ply for intraply laminates [14].

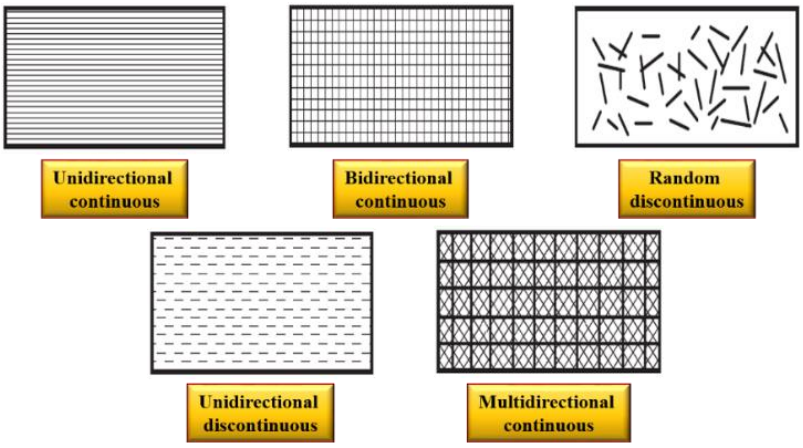


Figure 2.13: Fibre arrangements in lamina construction [14].

The fibre orientation of individual plies/laminas within a composite laminate has a significant influence on material properties and therefore an orientation coding system (shorthand) is used to identify/describe the laminate lay-up. Plies with the longitudinal fibre direction oriented along the x-axis is denoted as 0°, with positive ply angle rotation measured counter clockwise, as shown in Figure 2.14. The laminate lay-up description/code is detailed in square brackets with the orientations of consecutive laminae separated by a slash (/). A rounded bracket is used to indicate where there are two or more adjacent laminae arranged in the same direction within the lay-up, with a subscript to indicate the number of identically aligned plies. A symmetric laminate is where the lay-up configuration of half the plies is mirrored about the mid plane [31, 32], and is denoted by the subscript "S" outside the square brackets. In contrast, the subscript "f" is used to indicate woven fabrics/plies [31]. The laminate is considered to be balanced if an equal number of positive and negative oriented plies are employed [32]. Figure 2.15 illustrates example codes for different laminate lay-up configurations. While FRP composites are largely anisotropic materials, certain applications, particularly those in the aerospace sector, require composites with isotropic properties. Therefore, quasi-isotropic laminates have been developed, however the isotropy are usually only present in the two planar directions (x and y-

axes) [21, 32]. In order to fabricate quasi-isotropic laminates, they must contain at least three plies with each layer having the same stiffness and thickness [21]. Some of the common orientations of the stacked plies include 0°, 90°, 45° and -45° or 0°, 60° and 120°. Figure 2.16 illustrates the difference between unidirectional and quasi-isotropic laminate lay-ups.

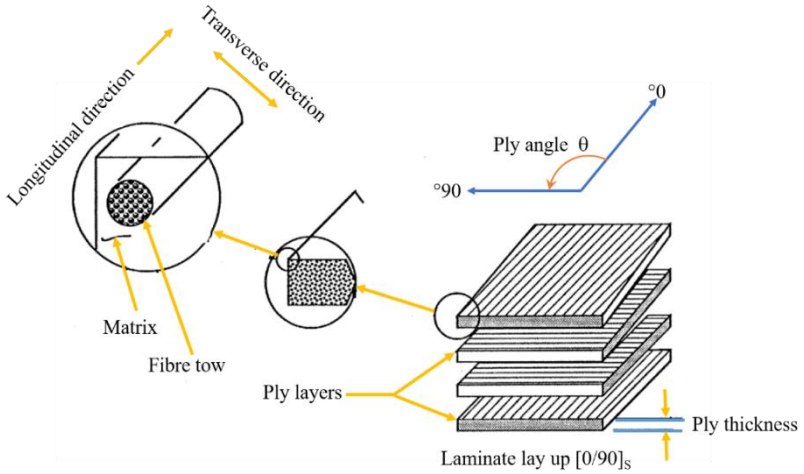


Figure 2.14: Composite laminate anatomy [21].

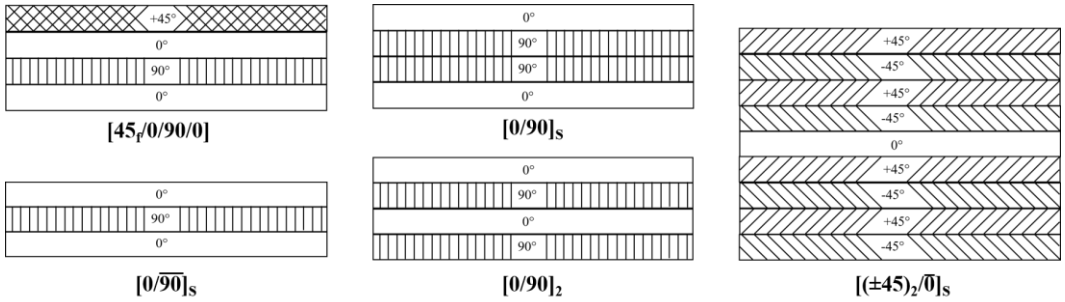


Figure 2.15: Laminate code examples [31].

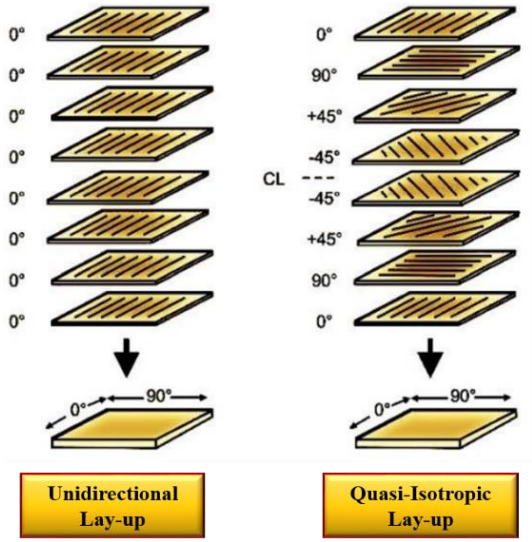


Figure 2.16: Comparison between unidirectional and quasi-isotropic lay-up [33].

2.3 Carbon fibre reinforced plastic (CFRP) composites

Carbon fibre reinforced plastic (CFRP) composites have been employed in the aerospace industry since the 1960s, due to its superior mechanical/physical properties over more conventional metallic alloys. These include high strength to weight ratio (~1200 to 4500 kN.m/kg), comparable elastic modulus (75-105% of steel), low weight/density (1.5 – 2 gm/cm^3), strong resistance to corrosion, flexibility for tailoring material properties for different applications, good dimensional stability due to extremely low (nearly zero) or negative thermal expansion coefficients and excellent damping characteristics [2, 9, 14, 25, 34-38]. The estimated weight reduction achieved by replacing titanium and aluminium alloys with CFRP in primary and secondary aircraft structures are up to 20% and 40% respectively [16, 26], resulting in lower fuel consumption and emissions, in addition to higher payload capacity [14, 16, 24, 25]. Figure 2.17 show examples of major structural components of the Airbus 380 that are designed and fabricated with monolithic CFRP [39], while the significant performance benefits of CFRP in terms of structural static and fatigue efficiency relative to AA7075 aluminium and Ti-6Al-4V titanium alloys are detailed in Figure 2.18. Apart from airframe components, CFRP is also increasingly employed in the space, marine and automotive industries, as well as for manufacturing sporting products (e.g. bike frames, rackets, fishing poles and skis), medical parts, piping, gas tanks, pressure vessels, engine casings and fan blades.

The manufacturing/fabrication processes for composite materials are typically categorised into two groups based on the type of polymer resin (thermoset or thermoplastic) used, although a large majority of composites (around 75%) utilise thermoset resins due to their superior characteristics (e.g. modulus of elasticity and tensile strength) compare to thermoplastics. There are several fabrication processes including manual lay-up that involves wet (hand laminating) or prepreg (autoclave processing/vacuum bagging) lay-up, spray-up, bag moulding process, pultrusion, filament winding, resin transfer moulding (RTM), reaction injection moulding (RIM), compression moulding and liquid composite moulding [1, 10, 40]. Table 2.3 outlines the various manufacturing processes typically employed based on matrix type.

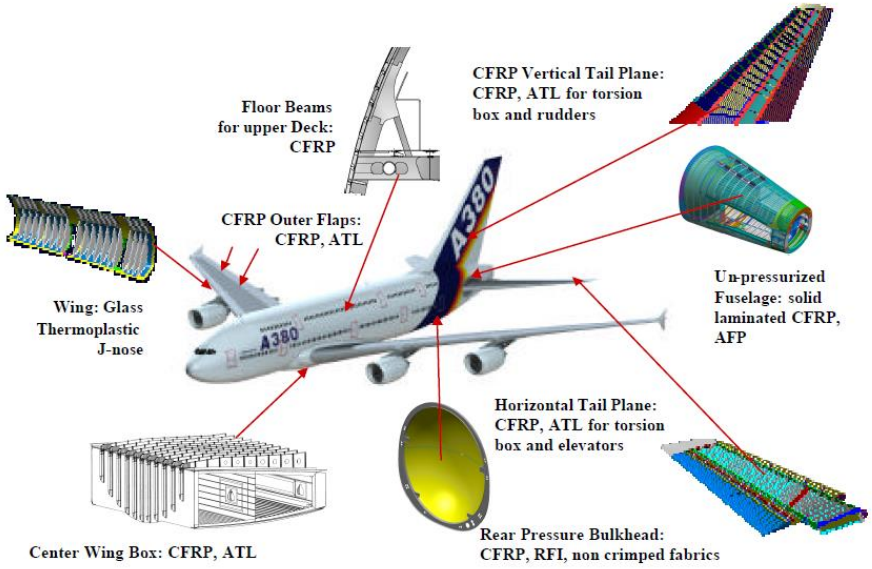


Figure 2.17: The main applications of monolithic CFRP in Airbus A380 [39].

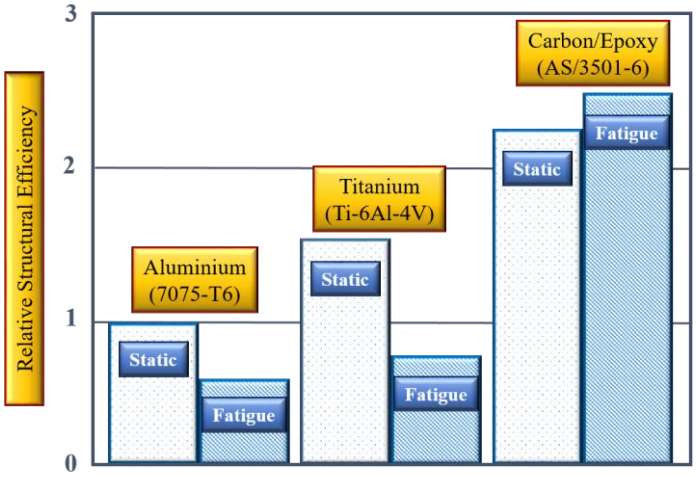


Figure 2.18: Relative efficiency of structural aerospace materials (adapted from [5]).

Table 2.3: Classification of manufacturing processes [10].

Composite manufacturing			
Thermoset		Thermoplastic	
Short fibre	Continuous fibre	Short fibre	Continuous fibre
- SMC moulding - SRIM - BMC moulding - Spray-up - Injection moulding	- Filament winding - Pultrusion - RTM - Hand lay-up - Autoclave process - Roll wrapping - SCRIMP - Bladder moulding	- Injection moulding - Blow moulding	- Thermoforming - Tape winding - Compression moulding - Autoclave - Diaphragm forming

2.3.1 Machinability of CFRP

Machining of CFRP is generally necessary to produce features/shapes and finish parts to the required final dimensions. While drilling is extensively used for most composite materials, other traditional machining operations such as milling, trimming/routing, grinding and turning are also employed for certain products or applications. The following sections will outline some of the key research in drilling and milling of CFRP as well as the associated challenges/limitations of conventional machining processes.

2.3.1.1 Drilling of CFRP

Drilling is the most common machining operation used on CFRP in the aerospace sector to generate holes of various sizes for rivets/bolts to facilitate the assembly of complex parts [41, 42] and represents almost 50% of the overall machining costs [43]. Holes drilled in small aircraft number over 100,000 whereas in large passenger airplanes, this can exceed a million holes. Additionally, private jets and bomber aircraft can have up to 400,000 and 2,000,000 holes respectively [43]. The importance and need to continuously improve process performance and part quality has resulted in considerable research to understand material behaviour and removal mechanisms during drilling of CFRP composite laminates.

A review of the literature reveals that a significant proportion of experimental research involving conventional drilling of CFRP has broadly focused on 4 areas; effect of cutting conditions on responses (e.g. thrust force, delamination and surface roughness), delamination free drilling, influence of geometry/materials of drill bit on hole quality and thrust force in addition influence of tool wear on thrust force and hole quality [44]. A commonly occurring defect in CFRP following drilling is delamination of the plies, particularly at the hole entrance and exit location, which severely compromises workpiece properties and hence joint integrity. Delamination is normally observed at the entrance (peel up mechanism) and exit (push out mechanism) of the holes as shown in Figure 2.19 [25, 45]. This mainly occurs when the thrust force during drilling exceeds the interlaminate strength of the CFRP, and addition improper fastening process [46-48]. Delamination is characterised by means of delamination factor which gained by dividing maximum damage diameter over nominal diameter for drilling however the diameter is replaced with damage width in milling process, see Figure 2.20.

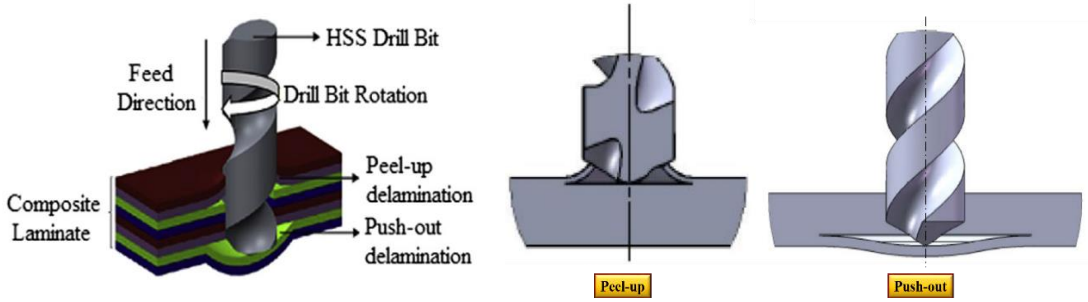


Figure 2.19: Schematic illustration for 2D and 3D delamination in drilling process [25].

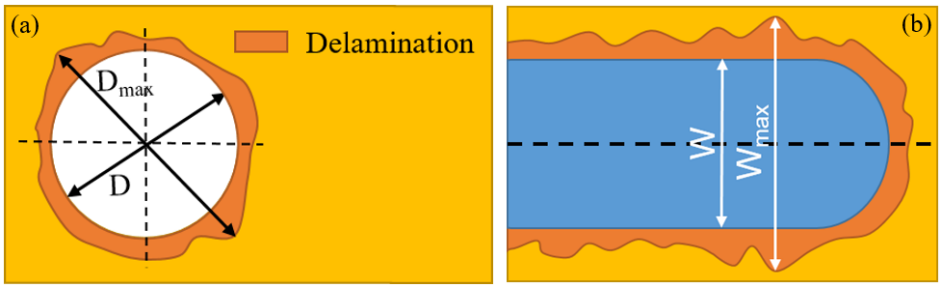


Figure 2.20: Schematic showing calculation of delamination factor in (a) drilling, and (b) milling [25, 49].

Comprehensive studies involving the effect of key process variables including feed rate, workpiece material, tool geometry/material and cutting speed on delamination and thrust force have been reported by various researchers [46, 50-56]. The delamination factor (F_d) is a generally accepted empirical parameter to quantify the extent of machining induced delamination in CFRP. A novel digital image technique was proposed by Davim et al. [52] which utilised image analysis for determining adjusted delamination factor at the hole entry and exit in CFRP laminates. This proposed factor considered area damage including cracks/breaks induced through drilling process. Accordingly, the outcomes pointed out the suitability of this approach in delamination assessment where both factors revealed close values (F_d=1.15 and F_{da} = 1.16) at small area damage meanwhile adjusted factor (F_{da} = 1.88) is higher than conventional one (F_d=1.76) by increasing this area. Moreover, this approach clarified the developed damage by changing cutting conditions and area of damage could be recorded using acquisition system. Furthermore, new analytical model via dry and cryogenic drilling has been proposed by Joshi et al. [57] to estimate delamination factor (F_{fa}) where the effect of thrust force was considered in the proposed model. The obtained factors evaluated at different levels of feed rate (0.03, 0.06 and 0.09 mm/rev)/cutting speed (100, 125 and 150 m/min) and compared with those gained by Davim's (F_{da}) and two-dimensional models (F_a). Surface roughness and thrust force have been investigated as well. It was found that the predicted values of proposed factor (F_{fa}) were close values to Davim's factors (F_{da}) during dry cutting meanwhile they revealed closeness to two-

dimensional factors via cryogenic machining. Finally, high feed rate resulted in increasing thrust force, surface roughness and delamination factor for both cutting methods.

The effect of prepreg form (UD/woven/type 977-2/HTS, 8552/AS4 and MTM44-1/HTS) and feed rate on torque/thrust force, hole circularity and delamination (hole entry and exit) when drilling CFRP using tungsten carbide tools (1.0/1.5 mm for pilot/sizing diameter respectively) was evaluated by Shyha et al. [51]. The longest tool life (3750 drilled holes) was obtained at high feed rate (0.4 mm/rev) when drilling the woven laminates (MTM44-1/HTS) and low feed rate (0.2 mm/rev) was recommended in order to avoid drill fracture. The maximum thrust force and torque did not exceed 125 N and 65 N.mm respectively in any of the tests. Delamination factor results indicated that delamination was typically more severe at hole exit (maximum F_d of 2.1) compared to the entrance position (maximum F_d of 1.8). Tsao and Hocheng [58] employed advanced imaging techniques involving X-ray/CT (computed tomography) scan and ultrasonic C-scan to examine the delamination in drilled CFRP workpieces to overcome the difficulty of visual inspection caused by dark colour of fibres. Based on the results, it was concluded that X-ray revealed its feasibility in delamination assessment by achieving similar performance to C-scan that was widely used for this test. However, it overrides the problem of acoustic scattering takes place through composite detection by C-scan.

A neural network system was implemented by Stone and Krishnamurthy [59] to identify the correlation between feed rate and thrust force when drilling CFRP in order to reduce/minimise delamination. The proposed scheme showed an acceptable level of error of thrust force and was found to be a viable method for reducing workpiece delamination where the obtained delamination diameter using neural controller (6.9 and 8.4 mm) was quite small compared with constant feed rate approach (8.4 and 9.9 mm) for hole diameters of 6.65 and 8.33 respectively. Likewise, a combination of Taguchi experimental design and multiple response optimisation was employed to identify process conditions for damage free drilling [60]. The results were used to produce a process parameter map, which suggested operating at high cutting speed and low feed rate to obtain delamination free surfaces with low roughness. Workpiece delamination was also shown to be significantly reduced or prevented when pre-drilling smaller pilot holes prior to the full sized holes was employed because of its influence in reducing thrust force (~ 25 to 50%) and the critical value of thrust force (11%) [61]. The delamination takes place when the thrust force is higher than critical value, therefore the proposed approach assisted in delamination reduction. The use of a novel V-shape drill design proposed by Su et al. [62]

exhibited reduced workpiece damage in terms of delamination which reached up to 74 and 74.7% compared to dagger and brad-spur drills. Durante et al. [63] evaluated the performance of a circular drilling strategy using a range of tool diameters and operating parameters (feed rate and cutting speed) in an effort to eliminate delamination when drilling CFRP. Lower thrust forces as well as superior hole quality/reduced damage was obtained in comparison to conventional drilling as shown in Figure 2.21.

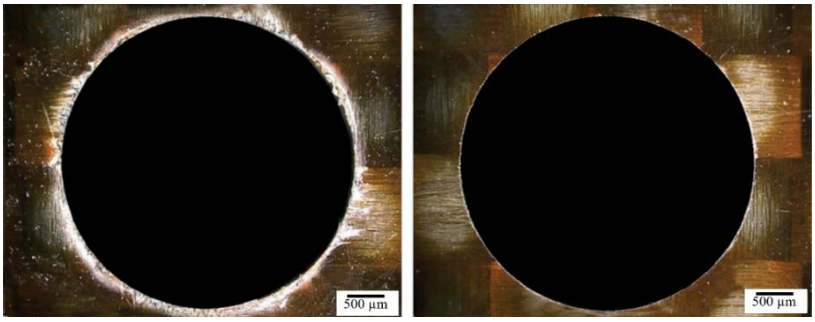


Figure 2.21: Exit hole surface induced at same cutting conditions (*Vc* =75 m/min and *f*= 62 mm/min) and tool diameter (ϕ 6 mm) via (a) conventional drilling and (b) circular drilling [63].

2.3.1.2 Milling/trimming of CFRP

Fibre reinforced plastic composite parts are typically designed and fabricated to near net shape, however machining is still normally required for removing excess material to achieve desired dimensional tolerance/accuracy. Here, milling is commonly employed for various operations including end/profile cutting, slotting, deburring and edge trimming [64], with a number of examples illustrated in Figure 2.22.

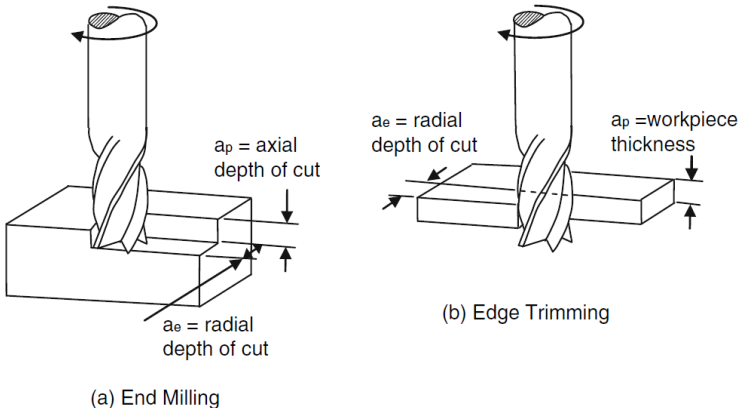


Figure 2.22: Common milling operations for CFRP; (a) End milling, and (b) Edge trimming [9].

Although there has been considerably less research involving milling/trimming of CFRP compared to drilling, the majority of available work has focussed on investigating the effect of cutting variables (e.g. cutting speed, feed rate, depth of cut), fibre direction and tool geometry/configuration/material on tool wear, cutting forces and workpiece surface integrity

(e.g. surface roughness/damage and delamination) [49, 65-67]. Pecat et al. [66] carried out experiments to study the influence of workpiece temperature on cutting force and surface/subsurface damage when milling unidirectional CFRP at different fibre orientations over a range of cutting speeds. Severe damage including large cracks (300 µm) from the surface into the workpiece material was observed when machining -45°orientation (V_c=100 m/min and T_w=20°C) followed by 90°, while apparent cracks extended into the workpiece at an angle of 18° from the machined surface at workpiece temperatures of -40 and 20°C (V_c=100 m/min and 90°). These cracks disappeared at high temperatures likely due to the absence of brittleness. Decreasing workpiece temperature generally resulted in higher cutting forces as shown in Figure 2.23, with the best results obtained at 80°C regardless of cutting speed, which was closest to the epoxy transition temperature. The application of low frequency oscillation (29.08 Hz) using a special CFRP-tool (slot drill) and 0.011 mm spindle stroke [68] eliminated workpiece delamination however there was no notable improvement in surface roughness compared to conventional milling. Hintze and Brugmann [69] reported that milling unidirectional CFRP with an inclined end mill (φ 8 mm) axis toward and perpendicular to feed direction resulted in a delamination free surface on the top layer of the workpiece and elimination of fibre protrusion by following the optimized strategies for up/down milling.

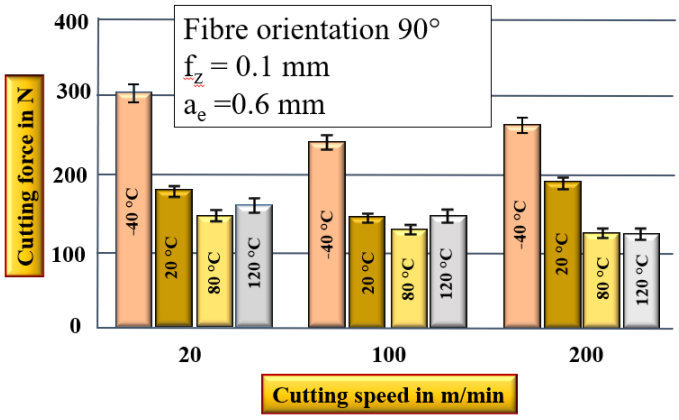
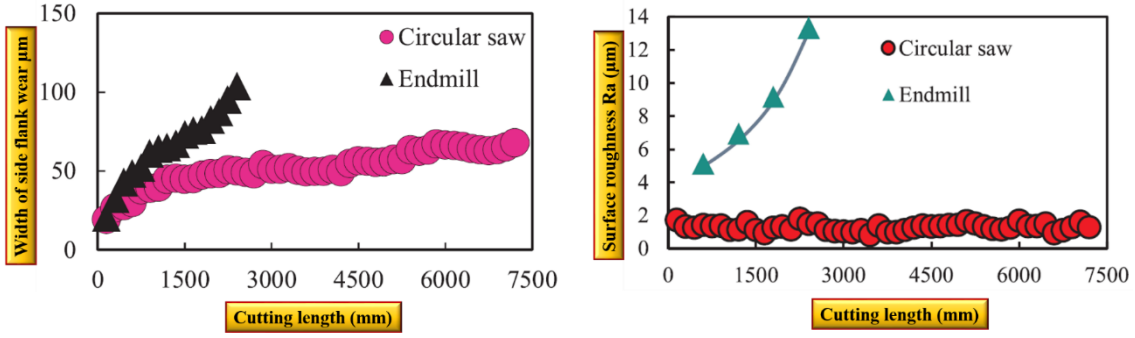


Figure 2.23: Effect of workpiece temperature on cutting force at different cutting speeds (adapted from [66]).

El-Hofy et al. [70] compared the performance of polycrystalline diamond (PCD) and tungsten carbide (WC) end mills when routing unidirectional CFRP at different fibre orientations under dry and chilled air environments. Machining with chilled air was found to significantly reduce workpiece damage compared to dry conditions, where burning and resin melting was prevalent. Surface defects were minimised when machining along the 0° fibre direction whereas matrix cracking and fibre pull out were evident when cutting at fibre orientations of 90° and 135°. The

PCD tools achieved higher tool life with cut length up to 28000 mm and flank wear less than 0.18 mm (~0.1 mm for CTB-010) compared to WC tools (less than 900 mm cut length for 0.3 mm wear). Additionally, the lowest roughness of 3.6/3.65 µm for Ra and Sa respectively was achieved with PCD (CMX-850 grade).

A comparison between circular sawing and end milling for cutting multidirectional CFRP was evaluated with respect to workpiece surface roughness and tool wear [71]. Lower workpiece surface roughness and longer tool life was obtained when sawing compared to end milling, see Figure 2.24. This was due in part to the use of damping sheets (manganese) placed on both sides of the cutting disc to suppress vibration in circular sawing.



(a) (b)

Figure 2.24: Comparison between circular saw and end milling via multidirectional CFRP machining (a) Flank wear and (b) Surface roughness [71].

2.3.2 Challenges in conventional machining of CFRP

Despite the considerable amount of research over the past two decades, there remains a number of challenges and shortcomings relating to the conventional machining of CFRP composites. Rapid tool wear leading to short tool life is typically encountered even with WC tooling, due to the highly abrasive nature of carbon fibres and heterogeneity/anisotropy of CFRP [51, 59], although the use of advanced coatings and PCD cutters have partially mitigated this issue. The elevation of tool wear and deterioration in tool geometry further exacerbates workpiece damage such as fibre pull out, fibre fracture, delamination, interlaminar/matrix cracking, splintering, fuzzing, fibre-resin de-bonding, spalling and thermal degradation [25, 37, 48, 54, 60]. Workpiece delamination is the predominant defect observed especially in drilling, which leads to diminished load bearing capacity, compression/fatigue strength, assembly tolerance and structural integrity of the part [5, 37, 48, 72]. Indeed, approximately 60% of assembled CFRP components in the aircraft industry are rejected/scrapped due to delamination [57, 59].

Aside from workpiece integrity and tool life limitations, another important albeit less often considered issue, is that related to health and safety. Unlike metallic materials, the swarf generated during conventional cutting of CFRP is largely in the form of dust sized particles (average size of ~6 μm) consisting of the matrix resin and carbon fibres, which are generally airborne especially under dry machining conditions. Additionally, epoxy decomposition resulting from high cutting temperatures can discharge harmful fumes. Exposure to the CFRP debris and gasses are potentially hazardous to operators, which can be inhaled or cause irritation to skin and eyes. Furthermore, the abrasive carbon fibres can lead to progressive wear of machine tool guideways and spindles, as well as short-circuiting of internal electrical components [9, 24].

The problems/challenges associated with conventional machining of CFRP composites have motivated research to explore alternative techniques such as non-conventional machining processes, which are discussed in the following section.

2.4 Non-conventional machining of CFRP

2.4.1 Water jet machining

Water jet machining (WJM) utilises a focussed, high-pressure (up to 450 MPa) stream of water, which is capable of cutting a wide range or metallic and non-metallic materials. Amongst the principal advantages of pure WJM (PWJM) over conventional cutting processes include the absence of tool wear or any adverse thermal effects (e.g. no heat affected zones), relatively low machining forces (15 – 47 N) [73] and non-toxic/environmentally safe operating conditions [9, 74, 75]. A more commonly employed process configuration is abrasive water jet machining (AWJM), which involves the addition/mixture of abrasive particles (e.g. garnet) into the water to increase cutting efficiency/productivity, particularly for hard or difficult to cut workpiece materials including CFRP composites.

2.4.1.1 Drilling operation

The use of water jet machining for drilling has largely involved two operating configurations typically referred to as hole drilling/piercing and hole cutting. In hole drilling/piercing, the nozzle is stationary and therefore the hole diameter is relatively larger than the jet diameter. Conversely, for hole cutting, the nozzle travels in a circular/peripheral path in order to produce holes that are considerably larger than the diameter of the jet.

The performance of the different process configurations at various machining parameters (e.g. pressure, abrasive flow rate, standoff distance (SOD) and traverse speed) was evaluated with

respect to hole quality and integrity (top/bottom surface chipping, edge quality, matrix cracking, hole taper and delamination) when drilling woven CFRP [76]. Positive tapered holes were observed for both process configurations with hole drilling exhibiting more severe damage (e.g. delamination, edge deformation, uncut fibre, surface chipping and internal cracks) compared to the hole cutting operation, likely due to the higher impact of the jet with the surface in the former. Surface defects were mainly influenced by jet pressure however, the level of hole wall inclination generally decreased with increasing pressure, regardless of operating configuration. Dhakal et al. [77] investigated the workpiece surface roughness and delamination obtained when drilling different types of composites (10 mm diameter) comprising FFRP (natural flax), CFRP and C-FFRP (hybrid (carbon – flax) over a range traverse speeds (hole cutting configuration). Increasing traverse speed was found to cause greater damage in all 3 types of composites. The CFRP composites exhibited the best surface finish while UD-FFRP had the highest surface roughness due to the mechanical characteristics of the fibres. Conversely, the highest delamination was observed on the C-FFRP due to the presence of hybrid fibres with different mechanical properties/ply orientation as well as the embedment of particles.

Li et al. [78] compared the difference in hole quality and its subsequent effect on workpiece tensile strength when drilling woven CFRP using pure and abrasive water jet machining at varying jet pressures (240 and 320 MPa) and traverse speeds (450 and 900 mm/min). Relatively poor hole quality/surfaces were observed when employing PWJM, with major defects including uncut fibres, heavy delamination at hole entry/exit and fibre burrs evident in most of the trials. Conversely, the use of AWJM led to significantly improved hole quality and accuracy, with minimal surface damage, see Figure 2.25. Both delamination (F_d = 1.11) and damage area (1.57 mm^2) of the holes produced by AWJM were minimised when operating at high jet pressure (320 MPa) and traverse speed (900 mm/min) parameters due to the reduction in abrasive density by increasing pressure. The tensile strength of the machined workpieces were strongly related to the quality of the machined hole and use of abrasives. It was observed that the tensile strength obtained with AWJM increased by ~22% (130 MPa) compared to PWJM at equivalent cutting parameters (240 MPa and 450 mm/min). Increasing traverse speed to 900 mm/min increased the deterioration in tensile strength of the workpieces machined using AWJM by 77 MPa (11%), most likely caused by the lower interaction/exposure time between jet and workpiece and hence decreased damage. The principal failure modes of the holes were due to delamination and fibre breakage, irrespective of the process configuration.

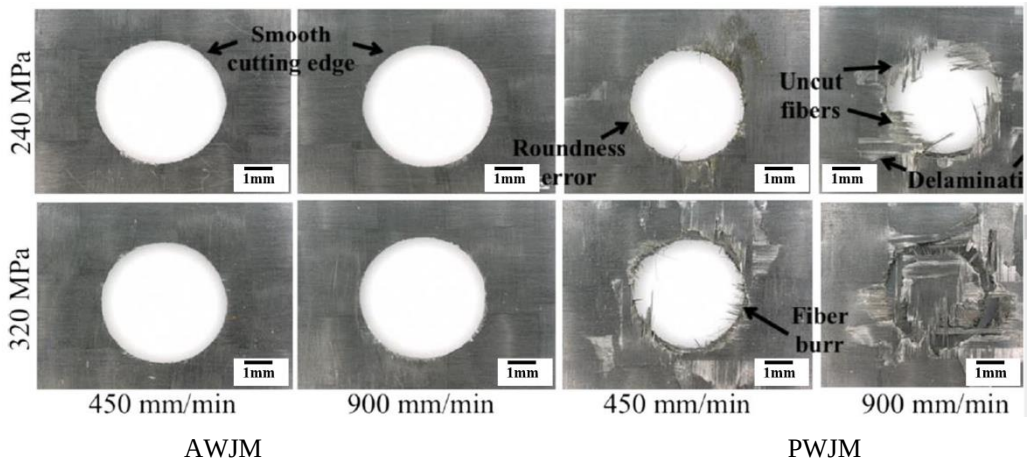


Figure 2.25: Morphology of machined surface at hole exit for various machining parameters and process types (adapted from [78]).

With regard to the drilling of CFRP-metallic stacks, Escobar-Palafox et al. [79] investigated the influence of abrasive water jet drilling parameters (jet pressure, traverse speed and abrasive flow rate) and stacking arrangement (CFRP/Ti and Ti/CFRP) on hole diameter and surface quality. Surface roughness was found to decrease with increasing abrasive flow rate as well as in the material placed at the top of the stack. Higher traverse speeds however reduced the surface roughness in the bottom layer, regardless the stacking configuration.

Similarly, the effects of jet pressure, traverse speed and mass flow rates were evaluated in abrasive water jet cutting and drilling of CFRP/AA7075 and AA7075/CFRP stacks [80]. The key performance measures included surface roughness and kerf taper for the cutting trials while hole roundness, cylindricity and straightness were assessed following drilling. No thermal damage/delamination were observed when operating at the high parameter levels except traverse speed (250 MPa, 15 mm/min and 340 g/min), although the entrance side of the CFRP layer showed signs of impact deformation caused by the abrasive particles. The AA7075/CFRP stack configuration showed lower kerf taper, surface roughness and cylindricity due to reduced impact energy between the jet and aluminium. However, the CFRP/AA7075 arrangement showed less micro geometric deviations because of lower energy loss.

2.4.1.2 Milling operation

Hocheng et al. [81] investigated the feasibility of AWJM for milling/through cutting of CFRP, with tests involving single, double and multiple (six) pass strategies. The key machining variables were jet pressure, mass flow rate, standoff distance (SOD), jet traverse speed and fibre orientation (0° and 90°), with performance assessed against resulting depth/width of cut, width to depth ratio (WTD), MRR and workpiece surface roughness (Ra). It was found that jet

pressure and traverse speed had a significant effect on MRR and cut depth whereas standoff distance was the main factor affecting cut width. In contrast, MRR and surface roughness were not influenced by fibre orientation, although both lateral feed and WTD were important for producing acceptable surfaces.

The mechanism of delamination formation and associated morphology following AWJM of CFRP was studied by Mayuet et al. [82] at various abrasive flow rates (300 and 600 g/min), feed rates (300, 900, 1500 and 2100 m/min) and SOD (1.0, 3.0 and 4.5 mm). Results showed that abrasive flow was the most significant parameter affecting delamination formation, with the use of intermediate feed rates/speeds and high abrasive flow rate recommended in order to minimise workpiece defects. Figure 2.26 shows the delamination/workpiece damage following AWJM of CFRP. The impact of the high-speed jet and abrasive particles on the surface causes cracks initiation, which becomes larger as cutting progresses leading to penetration and embedment of the abrasive particles between the plies. Similarly, Shanmugam et al. [83] investigated the formation mechanism of delamination in CFRP following AWJM and suggested that jet impingement initiated cracking of the interlaminate bonding followed by water seepage between the plies and finally abrasive penetration/embedment, which erodes the bonds as illustrated in Figure 2.27.

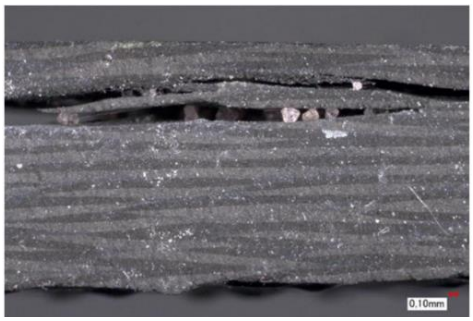


Figure 2.26: Morphology of CFRP delamination caused by abrasive particles [82].

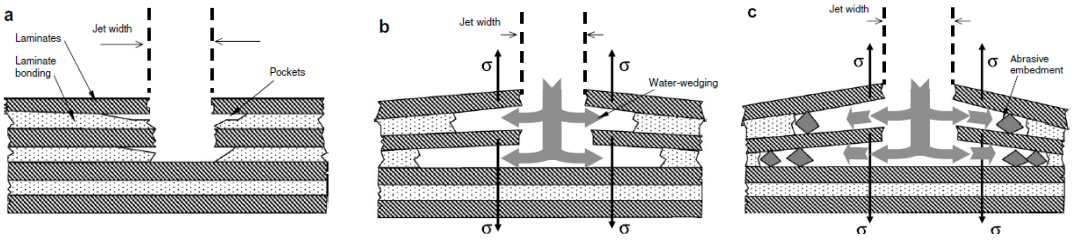


Figure 2.27: Mechanism of workpiece delamination in CFRP composite following AWJM; (a) crack initiation; (b) water indentation; (c) abrasive penetration [83].

Several researchers have evaluated the performance of AWJM for cutting metallic-composite stacks. Alberdi et al. [84] investigated the effect of stacking configuration, jet pressure, traverse

speed/feed rate and cutting tool (mixture between orifice/tube diameter and flow rate) on resulting kerf width (top and bottom), surface roughness and taper angle when AWJM stacks comprising CFRP and Ti-6Al-4V. An analysis of the machined cross sections revealed that in general, a negative taper was formed in the CFRP layer while a positive taper was observed in the Ti-6Al-4V section, which was attributed to the difference in machinability indices of the materials that influences the width of cut at the stack interface. This trend was evident in both stack configurations (CFRP/Ti and Ti/CFRP) as well as for the range of traverse speeds tested, see Figure 2.28. Jet pressure and stack configuration were the most significant parameters affecting taper angle while traverse speed was the main factor influencing surface roughness. Taper angle decreased with increasing pressure due to the higher energy of the jet that is capable to remove the material through the entire depth leaving close width dimensions. The Ti-6Al-4V section showed smaller tapers when placed at the top due to the higher jet energy upon impact. Increasing traverse speed resulted in high surface roughness due to the low interaction/exposure time. The workpiece surface roughness in both layers were less than 6.5 µm Ra when machining the CFRP/Ti-6Al-4V stack at high jet pressure (360 MPa). A semi-analytical model to predict the depth of penetration when AWJM of Ti-6Al-4V/CFRP stacks was developed by Pahuja and Ramulu [85]. It was observed that the CFRP was prone to delamination while the titanium layer exhibited kerf erosion/rounding during cutting. In general, the model showed a linear correlation between depth of penetration and jet power to speed ratio (represents the energy applied for distance achieved using the jet) and exhibited closer agreement with experimental results (R^2= 97%) compared to a regression analysis (R^2=88%).

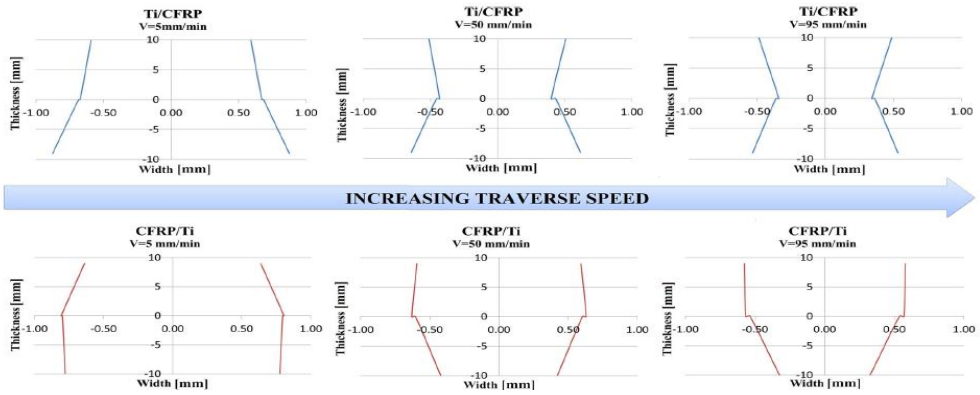


Figure 2.28: Kerf profile of Ti/CFRP and CFRP/Ti stacks at various traverse speeds [84].

2.4.2 Laser beam machining

Laser beam machining (LBM) utilises a highly focused and coherent beam of photonic energy to melt, vaporise or chemically degrade the target workpiece and is increasingly used for cutting a wide range of metallic and non-metallic engineering materials. A typical laser system comprises three major components, which includes the lasing medium, energy source and the optical delivery and feedback units [86]. The principal types of lasing mediums are solid state (Nd: YAG), gas (Neon, carbon dioxide and Helium) or liquid (e.g. dye) based [86, 87]. Some of the key benefits of LBM include high cutting rates (32 to 1000 mm^2/s) [88], the lack of mechanical interaction with the workpiece (i.e. zero cutting forces) and no tool wear or mechanical vibration [86]. However, the process has a relatively high-power consumption and machined workpieces typically suffer from thermally induced damage, while highly reflective materials are difficult to cut using lasers. Figure 2.29 shows the schematic of Nd:YAG (neodymium-doped yttrium aluminium garnet) laser system, which is the most commonly used solid state laser.

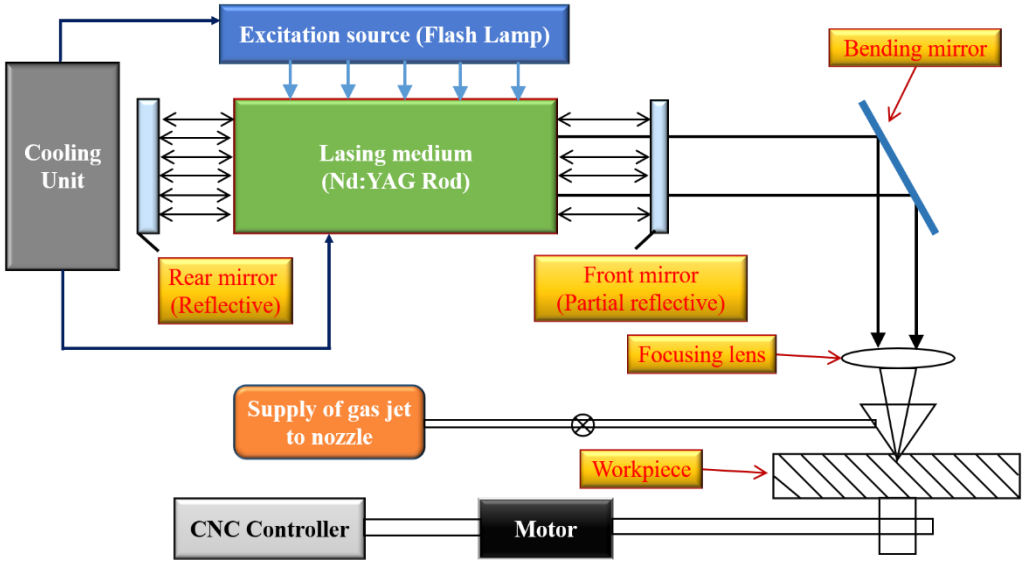


Figure 2.29: Schematic illustration of solid state (Nd:YAG) laser cutting system (adapted from [86]).

Different types of fibre laser sources including Nd:YAG, Yb:YAG and Nd:YVO_4 have been utilised for machining CFRP at different wavelengths and pulse durations (e.g. nanosecond and picosecond). Laser power, scanning/cutting speed, scan/hatching distance, pulse frequency, number of repetitions, pulse duration, laser mode (continuous or pulsed wave) and cutting strategy (single and multi-pass) are the key process parameters evaluated in machining operations. The effects of the process parameters are typically assessed against performance

characteristics including ablation depth, MRR, kerf width/taper angle, surface roughness/damage and heat affected zone (HAZ) [89-107].

2.4.2.1 Drilling operation

Li et al. [92] examined the feasibility and effect of single and multi-pass cutting strategies on hole quality (2 and 6 mm diameter) when drilling CFRP (2 mm thick) using a continuous wave (CW) fibre laser (max of 5 KW). The study revealed that HAZ and $HAZ_{ellipse}$ (difference in area between machined hole and ellipse generated by variation of heat conductivities along axial and perpendicular orientations of fibres) were significantly influenced by parameters (power and cutting speed) at the hole exit location and reached its maximum value (~25 mm^2) by raising E_l (energy/length) from 40 to 150 J/mm. It was recommended to set E_l > 40 J/mm to achieve successful machining through the workpiece. Limited reduction in HAZ was achieved with the multi-pass strategy compared with single pass even at high cutting speed (10000 mm/min). Furthermore, the use of high power fibre lasers (up to 950 W) was not recommended for drilling small diameter holes (2 mm), in order to avoid excessive damage and poor hole quality as shown in Figure 2.30.

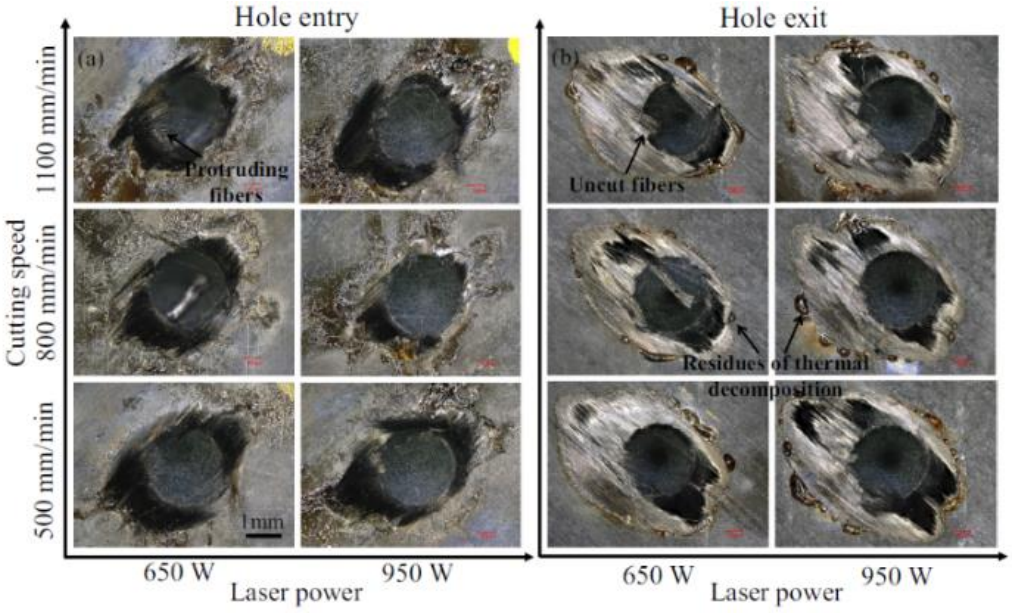


Figure 2.30: Surface morphology of 2 mm hole obtained through fibre laser machining of CFRP (a) hole entry and (b) hole exit [92].

Ablation depth and HAZ were evaluated by Salama et al. [99] when drilling CFRP with a multi-ring strategy using a picosecond laser (max 400 W) at different laser power (from 6 to 30 W), scan speed and rate of repetition (0.5 MHz), see Figure 2.31. It was found that high quality holes (6 mm depth and diameter) were achieved at 2 m/s scanning speed with HAZ width

limited to 25 μm at hole entrance while no obvious HAZ was evident underneath the surface. An investigation on the influence of different laser wavelengths (1064, 532 and 355 nm) showed that maximum values of MRR (~ 18 mm^3/min) and HAZ (57 μm) were recorded at 1064 nm [100]. In addition, a comparison between single and multi-ring strategies revealed that higher ablation depth and material removal was obtained when using the multi-ring cutter path [108].

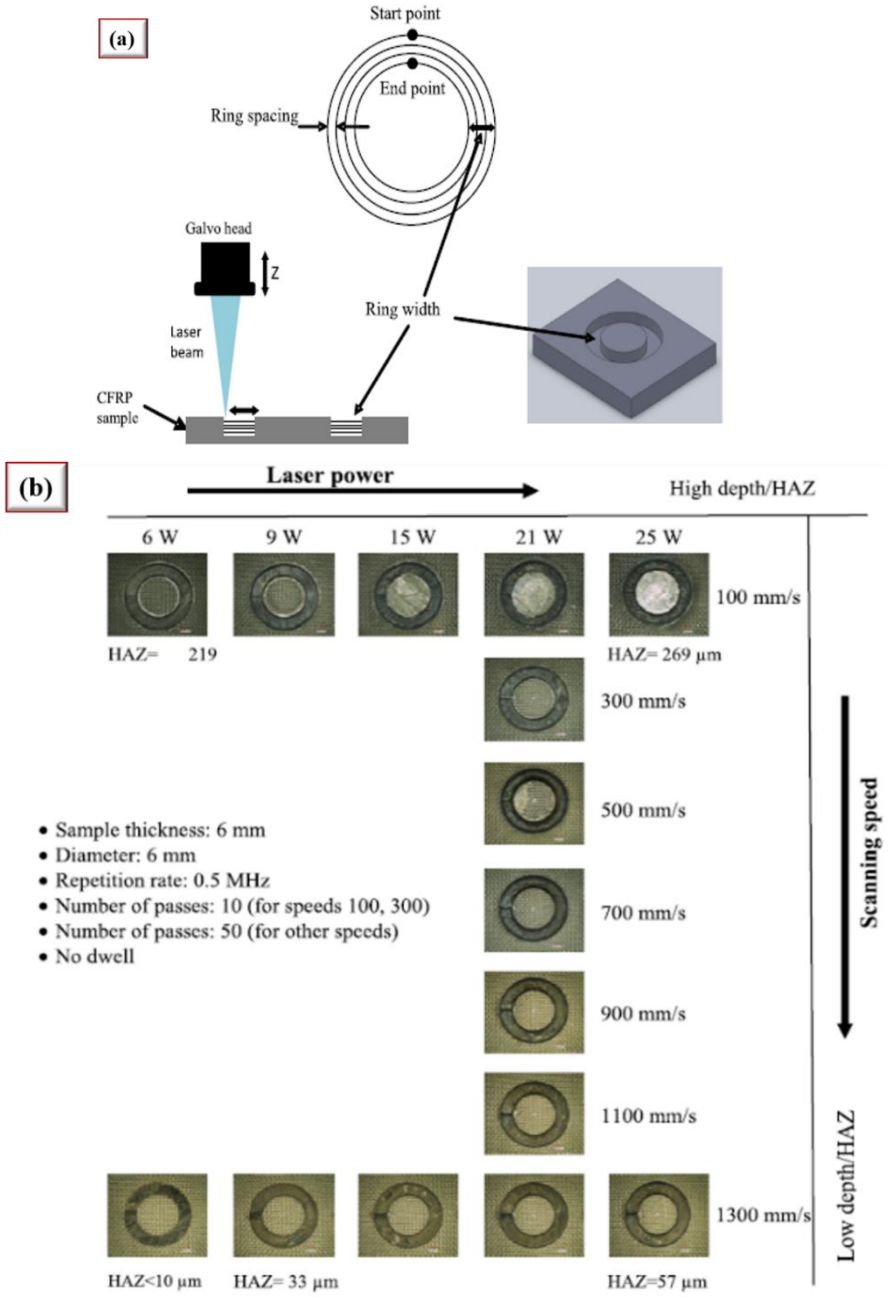


Figure 2.31: Laser drilling of CFRP (a) multi rings strategy and (b) HAZ at various power and speed levels [99].

The resulting workpiece surface roughness and HAZ following drilling using erbium [91] and UV DPSS lasers [103] were investigated. For tests with the erbium laser, the lowest HAZ width (1.227 mm) and surface roughness (1.143 µm Ra) were obtained when operating at 300 W, 200 mm/s and 0.8 mm of power, scan speed and SOD respectively [91]. Conversely, the UV laser with short pulses induced smaller HAZ widths of ~50 µm [103]. The ablation mechanism at different waveforms involving continuous and short/long pulse duration was studied by Wu et al. [109]. It was found that long pulse duration produced conical holes in all of the laminates while uniform ablation was achieved with the continuous wave laser. However, only surface ablation was observed without through penetration of the workpiece when machining with short pulse duration. Staehr et al. [110] eliminated the problem of narrow and tapered holes when drilling with a new short pulsed laser at small focus diameter (down to 84 µm), by employing two finishing steps post machining. The hole walls were found to be parallel and the process was successfully demonstrated in riveting boreholes.

2.4.2.2 Milling operation

A number of limited studies involving the use of gas based CO_2 lasers for the cutting/milling of CFRP has been reported in the literature. The effect of CO_2 laser variables (speed, power and pressure) on MRR and kerf width was assessed by Shyha [111] when machining CFRP and GFRP. The results demonstrated that higher MRR was achieved when machining GFRP (up to 8 cm^3/min) compared to CFRP (4 cm^3/min), albeit with larger kerf width of up to 0.5 mm as opposed to a maximum of 0.28 mm for CFRP. The use of a short pulsed TEA (transversely excited atmospheric) CO_2 laser at different machining parameters (fluence, speed and repetition rate) was employed to investigate MRR, HAZ and machining depth [112]. The short pulsed CO_2 laser showed relatively good performance in terms of MRR (11 ± 0.4 mm^3/min) and depth of cut (5.8 ± 0.3 µm/pass) as well as smaller HAZ width (21 ± 4 µm) compared with other laser systems, as detailed in Figure 2.32. The ANOVA showed that repetition rate, scanning speed and the corresponding second order terms had a significant effect on HAZ.

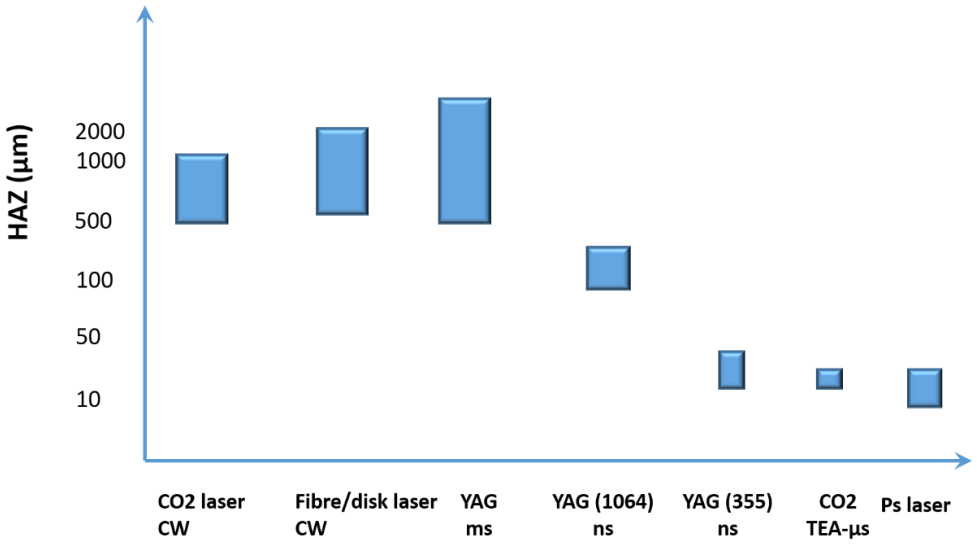


Figure 2.32: Comparison between HAZ levels for different laser types (adapted from [112]).

Solid state lasers are the most widely used for milling/cutting of CFRP. Genna et al. [90] employed a response surface methodology based central composite design (CCD) to study the effect of Q-switched (Yb:YAG) fibre laser machining parameters (speed, frequency, number of pattern repetitions and spacing distance) on MRR and cut depth when milling square pockets (8 x 8 mm). Results showed that pocket depth decreased by reducing the number of repetitions and increasing both scan speed and hatch distance while increasing hatch distance and decreasing repetitions resulted in higher MRR. According to the RSM model, the target pocket depth (with 3% error) as well as an MRR greater than 0.0019 g/s was achieved. Further investigation by Genna et al. [106] focused on assessing HAZ, however none of the process parameters had a significant effect on HAZ.

Xu and Hu [89] reported that matrix pyrolysis caused by laser ablation and mechanical erosion were the main material removal mechanisms in laser cutting of CFRP. A numerical model to describe the removal mechanism also demonstrated the prediction of ablation depth at optimal hatching distance. Likewise, Leone et al. [113] concluded that the material removal mechanism in laser cutting of CFRP was due to ablation, burning of the matrix and mechanical effects caused by recoil force/pressure. In addition, the HAZ was found to increase due to high frequency operation, beam defocusing as well as accumulation of burnt material.

Several researchers studied the performance of different laser types and wavelengths when laser cutting CFRP with regard to HAZ and cut quality [93, 96, 98, 101, 104, 105]. Leneo and Genna [93] reported that a machining rate of up to 10.8 mm/min was achieved when cutting 1mm thick

CFRP using a pulsed Nd:YAG laser, with appropriate selection of parameters key to maximising cutting speed and reducing HAZ. Workpiece damage included cavities, matrix degradation, fibre pull out and HAZ, which varied between 170 to 1600 µm. Matrix evaporation and fibre pull out were the key defects observed when cutting a 1.15 mm thick CFRP workpiece using a 2 kW fibre laser, see Figure 2.33 [96]. The smallest kerf width (184 µm) and reduced HAZ were achieved when operating at a duty cycle of 25% (pulsed) compared with 100% (continuous), although the latter condition also resulted in excessive damage to the matrix material and a wider kerf.

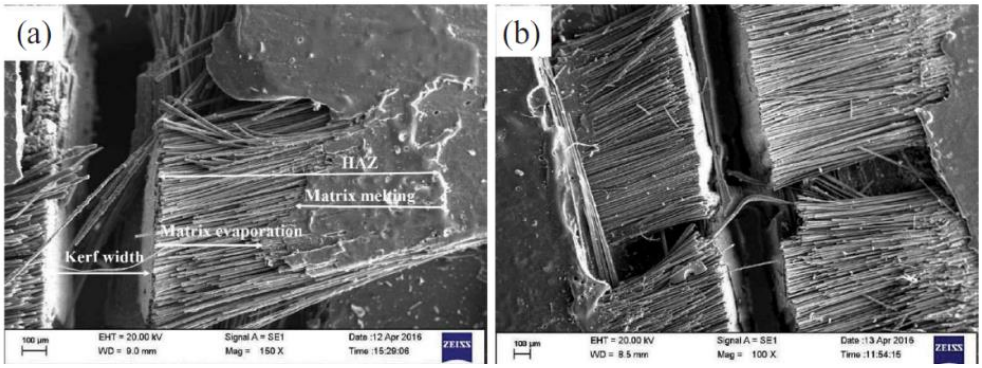


Figure 2.33: Defects induced by laser cutting at different kerf zones [96].

The performance of Q- switched and ultra violet diode-pumped solid state (DPSS) lasers were evaluated for cutting CFRP with thicknesses of 0.5 and 2 mm respectively [98, 101]. The UV-DPSS laser exhibited superior quality on both the top surface and machined sidewalls together with negligible signs of HAZ. Another study was carried out to investigate thermal degradation, kerf geometry and MRR following machining using a nanosecond DPSS pulsed laser in the presence of low content oxygen and inert gas [105]. Analysis showed that best results were achieved by using a mixture of oxygen (12.5%) and nitrogen supplied at 8 bar, with fibre pull out seen to reduce by ~55%.

2.4.3 Ultrasonic machining

Traditional ultrasonic machining (USM) involves a tool that is ultrasonically vibrated (18 - 20 kHz) against an abrasive slurry supplied to the workpiece causing controlled erosion/fracture, which is generally employed for machining hard/brittle materials above 40 HRC [88, 114]. Figure 2.34 depicts the main components of the USM system. Amongst the key benefits of USM is there is no thermal or chemical damage to the workpiece, however the process suffers from relatively low material removal rates, rapid tool wear and high power consumption [115].

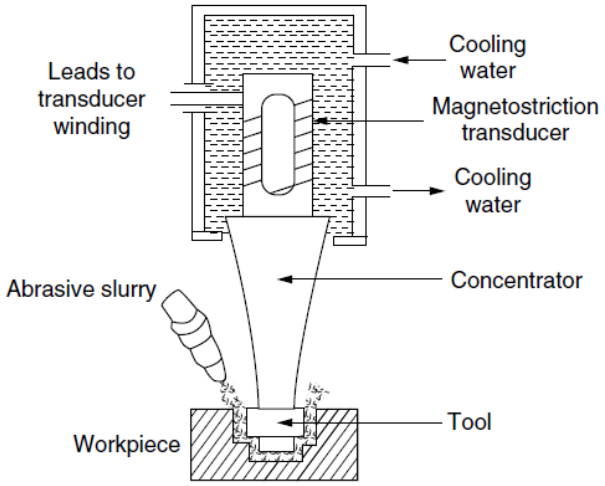


Figure 2.34: Schematic diagram illustrate the main components of USM [88].

A more commonly utilised process configuration in recent years is rotary ultrasonic machining (RUM), where the tool is tubular shaped with abrasives electroplated at one end and rotating while simultaneously being ultrasonically actuated/vibrated in the axial direction to achieve material removal as shown by the schematic in Figure 2.35. This hybrid process configuration has been employed for drilling, milling and grinding operations on brittle and ductile materials as well as CFRP composites [116-118].

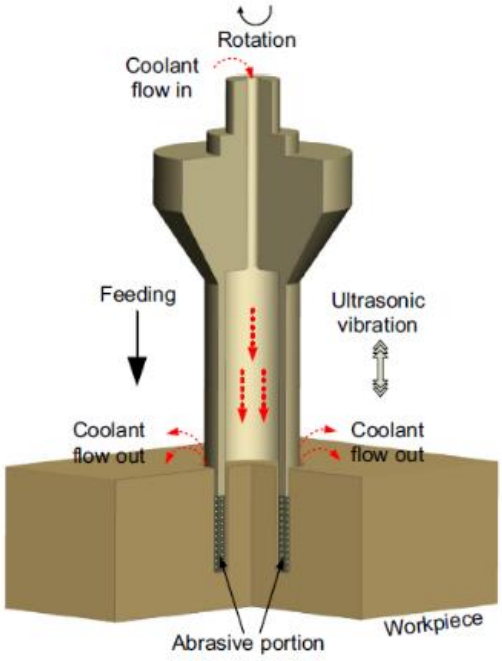


Figure 2.35: Schematic representation of RUM process [116].

2.4.3.1 Drilling operation

The feasibility of drilling CFRP using RUM was examined by Feng et al. [119] at different feed rate, vibration amplitude and rotational speed against resulting workpiece surface roughness,

thrust force, tool wear and chip formation. The holes produced were free of tapering or fibre while lower thrust forces (100 to 110 N) and surface roughness (Ra < 2 µm) were recorded when operating at higher cutting speeds and lower feed rates. Additionally, the variation in hole diameters and chip size were less than 1% and 300 µm respectively. Likewise, Slimane et al. [120] employed response surface methodology to assess the effects of feed rate, vibration amplitude and rotational speed when drilling of CFRP with RUM. Feed rate was identified to be the most influential parameter with regard to optimisation of cutting forces. Cong et al. [121] investigated the effect of speed, feed rate and ultrasonic power on surface roughness, torque, tool wear and machined surface burn when drilling CFRP with cold air. The results were compared with outcomes from a similar study but involving machining with cutting fluid [122]. Machining with cold air induced higher cutting force/torque, surface roughness and severe tool wear compared with cutting fluid. Furthermore, heavily burnt surfaces were observed in tests employing cold air at high feed rate/power and low cutting speed, while no apparent signs of burning were found in equivalent trials with cutting fluid.

Studies involving the drilling of CFRP/Ti stacks using RUM at variable feed rate have been reported [123]. In general, the application of variable feed rate (changing feed rate from 0.5 to 0.05 mm/s when moving from CFRP to Ti) produced lower process cycle times (200 s) and cutting force/torque at all input parameter levels (ultrasonic power and rotation speed), except at 7000 rpm for torque, compared with constant feed rate operation (0.05 mm/s). However, fixed feed rate operation induced smaller groove depth than variable feed rate at different power levels. Tool wear was also found to be lower when employing variable feed rate strategy for ultrasonic power not exceeding 40%. In terms of surface roughness, it was observed that variable feed rate produced higher roughness in the CFRP layer at different power levels while Ti achieved lower roughness of 1.2 µm compared to 3 µm Ra under conventional drilling conditions (no ultrasonic actuation). Fernando et al. [124] investigated the influence of using a backing plate when drilling CFRP with RUM. It was observed that the backing plate prevented delamination formation at the hole exit surface, although some degree of edge damage was visible.

Several researchers have compared the performance of ultrasonic assisted drilling (UAD) against conventional drilling (CD) using twist drills. Sanda et al. [125] showed a 30% reduction in thrust force was obtained when UAD of CFRP compared to CD, in addition to lower delamination, process temperature and surface roughness, as detailed in Figure 2.36. Similarly,

Phadnis et al. [126] also recorded lower thrust forces of up to 30% when employing UAD compared with CD, although force reductions of up to 60% when using UAD have been reported [127, 128].

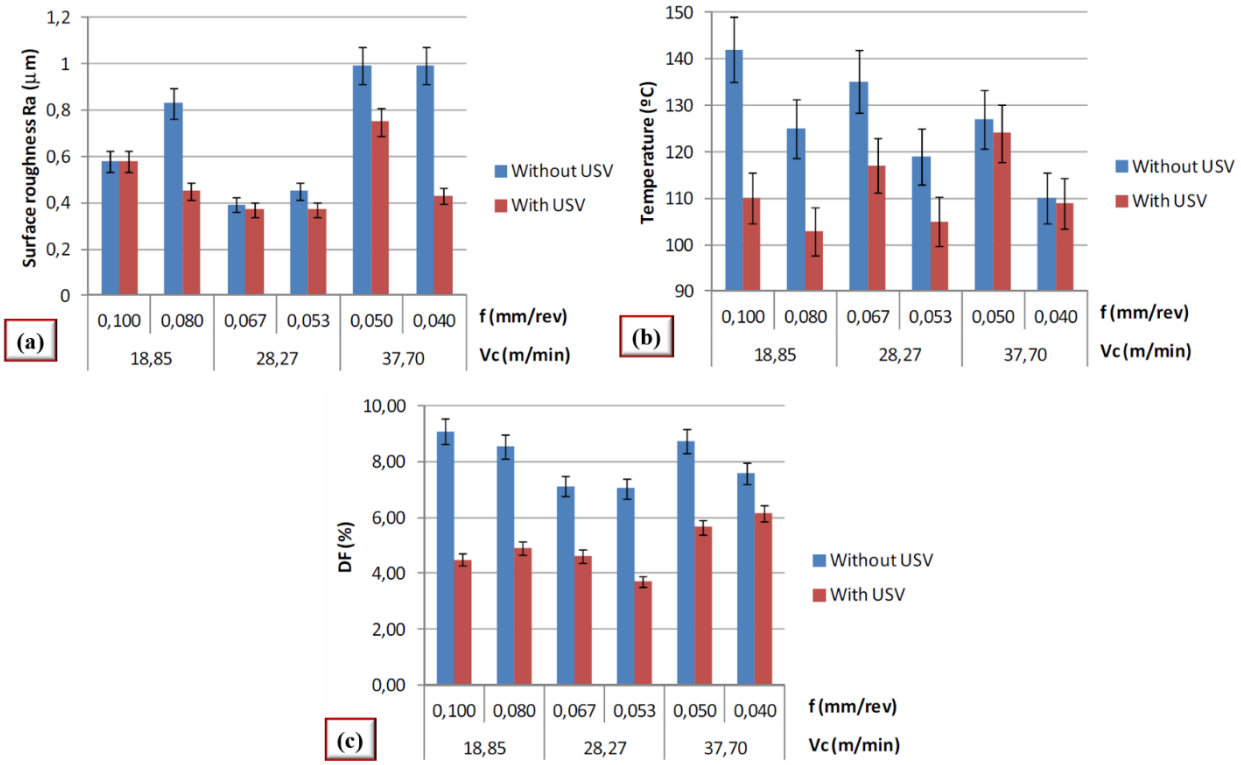


Figure 2.36: Comparison between CD and UAD of CFRP in terms of (a) surface roughness, (b) process temperature and (c) delamination factor [125].

Liu et al. [129] investigated the performance of rotary ultrasonic elliptical machining (RUEM) for drilling CFRP. It was shown that RUEM demonstrated improved surface quality, material removal rate, hole precision as well as lower tool wear and prevented delamination at the hole exit compared to conventional drilling. Geng et al. [130] studied the tool wear mechanism of diamond drills when RUEM of CFRP. The steady wear region length and tool life increased by 39% and 28% respectively in RUEM compared to CD. Li et al. [131] analysed chip removal during dry rotary ultrasonic assisted drilling (RUAD) and conventional drilling of CFRP using electroplated core drills. Tests performed at vibration amplitudes of 5 and 7.5 µm showed that RUAD outperformed conventional drilling by reducing surface roughness, cutting forces and fragmentation/jamming of the tool, see Figure 2.37. Additionally, superior hole dimensional accuracy was obtained with RUAD compared to CD.

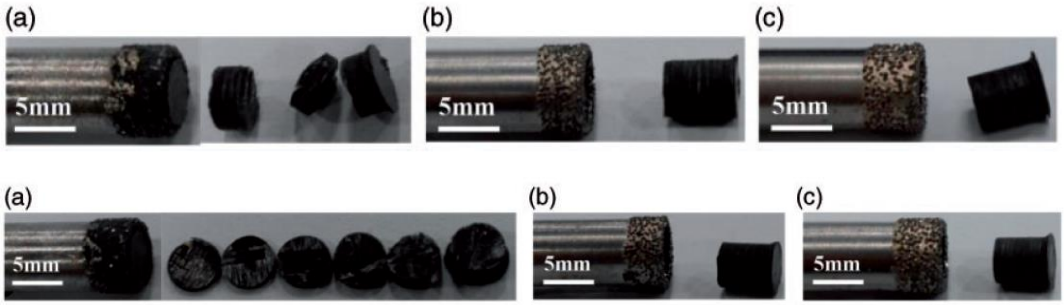
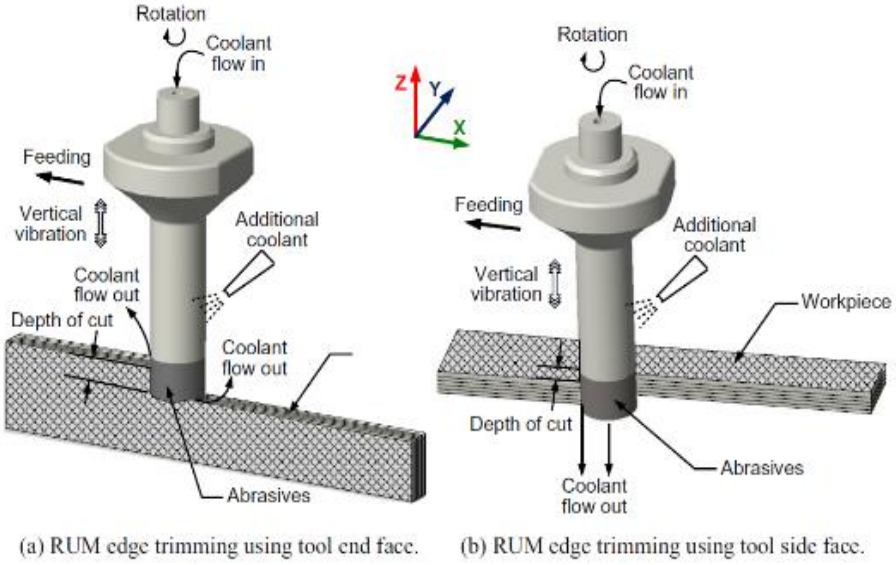


Figure 2.37: Chip removal at first and fifth holes (a) CD, (b) RUAD 5 μm and (c) RUAD 7.5 μm [131].

2.4.3.2 Milling operation

Several researchers have investigated the use of RUM for the milling/trimming of composite materials including CFRP. Wang et al. [132] studied the influence of cutting orientation involving use of the end and side face of the tool when RUM edge trimming of CFRP, see Figure 2.38. Lower cutting forces including $F_{x,}$ F_z, $F_{resultant}$ and higher F_y were generated when machining with the side face of the tool compared to the end face. The was attributed to the higher interface area when machining with the side face (2.7 mm^2) as opposed to the end face (0.54 mm^2) while the greater friction in cutting with the end face induced higher F_z. It was observed that both configurations produced lower cutting forces when decreasing cutting depth/feed rate and increasing rotational speed/ultrasonic amplitude. Similarly, high speed and low feed rate/depth resulted in lower roughness when applying small and large amplitudes during machining with the end and side faces respectively. Furthermore, the end face orientation produced lower surface roughness (ranging between 0.89 and 1.48 μm) due to the longer time of contact between the abrasives and CFRP. With regard to surface quality, trimming with the end face reduced grinding/striation marks due to the periodical contact between the abrasives and workpiece surface, while cutting with the side face caused fibre pull out as the rotation of the tool/abrasives was parallel to fibre orientation. Inspection of the edge quality revealed that less debris and microcracking was observed when machining with the end face due to the higher F_z, contact time and indentation of the abrasive into the surface.



(a) RUM edge trimming using tool end face. (b) RUM edge trimming using tool side face.

Figure 2.38: Cutting orientations when edge trimming of CFRP using RUM [132].

Chip blockage/jamming of the tool in RUM is a significant issue, which was investigated when milling two different composite materials; C/SiC and CFRP T700 [133]. When machining C/SiC composites, tool blockage was prevented when the chip length (C_l) was smaller than the chip space (space between adjacent abrasive grains), with experimental results recommending that chip length should be within $C_l \leq 0.45R_r$ where R_r is the chip space radius. In contrast, the chip space should be 8 times larger than the chip length to avoid tool blockage when milling CFRP-T700. This difference was attributed to variation in chip forms including powder and bulk (caused by chip secondary adhesion) for C/SiC and CFRP respectively. By employing scratch tests, Wang et al. [134] showed that a ductile based material removal mechanism was predominant when rotary ultrasonic surface machining (RUSM) of CFRP at small depths of cut, while brittle fracture was prevalent when operating at higher cut depths. Geng et al. [135] evaluated the edge routing of CFRP using RUEM at different speed ratios (0.1 and 0.8). Machining with the lower speed ratio was found to reduce tool wear (<34%), surface roughness and force components (19% for normal and 17% for tangential).

An investigation involving ultrasonic assisted milling (UAM) and conventional milling (CM) of CFRP was carried out at varying feed rate, cutting speed and depth of cut by Li et al. [136]. Cutting forces were typically lower with UAM coupled with reduced vibration and improved process stability. Similarly, Halim et al. [137] compared the performance of UAM and CM in terms of tool wear, cutting force, cutting temperature and surface roughness when machining CFRP at equivalent operating parameters. The results revealed that while UAM induced higher tool wear rate and workpiece surface roughness (5-25%), both cutting force (up to 20%) and

cutting temperatures (up to 15%) were lower compared to CM, as shown in Figure 2.39. Similar studies involving UAM using commercial tools with bonded diamond grits [138] and special end mill designs (Hexacut) [139] also reported lower cutting load (~60%) and delamination width (~11%) in comparison to conventional milling operations.

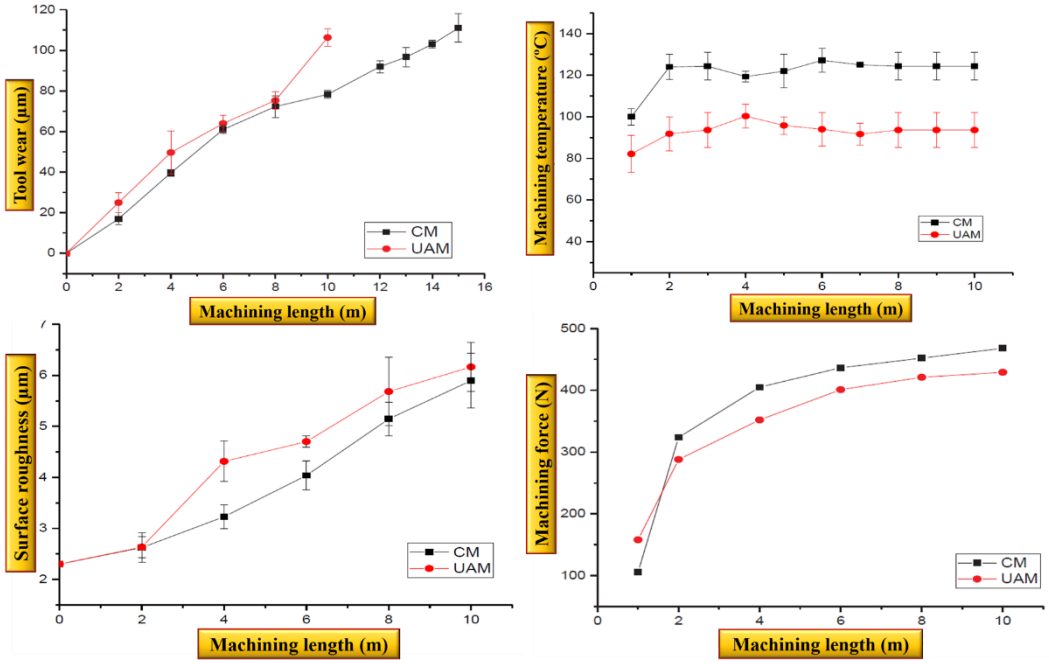


Figure 2.39: Comparative performance of UAM and CM for various response measures (adapted from [137]).

2.4.4 Electrical discharge machining (EDM)

Electrical discharge machining (EDM) uses thermo-electrical energy to erode/melt/vaporise electrically conductive materials by repeated and controlled spark discharges between an electrode and workpiece in the presence of a dielectric fluid [140, 141]. There are two primary process configurations involving die sink EDM and wire EDM (WEDM), as illustrated in Figure 2.40. Unlike conventional machining processes, the mechanical properties such as strength and hardness of the workpiece do not hinder material removal in EDM [142]. More recently, there has been increasing research to assess the performance of EDM for cutting CFRP, despite the relatively low electrical conductivity of the material.

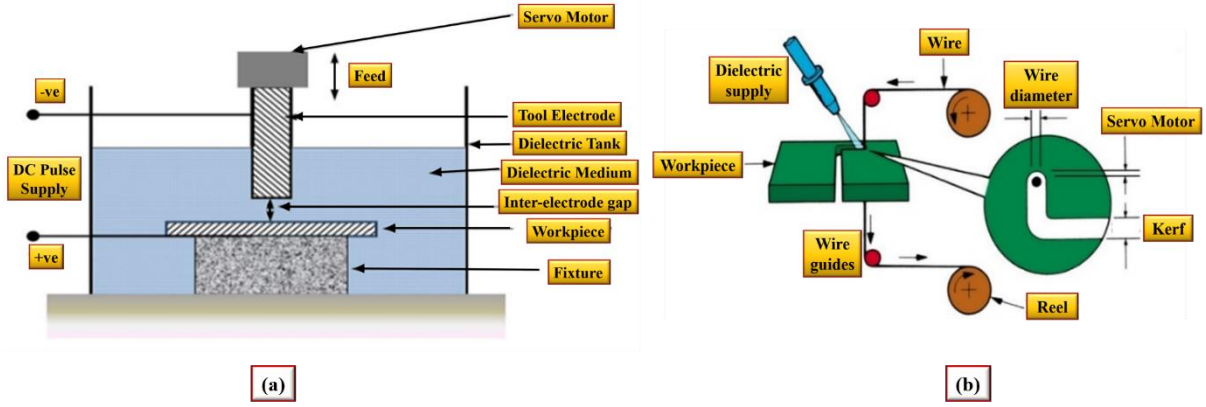


Figure 2.40: Schematic representation of main EDM process configurations, (a) die sink EDM, (b) wire EDM (adapted from [143, 144]).

2.4.4.1 Die- sink EDM

Influence of operating conditions

Material removal rate, surface roughness and tool wear rate are commonly evaluated performance measures in research involving the EDM of CFRP [43, 145-150]. The primary EDM process parameters investigated include pulse on/off time, tool polarity/type (Cu/Gr), peak current, voltage and tool rotational speed. A number of publications have reported lower tool wear rate (TWR) [43, 145, 147] and surface roughness [145, 146] was achieved when machining with copper instead of graphite electrodes, however the latter resulted in higher MRR [43, 146, 147]. Wang at al. [142] investigated the influence of key operating parameters when EDM die sinking of CFRP in comparison to a tool steel (SKD11). When operating at a low current level of 3 A, higher MRR was observed when machining the CFRP compared to SKD11, which increased with pulse duration regardless of electrode type, see Figure 2.41. This trend was also mirrored in terms of workpiece surface roughness. Increasing current to 20 A with a pulse on time of 50 µs however resulted in significantly greater MRR and lower surface roughness for the SKD11 workpiece (10.5 mm^3/min, 30 µm Rz) compared to CFRP (0.41 mm^3/min, 76.5 µm Rz).

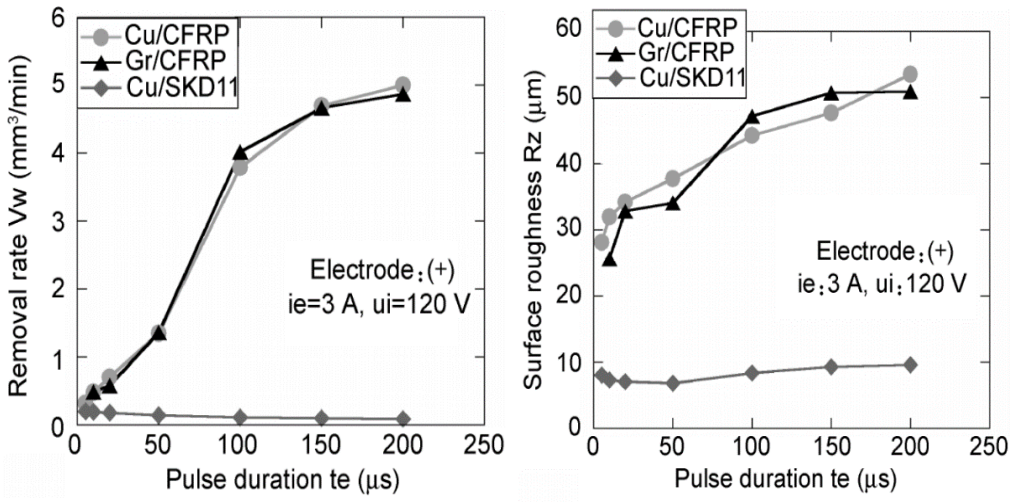


Figure 2.41: Effect of pulse duration on removal rate and surface roughness for various tool/workpiece materials [142].

Research was further extended to evaluate the influence of cutting direction (parallel and perpendicular to fibre orientation) during EDM of unidirectional (CFRP1) as well as bidirectional/woven (CFRP2) workpieces [151], as shown in Figure 2.42. Higher MRR was observed when machining perpendicular to fibre orientation for the unidirectional CFRP1, however surface roughness (Rz) was lower when cutting parallel to fibre direction. The MRR was up to ~25% higher during EDM of the bidirectional/woven CFRP compared to the unidirectional workpieces due to greater levels of the polymer matrix in the former. Ichii et al. [152] similarly reported faster removal rates when machining UD-CFRP perpendicular to fibre direction, while adhesion of resolved carbon from the kerosene and resin on the tool electrode minimised tool wear. Taguchi experimental designs have been employed by several researchers to optimise tool wear rate [141] and workpiece surface roughness following EDM of CFRP [149]. Peak current exhibited the strongest influence on tool wear [141], while both current and pulse on time were significant factors affecting surface roughness [149]. Results from the confirmation test revealed strong agreement with predicted values, which was reflected by the low total error of ~2.43% [149].

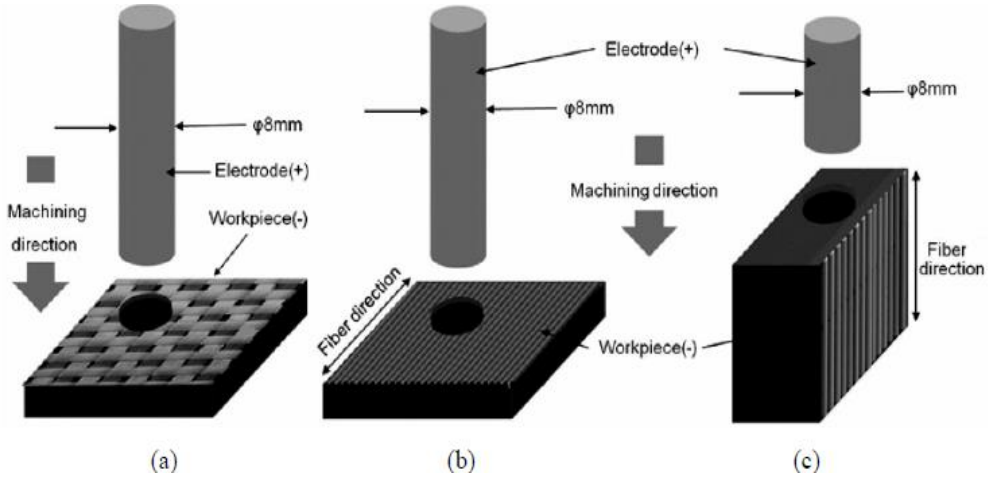


Figure 2.42: Schematic illustration of machining in different fibre directions; (a) perpendicular CFRP2, (b) perpendicular CFRP1 and (c) parallel CFRP1 [151].

Material removal mechanism and short-circuiting

A number of researchers have studied the material removal mechanism during EDM of CFRP [153-155]. It was reported that material removal occurred as a result of epoxy matrix decomposition and fracture/vaporisation of fibres due to the high temperature of the plasma as well as Joule heating caused by short-circuiting of the conductive fibres [154]. Yue et al. [155] comprehensively investigated the various mechanisms of material removal during EDM of CFRP including thermal, mechanical and chemical modes as well as the effect of cutting direction (parallel or vertical to fibre orientation) for different mechanisms. It was observed that in addition to heat from the plasma channel formed during EDM, material erosion is also caused by Joule heating resulting in decomposition, oxidation and vaporisation of the epoxy matrix as well as sublimation and oxidation of fibres leading to the emission of debris jets into the spark gap. Furthermore, the force of the high-speed gaseous jets also contributed to material removal particularly when the fibres are in orthogonal to the jet direction, due to the low bending strength of fibres compared with corresponding axial tensile strength. In terms of the dielectric fluid, higher cutting rates were obtained when machining with deionised water (~0.6 mg/min at 5 kHz) compared to hydrocarbon oil (~0.2 mg/min) due to the oxygen produced by dissociation of deionised water increased burning of the carbon fibre as well as enhancing flow of the gaseous jets.

Typically, short circuit between the electrode and workpiece is undesirable in EDM as it reduces machining efficiency. However, it contributes to material removal in EDM of CFRP as reported by Ito et al. [150, 156] as it removes long fibres following resin evaporation. Short-circuiting occurs frequently when machining CFRP particularly in the presence of frayed

carbon fibres. The short-circuit pulses can constitute 10% to 60% of total pulses, which can influence the material removal rate of the process because it was found that the degree of short-circuiting increased from 10 to 40% at constant feed rate of 0.13 mm/min for different machining times of 4 to 8 and 12 to 16 minutes respectively. Figure 2.43 exhibits the gap voltage and current pulse profiles during short-circuiting and normal sparking. The effect of fibre orientation on short-circuiting at different gap voltages was studied by Hayakawa et al. [157]. The results showed that the short circuit frequency was reduced by decreasing gap voltage while MRR was higher and tool wear was reduced when machining parallel to fibre orientation. Figure 2.44 details cross sectional micrographs of the workpieces after different machining times, which showed uneven damage widths due to the difference between MRR and wear ratios of the electrode between the prepregs.

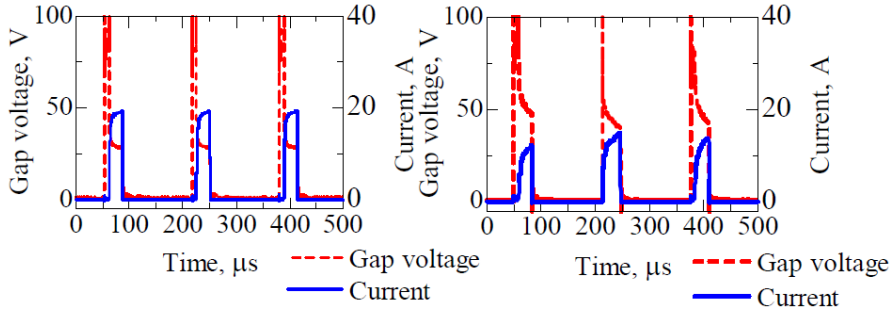


Figure 2.43: Voltage and current waveforms during (a) short-circuiting and (b) normal discharge [156].

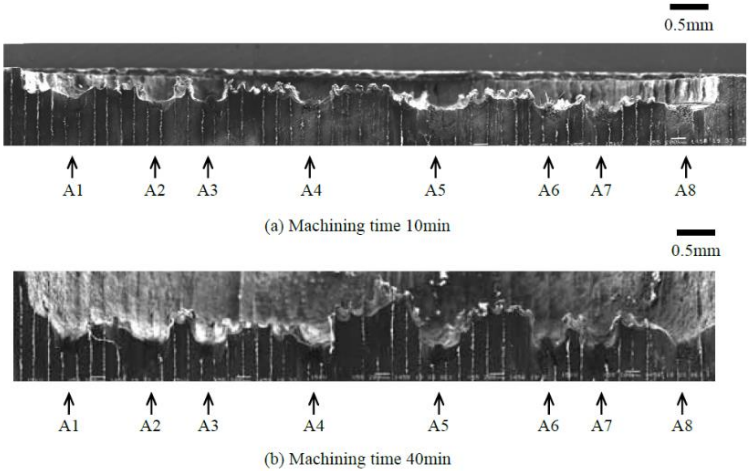


Figure 2.44: Cross section of drilled holes at different machining times (a) 10 minutes and (b) 40 minutes [157].

Workpiece surface integrity

Sheikh-Ahmed and Shinde [43, 147] evaluated the effect of varying current, pulse duration and electrode type on workpiece delamination and hole tapering/dimensional deviation following EDM drilling of CFRP. It was observed that a low delamination factor of ~1.2 was obtained when operating at low current (0.4 A) and pulse on time ranging from 80 – 105 µs [43, 147]. Hole tapering and size deviation were primarily affected by current and pulse duration, with graphite typically producing holes with larger tapers and hole sizes compared to copper electrodes [43]. A related study reported that hole entry delamination was significantly influenced by current whereas pulse on time was the main factor affecting HAZ and hole tapering [154]. Korlos et al. [158] employed X-ray computed tomography (CT) to detect delamination after EDM drilling of woven CFRP at varying current (1, 2 and 3 A)/pulse on time (100, 200 and 300 µs) combination levels, while finite element analysis and the point stress criterion (PSC) were employed to estimate stress concentrations and failure strength of the open holes. The X-ray CT scans were capable of detecting even small levels of delamination, with the results used in the finite element model incorporating the PSC (point stress) criterion to predict failure strength and stress distributions of the drilled specimens. It was found that the variation between experimental and theoretical values was between 0.3 and 4%.

2.4.4.2 Wire EDM

Published research to date concerning the WEDM of CFRP is extremely limited. Preliminary trials involving WEDM of thin CFRP laminates (2 mm thickness) were performed by Yue et al. [155] using brass wire, with cutting carried out parallel and perpendicular to the fibre direction. Machining parallel to the fibres resulted in ~18% higher cutting speed due to the increased electrical and thermal conductivity of fibres in the axial compared to transverse orientation. Lau and Lee [159] detailed one of the earliest studies comparing the performance of WEDM and laser cutting of woven CFRP (2.5 mm thick) in terms of MRR, edge tapering and workpiece surface damage. Laser machining demonstrated significantly superior MRR (~95 mm^2/min) compared to WEDM (~12 mm^2/min), although the latter showed better edge quality together with lower surface damage and HAZ. Abdallah et al. [160] recently reported results from a preliminary study to investigate the feasibility of WEDM for cutting 8.4 mm thick unidirectional (UD) CFRP plates using zinc coated brass wire fed parallel to the fibres. The variable parameters included open voltage, ignition current and pulse on/off time, with the effects on MRR, kerf widths and surface damage on the top and bottom surfaces of the

workpieces assessed. In general, there was no visible damage along the edges of the machined kerfs in any of tests although the kerf widths were generally inconsistent over the length of cut due to variation in the top nozzle standoff distances, which affected flushing efficiency. The associated ANOVA indicated that ignition current had a major influence on MRR and kerf width on the top surface, while pulse off time was a significant factor affecting MRR. The feasibility of machining woven CFRP (1 mm thick) using 0.18 mm diameter molybdenum wire was investigated by Dutta et al. [161]. The workpiece was stacked together with a metallic layer (2 mm thick) acting as an assisted electrode to help in spark initiation. The machining time was evaluated over a 4 mm cut length by changing current (2, 4 and 6 A), pulse on (30, 40 and 50 µs) and off time (15, 25 and 35 µs). It was concluded that the assisted electrode generated the sparks/heat, which propagated through the CFRP causing material removal. The results revealed that machining time was increased by increasing pulse on time at current of 2 A, while increasing current levels had no significant effect on cut time. Higher pulse off times also led to increase in machining time. However, increasing current levels from 2 to 6 A reduced the cut time by 41-52% (depending on pulse off time).

2.5 Wire electrodes

Figure 2.45 illustrates the various parameters/factors that influences the resulting performance measures in WEDM [162]. Apart from the electrical process parameters, the wire electrode is an important consideration, particularly in cases where process stability is poor, which leads to an increased risk of wire breakage/rupture.

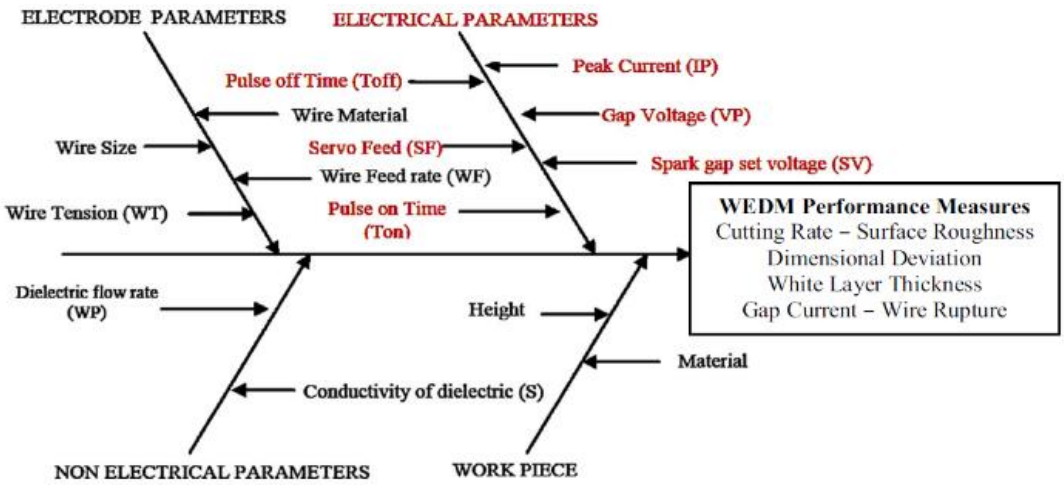


Figure 2.45: Effect of different factors on performance attributes [162].

2.5.1 Characteristics of wire electrodes

The key characteristics to consider when selecting a wire electrode are heat release/resistance, low calorification and discharge performance [163], in addition to workpiece quality requirements, compatibility to machine tool, cutting speed and wire/changeover costs [164], see Figure 2.46. The physical and mechanical properties that significantly affect wire performance include its electrical conductivity, tensile strength, melting point, elongation, flushability and straightness [165]. Wire electrical conductivity is defined as the extent of discharge energy into spark gap and is usually expressed as a proportion of the International Annealed Copper Standard (IACS), which is equivalent to 58 x 10^6 S/m. A low conductivity value generally leads to energy loss and voltage drop during machining. The tensile strength determines the level of tensioning that the wire can withstand during cutting in order to maintain straightness and eliminate vibration. Elongation describes the degree of plastic deformation of the wire prior rupture, while flushability indicates the ability to remove debris from the spark gap to maintain stable discharge, which influences the machining speed.

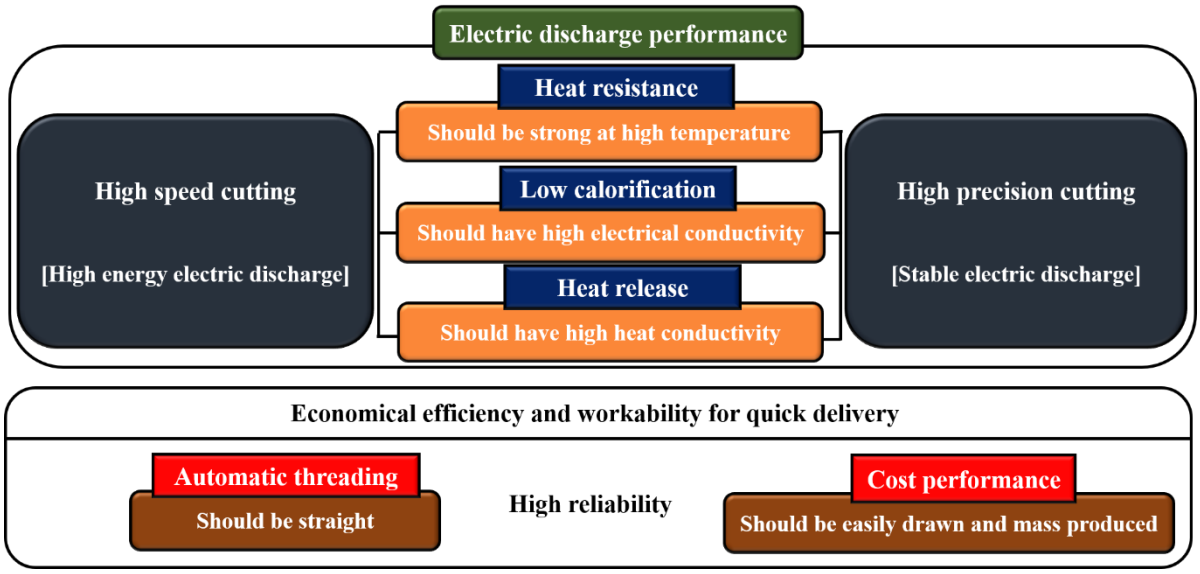


Figure 2.46: The main characteristics to consider in wire electrode selection (adapted from [163]).

2.5.2 Types of wire electrodes

The diameters of commercial electrodes supplied for WEDM operation typically ranges from 0.02 to 0.36 mm depending on the machine tool employed, although the most common size is 0.25 mm [162]. Larger wire diameters can conduct and discharge higher energy, resulting in faster machining speed/MRR [162]. Wire electrodes are generally classified according to its composition and tensile strength. In terms of composition, the main types are plain, coated,

diffusion annealed and composite wires while the categories based on tensile strength are hard (900 MPa), half hard (~490 MPa) and soft (< 440 MPa) [162, 165]. Figure 2.47 details a chart showing the different categories of wire electrodes.

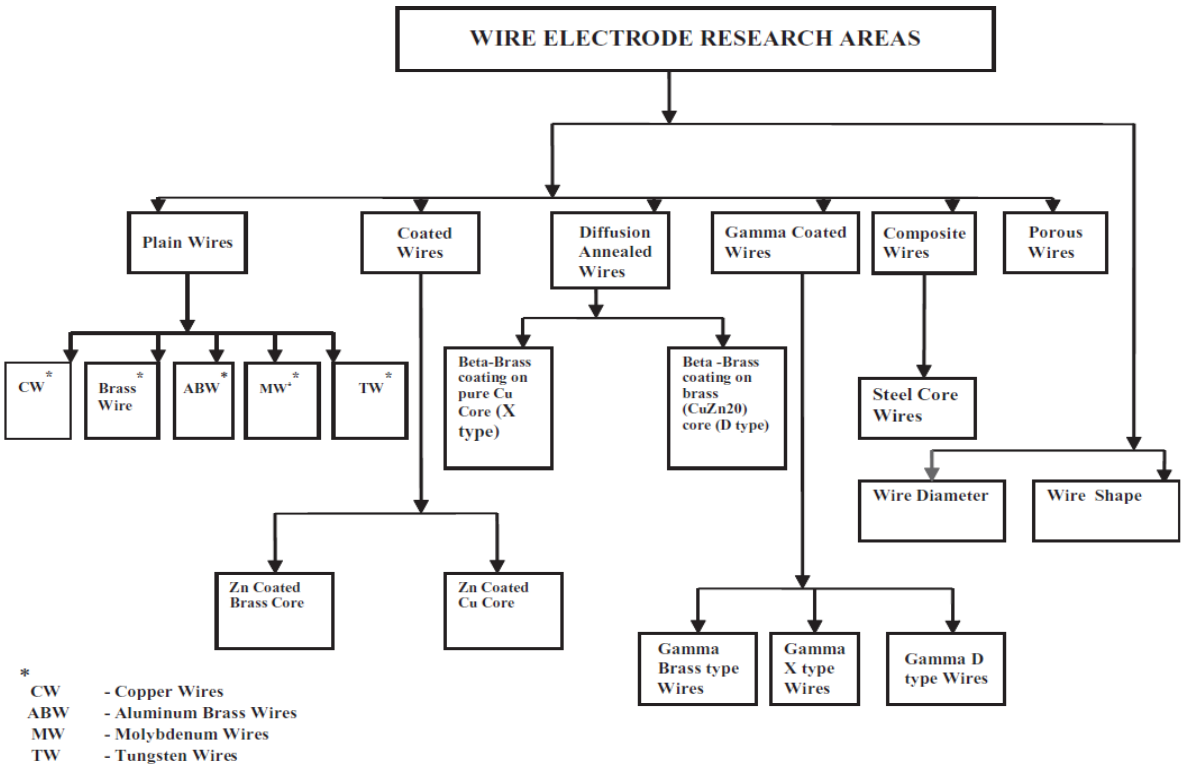


Figure 2.47: Classification/categories of wire electrodes [166].

2.5.2.1 Plain wires

Plain wires consist of a single homogeneous structure such as copper, brass, aluminium brass and molybdenum, which are supplied without any coatings or combined phases [162, 165, 166]. The original material that employed as a plain electrode for WEDM was copper due to its outstanding electrical conductivity and elevated elongation (up to 50%), although its relatively low strength precludes its use in certain applications. Therefore, the development of brass wires that constitutes a mixture of copper (63%-65%) and zinc (35%-37%) has led to improvements such as higher cutting speed due to superior discharge stability [166], greater cooling (due to the lower melting point of zinc which vaporises and cools the wire) and flushability due to rapid evaporation of zinc [162, 166]. Aluminium brass wires comprises brass and a small addition of aluminium leading to increased strength of up to 1200 MPa [162, 165]. Molybdenum wires also have high strength (>1900 MPa) and elevated melting point (2610 ± 10 °C) [167], however

poor flushing, low conductivity, high cost and wear of the wire guides are major drawbacks [162, 164, 165].

2.5.2.2 Coated wires

Although a remarkable improvement in cutting speed was achieved with brass wires, the drawing/manufacturing was more difficult for brass wires with a zinc content above 40%. Therefore, coated wires were developed where an outer layer of zinc was applied without combining it with the copper core [162, 165, 168], which also serves to protect the core from thermal shock and breakage [168, 169]. While the primary benefit of increasing zinc content was to improve cutting speed [166], other materials such as cadmium and magnesium provide better flushability compared to zinc, however their toxicity and reactivity have restricted their wider application [165]. There are various categories relevant to brass-based coatings with different core materials such as high hawk (HIH), falcon (HIF), eagle (HIE), real (HIR) and sonic (HIS) [162]. Figure 2.48 shows the effect of core materials and brass coating on cutting speed and roughness.

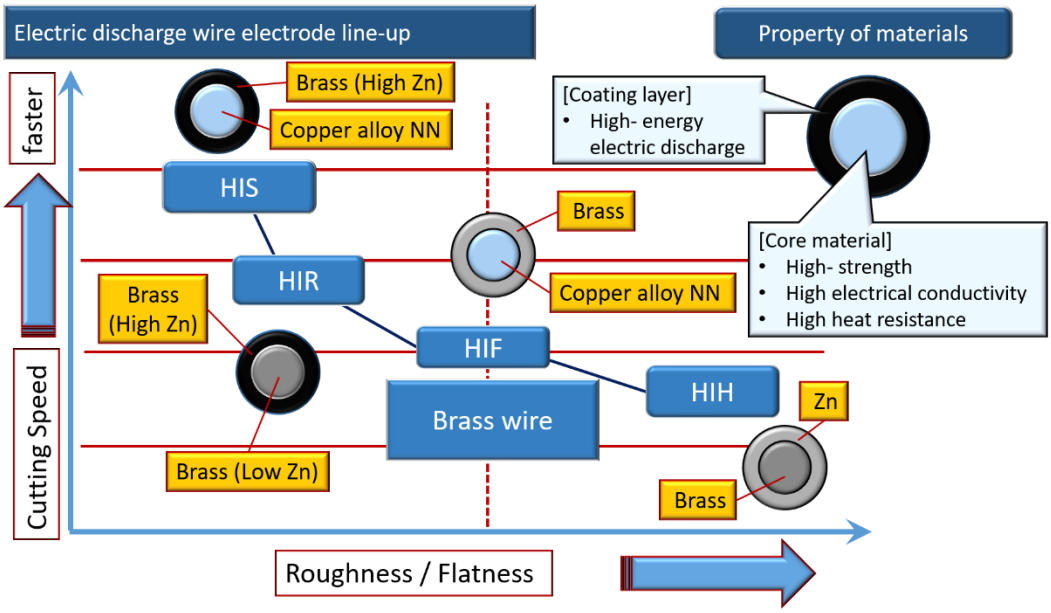


Figure 2.48: Influence of wire core and coating on cutting speed and roughness (adapted from [162]).

2.5.2.3 Diffusion annealed coated wires

While zinc coated wires improves cutting speed and flushing compared to plain electrodes, it suffers from a low melting point that can cause rapid vaporisation of the coating. The diffusion annealed process carried out at elevated temperature in an inert gas environment was employed to produce a brass alloy layer with a high melting point coupled with strong adhesion to the wire core [162]. The brass layer has three phases namely alpha (up to 39% Zn), beta (40-53%

Zn) and gamma (57-70%Zn) [165]. Figure 2.49 shows the composition of several different diffusion annealed wires in comparison to the zinc coated brass wire.

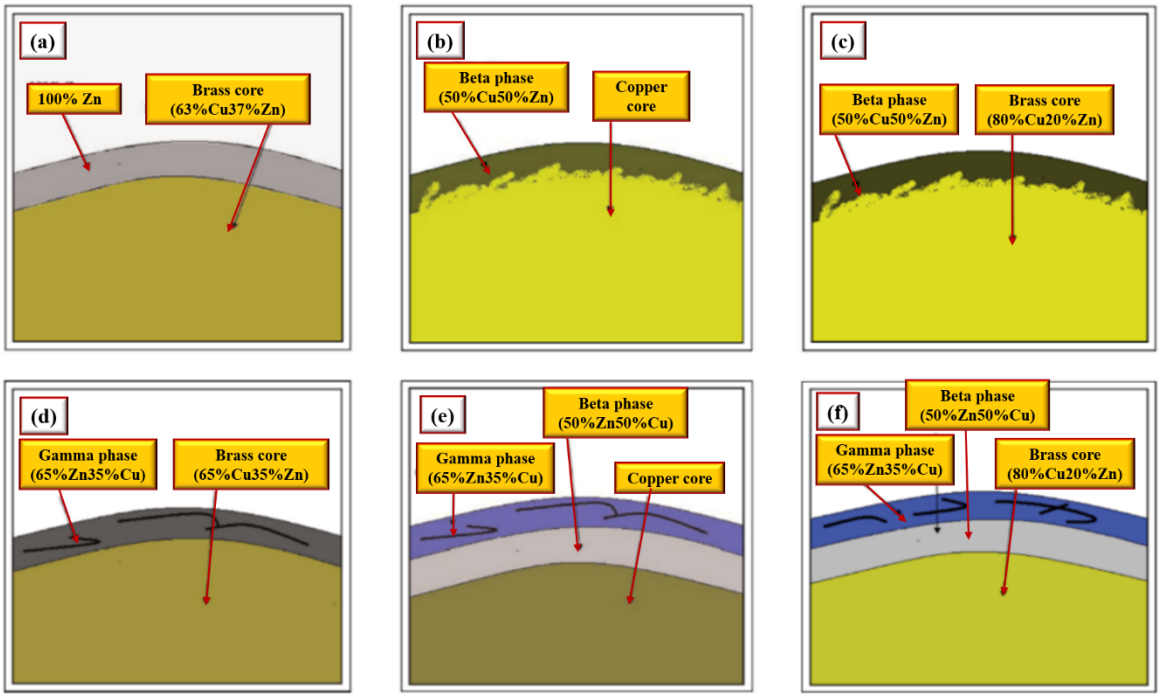


Figure 2.49: Composition of different coated and diffusion annealed wires; (a) zinc coated brass, (b) X type, (c) D type, (d) Gamma brass, (e) Gamma X and (f) Gamma D [166].

2.5.2.4 Composite wires

Composite wires or copper clad steel, comprises a steel core coated with copper and beta phase brass layers, as shown in Figure 2.50. Examples of commercial composite wires include Compeed and Micro/Macro Cut [162, 165]. Composite wires typically have high conductivity, strength and toughness, with the capability for operating under poor flushing conditions as well as having exceptional breakage resistance [162, 165, 166]. The main reasons for wire breakage during WEDM include short-circuits, poor flushing, excessive heat generation, arcing and a sudden rise in sparking or pulse frequency [170, 171]. The repeated sparks cause a crater/flaw in the wire material leading to a reduction in cross sectional area as well as tensile strength. When the flaw exceeds a critical size, wire rupture occurs rapidly [162]. The skin effect phenomenon where the current density is distributed from the core to the outer surface and increases the electrical resistance of the wire is another issue detrimental to the WEDM process. Figure 2.51 shows the current density distribution for steel and copper wires. However, this problem can be eliminated by applying a thick coating with non-magnetic and permeable

materials as reported by Schacht et al. [172]. The evolution and development of high-performance wires in terms cutting speed compared to brass wire is detailed in Figure 2.52.

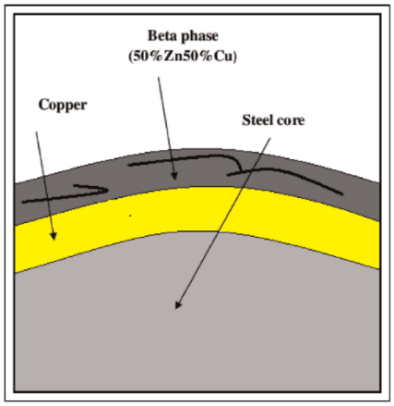


Figure 2.50: Schematic illustration for composite wires [166].

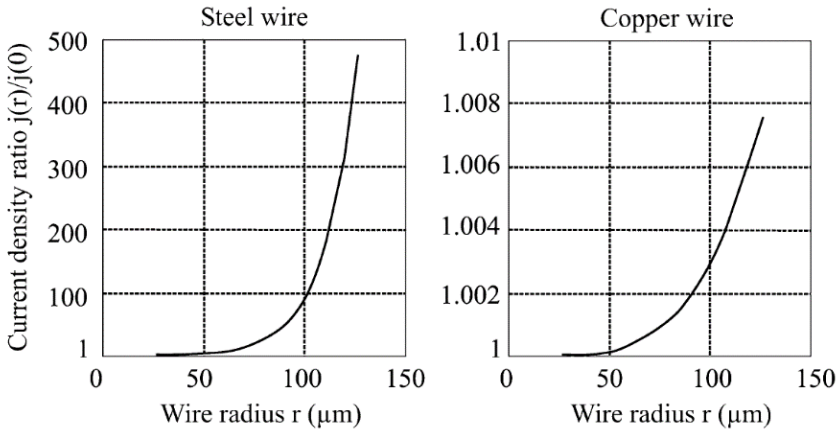


Figure 2.51: Influence of skin effect on current density distribution for different wires [172].

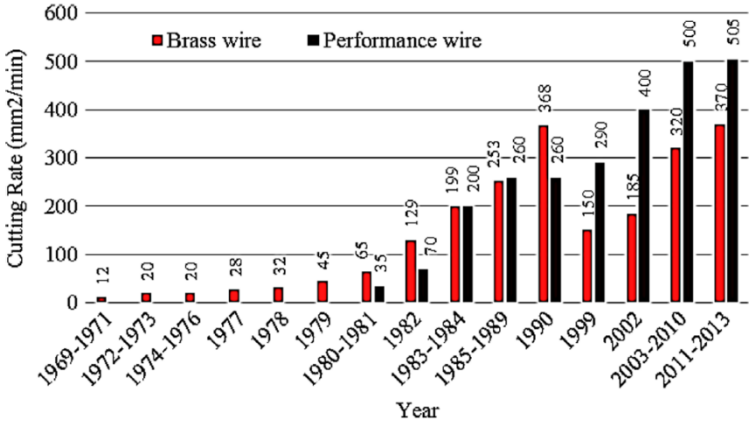


Figure 2.52: Comparison between the cutting speed of brass and performance wires [162].

2.6 Electrical resistivity measurement of CFRP

Carbon fibre reinforced plastic (CFRP) composite is an anisotropic material where the mechanical and physical properties vary in different directions. Therefore, the electrical

conductivity/resistivity of CFRP in different fibre orientations will have a key influence on the EDM process. Different methods have been explored to measure workpiece electrical conductivity including contact and non-contact methods such as two probe, four probe, atomic force microscopy and time domain spectroscopy. However, the two and four probe methods are the most commonly used techniques, as illustrated in Figure 2.53.

2.6.1 Two and four probe method

In the two probe approach, two terminals/probes are attached to opposite sides of the workpiece material where the current flows (typically supplied by a battery) along the sample length [173]. In this method, the voltage is measured using the same wires providing the current flow. The electrical resistance is recorded directly from the ohmmeter and the resistivity is calculated using Equation 2.1 [173, 174]. The shortcoming of this method is that measurements can be inaccurate for small/thin materials as wire, electrode and contact resistances are considered [173-175].

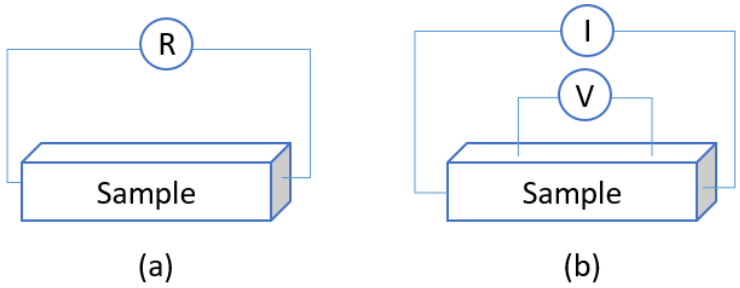


Figure 2.53: Schematic illustration for resistivity measurements using (a) two probe and (b) four probe methods (adapted from [176]).

$$\rho = \frac{RA_o}{L} \qquad (2.1)$$

where R is electrical resistance, A_o: cross sectional area and L: sample length.

Several researchers have employed this method to calculate/evaluate electrical resistivity of composite materials. Shin et al. [177] utilised the two probe method for resistance measurement of CFRP by polishing the sample's surface and coating it with silver paint prior to applying a force against the workpiece with copper sheets to eliminate contact resistance between them as shown in Figure 2.54. Similarly, Wang et al. [178] employed the same method to calculate the resistivity of carbon fibre/cement composite but without applied forces and using copper foils instead of sheets.

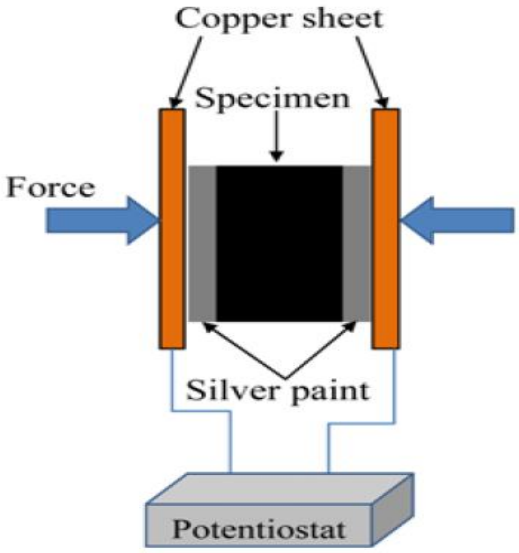


Figure 2.54: Electrical resistance measurement [177].

The four probe technique involves a similar principle, however four terminals are employed instead of two. Current is passed through the outer terminals while the two inner terminals measure the voltage. Hence, contact resistance is ignored by this method, with several publications reporting use of this approach [179-183].

2.7 Summary

The favourable properties of CFRP composites have led to its increasing use in various industrial sectors such as aerospace, automotive and leisure equipment, however the high degree of heterogeneity and anisotropy represented a real obstacle during machining processes. For instance, severe tool wear and short tool life are key problems in drilling and milling operations as well as delamination and fibre pull out that seriously influenced on material properties. Although several studies have been carried out to minimise delamination, several challenges remain. Therefore, non-conventional processes such as water jet machining, laser beam machining, ultrasonic assisted machining and electrical discharge machining have been evaluated as an alternative for machining CFRP. While benefits include the absence of tool wear, major delamination is observed in water jet machining while heat affected zones, surface damage/burn and tapered cuts were prevalent following laser machining. Research involving EDM drilling of CFRP have been reported, however there has been very limited work relating to wire EDM. The gaps in knowledge identified following the literature review is illustrated in Figure 2.55. The present research focusses on the WEDM of CFRP to identify the influence of different cutting conditions and wire electrode on various performance measures.

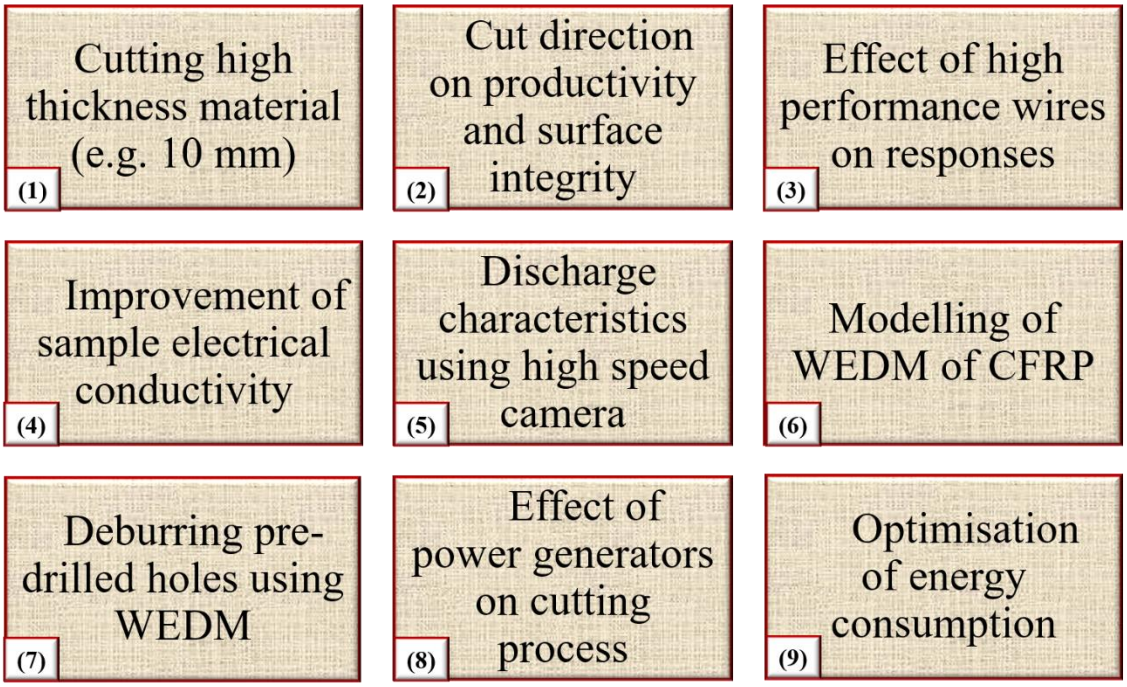


Figure 2.55: Illustration showing the gaps in knowledge relating to WEDM of CFRP.

3 EXPERIMENTAL WORK

Following initial preliminary testing to assess the basic machinability of CFRP composites using WEDM, 3 primary phases of experimental work were carried out to understand the influence of operating parameters, wire electrode material, cutting direction, material lay-up and stacking with a metallic sheet. Phase 1 and 2 focused on the effect of cutting direction with respect to fibre direction (parallel and perpendicular) in unidirectional CFRP at varying operating parameters using a zinc coated brass core (Topas plus D) and copper/brass coated steel core (Compeed) wire electrodes respectively. To increase the effective workpiece electrical conductivity, the performance of stacking UD-CFRP laminates with copper sheets was evaluated in Phase 3 trials, together with an investigation of industrially representative multidirectional CFRP laminate workpieces. Each phase was divided into a number of sub-phases as follows:

Phase 1A: Effect of operating parameters when cutting UD-CFRP parallel to fibre direction using zinc coated brass core wire.

Phase 1B: Effect of operating parameters when cutting UD-CFRP perpendicular to fibre direction using zinc coated brass core wire.

Phase 2A: Effect of operating parameters when cutting UD-CFRP parallel to fibre orientation using copper/brass coated steel core wire.

Phase 2B: Effect of operating parameters when cutting UD-CFRP perpendicular to fibre orientation using copper/brass coated steel core wire.

Phase 3A: Preliminary investigation on cutting UD-CFRP/Cu stacks using zinc coated brass and copper/brass coated steel core wires.

Phase 3B: Influence of operating parameters and wire electrode material when cutting UD-CFRP-metallic stacks.

Phase 3C: Influence of wire electrode material and operating conditions on cutting performance of multidirectional CFRP laminates.

Figure 3.1 summarises the experimental phases planned and carried out during this project. The following sections presents details of the workpiece/wire electrode materials, test equipment used in machining trials as well as corresponding experimental procedures and test arrays.

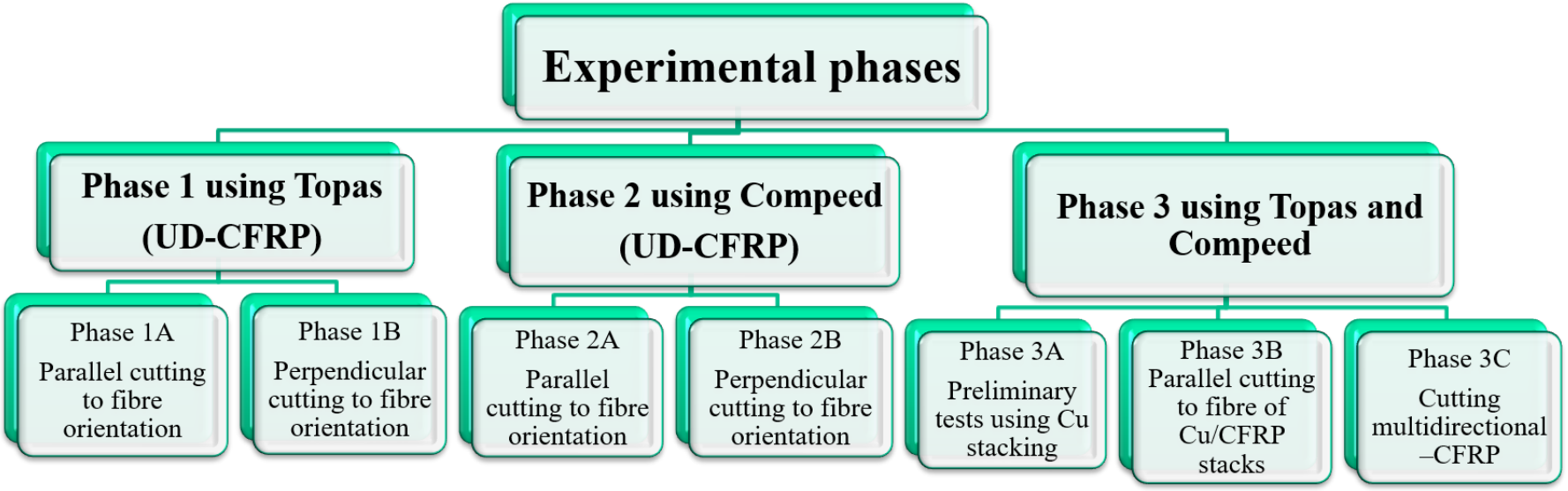


Figure 3.1: Flow graph illustrating the different experimental work phases.

3.1 Workpiece materials

The UD-CFRP workpieces used for the preliminary as well as mainstream Phase 1 and 2 tests were comprised of 32 unidirectional prepregs/plies, which were all manually laid up in a single direction (0° orientation) followed by autoclave curing to consolidate the material. The individual prepregs (each 0.26 mm thick) consisted of intermediate modulus (294 GPa) carbon fibres impregnated within an epoxy resin matrix [28]. The cured material was cut up into square plates measuring 100 x 100 x 8.4 mm as shown in Figure 3.2 together with the associated laminate cross section. The prepregs were produced by Toray Industries with a designation of Toray 3911/34%/UD268/T800SC-24K. The main properties of the carbon fibres are listed in Table 3.1. while detailed data sheets for the fibre properties and material safety are outlined in Appendix A and B respectively.

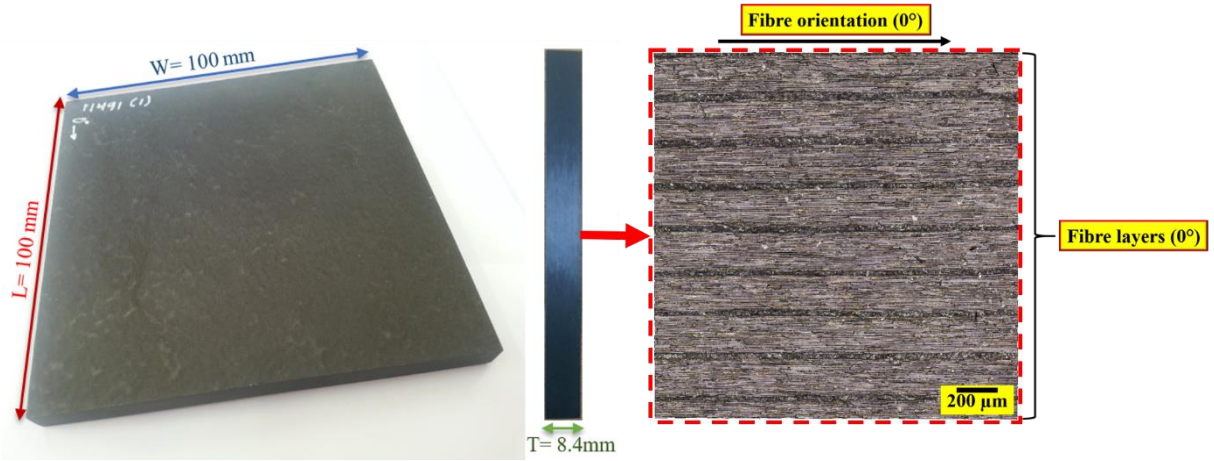


Figure 3.2: Unidirectional CFRP laminate with a micrograph of the cross section.

Table 3.1: Physical/mechanical properties of the carbon fibre used in the UD-CFRP laminates [28].

Parameter	Value
Fibre diameter	5 µm
Tensile modulus	294 GPa
Tensile strength	5880 MPa
Fibre areal weight	268 g/m^2
Density	1.8 g/cm^3
Thermal conductivity	70 W/m.K
Strain	2%

In Phase 3A and 3B, the UD-CFRP laminates were initially used in conjunction with thin adhesive copper foil (0.05 mm thickness) applied on both sides of the plates to improve the electrical conductivity of the workpiece material. However, the force from the flushing jets

caused severe damage and peeling of the foil during machining, see Figure 3.3, leading to a short-circuit and eventual wire breakage. Therefore, the foil was replaced with 1.2 mm thick copper sheets, which were clamped together according to the schematic shown in Figure 3.4.

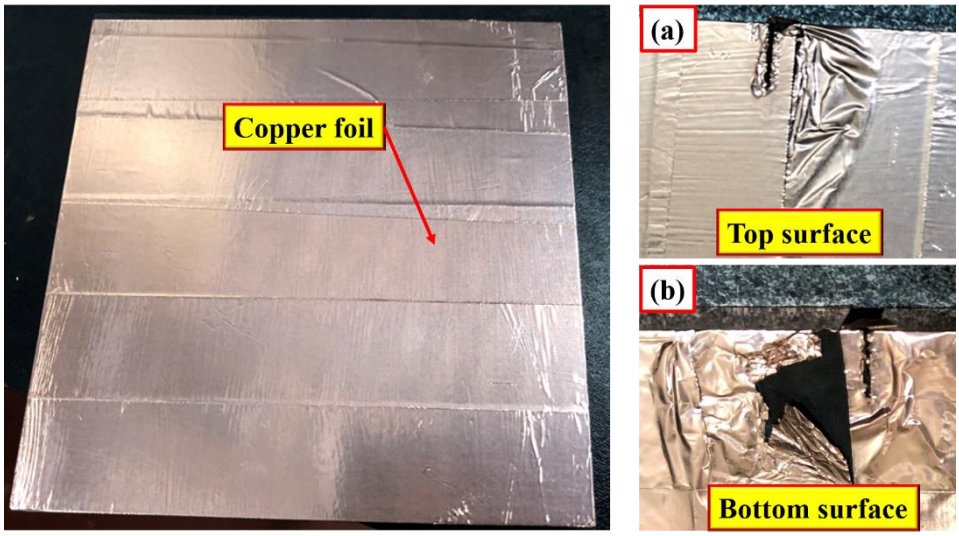


Figure 3.3: Unidirectional CFRP laminate covered with adhesive copper foil and machining damage after cutting on the (a) top and (b) bottom surfaces of the workpiece.

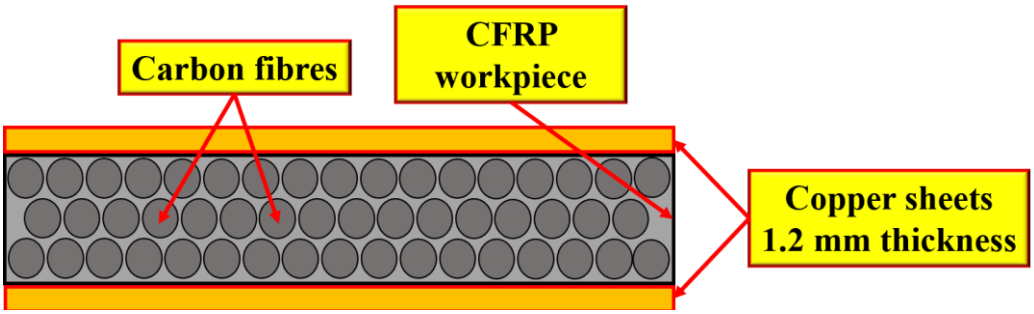


Figure 3.4: Schematic representation of CFRP/Cu stacks used in Phase 3A and 3B.

For Phase 3C tests, industrially representative multidirectional CFRP laminates measuring 122 x 122 x 8.75 mm were used, which involved 36 unidirectional plies (each 0.25 mm thick) laid up according to $[45°/0°/135°/90°/45°/0°]_{3S}$ orientation as shown by the cross sectional micrograph in Figure 3.5. The laminates were initially cured for 30 minutes at a dwell step of 80°C, then heated up to 135°C at a rate of 1 °C/min and kept in vacuum chamber for 4 hours at a pressure of 0.9 bar. The prepregs were manufactured by Advanced Composite Group (ACG) [184], with key properties of the prepregs and cured laminates detailed in Table 3.2.

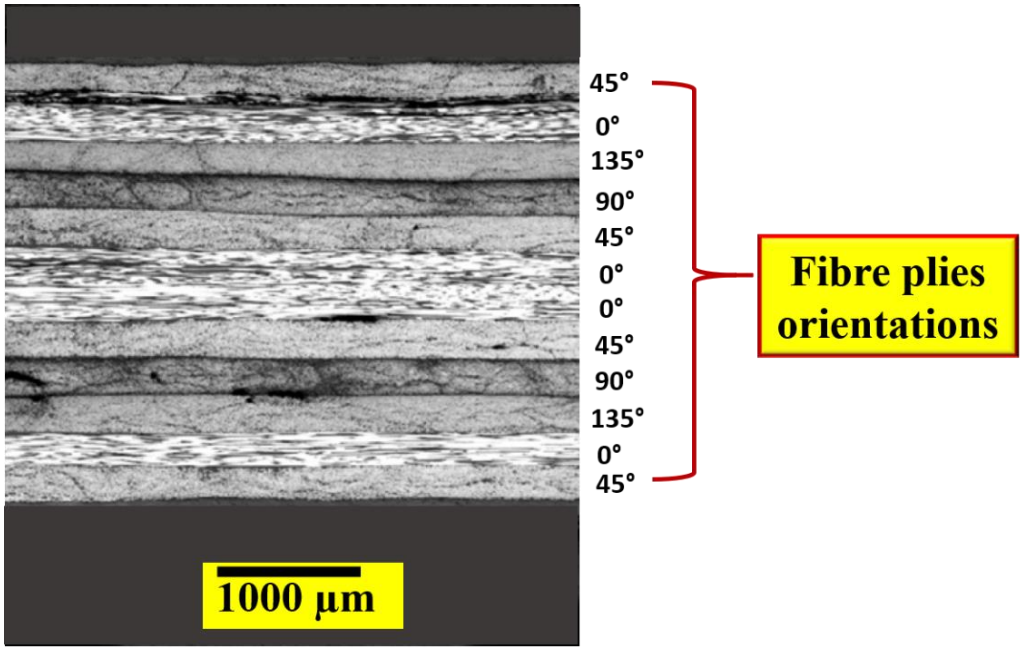


Figure 3.5: Micrograph showing the cross section of the multidirectional CFRP laminate [184, 185].

Table 3.2: Key properties of the prepreg layers and multidirectional CFRP laminate [184, 185].

Prepreg specifications	**Description**
Reinforcement	Toho Tenax HTS 12K, 268g/m^2, 1/4 mm (thickness), UD, 1.76g/cm^3(ρ)
Matrix	ACG MTM44-1, 1.18 g/cm^3 (ρ)
Fibre/resin code	ACG MTM44-1/HTS-268-12K (V_f = 56.5%)
Fibre weave type	Unidirectional (UD) prepregs
Fibre orientation (lay-up)	$[45°/0°/135°/90°/45°/0°]_{3s}$
Property (CFRP laminate)	**Unit**
Sample density	1.6 g/cm^3
Ultimate tensile strength	2000 MPa
Interlaminate shear strength	14 MPa
Elastic modulus	150 GPa

3.2 Wire electrodes

Two different high-performance wire electrodes were employed for the trials; diffusion annealed zinc coated brass (used in Phase 1 and 3 trials) and composite copper/brass coated steel core wires (used in Phase 2 and 3 tests). The diameter of both wires was 0.25 mm, which were selected for their good electrical conductivity, high cutting speed as well as increased resistance to wire rupture caused by a short circuit or excessive build-up of heat in the machining zone.

3.2.1 Zinc coated brass core wire electrode (Topas plus D)

The Topas plus D wire electrode (other commercial names include Thermo SE and AC cut VH) is composed of a brass core with 20% zinc and coated with a twin layer of zinc rich diffused β and γ brass phases as depicted in Figure 3.6. The composition of the wire provides a tensile strength of 800 to 900 MPa, good electrical conductivity of 28% IACS (International Annealed Copper Standard, which is equivalent to 58 x 10^6 S/m) and 30-35% higher machining speed compared to standard brass wire [186-188].

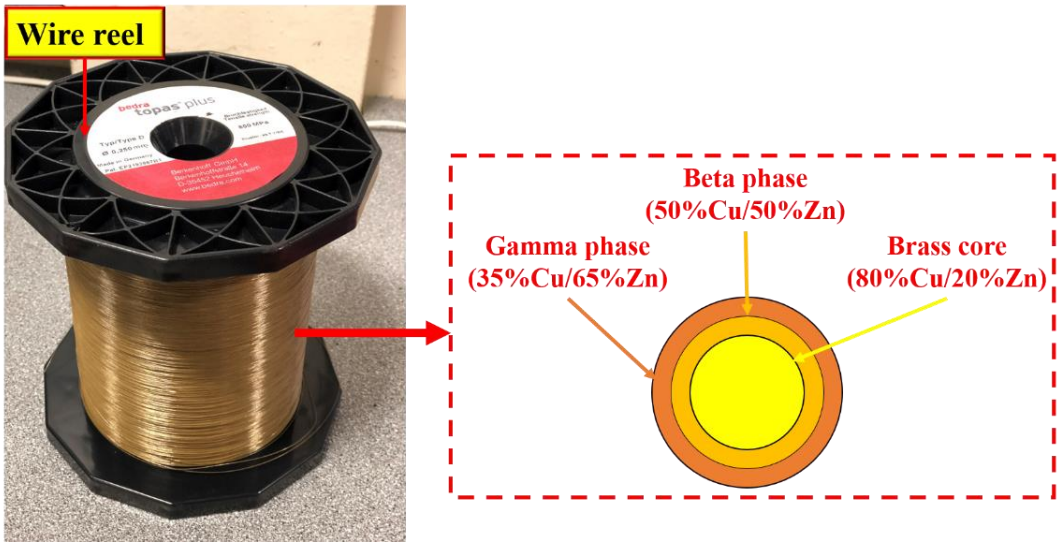


Figure 3.6: Topas plus D wire electrode and its composition.

3.2.2 Copper/brass coated steel core wire electrode (Compeed)

The Compeed wire comprised a steel core coated with a dual layer of copper and diffused brass (β-phase of Cu50%Zn50%), see Figure 3.7. The copper layer increased wire conductivity (50% IACS) leading to faster cutting speed while the β-phase brass provided for more stable spark discharges due to the zinc rich content, which provides improved flushability, with a room temperature tensile strength of 800 MPa. In addition, the Compeed wire exhibited superior high temperature strength of 300 MPa at 500°C, compared with hard (70 MPa) and extra hard (110 MPa) brass wires [189], as shown in Figure 3.8. Despite having similar tensile strengths, the Compeed wire has greater resistance to wire breakage due to the higher fracture toughness of the steel core in comparison to the Topas plus D wire.

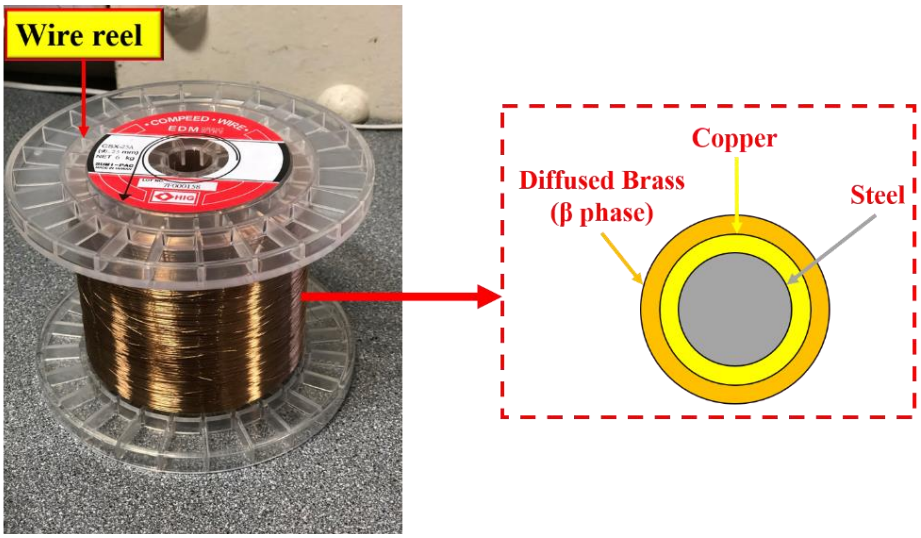


Figure 3.7: Compeed wire electrode and its composition.

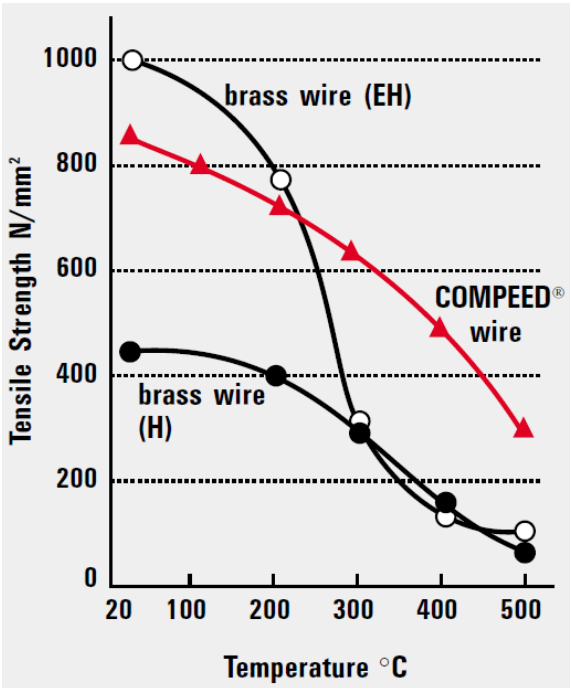


Figure 3.8: Comparison between tensile strength and different types of brass wire at various work zone temperatures [189].

3.3 Equipment, experimental setup and measurement procedures

3.3.1 WEDM machine tool

An AgieCharmilles Robofil FL240CC wire EDM machine as shown in Figure 3.9, was employed for all the machining experiments with deionised water as the dielectric, which was maintained at an electrical conductivity of ~ 5µS/cm. The machine was equipped with a modern CleanCut (CC) generator capable of cutting speeds of up to 400 mm^2/min and achieving workpiece surface roughness (Ra) levels of less than 0.1 µm [190]. Furthermore, the CC

generator comprises anti-electrolysis technology that prevents stray voltage interacting with debris in the dielectric. The technical specifications of the FL240CC WEDM machine are displayed in Table 3.3.

Table 3.3: Technical specifications of Robofil FL240CC WEDM machine [191].

Machine	Value
Equipment dimensions (m)	2.02 x 2.05 x 2.0
Equipment total weight (kg)	2450
Maximum workpiece dimensions (m)	1.0 x 0.55 x 0.22
Maximum workpiece weight (kg)	750
Table dimensions (m)	0.68 x 0.45
Front door dimensions (m)	0.82
Floor to table distance (m)	1.0
Dielectric volume (m^3)	0.91
X, Y, Z travel (m)	0.35 x 0.22 x 0.22
U, V travel (m)	0.35 x 0.22
Maximum allowed taper (°/m)	±45/0.22

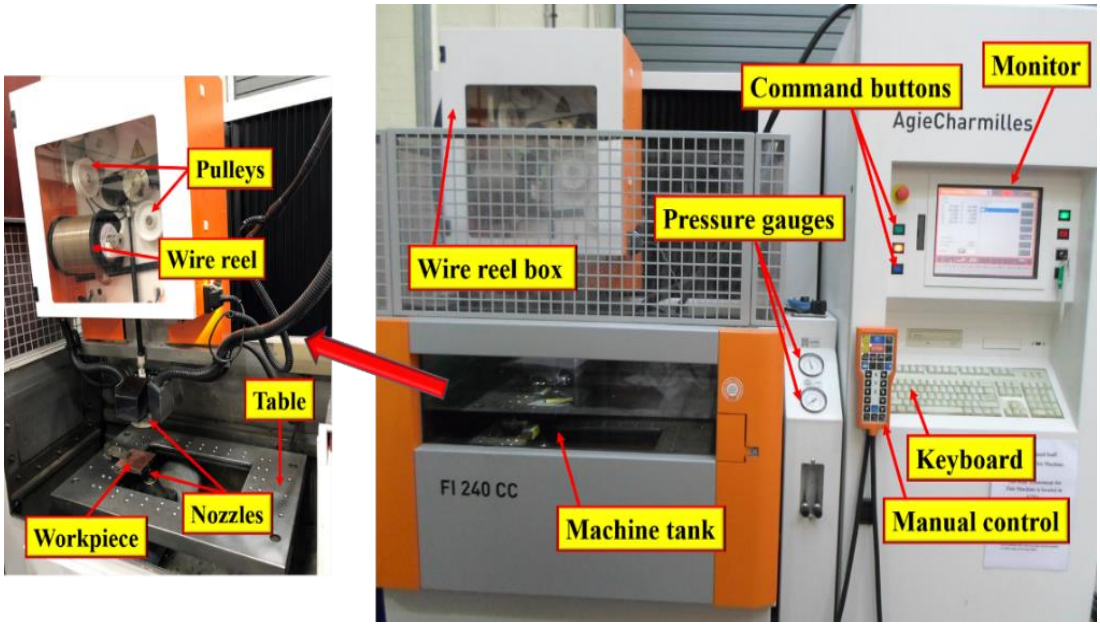


Figure 3.9: Robofil FL240CC wire EDM machine.

3.3.2 Experimental setup

The UD-CFRP workpieces were secured on the machine worktable using a rectangular block and screws. The feed of the wires were either parallel or perpendicular to the fibre directions for trials involving individual CFRP plates in Phase 1 and 2, as shown by the schematic in Figure 3.10. Experiments using the UD-CFRP/Cu stack arrangement were all performed with the wire feeding parallel to fibre orientation based on results from Phases 1 and 2, which

indicated superior cutting rates were generally achieved when machining along the fibre direction. Figure 3.11 illustrates the experimental setup for trials with individual CFRP and stacked metallic-CFRP workpieces.

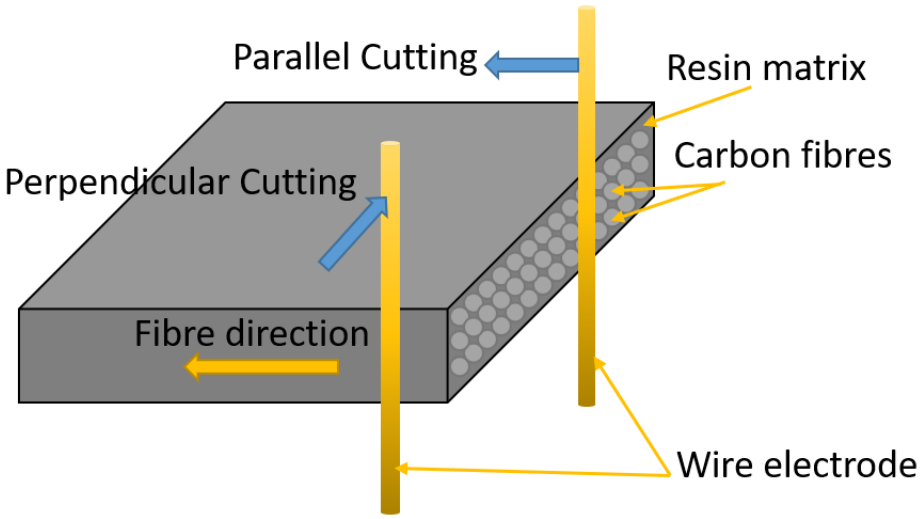


Figure 3.10: Schematic illustration for cutting to fibre orientations.

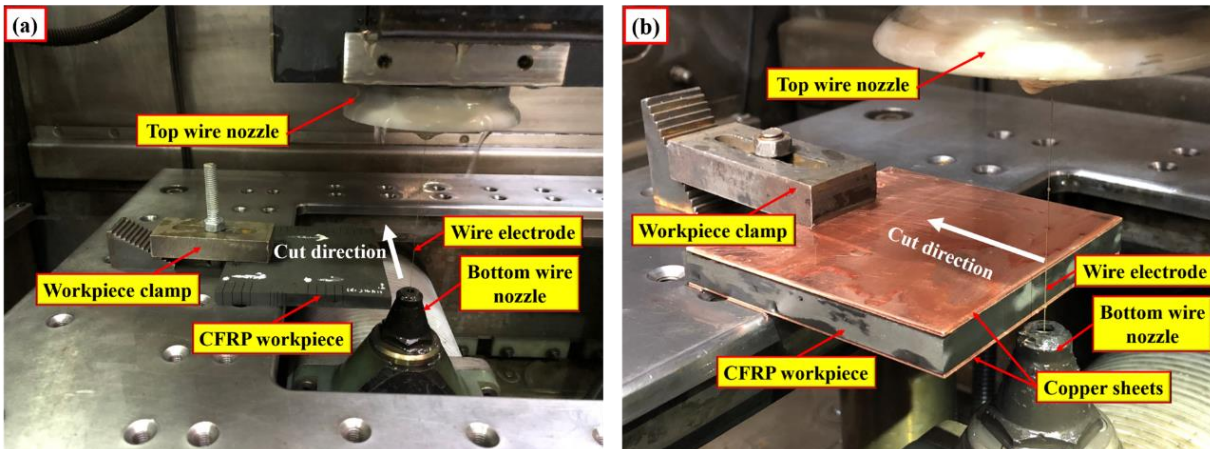


Figure 3.11: Experimental setup for tests involving; (a) individual CFRP and (b) metallic-CFRP stacked workpieces.

3.3.3 Material removal rate calculation

The machining time for the tests were recorded using a digital stopwatch. Following the conclusion of each trial, an air blower and hair drier were utilised to dry and evaporate the absorbed water in the CFRP plates. The mass of the workpiece specimens were weighed prior to and after each test using a precision digital scale having a measurement range of 0.5 to 3500 g and a minimum resolution of 0.01 g, as shown in Figure 3.12. The material removal rate was then calculated according to Eq. 3.1 [151]:

$$MRR = \frac{m_b - m_a}{\rho_o * t_m} \quad (3.1)$$

where the workpiece mass before and after machining are represented by m_b and m_a respectively, ρ_o is sample's density and t_m is the machining/cutting time.



Figure 3.12: Precision digital scale for workpiece weight measurement.

3.3.4 Kerf width measurement

The machined kerf width on the top and bottom surfaces of the CFRP samples was measured using an Alicona G5 InfiniteFocus 3D optical measurement device at 5X magnification. Image field mode was selected to scan the entire kerf length to produce a micrograph for width assessment using the in-built software as shown in Figure 3.13. The first measurement was recorded at 500 µm from the workpiece free edge to avoid any extreme/outlier values caused by damage at the entrance of the kerf. Nine width measurements at equidistant intervals along the kerf length were taken on both the top and bottom faces of the workpiece, with the effective kerf width expressed as the mean value of the top and bottom readings. Kerf widths were evaluated in all test phases except for Phase 3B, due to the excessive damage of the kerf edges, which made measurements difficult. For workpieces where edge delamination was observed, a delamination factor (F_d) was determined according to Eq. 3.2 [49]:

$$F_d = \frac{W_{max}}{W_a} \quad (3.2)$$

where W_{max} and W_a are the widths of maximum damage and average kerf respectively.

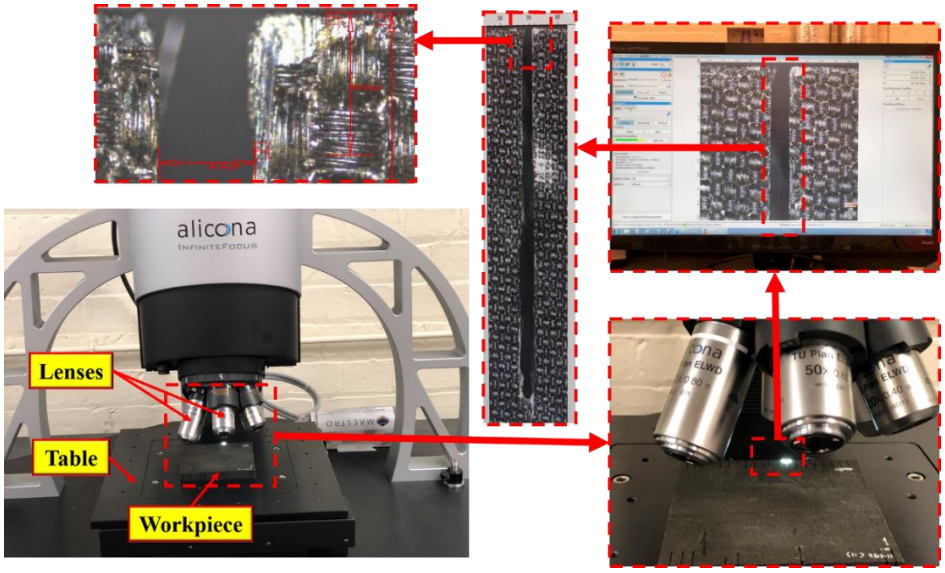


Figure 3.13: Kerf width measurement using Alicona G5 InfiniteFocus 3D optical measurement device.

3.3.5 Surface integrity evaluation

3.3.5.1 Surface roughness measurement

The Alicona G5 InfiniteFocus system was similarly utilised to measure surface roughness of the machined workpieces. A 20X magnification lens was used with vertical and lateral resolutions of 90 nm and 2.94 µm respectively. The microscope was calibrated using a standard roughness reference sample as shown in Figure 3.14. The measured results showed close agreement to the reference roughness values as detailed in Table 3.4. The 2D roughness values (Ra) were estimated based on the average of 5 measurements with cut off and evaluation lengths of 0.8 mm and 4 mm respectively, while the areal parameter (Sa) was evaluated over an area of 2 mm x 2 mm.

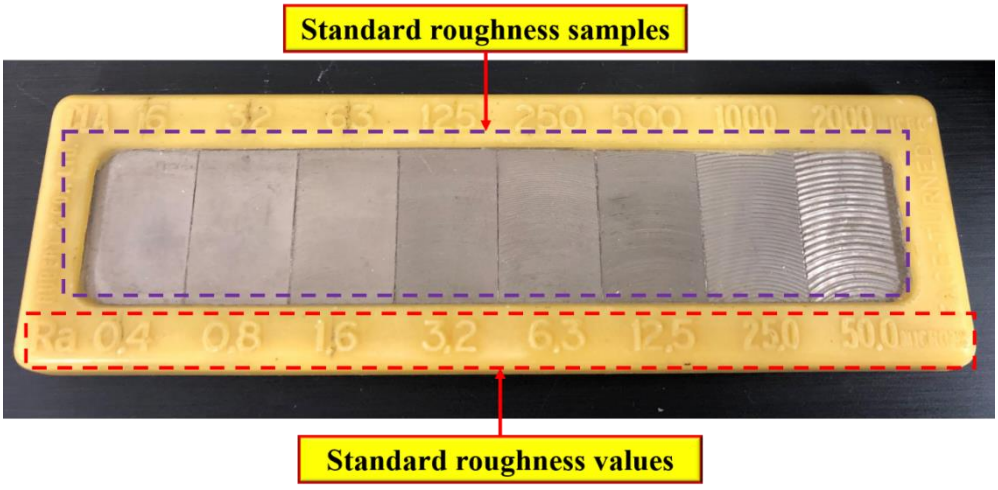


Figure 3.14: Standard reference sample for calibration of surface roughness.

Table 3.4: Comparison between surface roughness measured using Alicona and standard values.

Standard values	Alicona measured values
Ra 3.2 µm	Ra 3.00 µm/ Sa 2.92 µm
Ra 6.3 µm	Ra 6.32 µm/ Sa 6.25 µm
Ra 12.5 µm	Ra 12.02 µm/ Sa 11.88µm

Following completion of the machining experiments, the CFRP workpieces were cross sectioned into samples measuring 10 x 5 x 8.4 mm using a diamond disc cutter. Each sample was divided into 3 separate measurement zones (2 mm x 3 mm per zone) in order to avoid exceedingly large data files and reduce scan time. Figure 3.15 shows the experimental setup and various stages of the surface roughness measurements. Both linear roughness (Ra) and areal roughness (Sa) were evaluated to avoid extreme or outlier results caused by cavities generated due to resin evaporation, which would have a detrimental influence on the accuracy of the former. For Ra values, 6 measurements were recorded both horizontally (parallel to feed direction) and vertically (perpendicular to feed direction) in each zone, with the final value taken as the average of the 18 readings in each direction. In contrast, the areal roughness (Sa) value was obtained from the average of 3 readings, one from each zone. The cut-off lengths were 0.8 mm and 887 µm for the Ra and Sa measurements respectively. Table 3.5 details the technical specifications of the Alicona InfiniteFocus system.

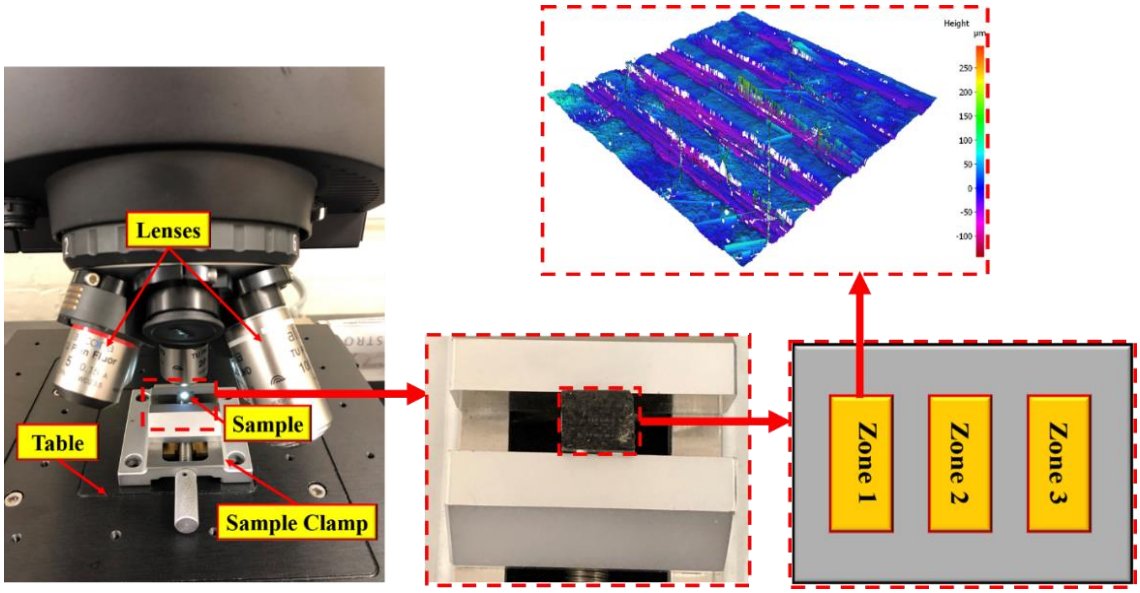


Figure 3.15: Experimental set up for surface roughness measurements.

Table 3.5: Technical specifications of the Alicona G5 InfiniteFocus microscope [192].

General specifications							
Max. number of measurement points in a single measurement	X: 1840, Y: 1840, X x Y: 3.3 million						
Max. number of measurement points	X: 540000, Y: 540000; X x Y: 500 million						
Travel range (X x Y x Z)	100 mm x 100 mm x 100 mm = 1000000 mm^3						
Dimensions (W x D x H)	Measurement instrument: 810 mm x 640 mm x 700 mm (up to 948 mm); control server HP: 200 mm x 490mm x 440mm						
Mass	Instrument: 105 kg - 120 kg; HP server: 16.9kg						
Temperature range	Instrument: possible: 18º C - 28º C; HP: possible: 0º C - 30º C						
Temperature gradient	Less than 1ºC/h						
Relative humidity	Recommended: 45 % (+/-5 %); possible: 45 % (+/-15%)						
Power supply	1000 W; 100 - 240 V; 50 - 60 Hz						
Measurement object							
Surface texture	Surface topography Ra above 0.009 µm with λc 2 µm; depending on surface structure						
Maximum height	100 mm - 345mm						
Maximum weight	30 kg; more on request						
Objective specific features							
Objective magnification (*)		2.5x	5x	10x	20x	50x	100x
Numerical aperture		0.075	0.15	0.3	0.4	0.6	0.8
Working distance	mm	8.8	23.5	17.5	19	11	4.5
Lateral measurement range (X, Y) and (X x Y)	mm	5.63	2.82	1.62	0.81	0.32	0.16
	mm^2	31.7	7.95	2.62	0.66	0.10	0.03
Measurement point distance	µm	3.52	1.76	0.88	0.44	0.18	0.09
Lateral limiting resolution	µm	4.35	2.18	1.09	0.82	0.54	0.41
Vertical resolution	nm	2300	410	100	50	20	10
Vertical range	mm	8	22.5	16.5	18	10	4
Vertical scanning speed	µm/s	3000	3000	1000 - 3000	500-3000	200 - 2000	100 - 1000
Measurement speed	≤ 1.7 million measurement points/sec.						
Minimum measurable height	µm	2.3	0.41	0.1	0.05	0.02	0.01
Maximum measurable height	mm	8	22.5	16.5	18	10	4
Measurement field X x Y	mm	5.63x 5.93	2.82x 2.82	1.62x 1.62	0.81 x0.81	0.32x 0.32	0.16x 0.16
Minimum roughness (Ra)	µm	7	1.2	0.3	0.15	0.06	0.03
Minimum roughness (Sa)	µm	3.5	0.6	0.15	0.075	0.03	0.015
Minimum radius	µm	20	10	5	3	2	1
Minimum wedge angle	°	20					
Maximum slope angle	°	87					

3.3.5.2 Surface damage and delamination

A toolmakers microscope with a micrometre XY stage connected to a Nikon EOS digital camera was utilised for capturing optical micrographs of workpiece damage (matrix burn, delamination, fuzzing, frayed fibres, etc.) on the top and bottom of the CFRP plates at 40X magnification. The images were processed using EOS software. The analysis setup is shown in Figure 3.16. Measurement of delamination widths was carried out using the Alicona InfiniteFocus unit as outlined in Section 3.3.4.

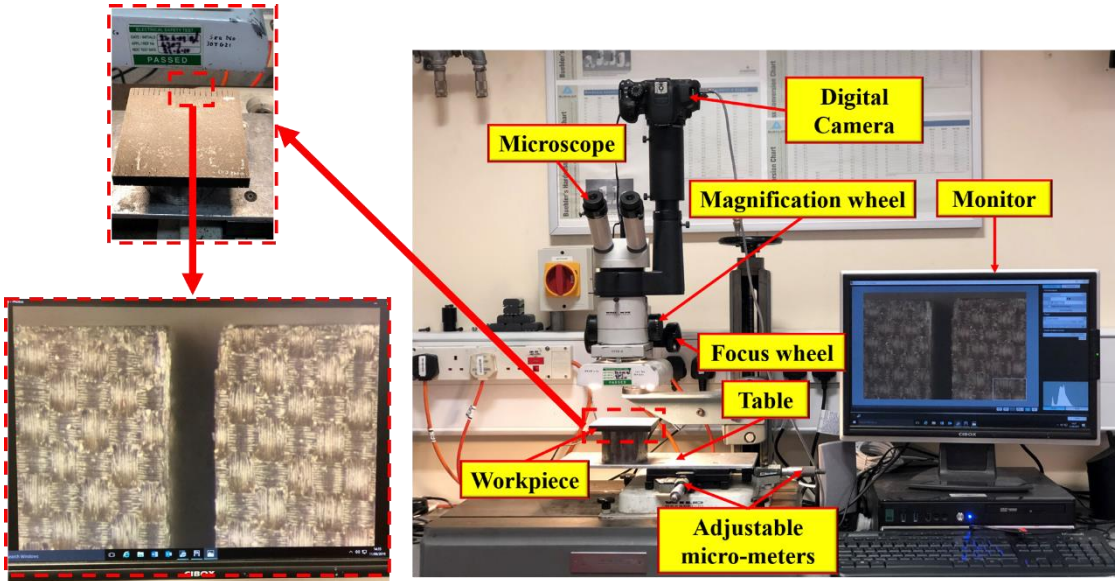


Figure 3.16: Optical micrographs captured using tool maker microscope.

3.3.5.3 Surface topography and structure

Three workpieces corresponding to tests achieving the highest, median and lowest MRR from each experimental array together with associated confirmation test specimens were selected for further in-depth surface integrity analysis. The surface topography, elemental composition as well as damage on machined surfaces generated along/between plies including re-solidified particles, fibre breakage, interlaminar cracks and fibre swelling were evaluated using a JEOL JCM-6000 Plus benchtop scanning electron microscope (SEM). The specimen sizes were restricted to dimensions of 7 cm diameter and 5 cm height, which were mounted on the sample holder using adhesive conductive tape of 10 mm diameter attached to the bottom of the sectioned workpieces. Figure 3.17 outlines the setup for the SEM analysis with technical specifications of the machine detailed in Table 3.6.

Table 3.6: Technical specifications of JCM-6000 SEM equipment [193].

Item	Value
Image mode	Secondary electron image (SEI) and Backscattered electron image (BEI)
Magnification	SEI: x10 to x60000 and BEI: x10 to x30000 Display size 120 mm x 90 mm
Displayed magnification	SEI: x23 to 141000 and BEI: x23 to x 70500 Display size 282 mm x 211 mm
Accelerating voltage	SEI: 5, 10 and 15 kV BEI: 5 and 10 kV
Specimen stage	Manual control XY: 35 mm x 35 mm
Max. sample size	70 mm diameter and 50 mm height
Metrology	Angles and distance among two points
Monitor	Touched 23 inch wide LCD monitor
File format	BMP, TIFF, JPEG

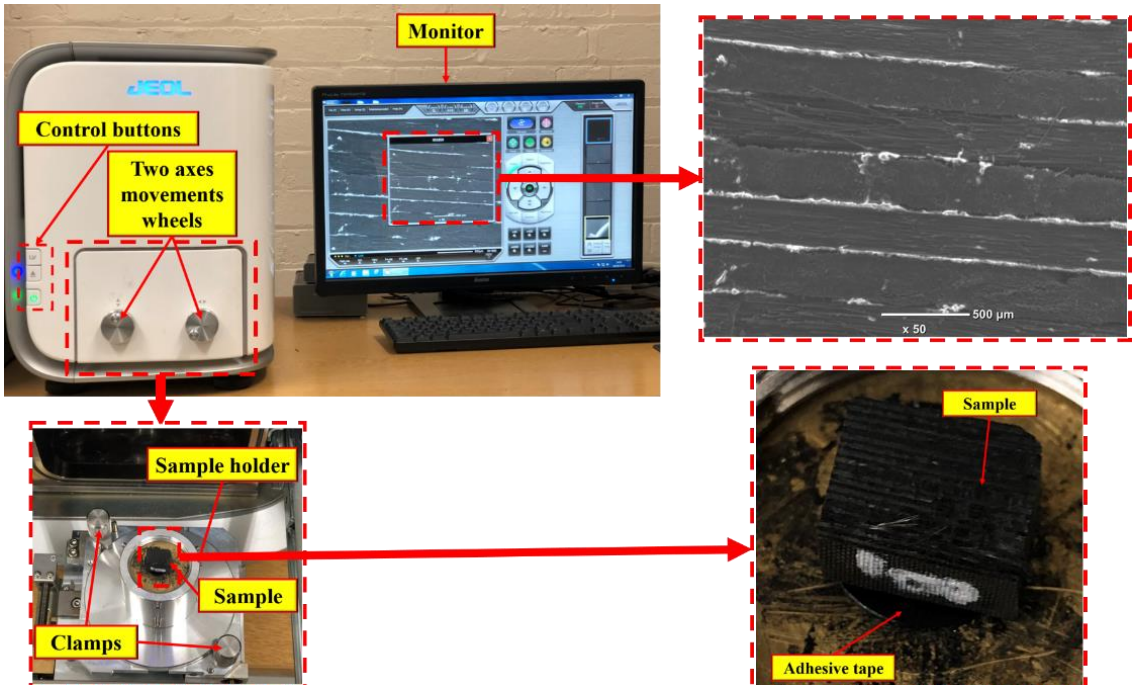


Figure 3.17: Setup for SEM surface topography assessment.

3.3.6 Electrical resistivity measurement

The bulk electrical resistivity of the CFRP laminates were measured using the two-probe method, where the probe terminals were adhered with copper sheets (100 mm x 100 mm x 1 mm) using solder core wire. The CFRP laminate was held in a benchtop vice, with wooden plates and copper sheets placed between the workpiece and jaws of the vice, as shown in Figure 3.18. The wooden plates were used to insulate the CFRP laminate from the vice while the probes were attached to the copper sheets, which were in contact with the edges of the workpiece. The

probes were connected to a digital multi-meter, which displayed the electrical resistance of the CFRP workpiece as the vice was tightened. The measurements were recorded for all specimen directions (X, Y and Z-axes). The measured resistivity of the workpieces utilised in the experimental phases are detailed in Appendix C. The resistivity was calculated using Eq. 3.3 [173, 174]:

$$\rho = \frac{RA_o}{L} \qquad (3.3)$$

where R is the electrical resistance (Ohm), A_o is the cross sectional area (m^2) of the sample and L is the length of the sample or the distance between probes (m).

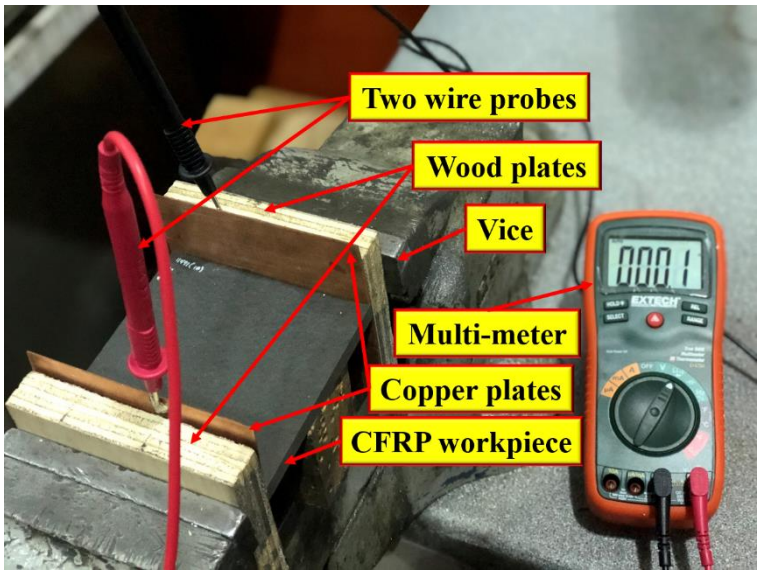


Figure 3.18: Two probe resistivity measurements.

3.4 Design of experiment and test arrays

Due to the scarcity of information/data in the literature relating to WEDM of CFRP materials, preliminary tests were carried out using the Topas plus D wire in order to identify basic working operating parameters. The variable parameters assessed were open gap voltage, ignition current, pulse on time and pulse off time, each at 2 levels. Table 3.7 details the variable and fixed parameters while Table 3.8 outlines the full factorial test array employed for the preliminary experimental trials. Cutting was performed parallel to fibre orientation with a test criterion of 2 mm cut length to determine feasibility of the selected operating parameter levels.

Table 3.7: Constant and variable machining parameters used in preliminary tests.

Machining variables		Levels
Constant	Wire tension	13 N
	Wire speed	10 m/min
	Servo voltage	15 V
	Flushing pressure	16 bar
Variable	Open gap voltage (V_o)	60 and 120 V
	Ignition current (IAL)	3 and 10 A
	Pulse on time (A)	0.8 and 1.0 µs
	Pulse off time (B)	4 and 16 µs

Table 3.8: Full factorial test array for preliminary trials.

Trial No.	Open gap voltage (V_o)	Ignition current (IAL)	Pulse on time (A)	Pulse off time (B)
1	60	3	0.8	4
2	120	3	0.8	4
3	60	10	0.8	4
4	120	10	0.8	4
5	60	3	1	4
6	120	3	1	4
7	60	10	1	4
8	120	10	1	4
9	60	3	0.8	16
10	120	3	0.8	16
11	60	10	0.8	16
12	120	10	0.8	16
13	60	3	1	16
14	120	3	1	16
15	60	10	1	16
16	120	10	1	16

3.4.1 Phase 1A: Effect of operating parameters when cutting UD-CFRP parallel to fibre direction using zinc coated brass core wire

A comprehensive investigation on the effects of the 4 process variables were carried out with the parameter levels refined based on results from the preliminary trials, see Table 3.9. Machining was performed parallel to fibre orientation of the CFRP workpiece using the Topas plus D zinc coated brass core wire for cut length of 12 mm. A Taguchi L18 fractional factorial experimental design was employed as shown in Table 3.10. Statistical analysis involving an ANOVA (analysis of variance) was carried out using MINITAB 16 software to determine significant factors with respect to material removal rate (MRR), average kerf width (Wa) and average surface roughness (Ra and Sa). Parameter optimisation was conducted according to

signal to noise (S/N) ratio analysis, with the objectives for maximising material removal rate while minimising kerf width and surface roughness as detailed in Eq. 3.4 and Eq. 3.5 respectively [194].

$$\eta = -10\log\frac{1}{n}\sum_{i=1}^{n}\frac{1}{y_i^2} \quad \text{(larger is better)} \qquad (3.4)$$

$$\eta = -10\log\frac{1}{n}\sum_{i=1}^{n}y_i^2 \quad \text{(smaller is better)} \qquad (3.5)$$

where η: signal to noise ratio; y_i: individual observation; n: number of repeated trials.

Table 3.9: Variable machining parameters and associated levels.

Parameters	Symbol and unit	Level 1	Level 2	Level 3
Open gap voltage	V_o, V	120	140	-
Ignition current	IAL, A	3	4	5
Pulse on time	A, µs	0.8	0.9	1
Pulse off time	B, µs	4	6	8

Table 3.10: Taguchi L18 orthogonal array.

Trial No.	Open voltage, V_o (V)	Ignition current, IAL (A)	Pulse on time, A (µs)	Pulse off time, B (µs)
1	120	3	0.8	4
2	120	3	0.9	6
3	120	3	1.0	8
4	120	4	0.8	4
5	120	4	0.9	6
6	120	4	1.0	8
7	120	5	0.8	6
8	120	5	0.9	8
9	120	5	1.0	4
10	140	3	0.8	8
11	140	3	0.9	4
12	140	3	1.0	6
13	140	4	0.8	6
14	140	4	0.9	8
15	140	4	1.0	4
16	140	5	0.8	8
17	140	5	0.9	4
18	140	5	1.0	6

The highest S/N ratio values indicated the optimal levels regardless of the target response. Confirmation tests were conducted for each response, with corresponding S/N ratio and mean values compared with those predicted by Eq. 3.6 [194] to estimate the relative error.

$$\hat{\eta} = \bar{\eta}_m + \sum_{i=1}^{n_o}(\bar{\eta}_i - \bar{\eta}_m) \qquad (3.6)$$

where $\hat{\eta}$ is the predicted value; $\bar{\eta}_m$: overall mean; $\bar{\eta}_i$: optimal level mean value.

3.4.2 Phase 1B: Effect of operating parameters when cutting UD-CFRP perpendicular to fibre direction using zinc coated brass core wire

Phase 1B tests were performed using the same procedures, wire electrode, parameter levels and experimental array utilised in Phase 1A, except that cutting was carried out perpendicular to the fibre orientation.

3.4.3 Phases 2A/2B: Effect of operating parameters when cutting UD-CFRP parallel / perpendicular to fibre orientation using copper/brass coated steel core wire

The experimental design, test procedures and analysis used for Phase 2A (machining parallel to fibre direction) and 2B (machining perpendicular to fibre direction) were analogous to Phase 1A and 1B respectively, except that the Compeed copper/brass coated steel core wire was utilised instead of the Topas plus D.

3.4.4 Phase 3A: Preliminary investigation on cutting UD-CFRP/Cu stacks using zinc coated brass and copper/brass coated steel core wires

A preliminary investigation on the cutting performance when stacking UD-CFRP with thin copper sheets (1.2 mm thick) was undertaken in Phase 3A. A total of four tests were carried out using both wire electrodes (Topas plus D and Compeed) with ignition current and pulse off time varied at the high and low levels utilised in Phase 1 and 2 trials to identify/determine feasibility of the test conditions for machining composite-metallic stacks. Open voltage and pulse on time were kept constant, with the test array detailed in Table 3.11. The material removal rate for each test was also recorded.

Table 3.11: Experimental array for preliminary testing for WEDM of CFRP/Cu stacks.

Trial No.	Wire type W	Open gap voltage V_o (V)	Ignition current IAL (A)	Pulse on time A (µs)	Pulse off time B (µs)
1	Topas (T)	120	5	0.6	4
2	Topas (T)	120	3	0.6	8
3	Compeed (C)	120	5	0.6	4
4	Compeed (C)	120	3	0.6	8

3.4.5 Phase 3B: Influence of operating parameters and wire electrode material when cutting UD-CFRP-metallic stacks

Frequent wire rupture/breakage occurred when operating with parameters in Phase 3A tests, possibly caused by resin/debris contamination of the dielectric. Therefore, the parameter levels were modified as detailed in Table 3.12. Phase 3B assessed the influence of wire electrode type together with ignition current and pulse off time on MRR and surface roughness when WEDM UD-CFRP/Cu stacks. Kerf width was ignored due to excessive fraying of the fibres at kerf edges caused by the flow of molten copper over the workpiece surfaces as shown in Figure 3.19. Response surface methodology (RSM) was employed in this phase of work in order to enable multiple response optimisation and evaluation of parameter interactions. A face-centred RSM design was formulated, which included 8 factorial points, 8 axial points and 10 centre points, giving a total or 26 tests as detailed in Table 3.13 for machining length of 12 mm.

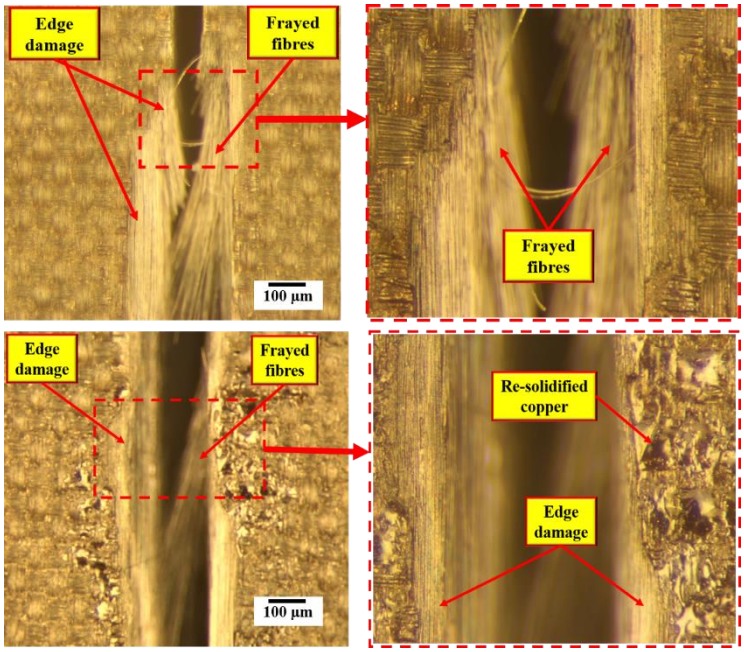


Figure 3.19: Micrograph of kerf damage caused by flow of molten copper.

Table 3.12: Variable machining parameters and their levels.

Parameters		Symbol and Unit	Level 1(-1)	Level 2(0)	Level 3(+1)
Variable	Ignition current	IAL, A	3	4	5
	Pulse off time	B, µs	8	9	10
	Wire type	W	Topas (T)	Compeed (C)	
Constant	Open gap voltage	V_o, V	100	-	-
	Pulse on time	A, µs	0.5	-	-

Table 3.13: Face centred response surface methodology test array.

Trial No.	Ignition current, IAL (A)	Pulse off time, B (µs)	Wire type W	Coded levels	
1	3	8	T	-1	-1
2	5	8	T	1	-1
3	3	10	T	-1	1
4	5	10	T	1	1
5	3	9	T	-1	0
6	5	9	T	1	0
7	4	8	T	0	-1
8	4	10	T	0	1
9	4	9	T	0	0
10	4	9	T	0	0
11	4	9	T	0	0
12	4	9	T	0	0
13	4	9	T	0	0
14	3	8	C	-1	-1
15	5	8	C	1	-1
16	3	10	C	-1	1
17	5	10	C	1	1
18	3	9	C	-1	0
19	5	9	C	1	0
20	4	8	C	0	-1
21	4	10	C	0	1
22	4	9	C	0	0
23	4	9	C	0	0
24	4	9	C	0	0
25	4	9	C	0	0
26	4	9	C	0	0

The variable parameter levels were coded -1, 0 and +1 to represent low, medium and high values respectively. The combination of -1 and +1 represents factorial points while ±1 and 0 represents axial points and zeros allocated for centre points. A face centred design meant that axial/star points were limited to -1 and +1 levels. Response optimisation was accomplished using desirability functions, which converts multiple responses into single dimensionless equation. Equations 3.7, 3.8 and 3.9 detail the desirability for maximum, minimum and gross functions [195, 196].

$$d_i = \begin{cases} 0 & Y_i < Low_i \\ \left(\frac{Y_i - Low_i}{High_i - Low_i}\right)^w & Low_i < Y_i < High_i \\ 1 & Y_i > High_i \end{cases} \quad (3.7)$$

$$d_i = \begin{cases} 1 & Y_i < Low_i \\ \left(\frac{High_i - Y_i}{High_i - Low_i}\right)^{wt} & Low_i < Y_i < High_i \\ 0 & Y_i > High_i \end{cases} \quad (3.8)$$

$$D = \left(\prod_{i=1}^{n} d_i^{r_i}\right)^{1/\sum r_i} \quad (3.9)$$

where d_i: desirability of the response; Y_i: response, $High_i$ and Low_i: are upper and lower limits/acceptable values of the response; wt: the weight/power; D: gross/global desirability; r_i: relative importance with other responses/variables.

3.4.6 Phase 3C: Influence of wire electrode material and operating conditions on cutting performance of multidirectional CFRP laminates

A full factorial experiment involving variation of ignition current, pulse off time and wire electrode (each at 2 levels) was employed for investigating the WEDM of multidirectional CFRP composites. Ignition current and pulse off time were varied as they were found to be significant factors with respect to MRR in previous test phases. Table 3.14 details the levels of the variable parameters while open gap voltage and pulse on time were fixed at 100 V and 0.6 µs respectively. The test array is outlined in Table 3.15 for machining length of 12 mm. Statistical analysis of the results were conducted using MINITAB software to determine the significance of the variable parameters with regard to MRR, average kerf width and workpiece surface roughness. Machined surface condition from selected tests were also assessed.

Table 3.14: Machining parameters and levels of full factorial plan.

Parameters		Symbol and Unit	Level 1	Level 2
Variable	Ignition current	IAL, A	3	5
	Pulse off time	B, µs	8	10
	Wire type	W	T	C
Constant	Open gap voltage	V_o, V	100	-
	Pulse on time	A, µs	0.6	-

Table 3.15: Full factorial test array.

Trial No.	Ignition current (IAL)	Pulse off time (B)	Wire type (W)
1	3	8	T
2	5	8	T
3	3	10	T
4	5	10	T
5	3	8	C
6	5	8	C
7	3	10	C
8	5	10	C

3.5 Summary

In this chapter, the research methodology employed to address the key challenges of machining thick CFRP composites in terms of wire breakage, cutting speed/spark stability and high electrical resistivity of the workpiece are outlined in Figure 3.20. High performance wire electrodes (e.g. diffusion annealed and composite wires) and stacking with copper plates were suggested and investigated as potential solutions. Details of workpiece materials, equipment and corresponding test setup utilised in the experimental trials were presented together with the statistically designed experiments for each phase of tests.

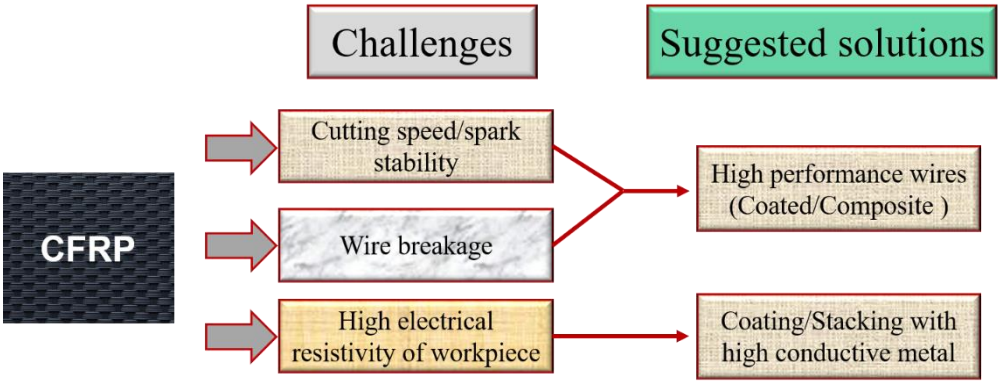


Figure 3.20: The key challenges and suggested solutions when WEDM of CFRP.

4 RESULTS AND DISCUSSION

Preliminary trials involving a full factorial test array to assess the feasibility and identify working operating windows for WEDM of unidirectional CFRP composites were carried out using zinc coated brass core (Topas plus D) wire. All of the tests were successful in machining a length of 2 mm parallel to the fibre orientation. However, utilising high current levels of 10 A together with open voltage of 120 V and pulse off time of 4 µs resulted in wire rupture and incomplete/unsuccessful cut due to unstable sparking. Therefore, lower current levels ranging between 3 and 5 A were employed for the mainstream experimental work to avoid wire breakage. Optical micrographs showing the machined kerf on the top and bottom surfaces of workpieces from each test are detailed in Appendix D. Kerf widths were the primary response evaluated from the preliminary trials to ascertain the capability of WEDM in machining CFRP. Five observations were recorded for each successful cut and the results revealed a variation between the top and bottom kerf widths, which were principally due to variation in standoff distances between the flushing nozzles and workpiece as well as the non-homogeneous behaviour of CFRP material. Therefore, the mean value between both kerfs was considered in the mainstream experimental phases. It was observed that increasing open voltage and pulse on time resulted in increasing top kerf width due to high discharge energy/spark width. However, a high current level of 10 A led to lower kerf width due to unstable spark discharges. The parameters showed similar trends on the bottom kerf but increasing open voltage led to decreasing width, likely due to variation in flushing of the debris as well as the lack of measurement data in cases of incomplete cuts.

4.1 Phase 1A: Effect of operating parameters when cutting UD-CFRP parallel to fibre direction using zinc coated brass core wire

4.1.1 Material removal rate

All of the tests completed a cut distance of 12 mm with machining times ranging from 13.3 to 49.1 minutes. Figure 4.1 shows the MRR obtained in each test, which varied between 0.43 and 2.41 mm^3/min. The peak MRR in the experiment was observed in Test 9, which corresponded to the combination involving the highest ignition current (5 A) and pulse on time (1 µs) levels coupled with the lowest pulse off time (4 µs) value, thus leading to the highest discharge energy. This was supported by the main effects plot in Figure 4.2, which illustrates that raising ignition/peak current and pulse on time increased MRR whereas higher pulse off times had the opposite effect due to lower discharge frequency. Surprisingly, mean MRR typically decreased

when increasing open gap voltage to 140 V, possibly due to spark instability caused by the rise in decomposed resin debris in the machining gap as a result of the more intense spark at higher voltage as well as Joule heating. The analysis of variance (ANOVA) of the results indicated that ignition current and pulse off time were both statistically significant factors with respect to MRR with percentage contribution ratios (PCR) of 48.47% and 24.27% respectively, see Table 4.1.

Table 4.1: ANOVA for MRR when cutting parallel to fibre direction using Topas wire.

Source	DF	Seq SS	Adj SS	Adj MS	F-Value	P-Value	PCR
V_o	1	0.3452	0.3452	0.34524	4.78	0.054	7.54%
IAL	2	2.2200	2.2200	1.11001	15.37	0.001*	48.47%
A	2	0.1814	0.1814	0.09071	1.26	0.326	3.96%
B	2	1.1116	1.1116	0.55582	7.70	0.009*	24.27%
Error	10	0.7221	0.7221	0.07221			15.77%
Total	17	4.5804					100.00%

* significant at the 5% level

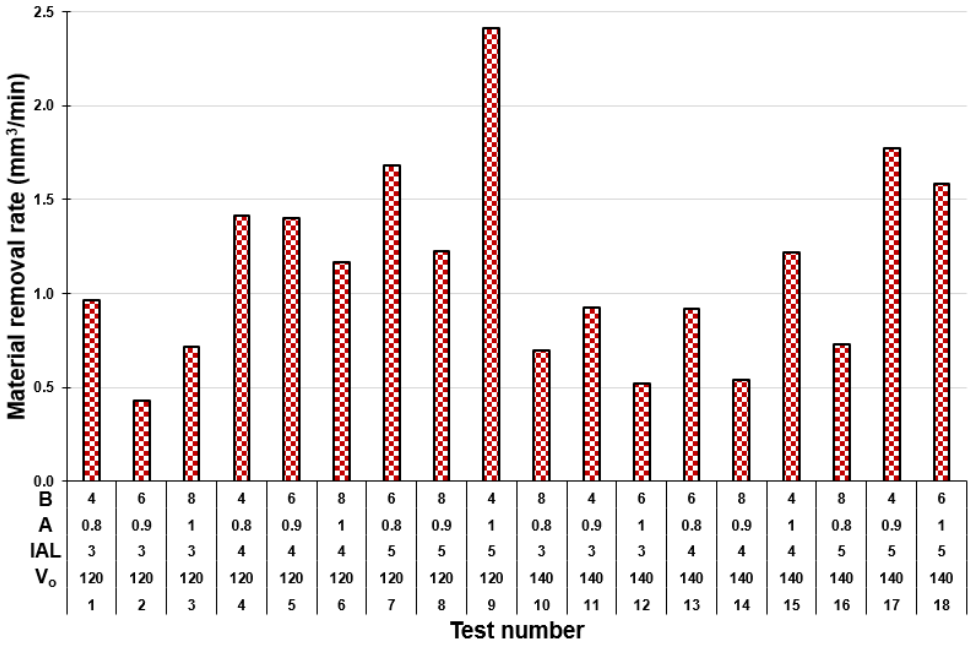


Figure 4.1: Material removal rate when machining parallel to fibre orientation using Topas wire.

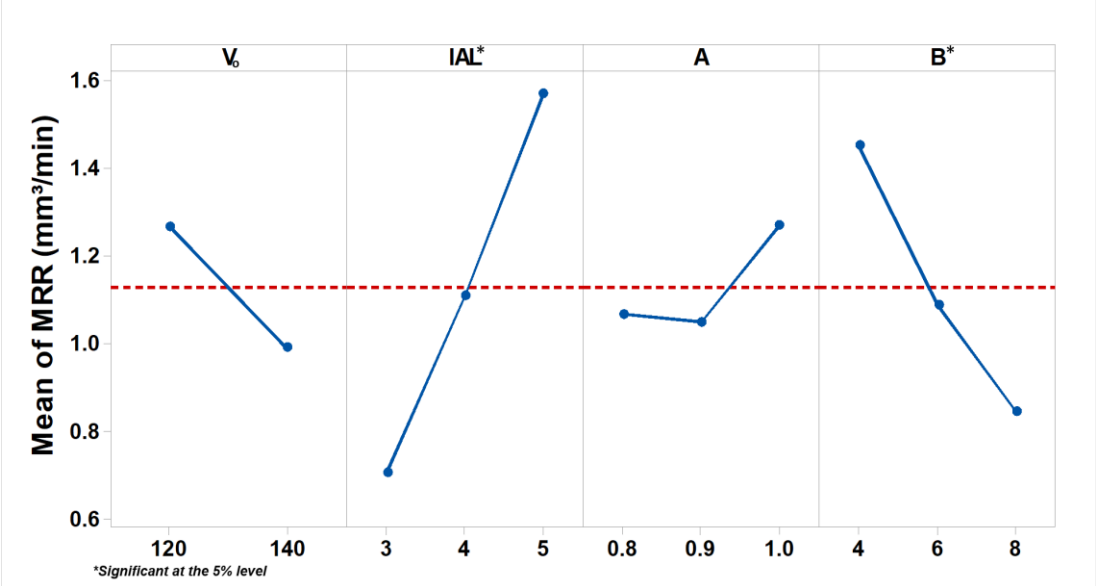


Figure 4.2: Main effects plot for MRR when cutting parallel to fibre orientation using Topas wire.

4.1.2 Kerf width

Due to the nature of the CFRP material, the kerf width was considered to be representative of the average (Wa) of the kerfs measured on the top and bottom of the workpiece. The mean kerf widths over the range of tests were found to vary between 260 to 283 µm, as shown in Figure 4.3. The relatively low variation was likely due to standoff distances between upper and lower nozzle that influenced flushing conditions and movement of wire through cutting.

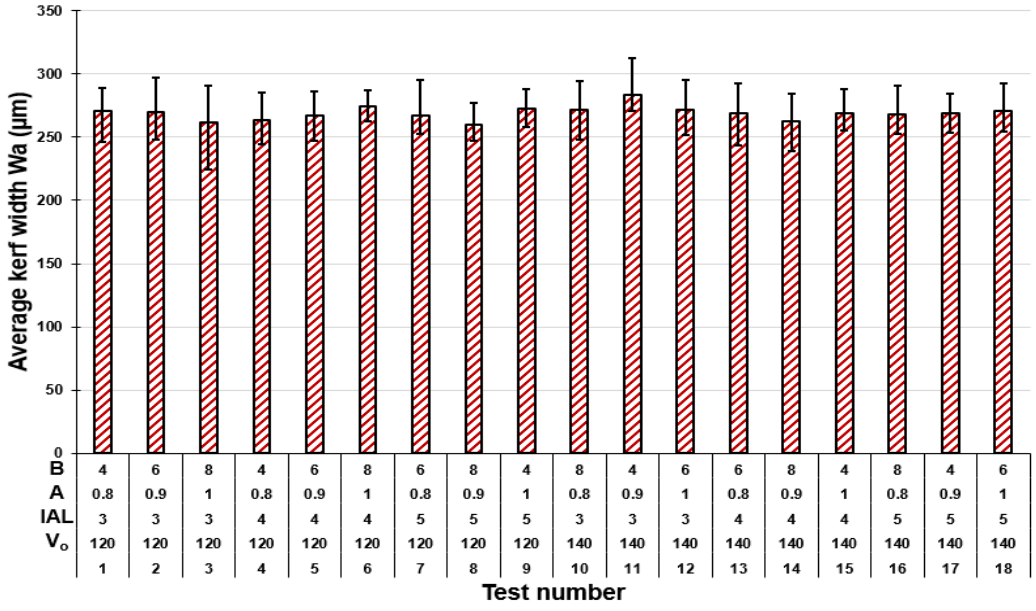


Figure 4.3: Average kerf width when machining parallel to fibre direction using Topas wire.

In general, wider kerfs were obtained when operating at the higher voltage of 140 V, a trend illustrated by the main effects plot for average kerf widths shown in Figure 4.4. This was attributed to the larger spark gap at elevated voltage while increasing pulse on time also led to wider kerfs due to higher discharge energies. Conversely, increasing pulse off time typically reduced kerf widths as a result of lower pulse frequency and intensity. Additionally, greater current levels also showed a similar trend to pulse off time due to higher discharge energy, which increased the wire feed resulting in reduced interaction time between spark and workpiece. However, the corresponding ANOVA for average kerf width detailed in Table 4.2 indicated that none of the factors were statistically significant at the 5% level. Indeed, all of the variable parameters exhibited relatively low PCR values ranging from 2.13% to 17.49 %, with a large residual error of ~60%. This indicates that the linear model has a coefficient of determination (R^2) of ~40, suggesting that the variation in kerf width was likely influenced by other factors or interactions that have not been considered in the model.

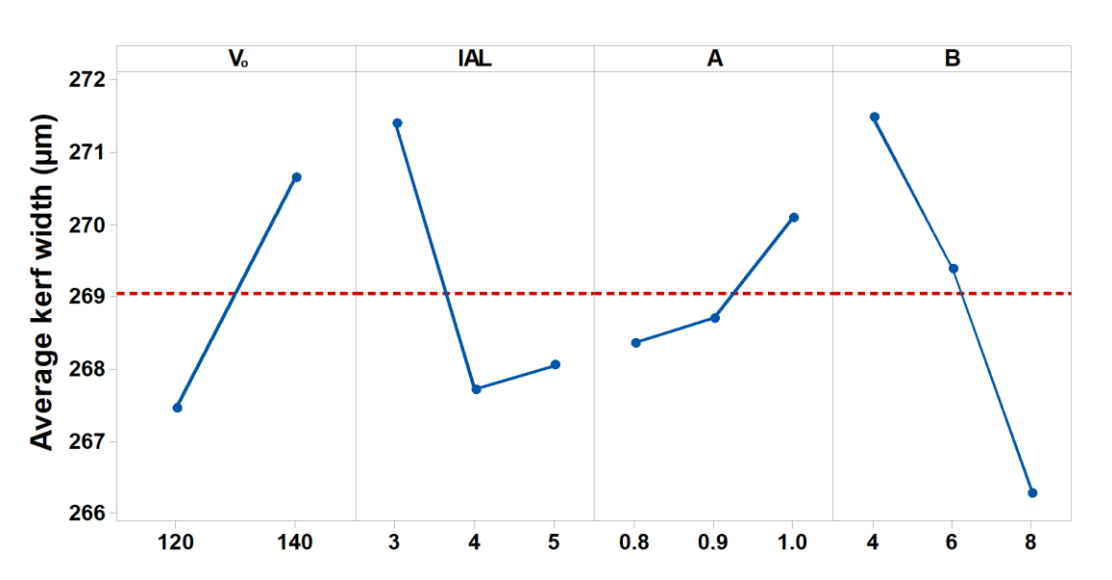


Figure 4.4: Main effects plot for average kerf width through parallel cutting to fibre orientation.

Table 4.2: ANOVA for average kerf width when cutting parallel to fibre orientation.

Source	DF	Seq SS	Adj SS	Adj MS	F-Value	P-Value	PCR
V_o	1	46.037	46.037	46.037	1.65	0.228	9.87%
IAL	2	49.405	49.405	24.703	0.88	0.443	10.60%
A	2	9.931	9.931	4.966	0.18	0.840	2.13%
B	2	81.554	81.554	40.777	1.46	0.278	17.49%
Error	10	279.298	279.298	27.930			59.91%
Total	17	466.227					100.00%

4.1.3 Surface roughness

The average linear (horizontal and vertical) and areal workpiece surface roughness measurements for each test are shown in Figure 4.5. The lowest Ra values were observed in the horizontal direction parallel to the fibre orientation whilst the corresponding roughness along the vertical direction (measured across several individual plies) was higher by a factor of ~1.5 to 3. The possible reason for this trend relates to the presence of gaps between fibre plies due to resin evaporation as well as re-solidified debris generated from epoxy decomposition adhering to the surface and spaces between fibres in vertical orientation. The 3D roughness (Sa) levels were relatively similar to the average Ra values in the vertical direction, but with significantly less variability. The areal roughness was found to vary between 4.53 µm and 9.48 µm Sa, with the highest level observed in Test 9 corresponding to the fastest MRR, which resulted in presence of frayed fibres and adhered re-solidified melted resin, see 3D topographical scan of the machined surface in Figure 4.6. Further topographical surface maps of machined surfaces from trials with the highest and lowest areal surface roughness are detailed in Appendix E.

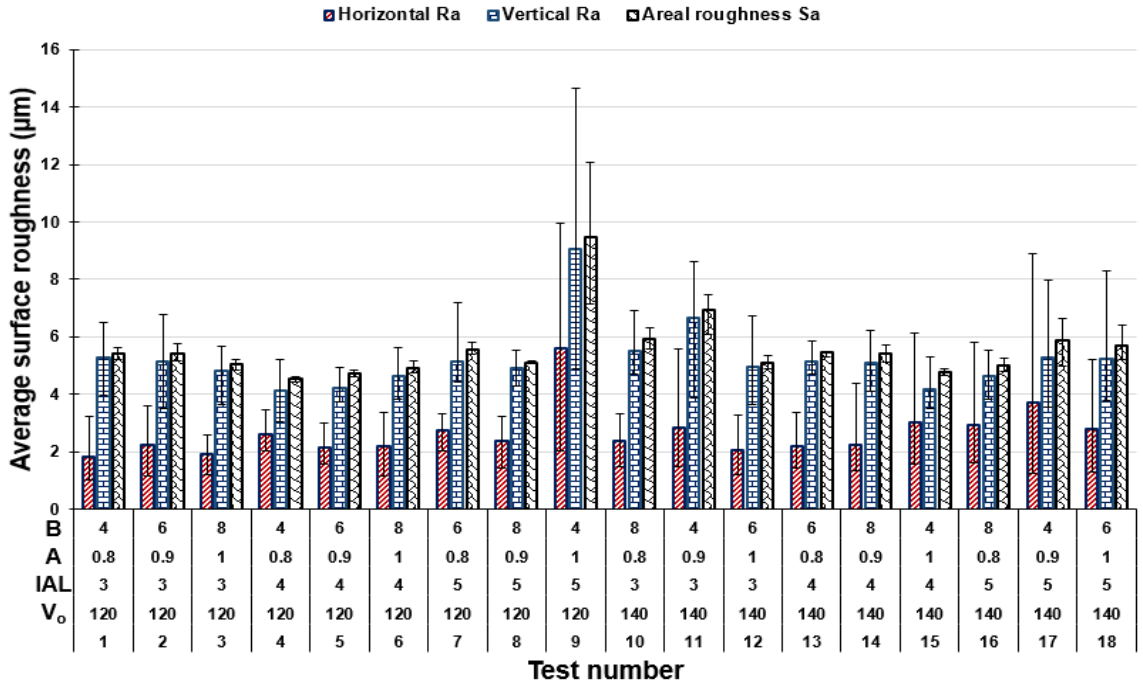


Figure 4.5: Average surface roughness when cutting parallel to fibre orientation using Topas wire.

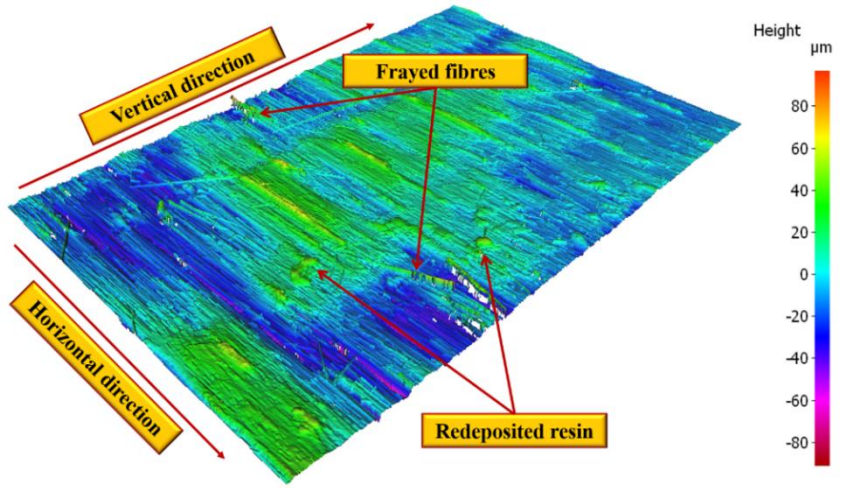


Figure 4.6: Surface topographical map of machined workpiece from Test 9 (highest MRR).

The main effects plot in Figure 4.7 showed that increasing pulse on time while reducing pulse off time resulted in higher mean surface roughness (Sa) due to higher discharge energy and reduced flushing efficiency respectively. Increasing ignition current from 3 to 4 A initially lowered surface roughness probably due to lack of sufficient energy to remove material at low current (3 A) leaving irregular surfaces or uncut/frayed fibres, but a significant rise in roughness was subsequently apparent as current was increased to 5 A caused by high discharge energy. The influence of gap voltage on mean surface roughness however appeared to be negligible. Statistical analysis of the results highlighted that none of the factors had a significant effect on workpiece surface roughness with associated PCRs not exceeding of 20%, as shown in Table 4.3 due to variation in outcomes according to surface situation leading into high residual error. The relatively high residual error suggests that there are other terms including interactions affecting the surface roughness that were not considered in the model.

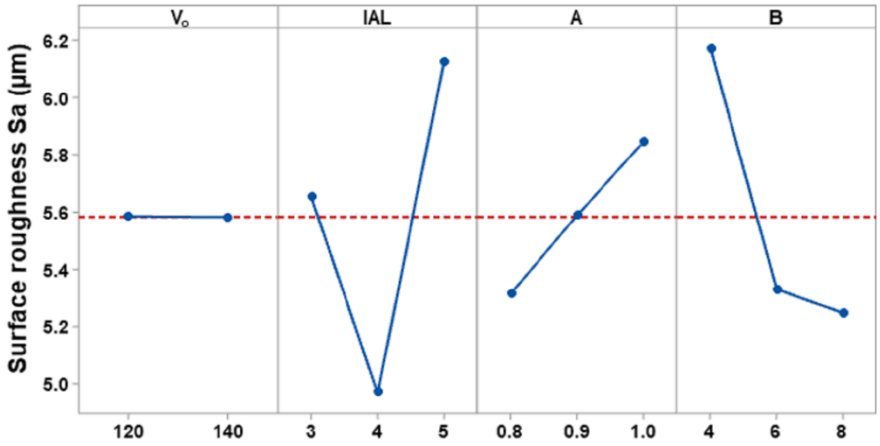


Figure 4.7: Main effects plot for surface roughness (Sa) when machining parallel cutting to fibre orientation.

Table 4.3: ANOVA for mean surface roughness (Sa) when cutting parallel to fibre orientation.

Source	DF	Seq SS	Adj SS	Adj MS	F-Value	P-Value	PCR
V_o	1	0.0000	0.0000	0.00004	0.00	0.996	0.00%
IAL	2	4.0430	4.0430	2.02149	1.52	0.265	18.95%
A	2	0.8456	0.8456	0.42281	0.32	0.735	3.96%
B	2	3.1407	3.1407	1.57036	1.18	0.347	14.72%
Error	10	13.3024	13.3024	1.33024			62.36%
Total	17	21.3318					100.00%

4.1.4 Surface damage

Figure 4.8 details optical micrographs of the machined kerf on both the top and bottom surfaces of the workpiece from Test 9, which achieved the highest MRR. Apart from some regions showing uneven edge profiles, there were no signs of major delamination or burnt matrix in the vicinity of the kerf. However, patches of bronze coloured debris/contaminants were evident on the bottom surface of the specimen, likely due to deposition of debris/impurities on the workpiece surface, possibly from the deionised water or residue on the machine table.

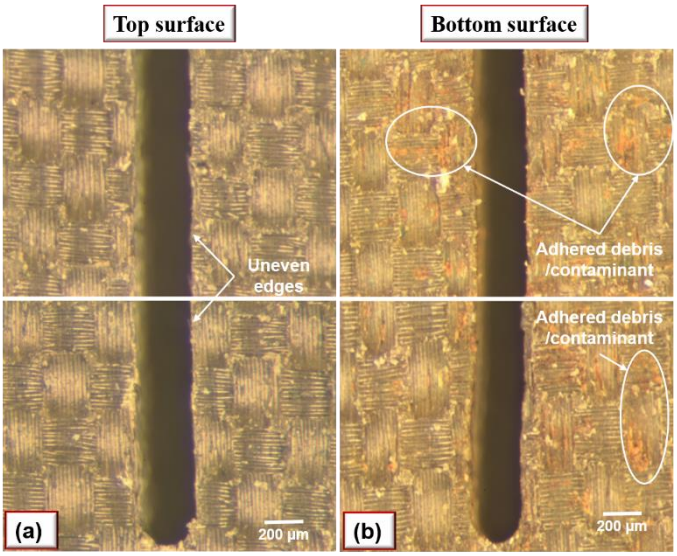


Figure 4.8: Optical micrographs of machined kerf on the (a) top and (b) bottom surfaces of the workpiece from Test 9 (highest MRR).

Figure 4.9 shows sample SEM micrographs of machined surfaces from tests achieving the lowest, median and highest MRR respectively. The surface damage on the workpiece machined at the lowest MRR (0.43 mm^3/min) was generally characterised by fibre breakage, matrix loss caused by vaporisation of the epoxy and re-deposited resin, see Figure 4.9(a). The ends of broken fibres were typically at oblique angles, many of which appeared swollen possibly due to the accumulation and transfer of heat generated by the spark discharges. The degree of fibre/matrix loss and swelling of the fibres increased in Test 6 (median MRR of 1.13 mm^3/min),

due to the higher discharge energy, with the presence of pits seen near the ends of severed fibres as a result of impact with sparks and gaseous jets which erode the fibre ends, as shown in Figure 4.9(b). Additionally, voids were evident on the re-solidified resin layers on the surface, which were possibly caused by trapped gas/bubbles resulting from the plasma explosion during discharge and vaporisation of the epoxy and carbon fibres. The machined surface quality further deteriorated in the test with the highest MRR (2.41 mm^3/min), with larger fibre strands and increased re-deposited resin adhering to the surface as observed in Figure 4.9(c). Relatively large cavities were also apparent on the adhered matrix layers likely due to entrapped gases generated at high discharge energy.

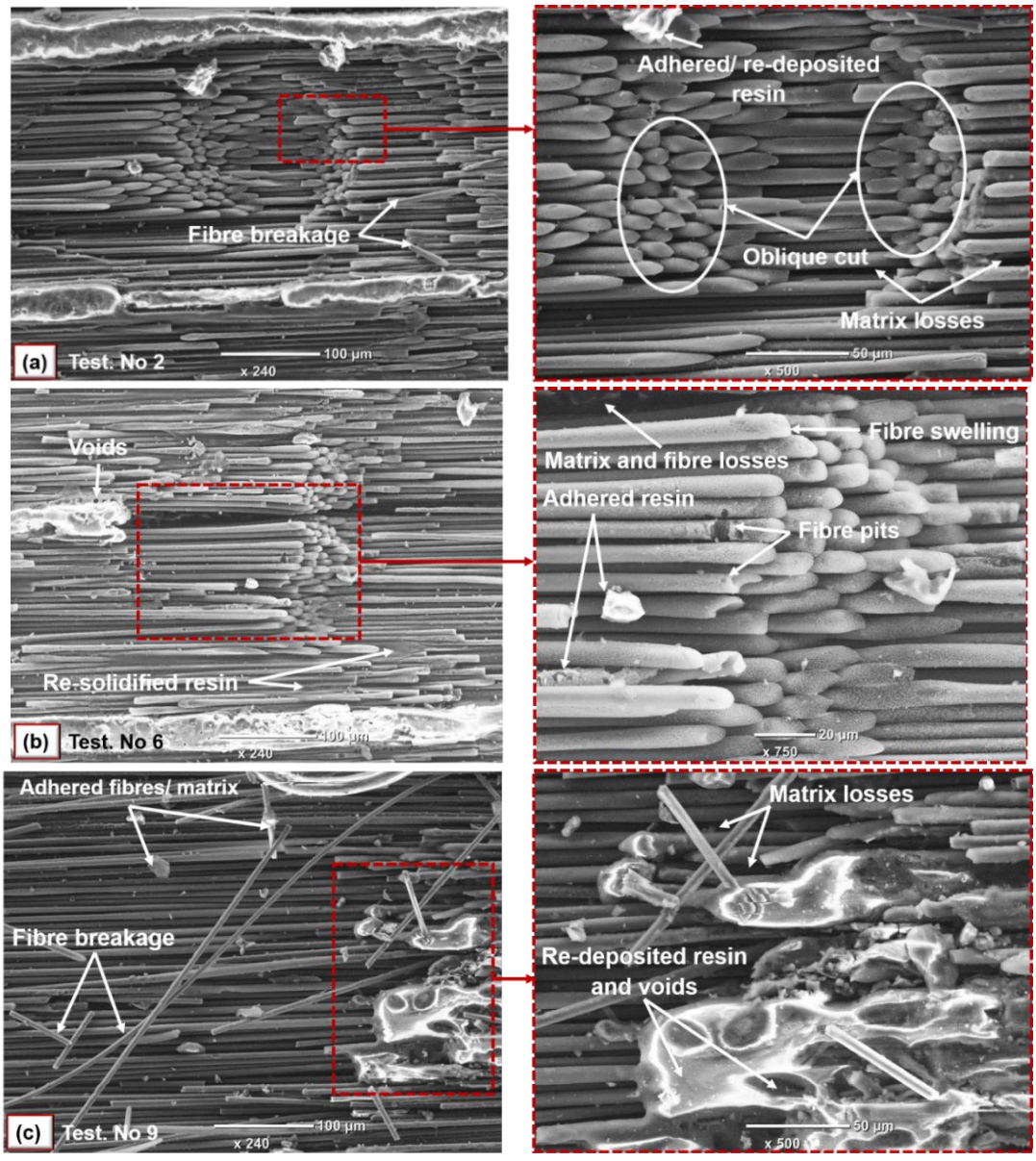


Figure 4.9: Sample SEM micrographs of machined surfaces in (a) Test 2 – lowest MRR, (b) Test 6 - median MRR and (c) Test 9 - highest MRR.

4.2 Phase 1B: Effect of operating parameters when cutting UD-CFRP perpendicular to fibre direction using zinc coated brass core wire.

4.2.1 Material removal rate

Figure 4.10 details the material removal rates achieved in each test after machining a distance of 12 mm perpendicular to the fibre direction, which varied between 0.69 and 1.94 mm^3/min. The highest MRR in Test 4 was approximately 20% lower than the corresponding result in Phase 1A when machining parallel to fibre direction. This was possibly due in part to the lower workpiece electrical conductivity in the transverse fibre direction (~14.1 x 10^{-2} S/cm) compared to the value along the fibre direction (~11.91 S/cm), which compromised spark efficiency. Additionally, the mechanical force of the flushing jets and high-speed streams of vaporised/gaseous debris from the plasma channel can lead to bending and fracture of the uncut/exposed fibres (following evaporation of the resin), which can infiltrate the spark gap causing unstable machining [154, 155]. Figure 4.11 shows the main effects plot for MRR when cutting perpendicular to fibre orientation, which largely exhibited similar trends to tests performed parallel to fibre direction (Phase 1A). Increasing ignition current generally led to higher MRR owing to greater discharge energies while a deterioration in MRR was observed at larger pulse off times and voltage. The lower MRR with increasing pulse off time was unsurprising, but the stronger spark intensity at the higher open voltage level was thought to have caused a greater flow of decomposed resin material in the spark gap, possibly resulting in lower machining stability and efficiency. The influence of pulse on time was somewhat unexpected, with higher MRR achieved at the lower pulse on time. This was possibly due to increased fibre breakage contamination of the spark gap at 0.9 µs leading machining instability, however a further rise in pulse on time caused sublimation of the fibres, resulting in more stable operation. According to the ANOVA in Table 4.4, all of the factors except for the pulse on time were found to be statistically significant with respect to MRR. Ignition current showed the highest PCR of 43.28%, while pulse off time and open voltage had somewhat more modest PCR levels of 18.56% and 16.56% respectively.

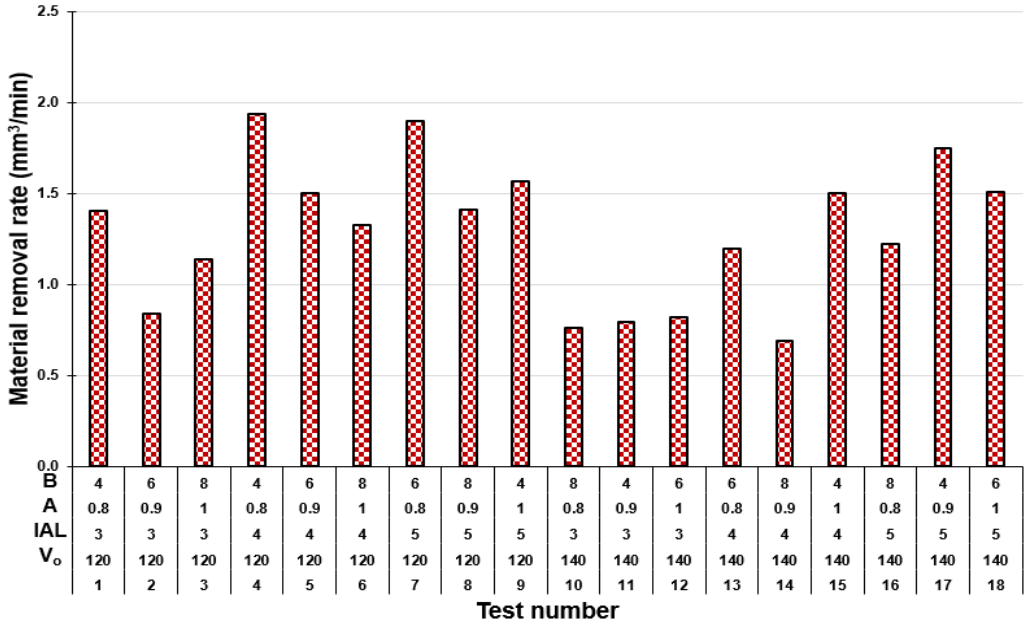


Figure 4.10: Material removal rate when cutting perpendicular cutting to fibre orientation using Topas wire.

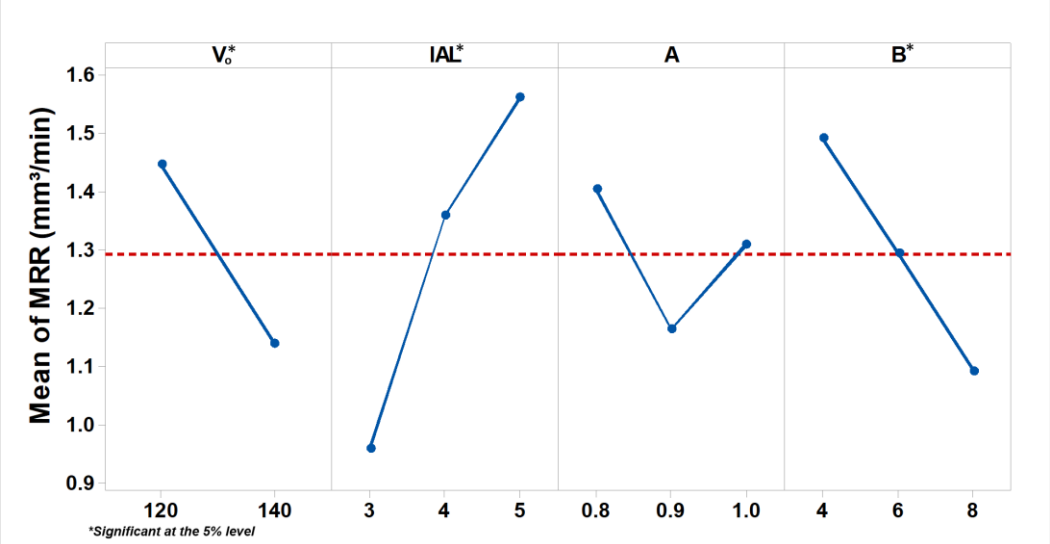


Figure 4.11: Main effects plot for MRR when machining perpendicular to fibre orientation.

Table 4.4: ANOVA for MRR when cutting perpendicular to fibre direction.

Source	DF	Seq SS	Adj SS	Adj MS	F-Value	P-Value	PCR
V_o	1	0.4284	0.4284	0.42835	11.15	0.008*	16.56%
IAL	2	1.1195	1.1195	0.55976	14.57	0.001*	43.28%
A	2	0.1746	0.1746	0.08729	2.27	0.154	6.75%
B	2	0.4801	0.4801	0.24006	6.25	0.017*	18.56%
Error	10	0.3843	0.3843	0.03843			14.86%
Total	17	2.5869					100.00%

* significant at the 5% level.

4.2.2 Kerf width

The average kerf widths measured in each test when cutting perpendicular to fibre orientation are detailed in Figure 4.12, which varied over a small range between 268 and 274 µm. The influence of gap voltage on mean kerf width was marginal, as shown by the main effects plot in Figure 4.13. The influence of varying voltage levels on average kerf width was largely negligible. Increasing pulse off time reduced the kerf width as anticipated due to lower spark frequency as well as longer cooling time that dissipates more of the heat generated in the discharge gap. In contrast, the intermediate current level (4 A) resulted in smaller kerf widths due to faster cutting rates while the intermediate pulse on time value (0.9 µs) tended to increase kerf width from the longer interaction time between the spark and workpiece. However, none of the variable factors were found to have a significant effect on kerf widths according to the ANOVA as shown in Table 4.5. Moderate PCR levels were observed for pulse on (19.96%) and off times (17.82%), but with a considerably high residual error of ~61%, suggesting that the linear model did not fully account for all the variation in the results.

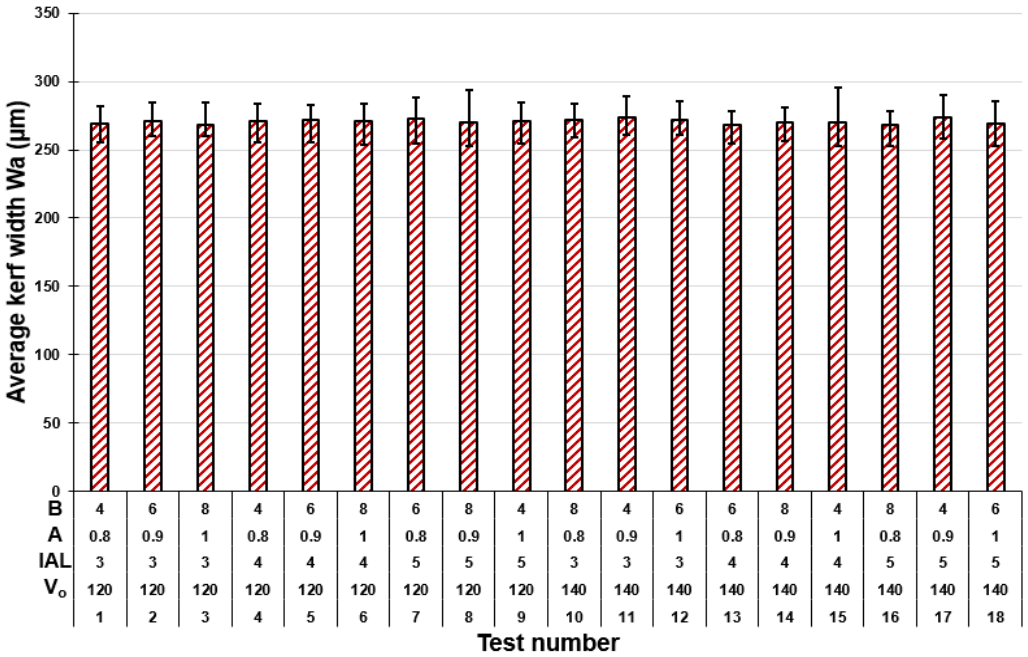


Figure 4.12: Average kerf width measurements cutting perpendicular to fibre orientation using Topas wire.

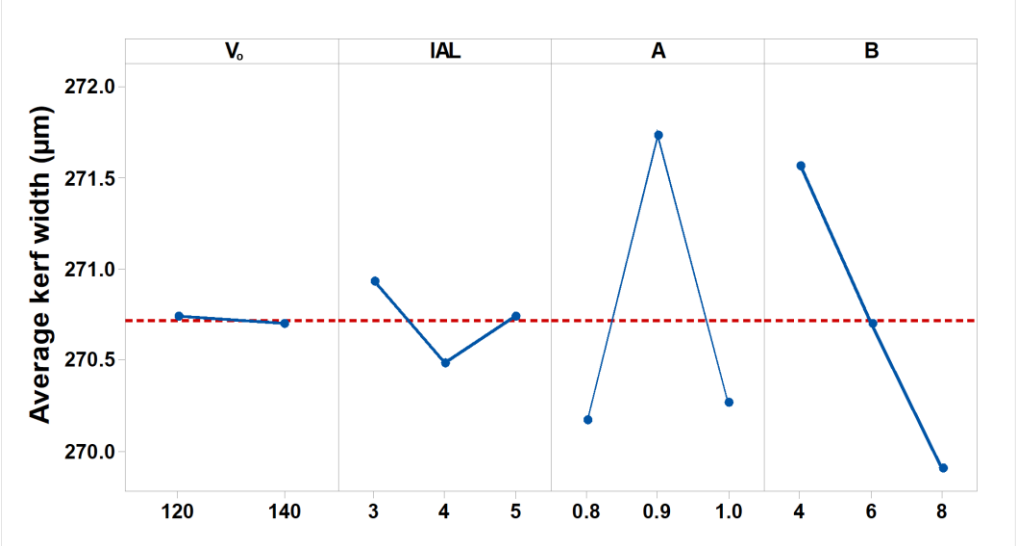


Figure 4.13: Main effects plot for average kerf width when cutting perpendicular to fibre orientation.

Table 4.5: ANOVA for mean kerf width when cutting perpendicular to fibre orientation.

Source	DF	Seq SS	Adj SS	Adj MS	F-Value	P-Value	PCR
V_o	1	0.0071	0.0071	0.00714	0.00	0.961	0.02%
IAL	2	0.6057	0.6057	0.30284	0.11	0.899	1.31%
A	2	9.2370	9.2370	4.61851	1.64	0.242	19.96%
B	2	8.2476	8.2476	4.12378	1.46	0.277	17.82%
Error	10	28.1778	28.1778	2.81778			60.89%
Total	17	46.2752					100.00%

4.2.3 Surface roughness

Figure 4.14 details the average linear surface roughness (Ra) measured parallel (horizontal) and perpendicular (vertical) to feed direction together with the corresponding 3D areal roughness parameter (Sa). The roughness along the feed was generally lower than the transverse direction although the spread of the measurements was considerable, similar to results in Phase 1A. Despite showing higher values compared to Ra, the variation in Sa results were significantly lower with mean roughness ranging between 3.3 and 6.84 µm. In general, tests with higher MRR tended to exhibit increased surface roughness, most likely due to greater workpiece damage in terms of adhered/re-deposited resin and the formation of gaps between plies due to epoxy decomposition, see Figure 4.15.

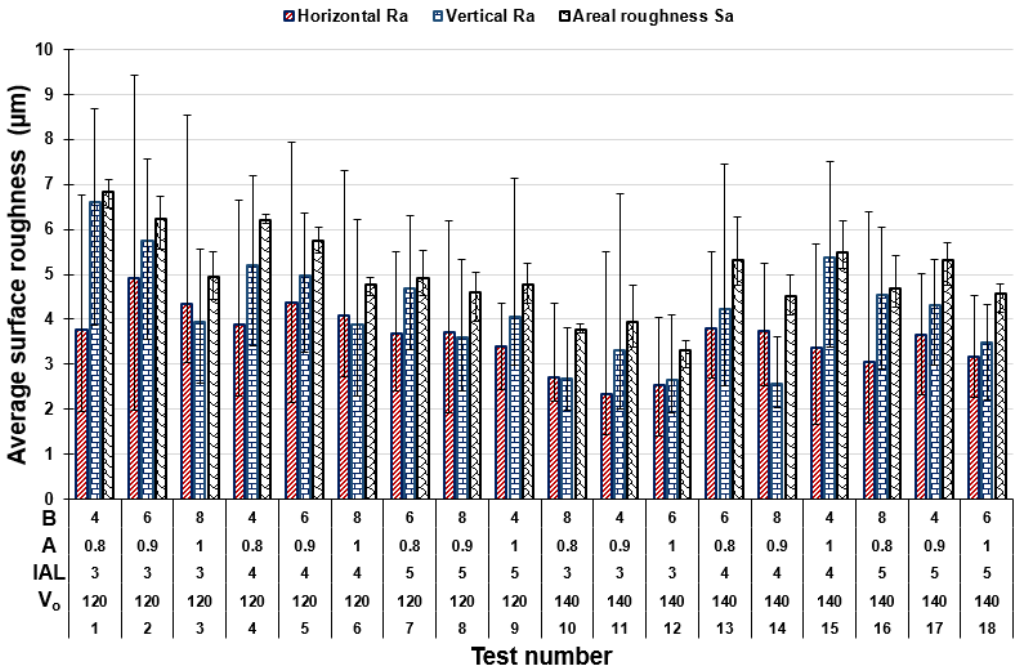


Figure 4.14: Average surface roughness when cutting perpendicular to fibre orientation using Topas wire.

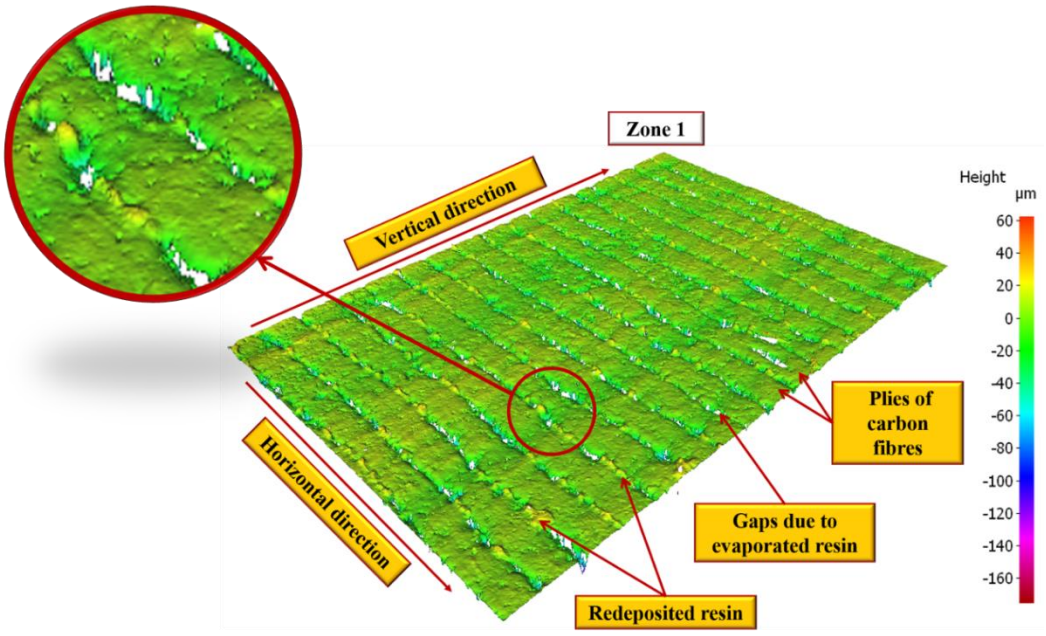


Figure 4.15: Surface topographical map of machined workpiece from Test 1 (highest Sa).

Figure 4.16 details the main effects plot for mean Sa, which shows the increasing voltage and pulse off time led to lower workpiece surface roughness. This was probably due in part to the lower spark frequency and MRR at higher pulse off time and voltage respectively, resulting in a reduced number of craters on the machined surface due to lower MRR. Increasing pulse on time was also found to reduce surface roughness as a result of unstable discharges caused by

greater fractured fibre debris leading to lower MRR, while the intermediate current level produced higher roughness because of the increase in MRR observed changing from 3 to 4 A.

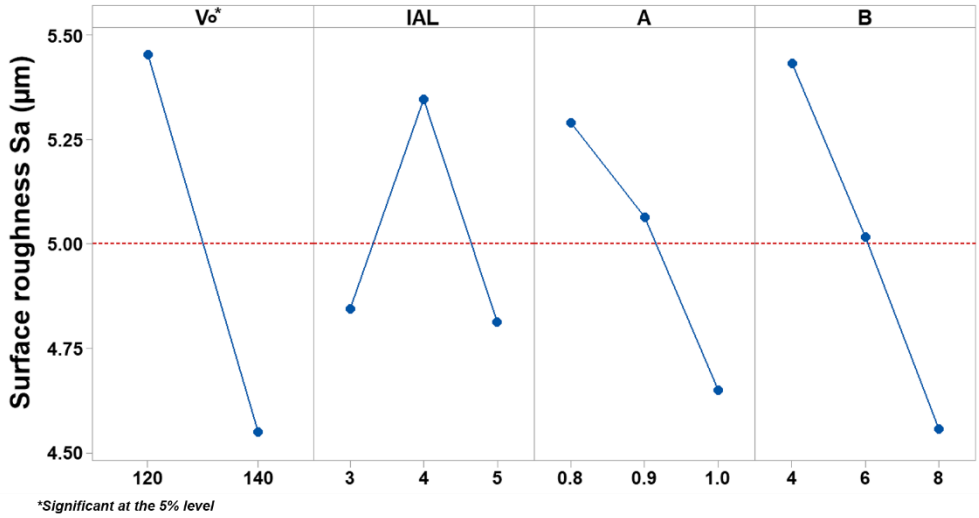


Figure 4.16: Main effects plot for surface roughness when cutting perpendicular to fibre orientation using Topas wire.

The corresponding ANOVA in Table 4.6 revealed that open gap voltage was the sole significant factor affecting workpiece surface roughness (Sa) with a PCR of ~27%. The residual error however was relatively high at ~39%.

Table 4.6: ANOVA for areal surface roughness when cutting perpendicular to fibre direction.

Source	DF	Seq SS	Adj SS	Adj MS	F-Value	P-Value	PCR
V_o	1	3.674	3.674	3.6745	6.93	0.025*	26.97%
IAL	2	1.073	1.073	0.5364	1.01	0.398	7.87%
A	2	1.267	1.267	0.6335	1.19	0.343	9.30%
B	2	2.306	2.306	1.1528	2.17	0.165	16.92%
Error	10	5.306	5.306	0.5306			38.94%
Total	17	13.626					100.00%

* significant at the 5% level

4.2.4 Surface damage

Figure 4.17 shows optical micrographs of the machined kerf on the top and bottom surfaces of the workpiece from Test 4 (highest MRR). In general, the kerf edges were even and free from damage such as frayed fibres or surface burn, except for heavy delamination and small traces of bronze coloured debris/contaminant on the surface. The delamination was thought to occur following decomposition/evaporation of the epoxy matrix due to high temperatures, with the exposed fibres being bent and broken by the impact of sparks, dielectric flow and jetting force generated by decomposition gases [154, 155], see Figure 4.18. Based on the width of the delamination, the delamination factor for the workpiece in Test 4 was calculated and found to

be similar at 1.97 and 1.96 for top and bottom surfaces respectively, which suggests that the maximum length of the delamination from the machined edge was approximately equivalent to the kerf width.

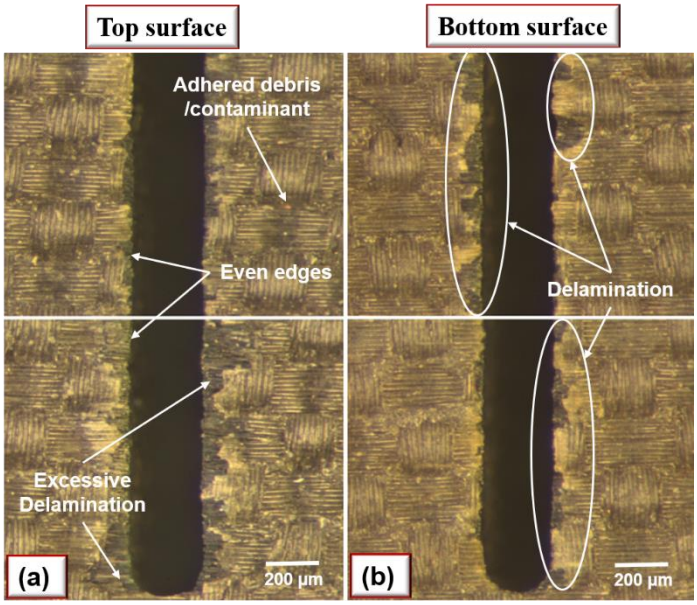


Figure 4.17: Optical micrographs of machined kerf on the (a) top and (b) bottom surfaces of the workpiece from Test 4 (highest MRR).

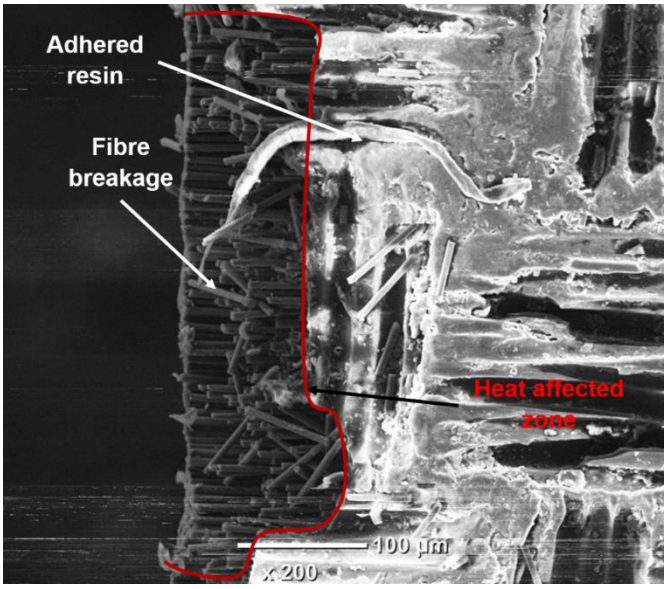


Figure 4.18: Sample SEM micrographs of surface delamination for Test 4 - highest MRR.

The machined surfaces from selected tests were further examined using high resolution SEM and are shown in Figure 4.19. The workpiece from Test 14 corresponding to the lowest MRR (0.69 mm^3/min) showed the presence of cavities due to loss of fibres and resin, which decomposed at 400°C [154], see Figure 4.19(a). This was primarily found at the interface regions between plies but also within individual prepregs layers, some of which were filled by

re-solidified epoxy material. Furthermore, hexagonal shaped fibre cross sections were observed, which are potentially related to compression and swelling of the cut ends caused by the elevated temperature in the machining gap [154]. Similar damage characteristics were evident on workpieces from Test 6 (median MRR - 1.29 mm^3/min) and Test 4 (highest MRR - 1.94 mm^3/min – Test 4) but with melted matrix covering the machined surfaces together with pieces of broken fibres, see Figure 4.19(b) and Figure 4.19(c) respectively. Craters and voids were also visible on the layer of melted epoxy, possibly due to higher discharge energies and entrapped gases produced from resin decomposition and evaporation.

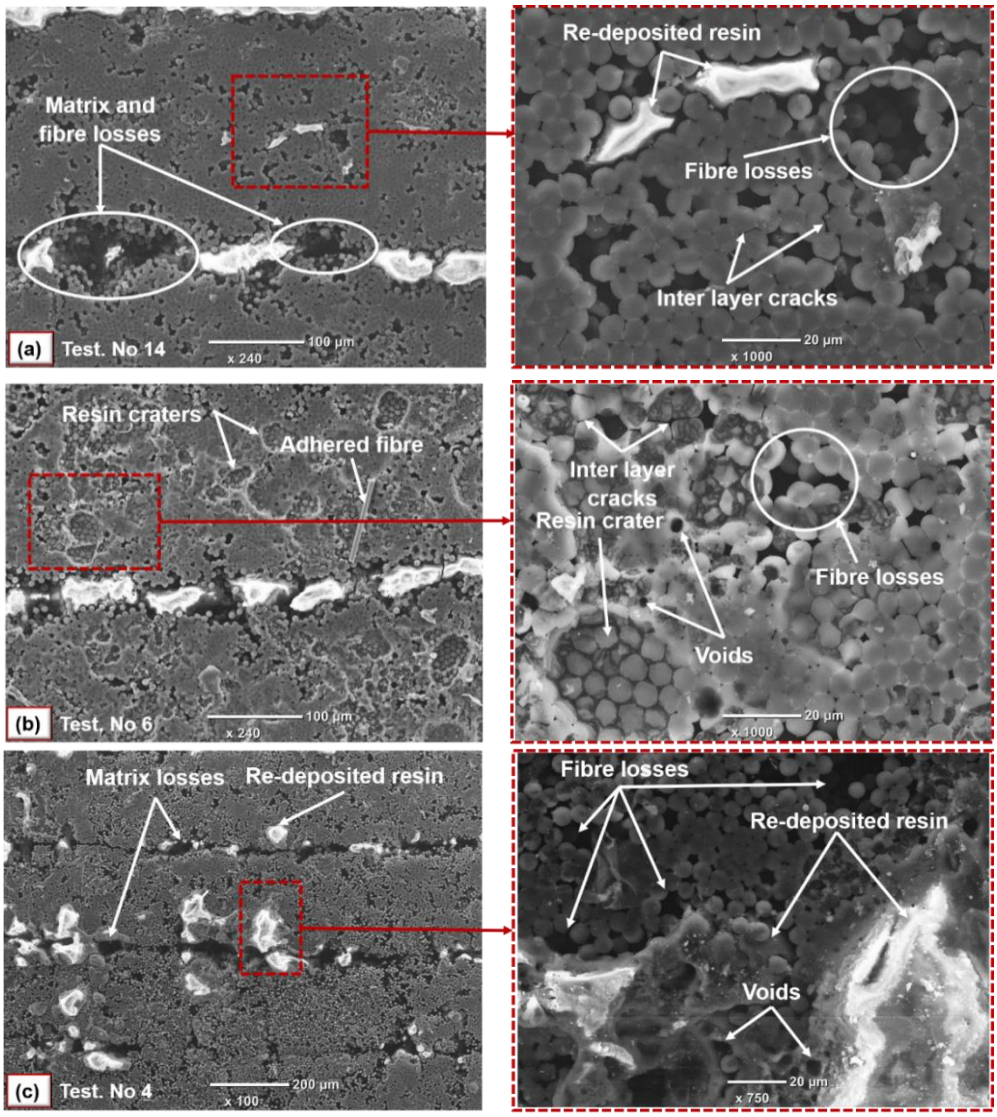


Figure 4.19: Sample SEM micrographs of machined surfaces in (a) Test 14 – lowest MRR, (b) Test 6 – median MRR and (c) Test 4 – highest MRR.

4.2.5 Confirmation tests for Phase 1 experiments

Based on the signal to noise ratio calculations and main effects plots, the preferred levels of variable factors for achieving maximum MRR as well as minimum kerf width and surface roughness were selected. While the test array included the preferred combination levels for some responses, separate confirmation tests were undertaken for each response to ensure repeatability and accuracy of the results. Table 4.7 details the predicted/experimental mean and S/N ratio of the respective responses from the confirmation tests in both Phase 1A and 1B. The percentage error between the experimental and predicted values of the mean results were also estimated. It was observed that the relative error for all responses were within 5% except for areal roughness in Phase 1A, which was ~10%.

Table 4.7: Predicted and experimental results from Phase 1 confirmation tests for various responses.

	Preferred levels	Response	Mean		S/N ratio (dB)		Error %
			Pred.	Exp.	Pred.	Exp.	
Phase 1A	$V_{o1}IAL_3A_3B_1$	MRR	2.17	2.28	7.79	7.16	4.82
	$V_{o1}IAL_2A_1B_3$	Wa	262.67	267.55	-48.39	-48.54	1.82
	$V_{o1}IAL_2A_1B_3$	Sa	4.37	4.89	-13.07	-13.79	10.63
Phase 1B	$V_{o1}IAL_3A_1B_1$	MRR	2.03	2.08	7.00	6.36	2.40
	$V_{o2}IAL_2A_1B_3$	Wa	269.10	268.73	-48.60	-48.59	0.14*
	$V_{o2}IAL_1A_3B_3$	Sa	3.60	3.79	-11.29	-11.57	5.01

*The experimental result is lower than the predicted value

The surface condition from the confirmation test for Phase 1A was similar to the results in Test 9 (highest MRR). The MRR for the confirmation test in Phase 1B was marginally higher at 2.08 mm^3/min compared to 1.94 mm^3/min in Test 4, however evaluation of the machined surface revealed considerable damage including large cavities with voids, matrix loss caused by resin evaporation and eroded fibre ends. There was also significant areas with re-solidified resin including cracks and voids over the surface, see Figure 4.20.

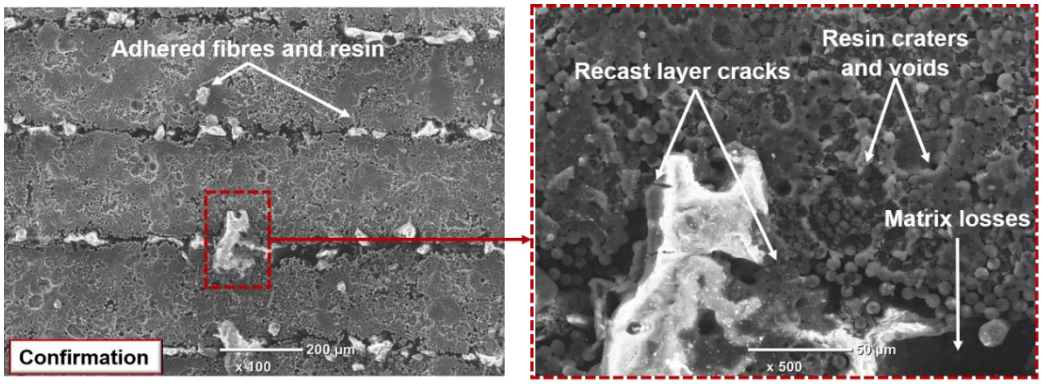


Figure 4.20: Sample SEM micrographs of machined surfaces from Phase 1B confirmation test.

4.3 Phase 2A: Effect of operating parameters when cutting UD-CFRP parallel to fibre orientation using copper/brass coated steel core wire

4.3.1 Material removal rate

Figure 4.21 shows the material removal rates for each test after cutting a length of 12 mm parallel to the fibre direction using the copper/brass coated steel core wire (Compeed). The MRR over the experiment varied from 1.17 to 4.7 mm^3/min, with the highest levels achieved in Test 7 and Test 9 (both exceeding 4.0 mm^3/min) involving high current (5 A) and low voltage (120 V) levels, which likely provided increased discharge energy together with spark stability. While tests at the higher voltage of 140 V was expected to further increase discharge energy, this did not generally correspond to higher MRR, possibly due to increased debris (decomposed resin and dislodged fibres) in the machining zone caused by greater temperatures and Joule heating leading to poorer spark efficiency.

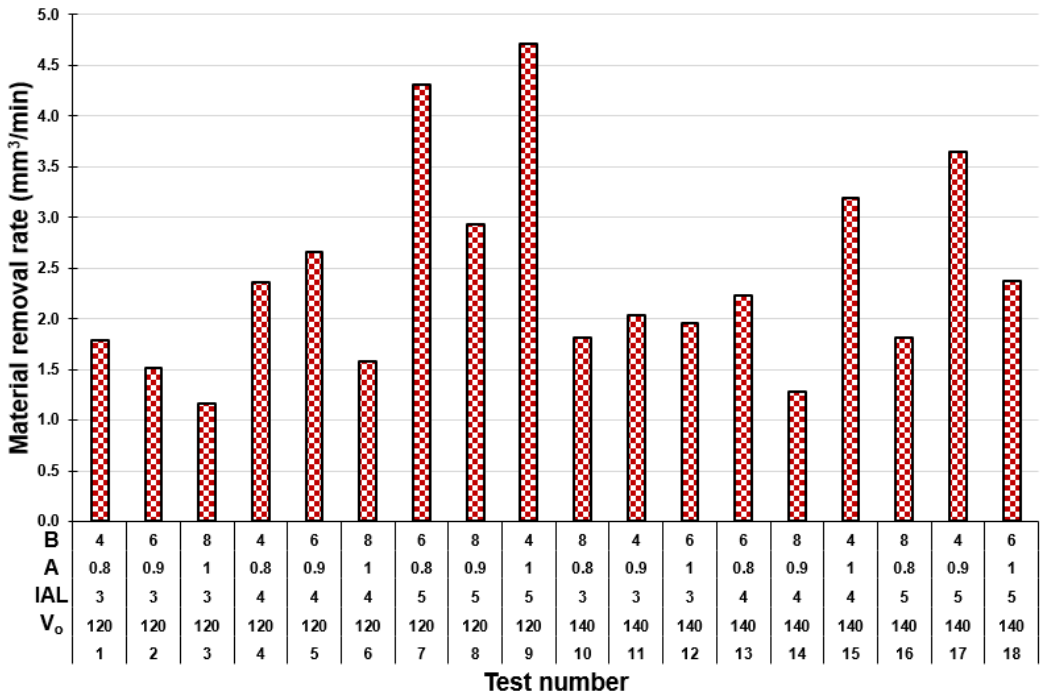


Figure 4.21: Material removal rate when cutting parallel to fibre direction using Compeed wire.

Figure 4.22 shows the main effects plot indicating that higher currents resulted in faster removal rates while MRR decreased with increasing gap voltage and pulse off time. In contrast, the variation in pulse on time exhibited only a marginal influence on MRR. The associated ANOVA showed that both ignition current and pulse off time were statistically significant at the 5% level for MRR with PCR's of 45.93% and 25.13% respectively; see Table 4.8.

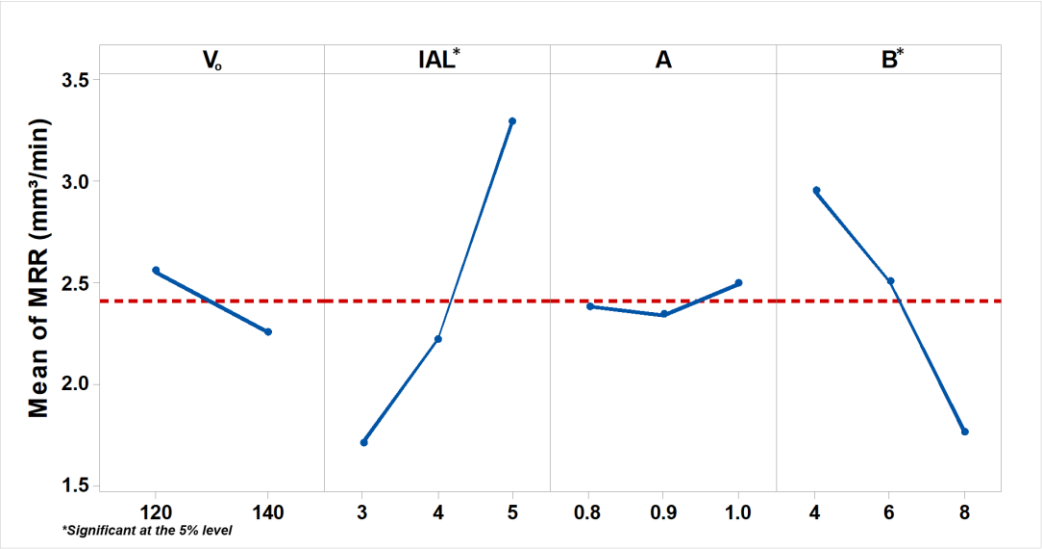


Figure 4.22: Main effects plot for MRR when cutting parallel to fibre orientation using Compeed wire.

Table 4.8: ANOVA for MRR when cutting parallel to fibre direction using Compeed wire.

Source	DF	Seq SS	Adj SS	Adj MS	F-Value	P-Value	PCR
V_o	1	0.3967	0.39673	0.39673	0.89	0.369	2.32%
IAL	2	7.8665	7.86646	3.93323	8.78	0.006*	45.93%
A	2	0.0765	0.07645	0.03823	0.09	0.919	0.45%
B	2	4.3038	4.30384	2.15192	4.80	0.035*	25.13%
Error	10	4.4823	4.48226	0.44823			26.17%
Total	17	17.1257					100.00%

* significant at the 5% level

4.3.2 Kerf width

Figure 4.23 outlines the average kerf widths generated in each test when machining parallel to the fibre direction using the Compeed wire, which varied between 288 up to 367 µm. The large overcuts (relative to 250 µm wire diameter) were partly attributed to the comparatively high electrical conductivity of the steel core wire (50% IACS), resulting in more intense spark discharges. Considerable variation/spread in the measurements were also observed, especially in tests performed at low voltage (120 V) with high current (5 A) levels, reflecting the highly irregular/uneven width along the length of the kerf. This was possibly aided by the dielectric flushing removing debris from the machining gap and coupled with the higher wire conductivity, promoted more efficient sparking. Figure 4.24 shows the main effects plot for average kerf width, where higher voltage and pulse off time produced narrower kerfs. Although the influence of pulse off time was not surprising, the trend exhibited by the gap voltage was unexpected which probably attributed to more generated energy at small machining gap caused by increasing voltage and high wire conductivity, which influence on spark intensity leading

into less material removal and kerf width. The high variation of outcomes including MRR/kerf width gained at different voltage levels resulted in this trend. Furthermore, the heterogeneity of the workpiece might contribute in this behaviour where the cutting rate varies between different sides of workpiece. The kerf width typically increased with current while the intermediate pulse on time level resulted in larger kerfs.

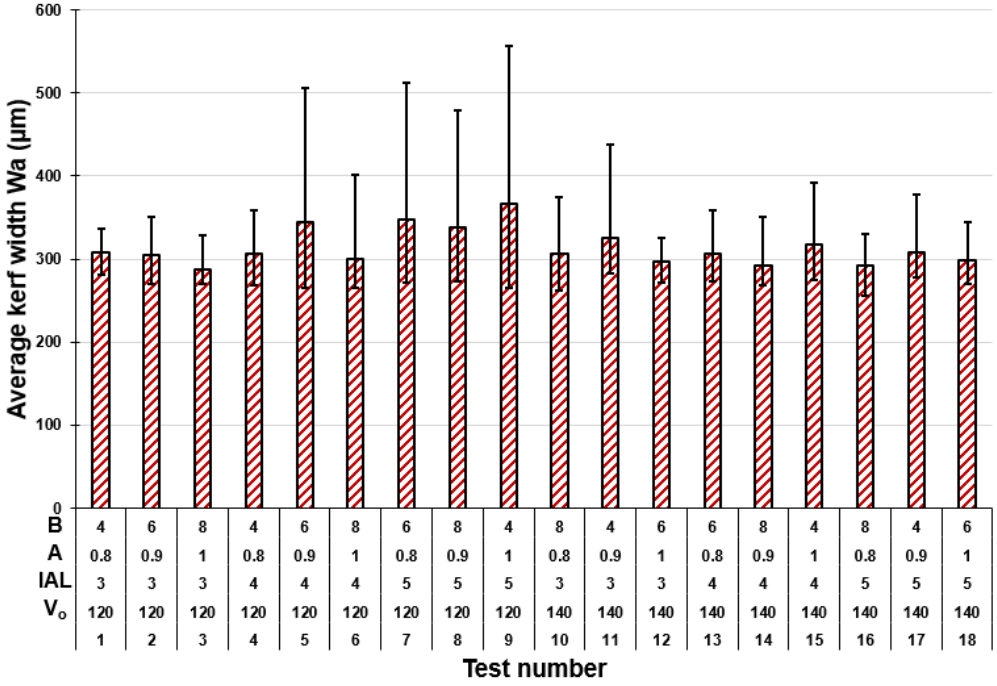


Figure 4.23: Average kerf width when cutting parallel to fibre orientation using Compeed wire.

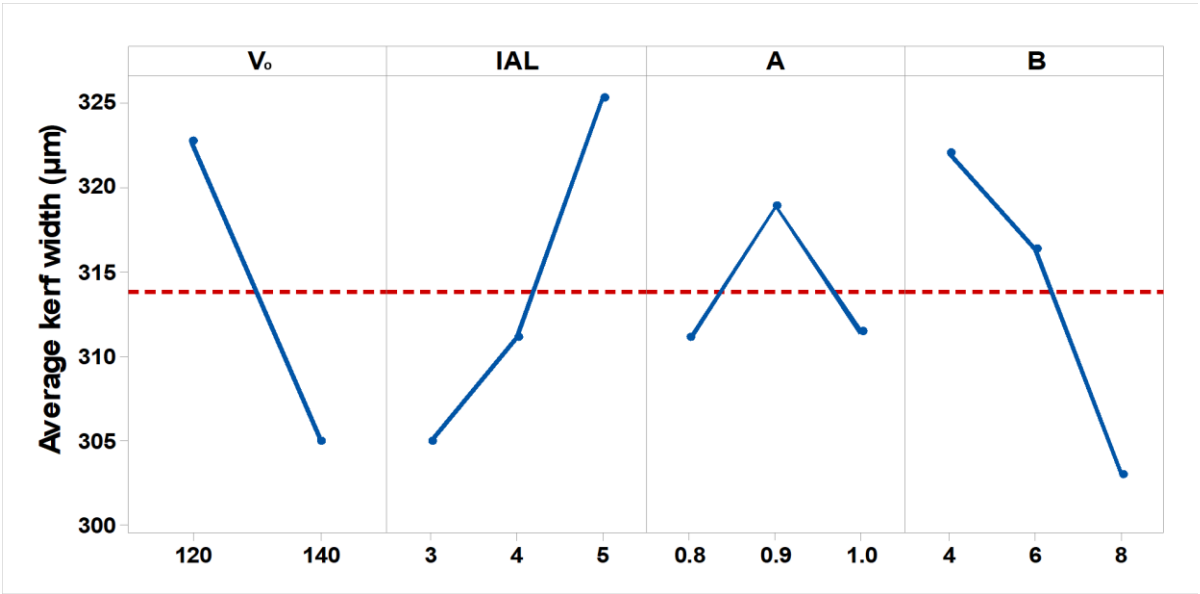


Figure 4.24: Main effects plot for average kerf width when cutting parallel to fibre orientation using Compeed wire.

The analysis of variance however revealed that none of variable parameters had a significant effect on average kerf width, which was likely due to the large variation in measured values over the length of the kerf, see Table 4.9. The PCR's for the individual factors did not exceed ~18% while a high residual error of ~50% was recorded.

Table 4.9: ANOVA for average kerf width when cutting parallel to fibre direction using Compeed wire.

Source	DF	Seq SS	Adj SS	Adj MS	F-Value	P-Value	PCR
V_o	1	1411.8	1411.8	1411.8	3.38	0.096	17.11%
IAL	2	1297.7	1297.7	648.8	1.55	0.259	15.73%
A	2	228.0	228.0	114.0	0.27	0.767	2.76%
B	2	1137.4	1137.4	568.7	1.36	0.300	13.78%
Error	10	4176.9	4176.9	417.7			50.62%
Total	17	8251.8					100.00%

4.3.3 Surface roughness

Figure 4.25 details the surface roughness measurements involving both linear (horizontal and vertical Ra) and areal (Sa) parameters when cutting parallel to fibre orientation. The Ra measured in the horizontal direction were typically lower compared to the vertical direction, with the latter being comparable to the 3D areal roughness parameter, which varied between 9.27 and 26.29 µm Sa. In general, the trials that demonstrated high MRR and kerf widths generally also exhibited elevated surface roughness. A sample 3D surface topographical map of the machined workpiece from Test 4 shown in Figure 4.26 revealed the presence of considerable frayed/bent fibres on the surface, which accounts for the high roughness level obtained (26.29 µm Sa). The exposed and distorted fibres were likely formed following melting/decomposition of the epoxy matrix combined with impingement of the dielectric/gaseous jets. Further 3D topographical maps showing the condition of machined surfaces from selected tests are detailed in Appendix E.

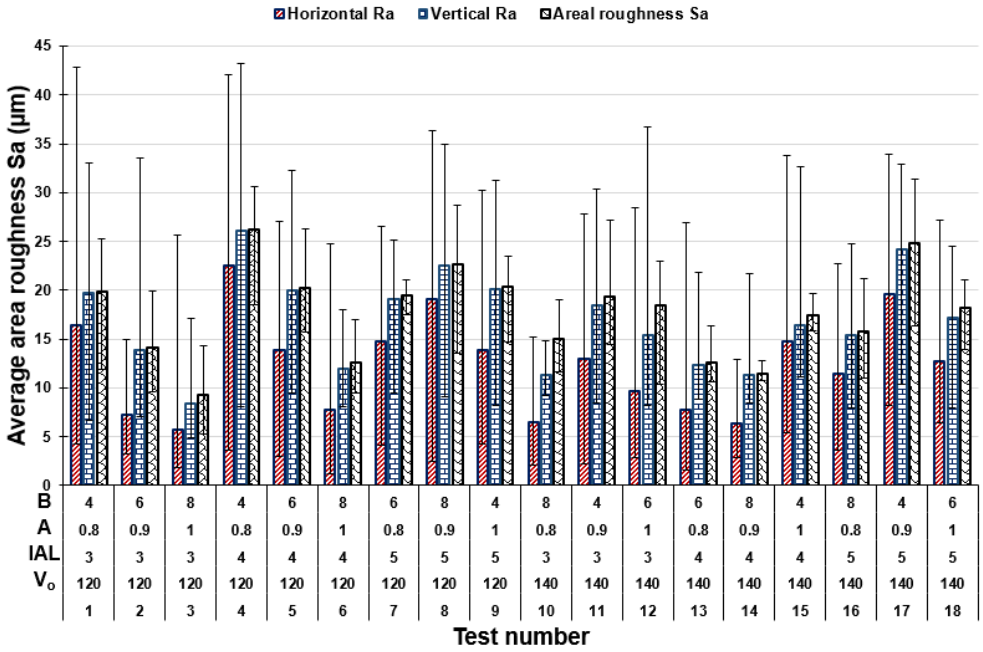


Figure 4.25: Bar chart illustrates average surface roughness during parallel cutting using Compeed wire.

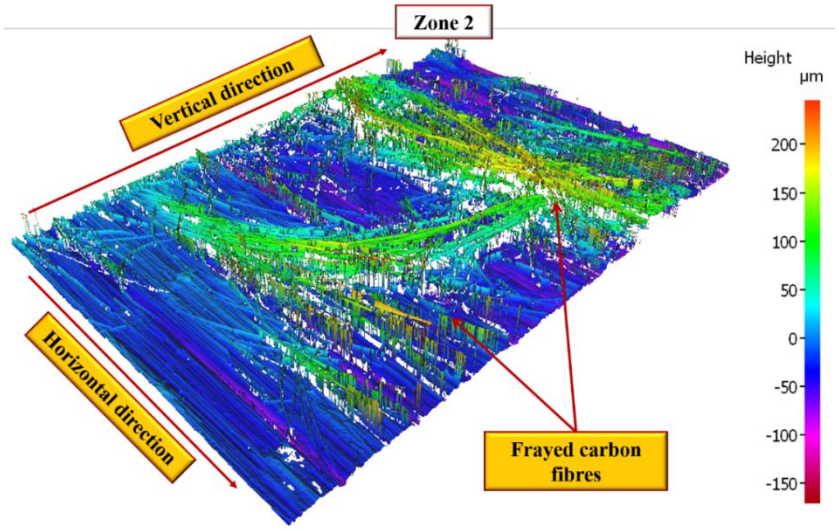


Figure 4.26: Surface topographical map of machined workpiece from Test 4 (highest Sa).

Figure 4.27 details the main effects plot for mean areal roughness (Sa), which indicated that raising voltage and pulse off time decreased surface roughness. This corresponded to lower MRR possibly due to unstable discharges and reduced spark frequency resulting in less frayed fibres adhered to the surface. As expected, increasing current led to higher roughness levels due to elevated discharge energies while raising pulse on time above 0.9 µs resulted in a decreasing trend for surface roughness. According to the ANOVA in Table 4.10, pulse off time was the only significant factor influencing areal surface roughness, with a PCR of 40.55%.

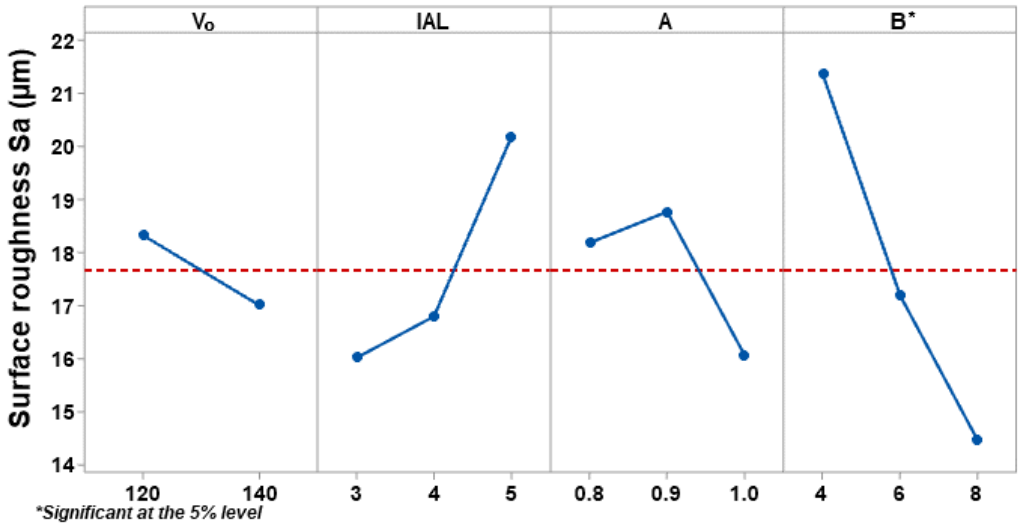


Figure 4.27: Main effects plot for Sa when cutting parallel to fibre orientation.

Table 4.10: ANOVA for Sa when cutting parallel to fibre orientation .

Source	DF	Seq SS	Adj SS	Adj MS	F-Value	P-Value	PCR
V_o	1	7.840	7.840	7.840	0.64	0.441	2.18%
IAL	2	59.240	59.240	29.620	2.43	0.138	16.51%
A	2	24.388	24.388	12.194	1.00	0.402	6.80%
B	2	145.524	145.524	72.762	5.97	0.020*	40.55%
Error	10	121.847	121.847	12.185			33.96%
Total	17	358.840					100.00%

4.3.4 Surface damage

Figure 4.28 shows optical micrographs of the machined kerf on the top and bottom surfaces from Test 9, corresponding to the highest MRR (4.7 mm^3/min) achieved when cutting parallel to the fibre orientation using the Compeed wire. The top surface appeared to be largely free of major damage apart from somewhat uneven kerf edges together with minor signs of delamination at the end of cut, see Figure 4.28(a). Additionally, bundles of frayed/uncut fibres were visible within the kerf originating from the machined surface, which suggested decomposition/vaporisation of the resin matrix. Similar defects were observed on the bottom surface, in addition to fibre debris and contaminants adhered to the surface as highlighted in Figure 4.28(b).

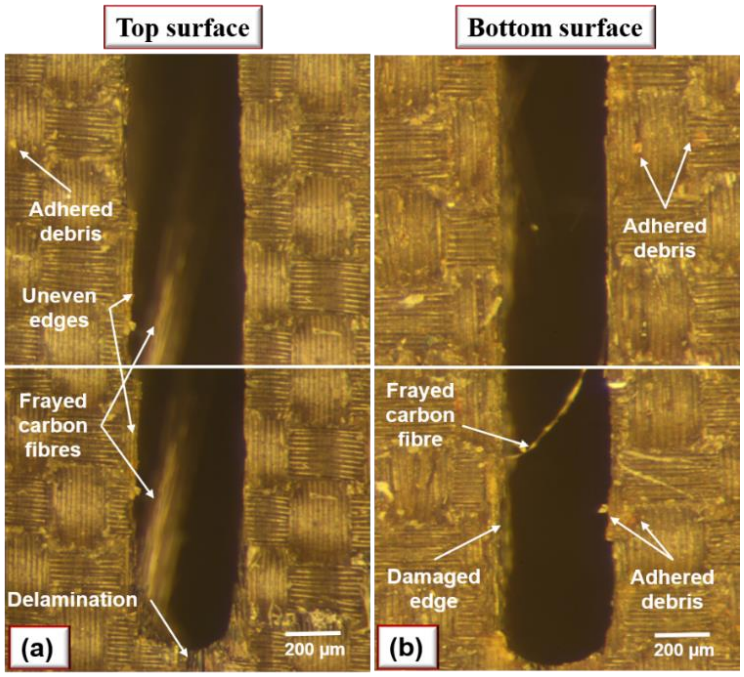


Figure 4.28: Optical micrographs of machined kerf accomplished at highest MRR using Compeed wire (a) top surface and (b) bottom surface.

The SEM micrographs of machined surfaces from selected trials corresponding to the lowest (Test 3), median (Test 18) and highest (Test 9) MRR obtained, are shown in Figure 4.29. Considerable amounts of broken fibre debris and decomposed/re-solidified epoxy resin were seen on the machined surface even for the test with the lowest MRR (1.17 mm^3/min), see Figure 4.29(a). A closer inspection revealed that the free ends of fibres were typically enlarged/swollen due to heat transfer and dissipation, together with voids and pits on the fibres and re-solidified adhered resin. Similar damage characteristics were found on the other workpieces analysed but with increased severity including greater space between fibres resulting from matrix loss, see Figure 4.29(b) and Figure 4.29(c).

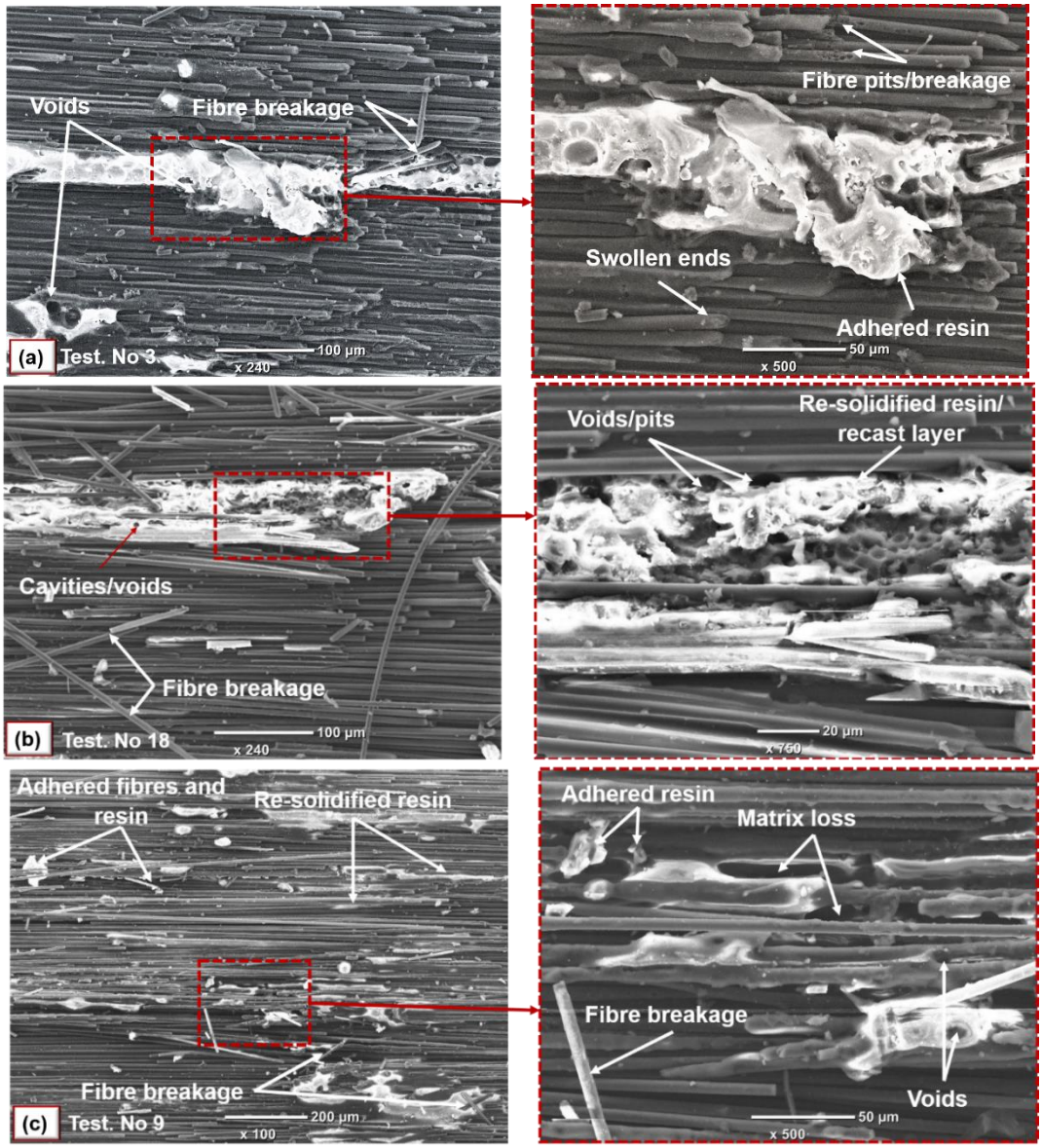


Figure 4.29: Sample SEM micrographs of machined surfaces in (a) Test 3 - lowest MRR, (b) Test 18 - median MRR and (c) Test 9 – highest MRR.

4.4 Phase 2B: Effect of operating parameters when cutting UD-CFRP perpendicular to fibre orientation using copper/brass coated steel core wire

4.4.1 Material removal rate

The calculated MRR for each test when cutting perpendicular to the fibre direction using the copper/brass coated steel core wire (Compeed) is shown in Figure 4.30. None of the trials exceeded 1.7 mm^3/min, which is considerably lower in comparison to results from Phase 2A when machining parallel to the fibres. This was primarily attributed to lower electrical conductivity of the CFRP in the transverse fibre direction in addition to the high resistivity of

the sample (24.7 Ω/mm or 4 x 10^{-5} S/cm) as detailed in Appendix C. The highest MRR of 1.68 mm^3/min was achieved in Test 7 involving high current, intermediate pulse off time and low voltage and pulse on time levels.

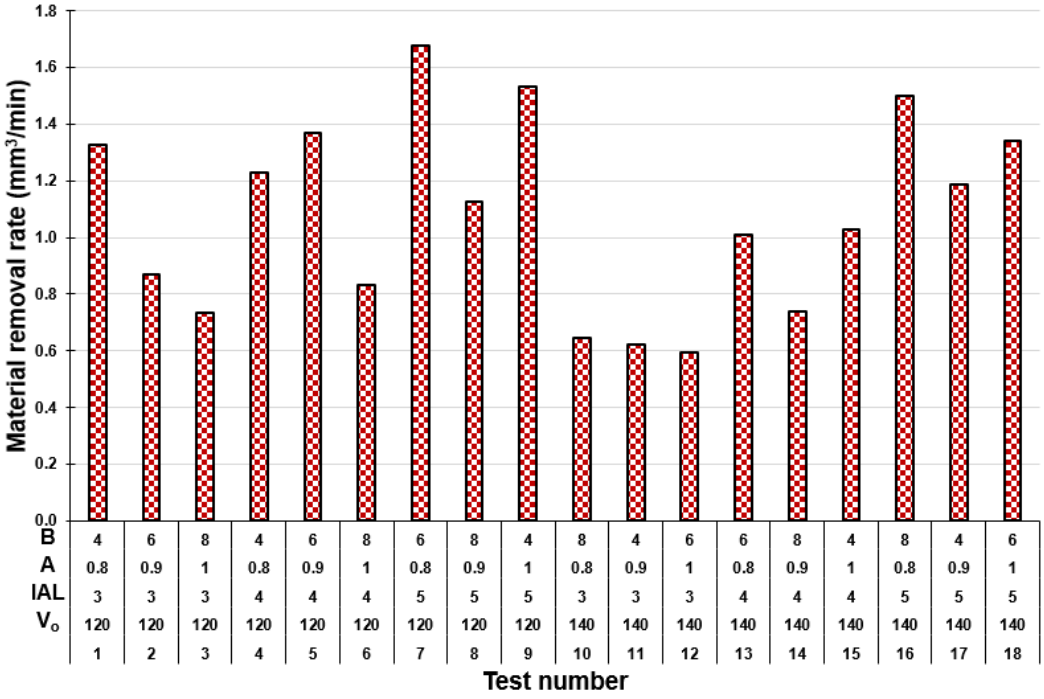


Figure 4.30: Material removal rate when cutting perpendicular to fibre direction using Compeed wire.

Figure 4.31 shows the main effects plot for mean MRR, which increased with higher current and lower pulse off time due to greater discharge energy. In contrast, increasing voltage and pulse on time both resulted in slower MRR, which was attributed to the greater release of fibre and resin debris into the machining gap contributing to poorer spark efficiency. The ANOVA outlined in Table 4.11 showed that ignition current, gap voltage and pulse on time were all found to be statistically significant at the 5% with regard to MRR. Ignition current was seen to have the largest influence with a PCR of 54.71%, while the effects of open voltage and pulse on time were somewhat more moderate with PCR's of of 11.64% and 11.20% respectively. Furthermore, the low residual error of ~13% suggests that the key factors influencing MRR were considered in the experiment.

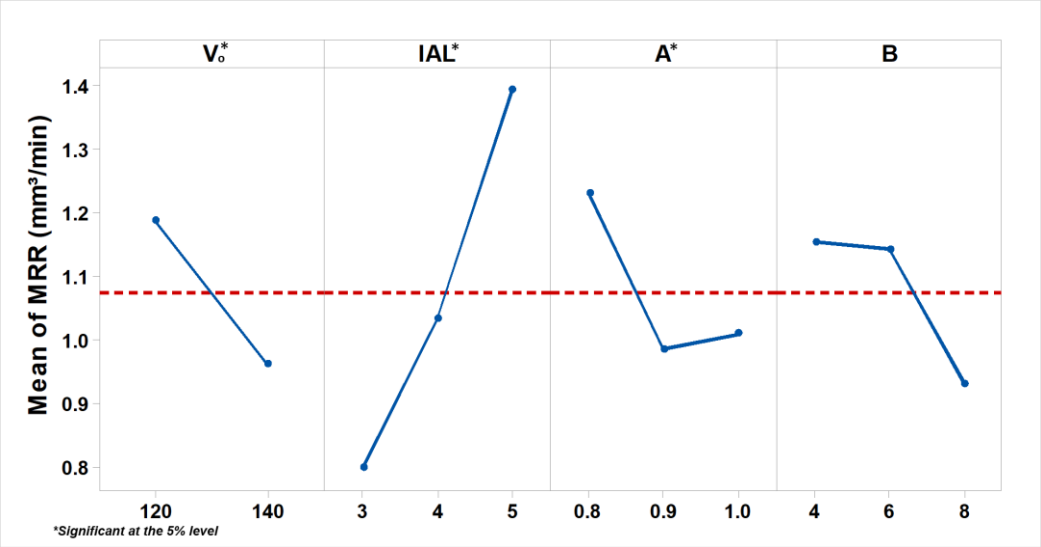


Figure 4.31: Main effects plot for MRR when cutting perpendicular to direction using Compeed wire.

Table 4.11: ANOVA for MRR when cutting perpendicular to direction using Compeed wire.

Source	DF	Seq SS	Adj SS	Adj MS	F-Value	P-Value	PCR
V_o	1	0.2295	0.2295	0.22951	9.15	0.013*	11.64%
IAL	2	1.0792	1.0792	0.53959	21.52	0.000*	54.71%
A	2	0.2210	0.2210	0.11048	4.41	0.042*	11.20%
B	2	0.1921	0.1921	0.09603	3.83	0.058	9.74%
Error	10	0.2507	0.2507	0.02507			12.71%
Total	17	1.9725					100.00%

* significant at the 5% level.

4.4.2 Kerf width

The average kerf widths when cutting perpendicular to the fibre direction ranged between 272 and 290 µm over the experiment, see Figure 4.32. The variation in average kerf width between tests as well as the spread of measurements were relatively small in comparison to results when machining parallel to fibre direction in Phase 2A, which suggests regular/even kerf edges. The main effects plot in Figure 4.33 indicates that average kerf width increased with voltage, which was understandable due to the larger spark gap. Similarly, mean kerf width generally increased with ignition current, despite showing a minor decreasing trend at the intermediate level (4 A), possibly due in part to differences in measurements at the top and bottom surfaces. In contrast, variation in pulse on time and off time had marginal effect on kerf width. This was supported by results from the ANOVA showing low PCR's of 0.11% and 2.18% for pulse on time and off time respectively, see Table 4.12. None of the factors however were statistically significant at the 5% level, despite PCR's of 32.89% and 15.92% for ignition current and open voltage respectively.

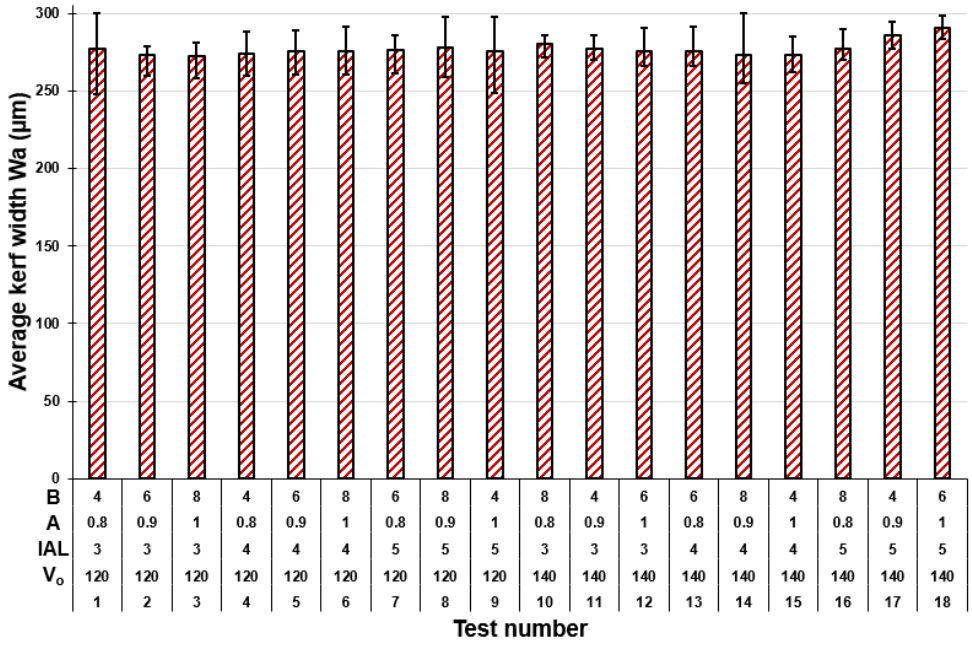


Figure 4.32: Average kerf width when cutting perpendicular to direction using Compeed wire.

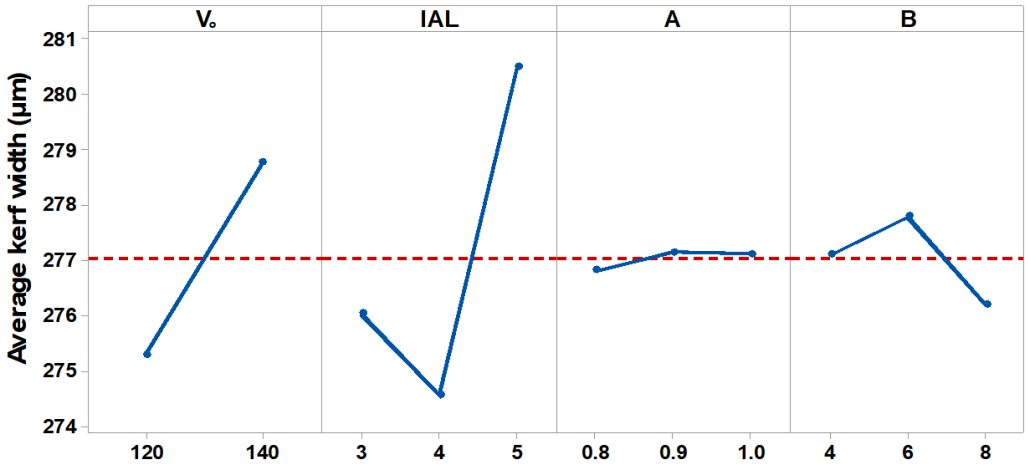


Figure 4.33: Main effects plot for average kerf width when cutting perpendicular to direction using Compeed wire.

Table 4.12: ANOVA for average kerf width when cutting perpendicular to direction using Compeed wire.

Source	DF	Seq SS	Adj SS	Adj MS	F-Value	P-Value	PCR
V_o	1	55.032	55.032	55.0325	3.26	0.101	15.92%
IAL	2	113.713	113.713	56.8565	3.36	0.076	32.89%
A	2	0.386	0.386	0.1928	0.01	0.989	0.11%
B	2	7.540	7.540	3.7700	0.22	0.804	2.18%
Error	10	169.051	169.051	16.9051			48.90%
Total	17	345.722					100.00%

4.4.3 Surface roughness

Figure 4.34 outlines the mean surface roughness in terms of 2D linear (Ra) and 3D areal (Sa) parameters for all tests when cutting perpendicular to fibre direction using the Compeed wire. The average surface roughness levels observed here were considerably lower compared to results when machining parallel to the fibres in Phase 2A, with Sa ranging between 4.36 and 7.77 µm. In general, the linear roughness in measured in the horizontal direction was higher than the vertical direction for tests performed at the low voltage level (120 V). This was due to the presence of cavities/pits within the fibre plies due to material eroded by the high discharge energy as well as wavy surfaces along the horizontal direction, see Figure 4.35(a). The Ra in the vertical direction however was typically higher in tests at 140 V, potentially due to the greater amount of gaps/cavities formed at the interface between fibre plies, see example from Test 11 in Figure 4.35(b) corresponding to the highest surface roughness achieved. Figure 4.36 shows the main effects plot for areal surface roughness (Sa). Increasing gap voltage and pulse off time tended to reduce surface roughness, which also corresponded to lower MRR possibly due to lower spark frequency. The trends for current and pulse on time were similar where intermediate levels resulted in elevated roughness. Although none of the factors were statistically significant, pulse off time achieved the highest percentage contribution ratio of 23.24% followed by ignition current at 15.40% as detailed by the ANOVA in Table 4.13. Nevertheless, a high residual error of 52.75% was also recorded.

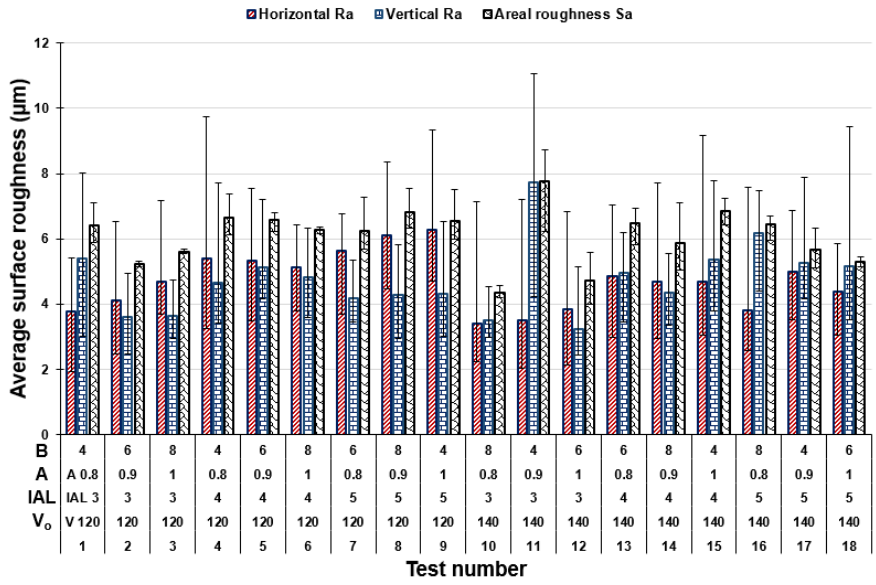


Figure 4.34: Average surface roughness when cutting perpendicular to direction using Compeed wire.

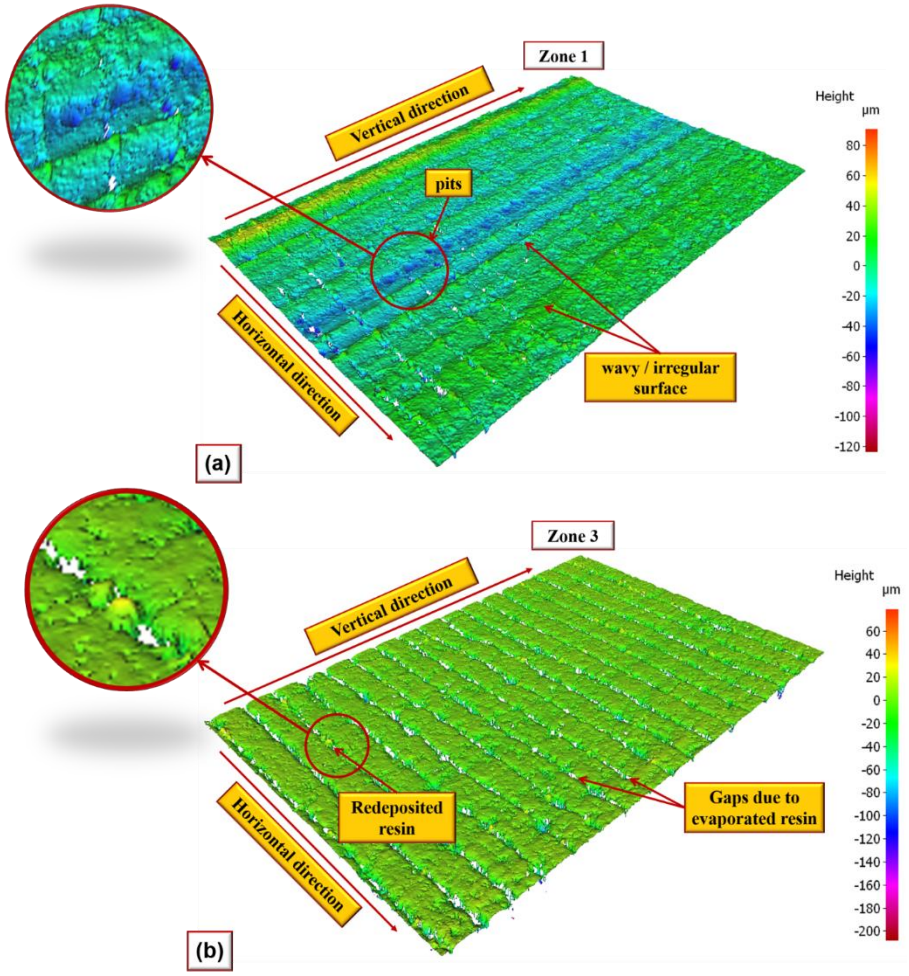


Figure 4.35: Surface topographical map of machined workpiece from (a) Test 7 – highest MRR and (b) Test 11 – highest Sa.

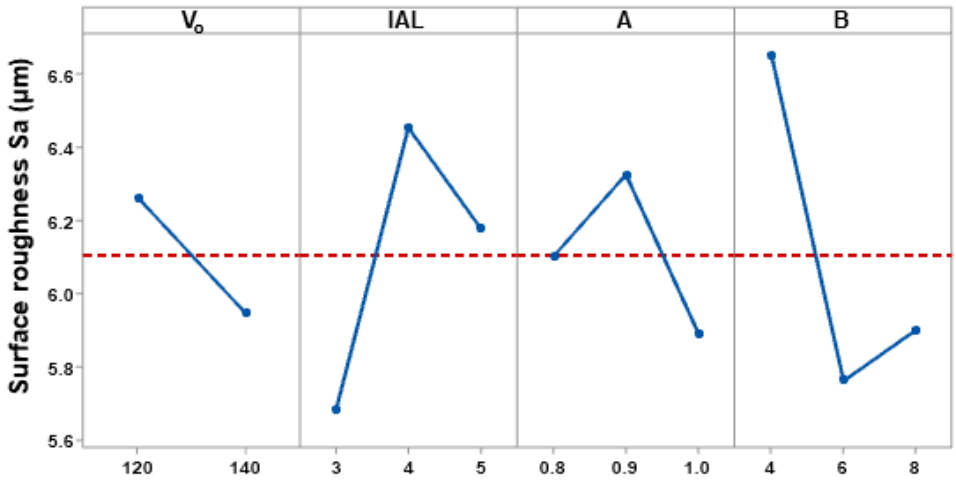


Figure 4.36: Main effects plot for Sa when cutting perpendicular to direction using Compeed wire.

Table 4.13: ANOVA for Sa when cutting perpendicular to direction using Compeed wire.

Source	DF	Seq SS	Adj SS	Adj MS	F-Value	P-Value	PCR
V_o	1	0.4526	0.4526	0.4526	0.72	0.415	3.81%
IAL	2	1.8281	1.8281	0.9141	1.46	0.278	15.40%
A	2	0.5697	0.5697	0.2849	0.45	0.647	4.80%
B	2	2.7589	2.7589	1.3795	2.20	0.161	23.24%
Error	10	6.2634	6.2634	0.6263			52.75%
Total	17	11.8727					100.00%

4.4.4 Surface damage

Optical micrographs of the machined kerf on the top and bottom surfaces from Test 7, which exhibited the highest MRR is shown in Figure 4.37. Considerable delamination was observed on both the top and bottom sides of the workpiece, together with evidence of broken fibres adhered on the top surface as shown in Figure 4.37(a). The kerf edges on the bottom of the workpiece however appeared to be relatively even in comparison to the top surface, despite the presence of contaminants, see Figure 4.37(b). Calculation of the delamination factor revealed that values on the top and bottom surfaces were approximately equivalent at ~2.05 and ~2.00 respectively.

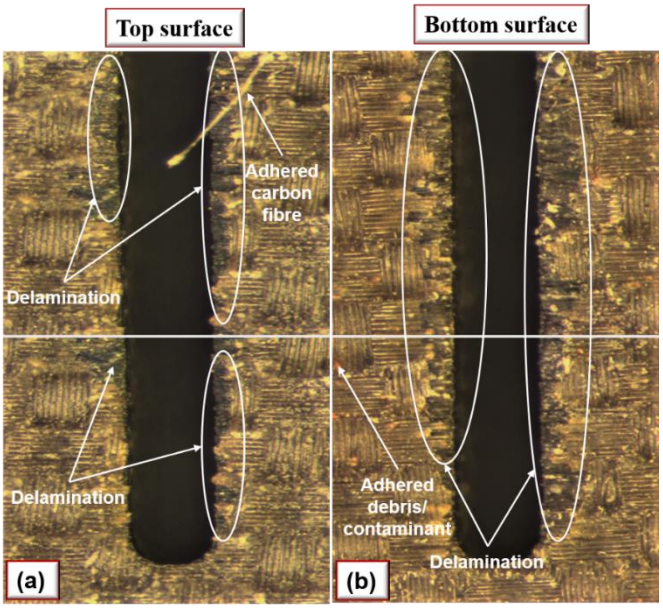


Figure 4.37: Optical micrographs of machined kerf on the; (a) top and (b) bottom surfaces from test at highest MRR using Compeed wire.

High resolution SEM micrographs of the machined surfaces from selected tests relating to the lowest, median and highest MRR obtained are illustrated in Figure 4.38. Regular/flat surfaces free from resin craters was observed in Test 12 (lowest MRR of 0.59 mm^3/min) as shown in Figure 4.38(a) due to low discharge energy achieved at low current of 3 A as well as intermediate pulse off time (6 µs). This reduced spark frequency and provided sufficient time

to evacuate debris from machining gap, preventing adhesion to the machined surface. All of the surfaces displayed areas with fibre and matrix loss likely due to sublimation of carbon fibres caused by discharge heat that passes through axial direction of fibres [154, 155]. The cavities formed from the removal of fibres/epoxy matrix were generally filled with decomposed/re-deposited resin material, particularly at the interface between individual plies. The damage was more severe on surfaces from tests at the median (1.08 mm^3/min) and high (1.68 mm^3/min) MRR, with adhered fibres, voids/pits and craters also visible, see Figure 4.38(b) and Figure 4.38(c). Furthermore, the voids and craters were wider and deeper on the surface from Test 7 (high MRR).

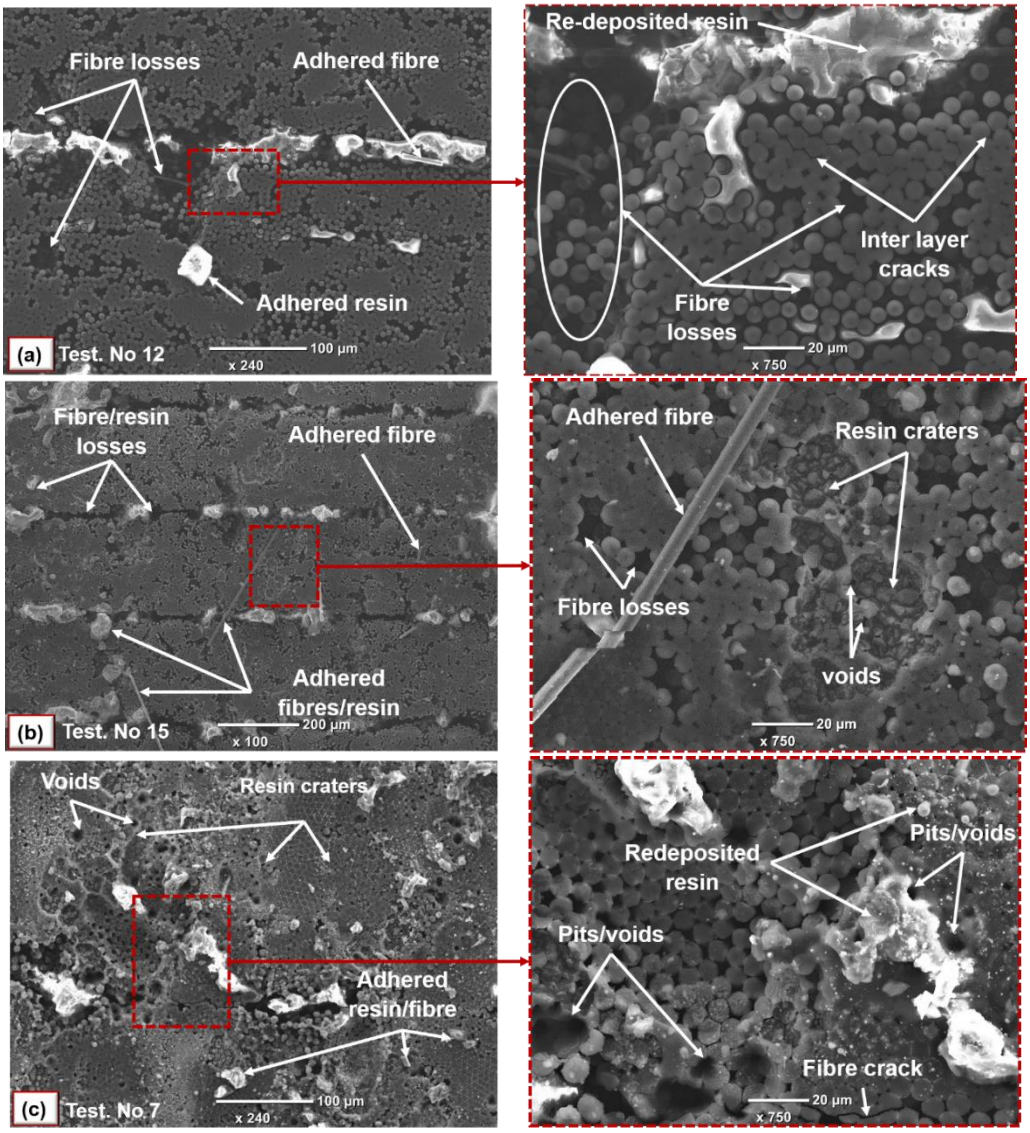


Figure 4.38: Sample SEM micrographs of machined surfaces in (a) Test 12 - lowest MRR, (b) Test 15 – median MRR and (c) Test 7 – highest MRR.

4.4.5 Confirmation tests

Confirmation tests were conducted based on the preferred factor levels identified from the main effects plots and S/N ratio analysis, with the aim of maximising MRR while minimising kerf width and surface roughness. Table 4.14 shows the experimental and predicted results for mean and S/N ratio values of the response parameters. The relative error between the predicted and experimental mean results were below 5% for kerf width and surface roughness when machining parallel to fibre direction (Phase 2A) while the difference between the experimental and predicted values for mean surface roughness exceeded 10% when operating perpendicular to the fibre orientation (Phase 2B).

Table 4.14: Predicted and experimental results from Phase 2 confirmation tests for various responses.

	Optimal levels	Response	Mean		S/N ratio (dB)		Error %
			Pred.	Exp.	Pred.	Exp.	
Phase 2A	$V_{o1}I_3A_3B_1$	MRR	4.08	4.36	12.16	12.79	6.42
	$V_{o2}I_1A_3B_3$	Wa	283	296.31	-49.07	-49.43	4.49
	$V_{o2}I_1A_3B_3$	Sa	10.53	10.96	-20.95	-20.80	3.92
Phase 2B	$V_{o1}I_3A_1B_1$	MRR	1.74	1.71	5.76	4.66	1.75*
	$V_{o1}I_2A_1B_3$	Wa	271.79	281.02	-48.69	-48.97	3.28
	$V_{o2}I_1A_3B_2$	Sa	4.97	5.56	-13.86	-14.90	10.61

* The experimental result is lower than predicted value.

The topography of the machined surface from the confirmation test in Phase 2B was examined, with considerable damage observed as shown in Figure 4.39. This included fibre fragments covered with bulky re-deposited resin due to the elevated discharge energy resulting from the high wire conductivity and selected cutting conditions. For Phase 2A, the parameters in the confirmation test were equivalent to those in Test 9.

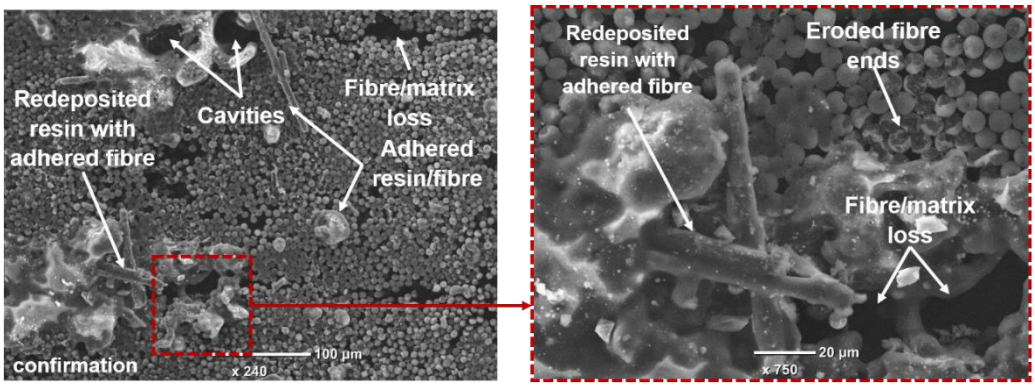


Figure 4.39: Sample SEM micrographs of machined surface from the confirmation test in Phase 2B.

4.5 Comparison between Phase 1 and 2 tests (effect of wire electrode)

The results from Phase 1 and 2 experiments in terms of MRR, Wa and Sa were compared in order to evaluate the performance of the Topas and Compeed wire electrodes at equivalent operating conditions. All of the relevant data tables are detailed in Appendix F.

4.5.1 Material removal rate

It was clearly observed that cutting parallel to fibre orientation resulted in higher MRR compared with the perpendicular direction, especially using the Compeed wire as shown Figure 4.40. This was primarily due to the higher electrical conductivity of the fibres/workpiece in axial (~11.91 S/cm) compared to the transverse (14.27 x 10^{-2} S/cm) direction. For the initial tests carried out parallel to the fibre direction, the standoff distance between the top flushing nozzle and the CFRP workpiece when utilising the Topas wire was ~ 4 cm, while this was reduced to 2 mm for trials involving the Compeed wire. The considerably larger standoff distance in tests with the Topas wire most likely had an adverse influence on the flushing efficiency and spark stability, which may have contributed to the lower MRR recorded. Therefore, an additional test employing parameters resulting in the highest MRR (Test 9 in Phase 1A) was performed using both the Topas and Compeed wires with the nozzle standoff distance at 2 mm. The test was repeated three times for different samples and results showed that the smaller standoff distance significantly improved the MRR achieved by the Topas wire, which was comparable to the Compeed wire as shown in Figure 4.41. The average MRR values indicated that the Compeed wire was marginally higher at 5.79 mm^3/min compared to 5.54 mm^3/min for the Topas wire.

Despite lower workpiece electrical conductivity, tests involving cutting perpendicular to the fibre direction with the Topas wire generally exhibited higher MRR values compared to corresponding trials performed parallel to the fibres, most likely due to the larger nozzle standoff distance in the latter. However, the Topas wire demonstrated marginally higher MRR than the Compeed wire in most cases when machining perpendicular to the fibre direction (both having equivalent nozzle standoff of 2 mm). This was partly attributed to the more intense sparks generated using the Compeed wire as a consequence of its higher electrical conductivity, which increased matrix/resin and fibre debris in the spark gap. The variation in bulk resistivity of the CFRP workpieces was also a likely influencing factor.

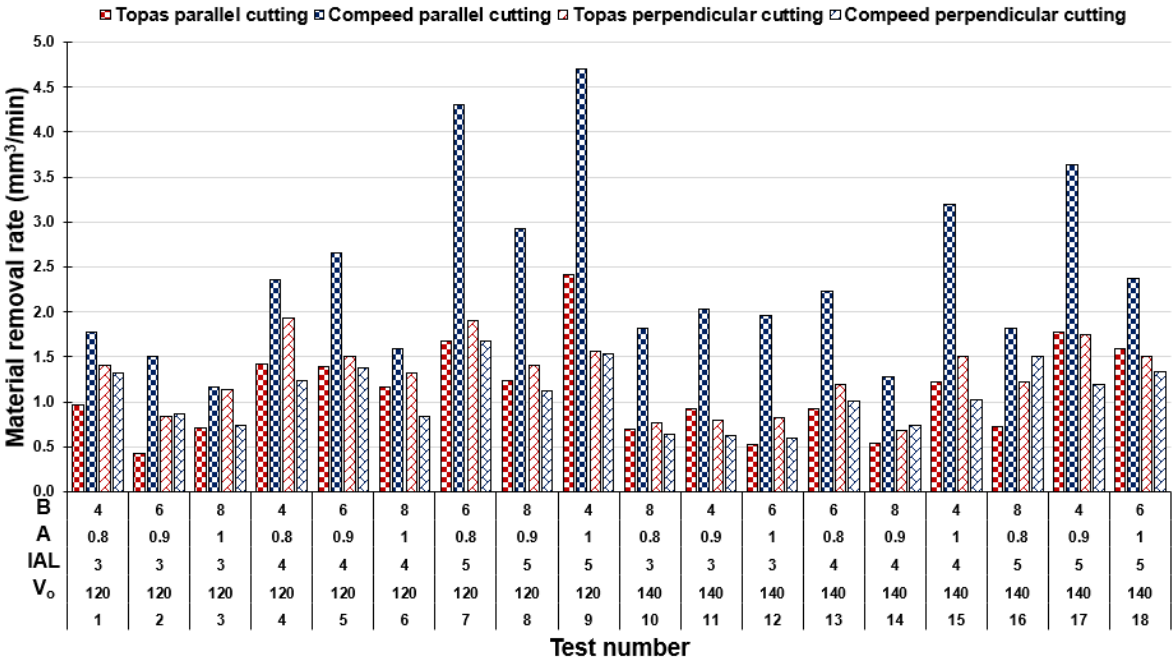


Figure 4.40: Comparison between material removal rates for Phases 1 and 2 using Topas and Compeed wire electrodes at different cutting orientations.

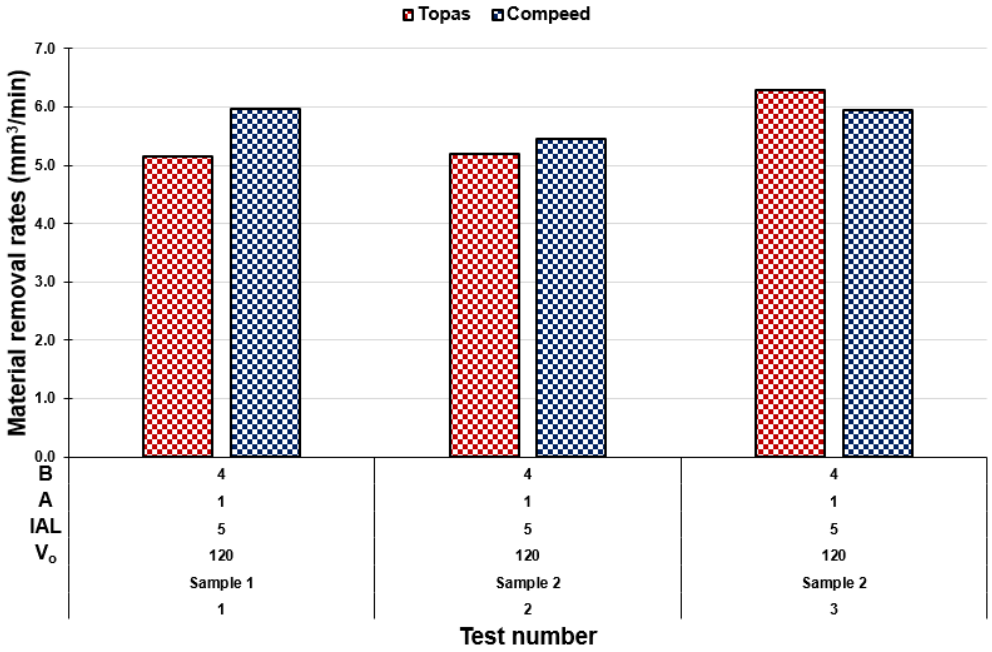


Figure 4.41: Comparison of MRR performance achieved by Topas and Compeed wires when cutting parallel to fibre direction at equivalent cutting conditions and nozzle standoff distance.

In addition to the higher MRR achieved by the Compeed wire when cutting parallel to the fibre direction, it was also observed to be less prone to breakage compared to the Topas wire. A comparative test was performed with both wires cutting a UD-CFRP laminate parallel to the fibres at a current of 6 A, pulse on time of 1 µs and pulse off time of 4 µs. The Topas wire was

found to fail/break repeatedly due to increased cavitation and erosion of the wire caused by the spark discharges, leading to a reduction in wire cross section and weakening of the electrode, see Figure 4.42.

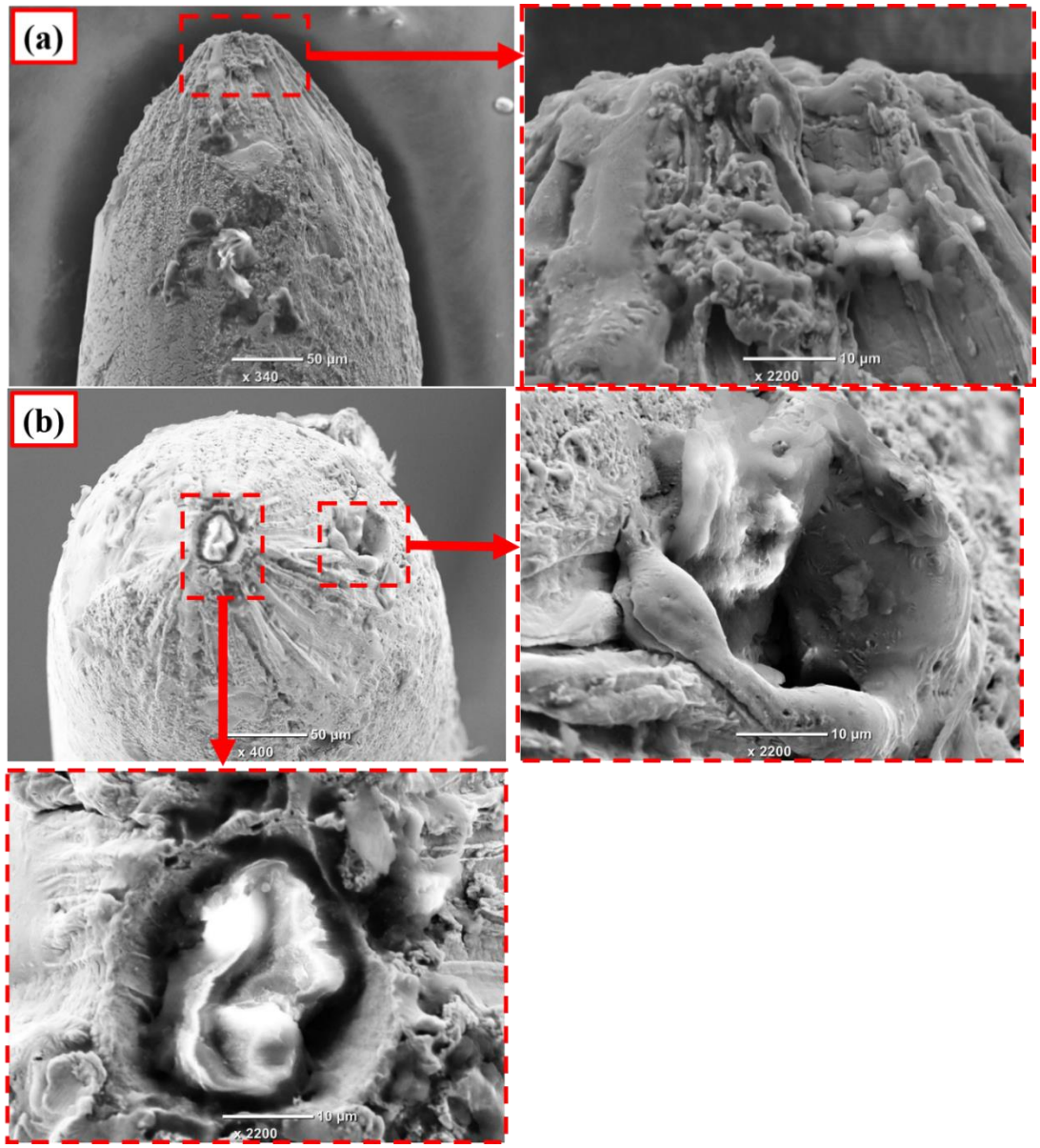


Figure 4.42: SEM micrographs of cavities and reduction in wire cross section of the Topas wire; (a) front view, and (b) top view.

4.5.2 Average kerf width

The average kerf widths were generally larger when machining parallel to the fibre direction particularly for the Compeed wire, as detailed in Figure 4.43. This was mainly attributed to the higher electrical conductivity of the workpiece along the fibre direction, which induced more effective spark discharges and greater Joule heating resulting in wider kerfs. Tests with the Compeed wire produced wider kerfs compared to the Topas wire regardless of cutting direction,

due to its higher electrical conductivity resulting in greater discharge intensity in the machining gap. Additionally, the spread of the measured kerf widths was also significantly larger with the Compeed wire, which reflects the variation of the kerf along the cut length.

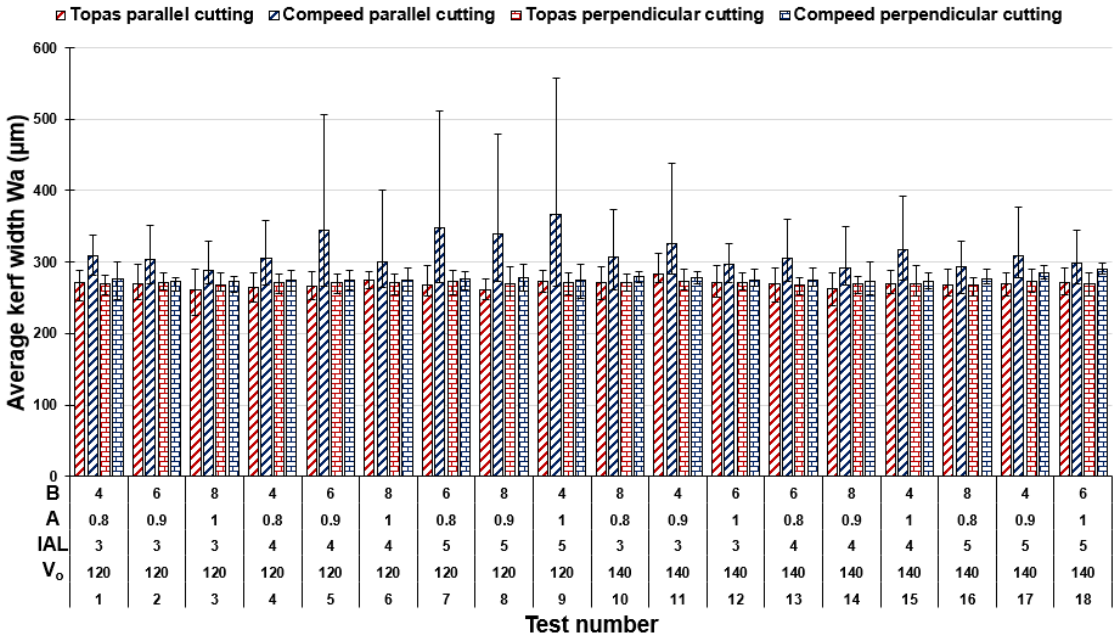


Figure 4.43: Comparison of average kerf widths obtained using Topas and Compeed wires when cutting parallel and perpendicular to fibre direction.

4.5.3 Average surface roughness

Figure 4.44 shows the average areal roughness obtained when cutting parallel and perpendicular to fibre orientation using the Topas and Compeed wires in Phase 1 and 2 tests respectively. In general, workpiece surface roughness was typically higher when machining parallel to the fibre direction, regardless of the wire material. This corresponded to conditions where higher MRR was achieved, with the machined surfaces generally characterised by high levels of frayed fibres and decomposed/re-solidified resin matrix. Surfaces machined with the Compeed wire exhibited higher average roughness levels of up to 26.29 µm Sa when operating parallel to the fibre direction. In contrast, surface roughness varied between 4.53 to 9.48 µm Sa when employing the Topas wire. Similarly, workpiece surface roughness when cutting perpendicular to the fibre direction was higher with the Compeed (4.36 and 7.77 µm Sa) compared to the Topas wire (3.3 and 6.84 µm Sa).

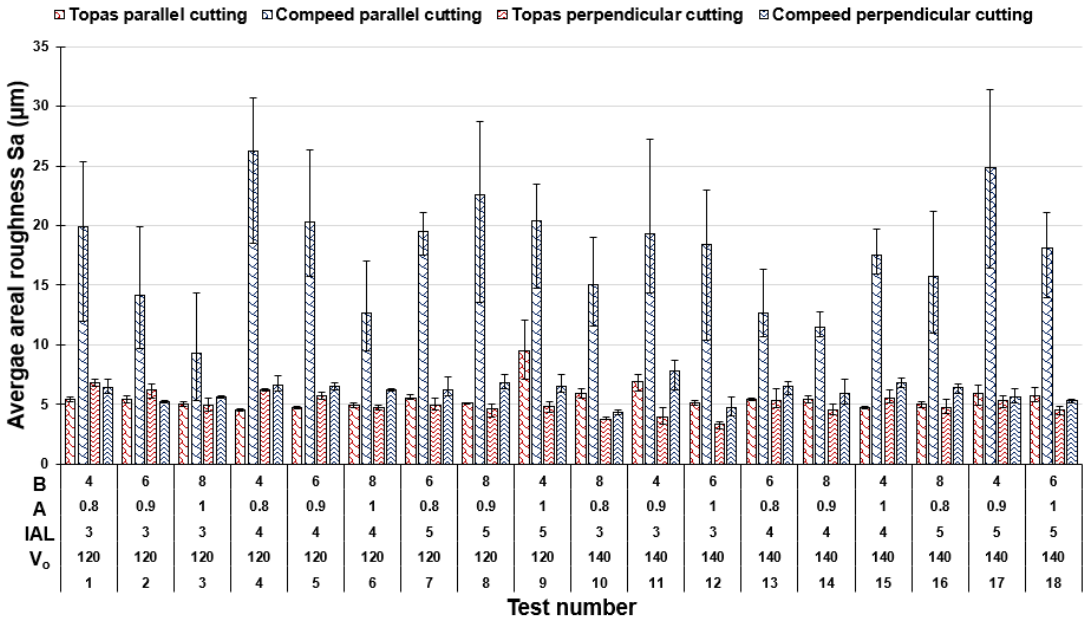


Figure 4.44: Comparison of average areal surface roughness obtained using Topas and Compeed wires when cutting parallel and perpendicular to fibre direction.

4.6 Phase 3A: Preliminary investigation on cutting UD-CFRP/Cu stacks using zinc coated brass and copper/brass coated steel core wires

4.6.1 Material removal rate

Preliminary tests were carried out to investigate the feasibility of cutting UD-CFRP stacked with copper sheets as well as determine the effect of stacking on material removal rate using both Topas and Compeed wires. Machining of the CFRP/Cu stacks were successful with higher MRR achieved despite employing a lower pulse on time (0.6 µs) compared to corresponding tests with plain CFRP (1 µs), see Figure 4.45. The MRR when cutting the CFRP/Cu stacks using the Topas and Compeed wires were 6.5 mm^3/min and 6.11 mm^3/min respectively, as opposed to 5.15 mm^3/min and 5.98 mm^3/min when machining the plain CFRP workpiece.

Tests at low current (3 A) and high pulse off time (8 µs) when cutting the CFRP/Cu stacks showed that Compeed wire achieved higher MRR of 2.45 mm^3/min compared to Topas (1.81 mm^3/min), due to the higher electrical conductivity of the Compeed wire, see Figure 4.46. However, increasing the current to 5 A and reducing the pulse off time to 4 µs resulted in higher MRR with the Topas wire. The larger discharge energies and greater spark intensity possibly led to unstable conditions at the machining gap (increased resin/fibre debris) when using the Compeed wire.

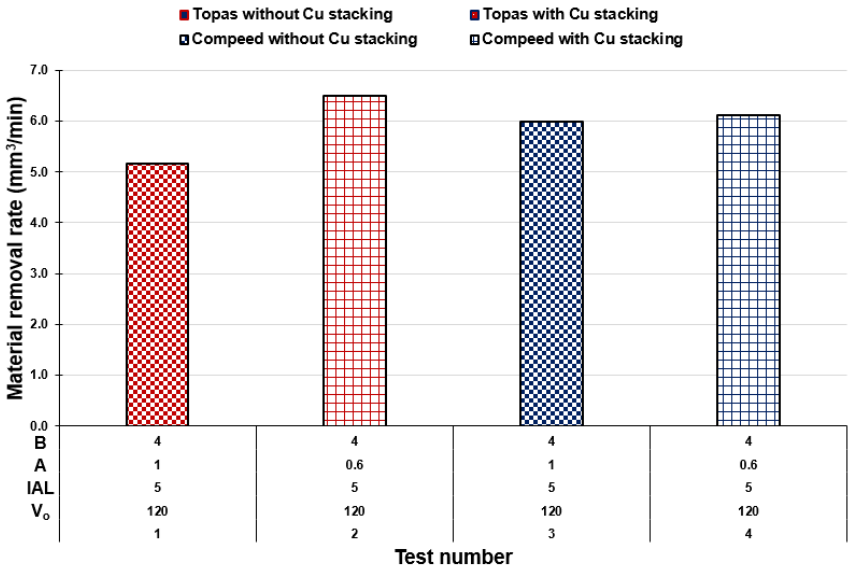


Figure 4.45: Comparison of MRR obtained when machining plain UD-CFRP and UD-CFRP/Cu stacks using Topas and Compeed wires.

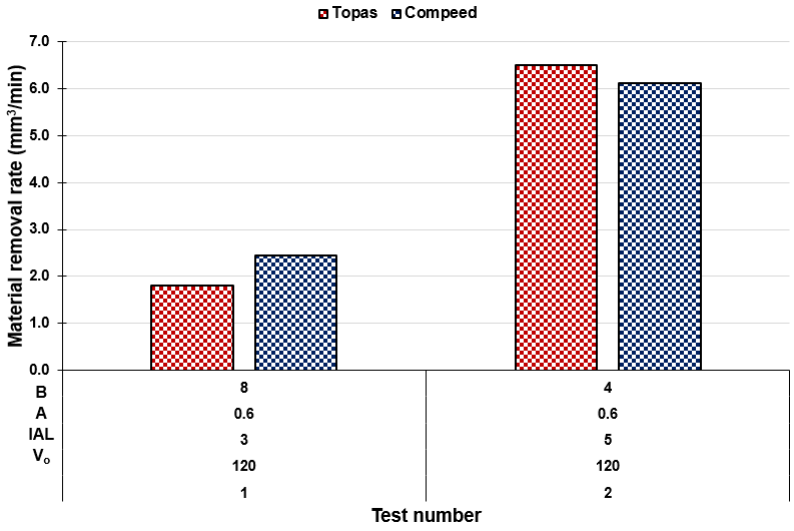


Figure 4.46: Comparison of MRR obtained when machining CFRP/Cu stacks using Topas and Compeed at different operating parameters.

4.7 Phase 3B: Influence of operating parameters and wire electrode material when cutting UD-CFRP-metallic stacks

4.7.1 Material removal rate

Despite employing parameters leading to lower discharge energies, material removal rates of up to 5.89 mm^3/min was obtained when cutting CFRP/Cu stacks, see Figure 4.47, as opposed to results when machining plain CFRP (2.41 mm^3/min for Phase 1A and 4.7 mm^3/min for Phase 2A). This was most likely due to the increased bulk electrical conductivity of the CFRP/Cu stacks. In contrast to results when machining plain CFRP, the MRR was typically higher when cutting the stacks with the Topas (2.89 to 5.89 mm^3/min) compared to the Compeed wire (1.82

to 5.35 mm^3/min). The enhancement in electrical conductivity due to the Cu layer provided an appropriate flow of current and discharge energy with stable discharge when using the Topas wire. Conversely, the higher conductivity of the Compeed wire produced greater energy in the machining gap leading to higher debris causing unstable sparking and lower MRR. Additionally, the non-homogeneity of the CFRP composite with possible variation of resin distribution within the material may have also affected the discharge process.

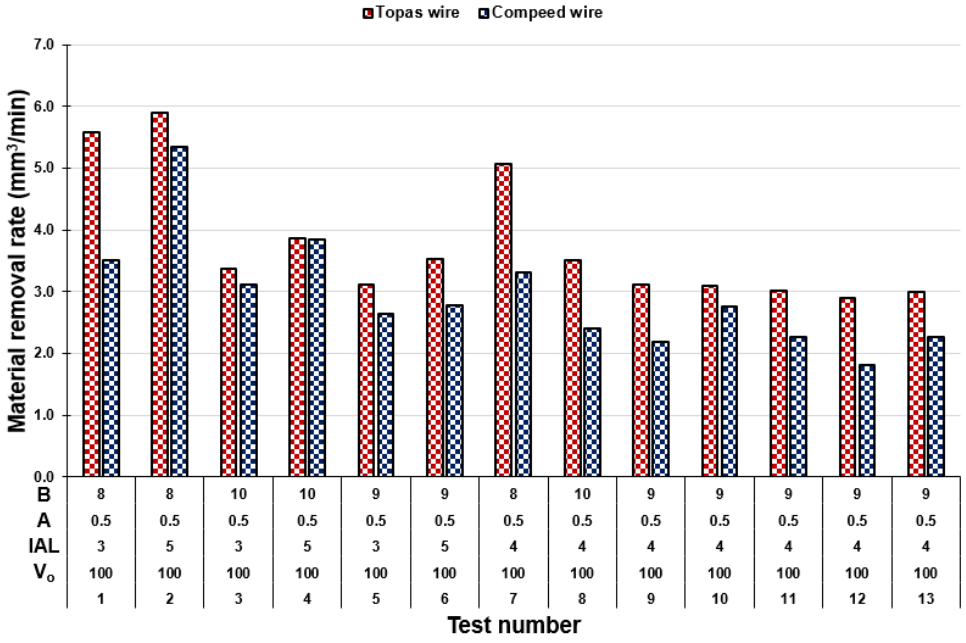


Figure 4.47: Comparison of MRR when machining CFRP/Cu stacks using Topas and Compeed wires.

According to the analysis of variance, it was observed that all of the linear factors and corresponding squared terms were significant with respect to MRR in the model. However, none of the two-way interactions had a major influence except for the interaction between pulse off and wire type as detailed in Table 4.15. Pulse off time exhibited highest PCR of 22.11% followed by wire type with 16.11%. The lack of fit was not significant, which suggests that no additional terms were required to fit the model. Additionally, the model showed good correlation with the experimental results based on the coefficient of determination (R^2) of 93.29% and adjusted R^2 of 90.14%. Table 4.16 details the regression equations for the Topas and Compeed wire electrodes as well as the model summary. Figure 4.48 presents the normal plot of standardised effects for MRR, which indicated that all the model terms significantly influenced on MRR, except for the two-way interaction between current and pulse off time/wire type.

Table 4.15: ANOVA for material removal rate when machining CFRP/Cu stacks.

Source	DF	Seq SS	Adj SS	Adj MS	F-Value	P-Value	PCR
Model	8	25.9511	25.9511	3.24389	29.56	0.000*	93.29%
Linear	3	11.9039	11.9039	3.96795	36.16	0.000*	42.79%
IAL	1	1.2742	1.2742	1.27424	11.61	0.003*	4.58%
B	1	6.1494	6.1494	6.14936	56.04	0.000*	22.11%
W	1	4.4803	4.4803	4.48026	40.83	0.000*	16.11%
Square	2	13.0092	13.0092	6.50461	59.28	0.000*	46.77%
IAL*IAL	1	6.1584	1.6832	1.68319	15.34	0.001*	22.14%
B*B	1	6.8508	6.8508	6.85083	62.43	0.000*	24.63%
2-Way Interaction	3	1.0380	1.0380	0.34601	3.15	0.052	3.73%
IAL*B	1	0.1048	0.1048	0.10478	0.95	0.342	0.38%
IAL*W	1	0.1810	0.1810	0.18102	1.65	0.216	0.65%
B*W	1	0.7522	0.7522	0.75224	6.86	0.018*	2.70%
Error	17	1.8654	1.8654	0.10973			6.71%
Lack-of-Fit	9	1.3931	1.3931	0.15478	2.62	0.095	5.01%
Pure Error	8	0.4724	0.4724	0.05904			1.70%
Total	25	27.8165					100.00%

* significant at the 5% level

Table 4.16: Regression equations and model summary for MRR.

Regression equations	
Topas	MRR =105.8 - 3.18 IAL - 20.55 B + 0.552 IAL*IAL + 1.114 B*B - 0.114 IAL*B
Compeed	MRR = 99.5 - 2.94 IAL - 20.05 B + 0.552 IAL*IAL + 1.114 B*B - 0.114 IAL*B

Model summary				
S	**R-sq**	**R-sq(adj)**	**PRESS**	**R-sq(pred)**
0.331255	93.29%	90.14%	5.76431	79.28%

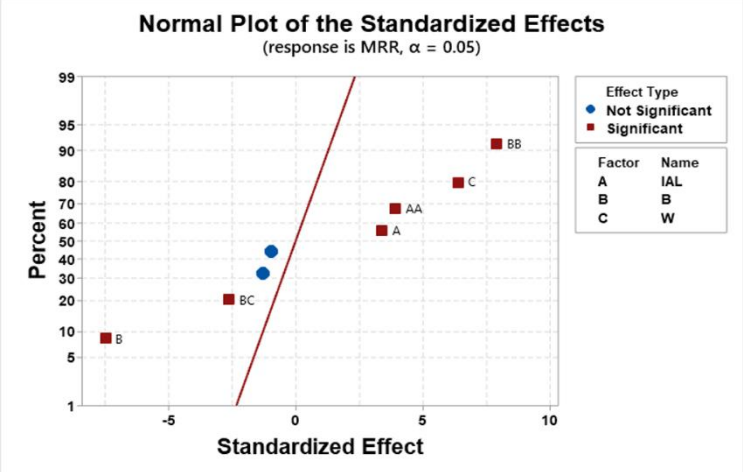


Figure 4.48: Normal plot of standardised effects for MRR.

Contour and surface plots show the effect of variation between the ignition current and pulse off time on MRR for both wire electrodes, see Figure 4.49. The highest MRR was obtained at high current and low pulse off time of 5 A and 8 µs respectively, represented by the dark green region of the contour plot. Conversely, lowest MRR levels were denoted by the dark blue area of the contour plot corresponding to low and intermediate current levels together with intermediate to high pulse off times.

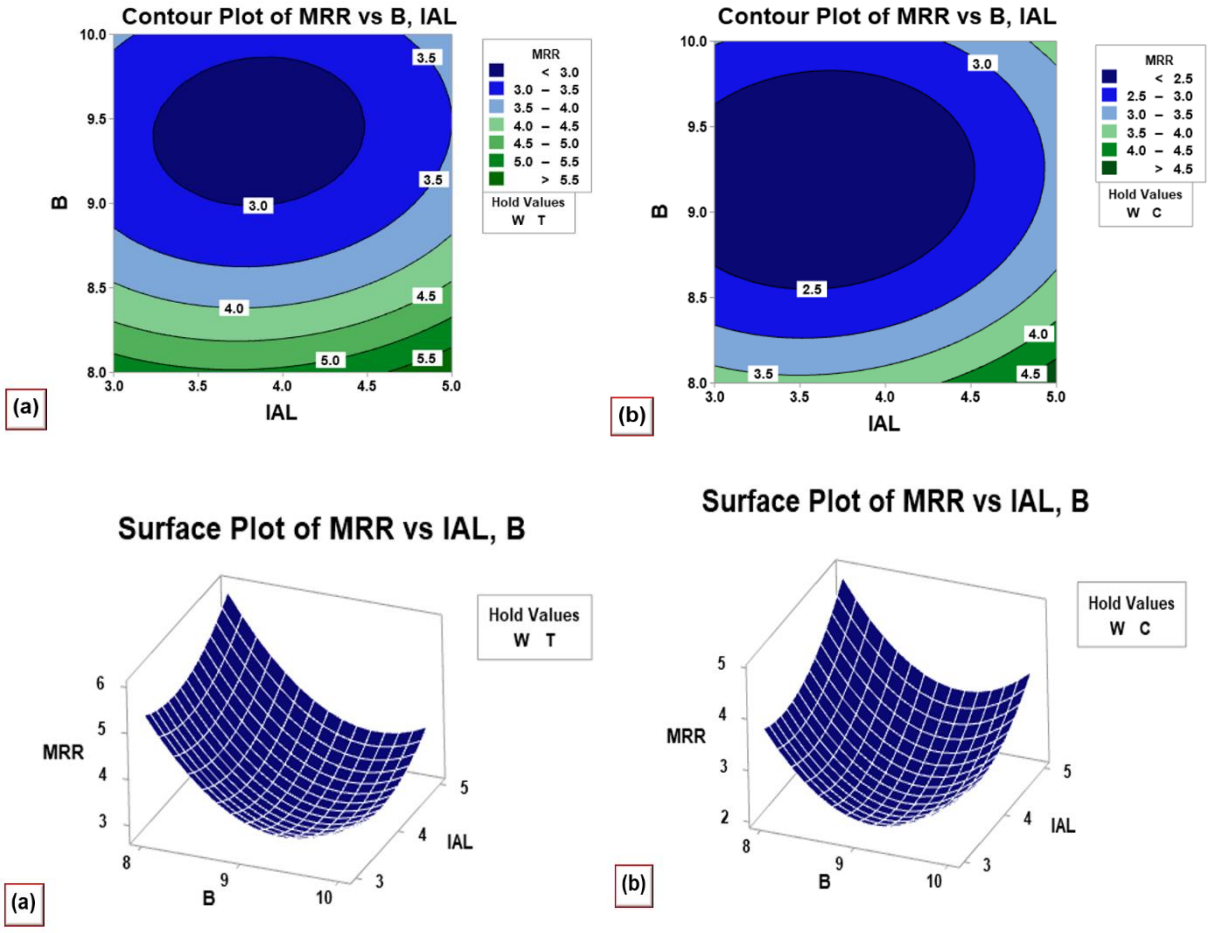


Figure 4.49: Contour and surface plots showing the relationship between machining variables and MRR for (a) Topas and (b) Compeed wires.

4.7.2 Surface roughness

For areal roughness, there were noticeable discrepancies between results within machining tests as shown in Figure 4.50, which was likely attributed to spark stability and variation in resin distribution throughout the CFRP, as cutting was performed at different sides of the workpiece. The highest roughness of 16.48 µm Sa was observed when using the Topas wire in Test 2, which corresponded to the highest MRR resulting in high levels of re-solidified resin debris and frayed fibres on the surface as revealed in Figure 4.51. The spread of roughness values were

larger on surfaces machined with the Compeed wire, which reflects the considerable variation between different measurement zones caused by the high discharge energy as well as the potential presence of frayed fibres in some areas as opposed to re-solidified resin in other areas. For more details of the roughness measurement zones, see Appendix E.

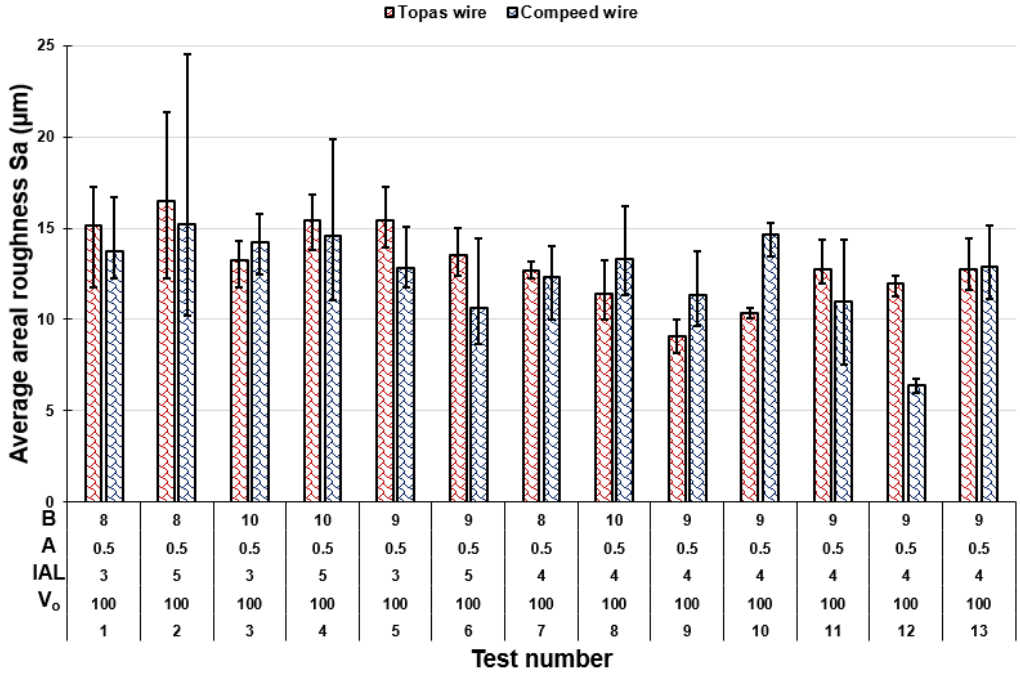


Figure 4.50: Average areal surface roughness when machining CFRP/Cu stacks for both wire electrodes.

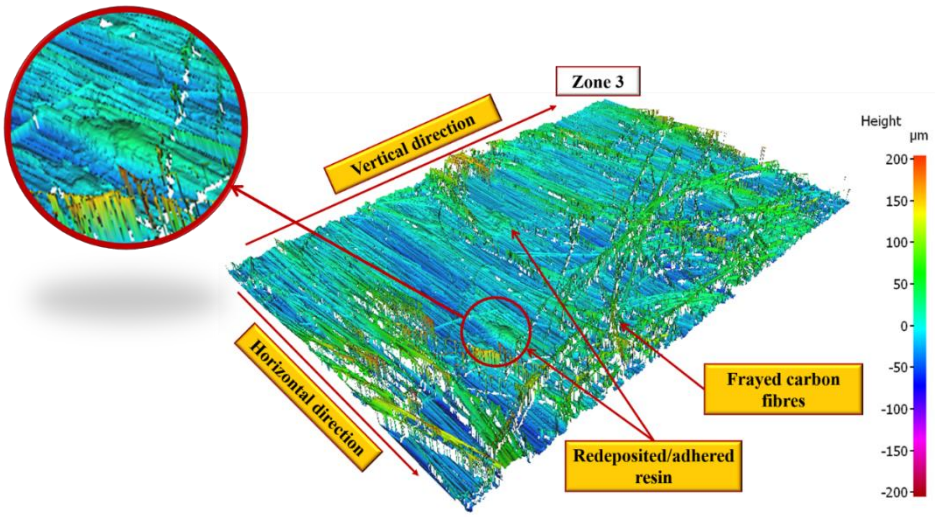


Figure 4.51: Surface topographical map of machined workpiece from Test 2 (highest Sa) using Topas plus D wire.

Due to the variation in results of surface condition obtained at different cutting conditions, the squared of ignition current was the sole term in the model that had a statistically significant effect on Sa with a PCR of 34.55%, see Figure 4.52. Conversely, the ANOVA showed that

there was a relatively high residual error with a PCR of 52.32%, as detailed in Table 4.17. Therefore, the efficiency of the model in representing the results reduced to 47.68%. Table 4.18 displays the regression model equations for both wire electrodes as well as the model summary.

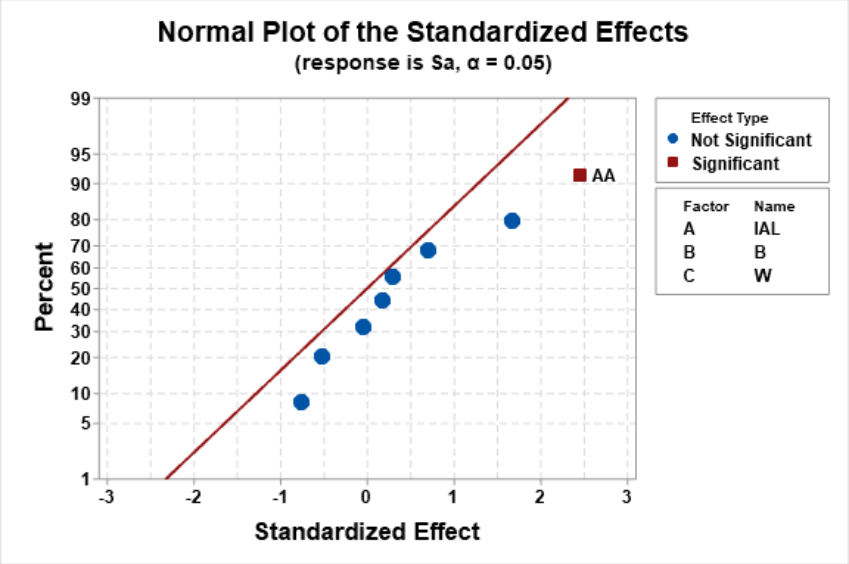


Figure 4.52: Normal plot of standardised effects for Sa.

Table 4.17: ANOVA for areal roughness (Sa) when machining CFRP/Cu stacks.

Source	DF	Seq SS	Adj SS	Adj MS	F-Value	P-Value	PCR
Model	8	58.440	58.4404	7.3051	1.94	0.120	47.68%
Linear	3	3.025	3.0249	1.0083	0.27	0.848	2.47%
IAL	1	0.113	0.1126	0.1126	0.03	0.865	0.09%
B	1	0.996	0.9965	0.9965	0.26	0.614	0.81%
W	1	1.916	1.9158	1.9158	0.51	0.486	1.56%
Square	2	52.924	52.9241	26.4621	7.02	0.006	43.18%
IAL*IAL	1	42.349	22.8299	22.8299	6.05	0.025*	34.55%
B*B	1	10.575	10.5752	10.5752	2.80	0.112	8.63%
2-Way Interaction	3	2.491	2.4914	0.8305	0.22	0.881	2.03%
IAL*B	1	0.008	0.0083	0.0083	0.00	0.963	0.01%
IAL*W	1	0.347	0.3466	0.3466	0.09	0.765	0.28%
B*W	1	2.136	2.1364	2.1364	0.57	0.462	1.74%
Error	17	64.125	64.1245	3.7720			52.32%
Lack-of-Fit	9	16.090	16.0903	1.7878	0.30	0.955	13.13%
Pure Error	8	48.034	48.0343	6.0043			39.19%
Total	25	122.565					100.00%

* significant at the 5% level

Table 4.18: Regression equations and model summary for Sa.

Regression equations				
Topas	Sa = 160.3 - 15.71 IAL - 25.5 B + 2.033 IAL*IAL + 1.384 B*B - 0.032 IAL*B			
Compeed	Sa = 153.5 - 16.05 IAL - 24.6 B + 2.033 IAL*IAL + 1.384 B*B - 0.032 IAL*B			
Model summary				
S	**R-sq**	**R-sq(adj)**	**PRESS**	**R-sq(pred)**
1.94217	47.68%	23.06%	114.780	6.35%

The contour and surface plots relating to surface roughness for the Topas and Compeed wires are shown in Figure 4.53(a) and Figure 4.53(b) respectively. The highest values of roughness are represented by the dark blue areas in the contour plots, which also corresponded to conditions for high MRR outlined in the previous section. The workpiece surface roughness was typically higher when machining with the Topas wire.

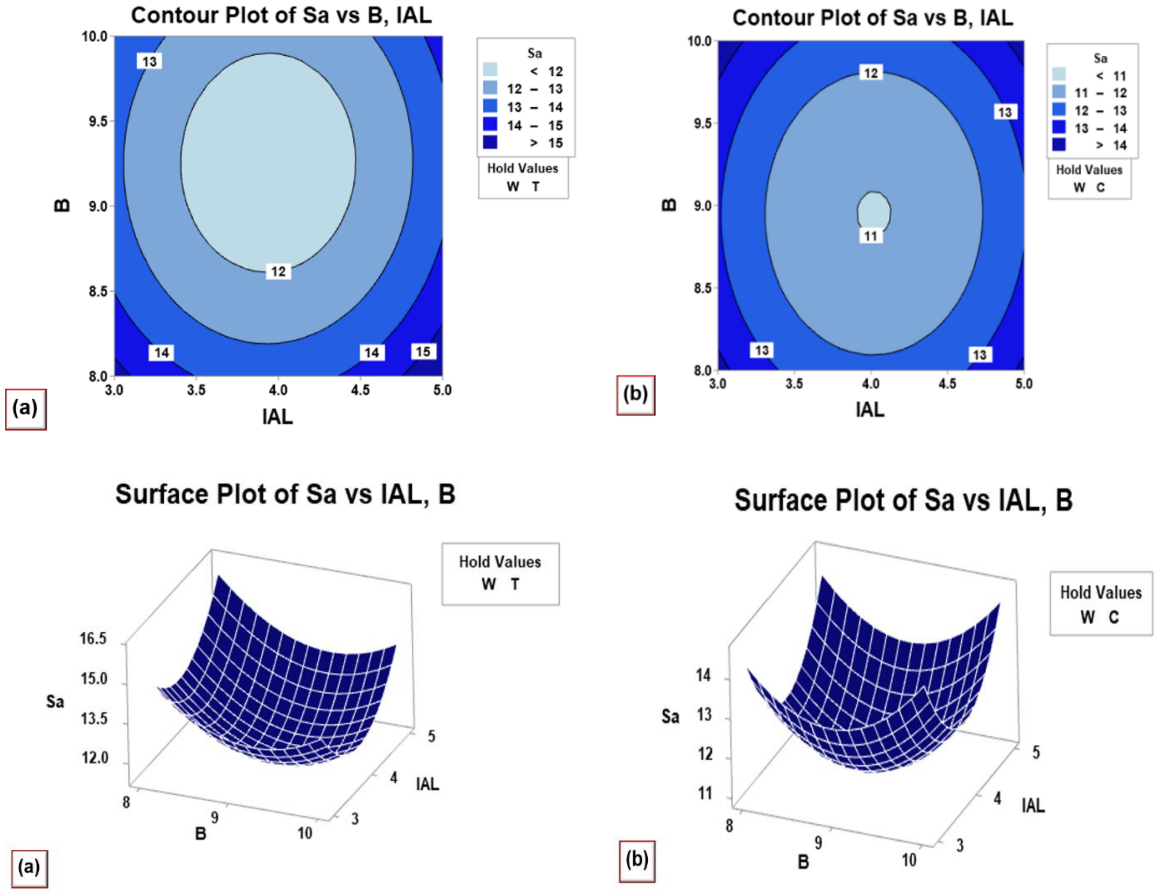


Figure 4.53: Contour and surface plots showing the influence of current and pulse off time on Sa for (a) Topas and (b) Compeed wires.

4.7.3 Surface integrity and damage

Figure 4.54 shows optical micrographs of the kerf machined using the Topas wire at different regions on the top and bottom surfaces of the CFRP workpiece from Test 2 (highest MRR). On the top surface of the workpiece, severe damage in terms of heavy delamination and large areas of uncut/frayed fibres were observed at the front section of the kerf leading to uneven edges, which also extended to the middle region of the slot. This was less apparent towards the back section of the kerf, although delamination was evident at the end of the slot, see Figure 4.54(c). The edge delamination and frayed fibres were possibly due to molten copper flowing on the top surface causing decomposition of the resin matrix leading to exposed fibres as well as pressure generated by vaporised gases. The front region of the kerf on the bottom surface of the workpiece similarly exhibited a significant amount of frayed fibres and delamination. However, unlike the top surface, the kerf damage at the middle region of the bottom surface mainly comprised irregular rounded edges with minor traces of broken fibres attached to the walls of the slot. At the end of the kerf, a V-shaped region of delamination/exposed fibres was observed as well as uneven kerf edges. The considerable damage on the CFRP surfaces were likely due to the increased discharge intensity and temperatures at machining gap as a result of the higher electrical conductivity of the CFRP/Cu stack arrangement.

The top and bottom surfaces of the kerf machined using the Compeed wire at conditions of highest MRR was also evaluated; see Figure 4.55. The results showed even greater damage was produced particularly on the top surface of the workpiece, with adhered re-solidified copper together with significant delamination and bundles of frayed/uncut fibres observed in all regions of the kerf edge. While traces of re-deposited copper was found in certain areas on the bottom surface, there was considerably less delamination and frayed fibres except towards the end section of the kerf as shown in Figure 4.55(c). Corresponding SEM micrographs of the machined surfaces from tests relating to the lowest (Test 12), median (Test 4) and highest (Test 2) MRR produced using the Topas wire are shown in Figure 4.56. Despite the relatively low MRR of 2.89 mm^3/min, damage in terms of adhered fibres/resin debris, recast layer with voids and swollen/eroded fibre ends were present as shown Figure 4.56(a). At the test with intermediate MRR (3.77 mm^3/min), accumulation of resin at the fibre ends increased together with the area covered with re-solidified material, while resin residue was found adhering to the fibres as shown in Figure 4.56(b). The surface produced in Test 2 (highest MRR) was

extensively covered with recast layer/re-solidified material containing of a large number of cavities/voids as well as broken fibre fragments as illustrated in Figure 4.56(c).

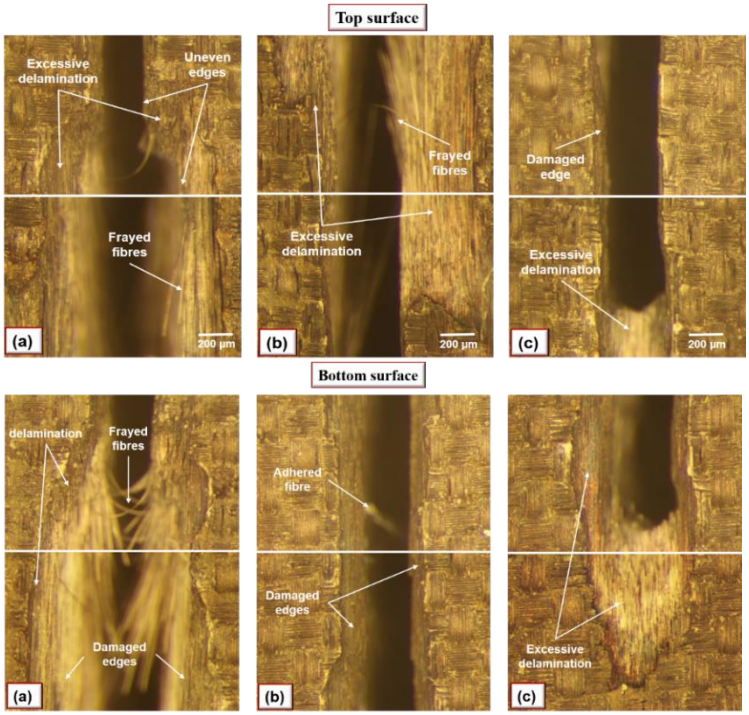


Figure 4.54: Optical micrographs of the top and bottom surfaces of the CFRP machined using Topas wire in Test 2 (highest MRR) at (a) front, (b) middle and (c) end kerf regions.

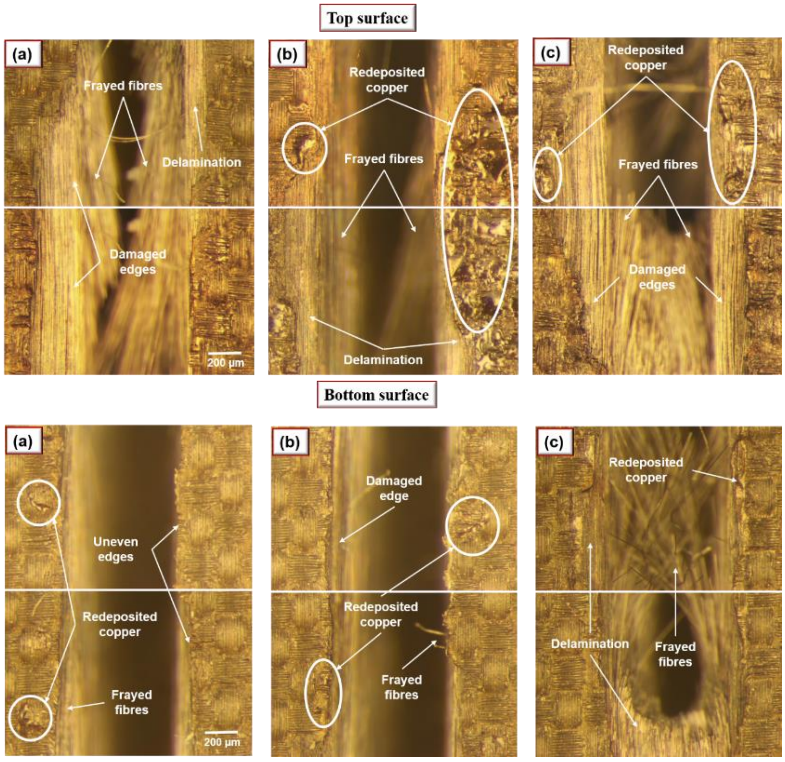


Figure 4.55: Optical micrographs of the top and bottom surfaces of the CFRP machined using Compeed wire in Test 2 (highest MRR) at (a) front, (b) middle and (c) end kerf regions.

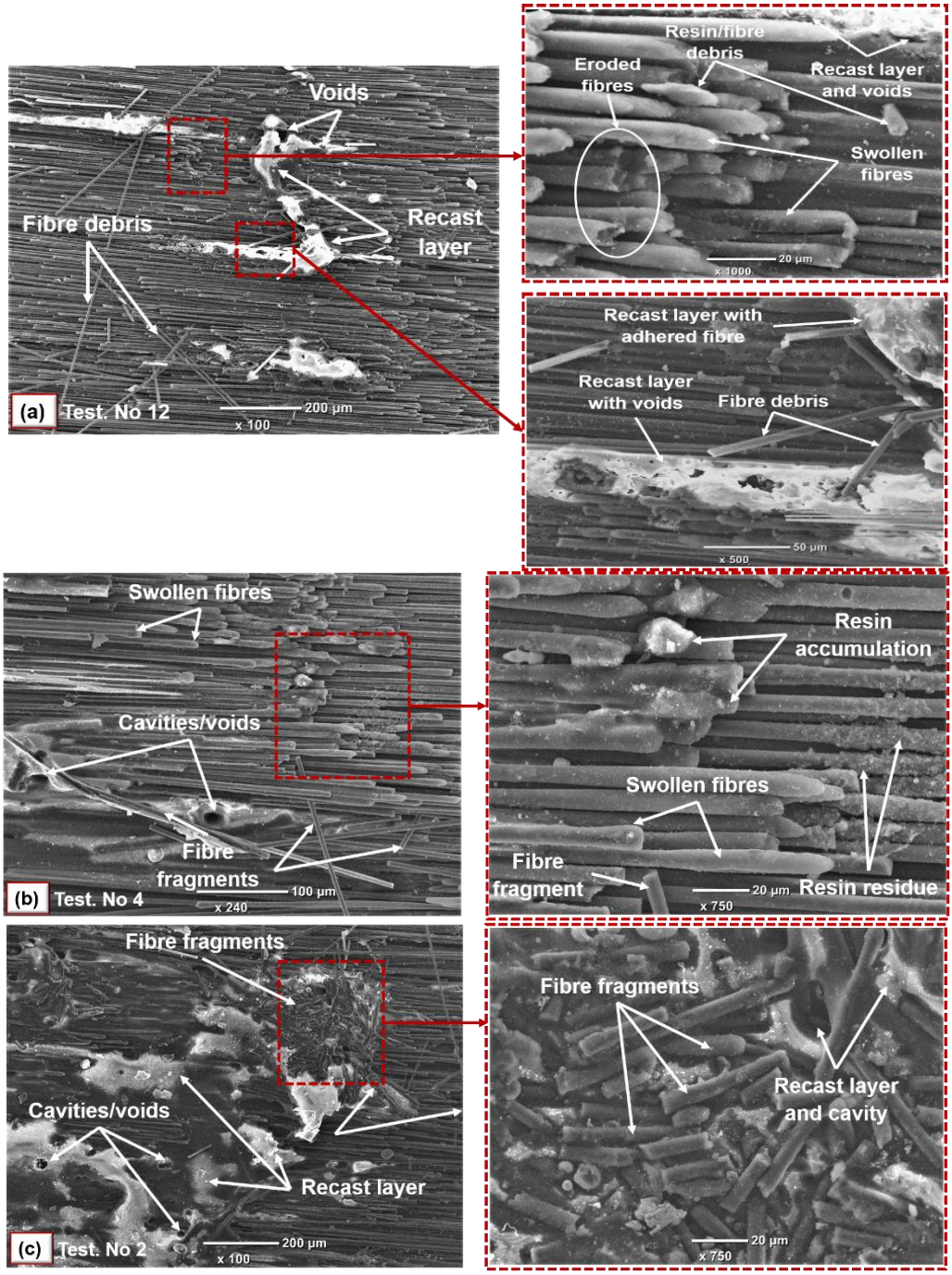


Figure 4.56: Sample SEM micrographs of machined surfaces using Topas wire in (a) Test 12 - lowest MRR, (b) Test 4 - median MRR and (c) Test 2 - highest MRR.

Similar SEM analysis was performed on surfaces machined by the Compeed wire corresponding to tests producing the lowest, intermediate and highest MRR levels, see Figure 4.57. In general, the machined surface integrity/quality deteriorated with increasing MRR, with the degree of re-solidified material, broken/swollen fibres and cavities/voids/cracks becoming progressively more severe.

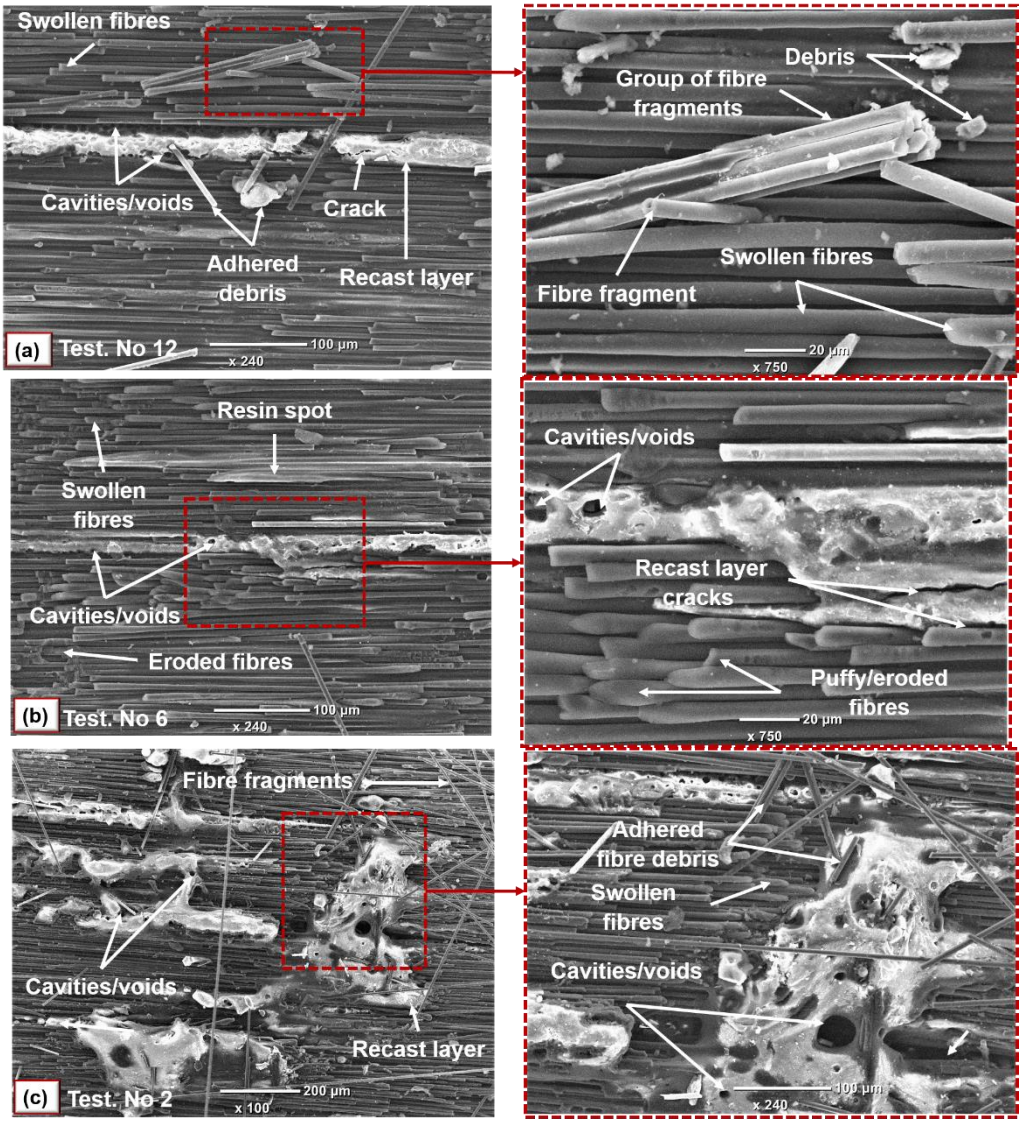


Figure 4.57: Sample SEM micrographs of machined surfaces in using Compeed wire in (a) Test 12 – lowest MRR, (b) Test 6 - median MRR and (c) Test 2 - highest MRR.

4.7.4 Confirmation tests

Based on the desirability function and multiple response optimisation, it was found that the intermediate level of current (4 A), low level of pulse off time (8 µs) and Topas wire are recommended for minimising surface roughness while maximising MRR, see Figure 4.58. The optimal points are represented by the intersection between the red lines and mean values of the respective output measures (Sa and MRR). Table 4.19 details the mean values of the MRR and Sa from the confirmation test compared to the corresponding predicted results. The relative error between the experimental and predicted results were less than 10% for both responses, indicating the accuracy of the optimisation model.

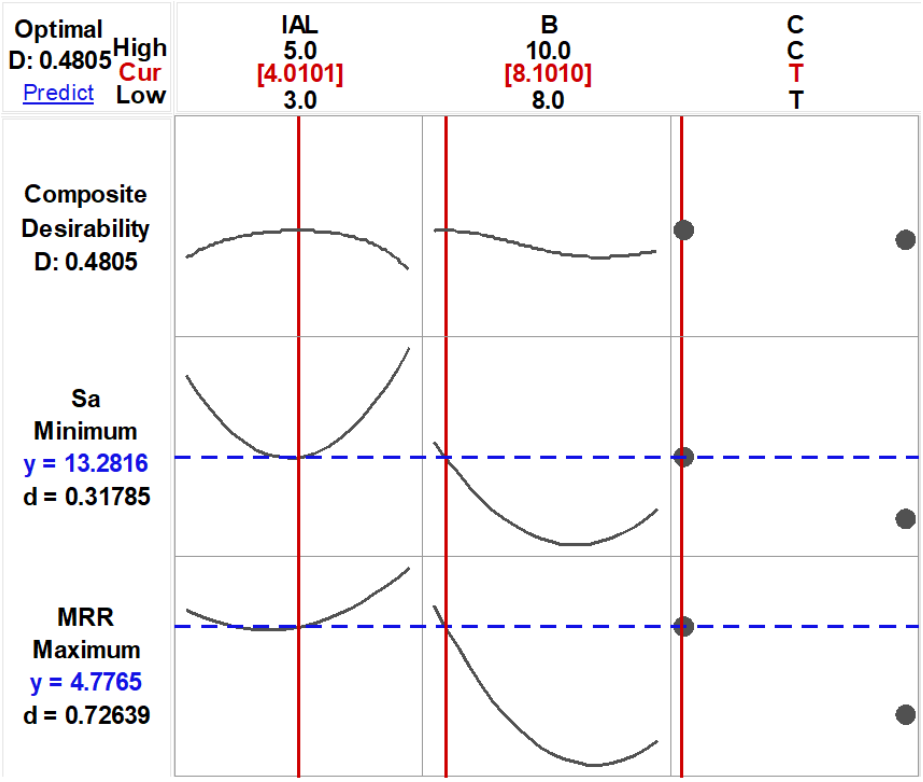


Figure 4.58: Optimisation plot of performance measurements.

Table 4.19: Confirmation tests for MRR and Sa.

Response	Mean		Error %
	Predicted	Experimental	
MRR (mm^3/min)	4.78	4.97	3.82
Sa (µm)	13.28	14.46	8.16

Optical micrographs of the machined kerf from the confirmation test based on the optimisation criteria revealed lower damage in terms of delamination compared to Test 2, which was likely attributed to the marginally lower MRR obtained, see Figure 4.59. However, uneven/irregular kerf edges were observed on the top surface as well as signs of frayed fibres, while a V-shaped delamination area was evident at the end of the kerf on the bottom surface together with frayed fibres stuck on the kerf edges. Figure 4.60 shows SEM micrographs of the machined surface from the confirmation test. It shows that the surface was almost entirely covered by re-solidified material with long cracks and deep valleys as well as fibre fragments.

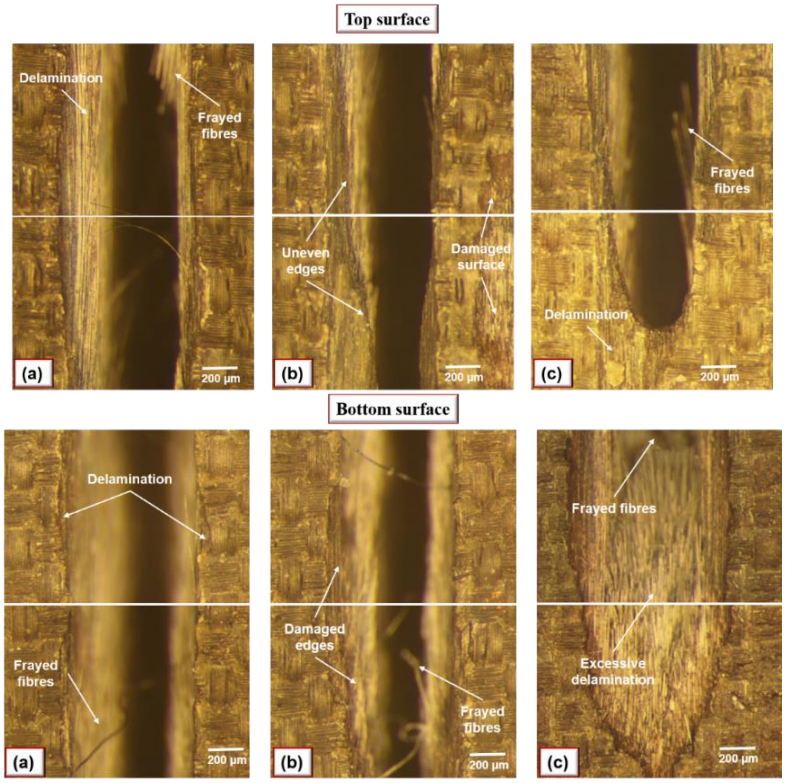


Figure 4.59: Optical micrographs for different regions on the top/bottom surfaces gained at confirmation test (a) front, (b) middle and (c) end kerf regions.

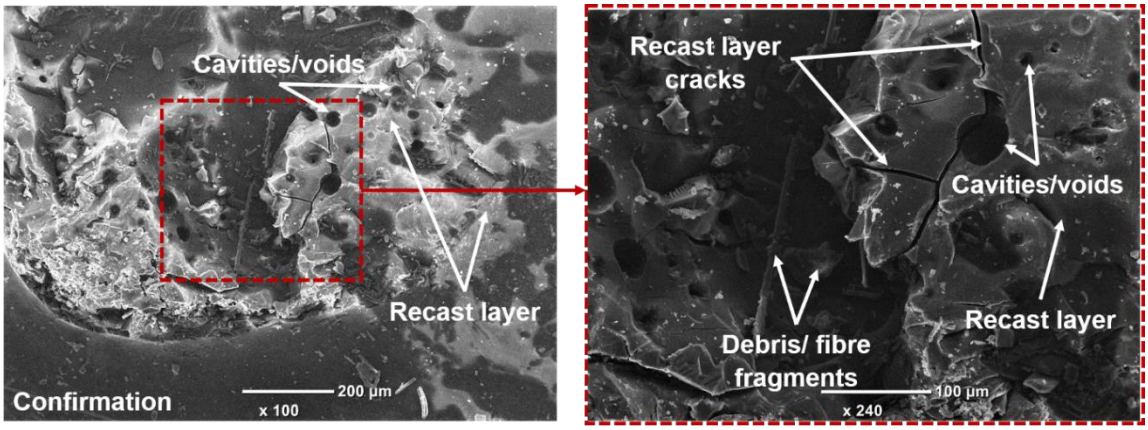


Figure 4.60: Sample SEM micrographs of machined surfaces in confirmation test using Topas wire.

Energy dispersive X-ray spectroscopy (EDS) evaluation was conducted to identify the elemental composition of the recast layer/re-solidified material observed on machined surfaces. Results from the analysis found that the key elements comprised carbon, oxygen and sulphur, which are the major constituents of resin material, with oxygen showing the highest atomic percentage followed by carbon as detailed in Table 4.20. Only minute traces of copper/zinc was detected (0.56% atomic percentage), which suggests that the wire material was not re-deposited

on the machined workpiece surfaces. Figure 4.61 shows the EDS spectra of the re-solidified material in the confirmation test.

Table 4.20: Elemental composition of recast/re-solidified material.

Element	(keV)	Mass%	Sigma	Atom%
C K	0.277	30.36	0.11	38.56
O K	0.525	59.24	1.84	56.49
S K	2.307	10.40	0.33	4.95
Total		100.00		100.00

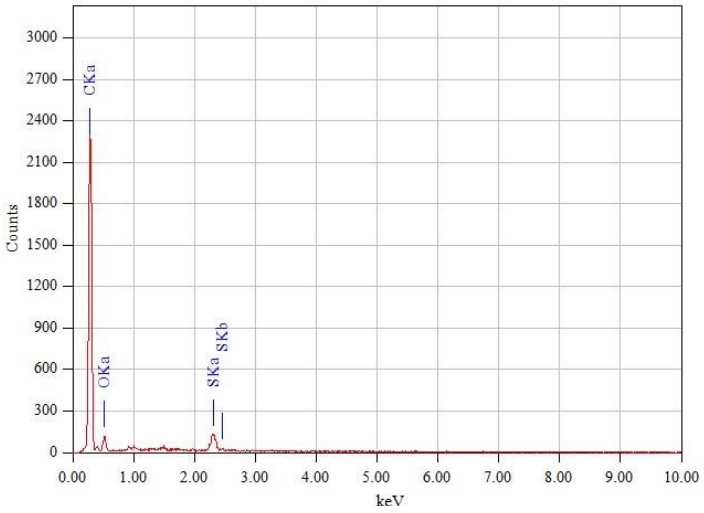


Figure 4.61: EDS spectra of the re-solidified layer in the confirmation test.

4.8 Phase 3C: Influence of wire electrode material and operating conditions on cutting performance of multidirectional CFRP laminates

4.8.1 Material removal rate

Figure 4.62 shows the effect of varying current and pulse off time on MRR when cutting multidirectional CFRP using Topas and Compeed wires. Considerably higher machining rates of up to 14.82 mm^3/min and 13.31 mm^3/min were observed for the Topas and Compeed wires respectively, compared to results when cutting unidirectional CFRP composites. This was mainly attributed to the lower electrical resistivity (ranging between ~34 and 92%) of the multidirectional CFRP workpieces, see Appendix C. In all of the tests, the MRR achieved by Topas wire was ~11% higher than the Compeed wire. The main effects plot in Figure 4.63 showed that MRR was higher with increasing current and lower pulse off time. Despite a higher conductivity, the lower MRR obtained when employing the Compeed wire possibly due to the increased debris generated by the more intense discharges, which resulted in greater instability in the spark gap.

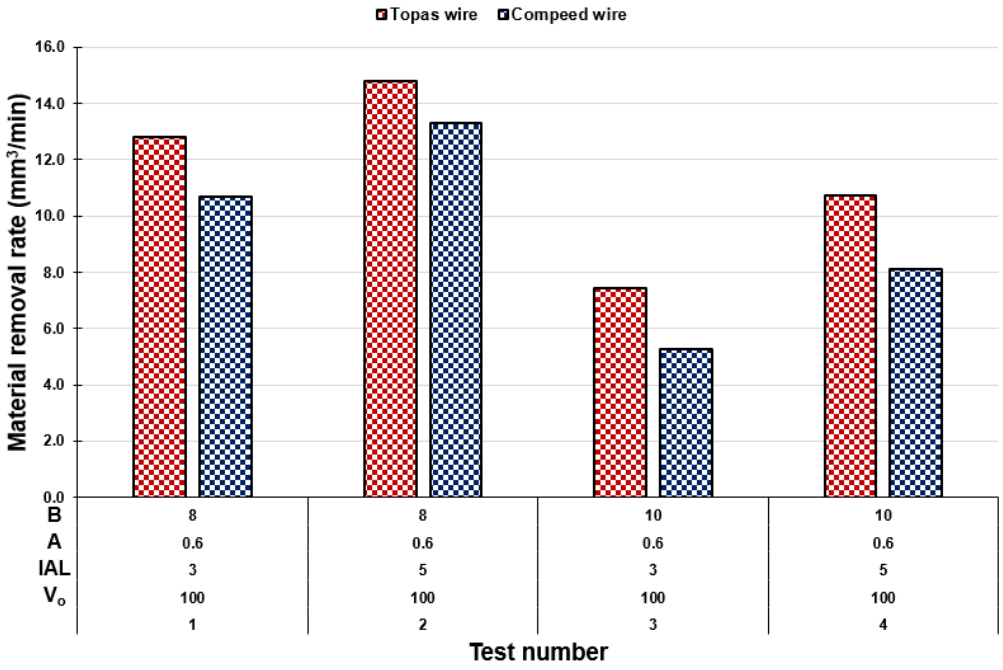


Figure 4.62: Material removal rate when machining multidirectional CFRP using Topas and Compeed wires.

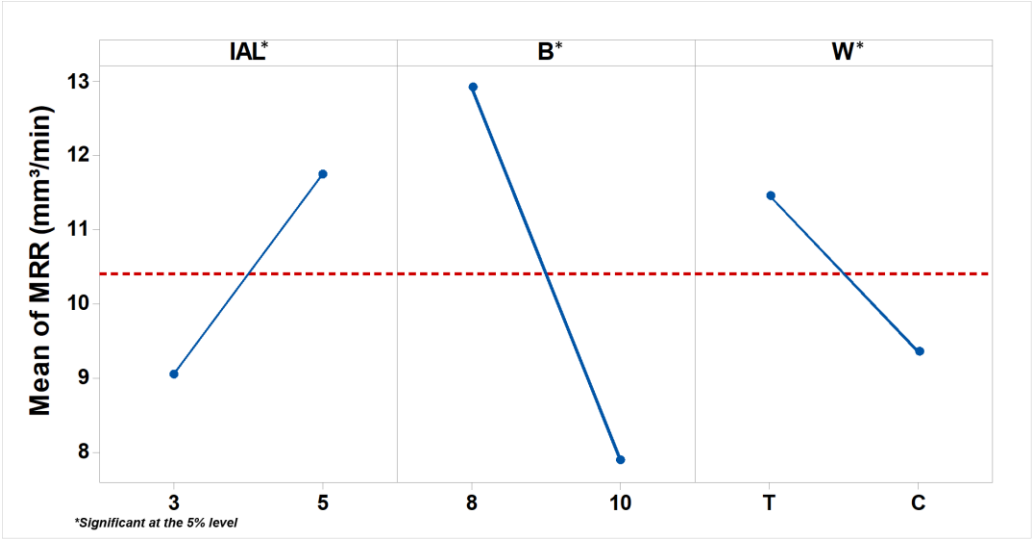


Figure 4.63: Main effects plot for MRR following machining of multidirectional CFRP.

According to the analysis of variance, all of the factors were significant at the 5% level with respect to MRR, but with pulse off time having the strongest influence with a PCR of 67.76%, see Table 4.21. The model showed good agreement with the fitted the data based on the coefficient of determination (R^2) of 99.17%. Additionally, the similarly high R^2adj (98.55%) indicated that the model likely included all the relevant terms for good correlation between the responses and machining variables.

Table 4.21: ANOVA for MRR following machining of multidirectional CFRP.

Source	DF	Seq SS	Adj SS	Adj MS	F-Value	P-Value	PCR
Model	3	73.5970	73.5970	24.5323	160.13	0.000	99.17%
Linear	3	73.5970	73.5970	24.5323	160.13	0.000	99.17%
IAL	1	14.5094	14.5094	14.5094	94.71	0.001*	19.55%
B	1	50.2810	50.2810	50.2810	328.19	0.000*	67.76%
W	1	8.8065	8.8065	8.8065	57.48	0.002*	11.87%
Error	4	0.6128	0.6128	0.1532			0.83%
Total	7	74.2098					100.00%
Model equation	MRR=27.58+1.347 IAL - 2.507 B - 1.049 W						
Model summary							
S	**R-sq**	**R-sq (adj)**	**PRESS**	**R-sq (pred)**			
0.391415	99.17%	98.55%	2.45129	96.70%			

* significant at the 5% level

By considering interactions between parameters in the ANOVA, a marginal improvement in R^2 to 99.79% but with no change in the R^2adj and pulse off time being the sole significant factor as shown in Table 4.22. The full matrix of interactions in Figure 4.64 revealed no intersections between any of the individual factors thus confirming none of the interactions were significant with regard to MRR.

Table 4.22: ANOVA for MRR including interactions following machining of multidirectional CFRP.

Source	DF	Seq SS	Adj SS	Adj MS	F-Value	P-Value	PCR
Model	6	74.0556	74.0556	12.3426	80.07	0.085	99.79%
Linear	3	73.5970	73.5970	24.5323	159.15	0.058	99.17%
IAL	1	14.5094	14.5094	14.5094	94.13	0.065	19.55%
B	1	50.2810	50.2810	50.2810	326.19	0.035*	67.76%
W	1	8.8065	8.8065	8.8065	57.13	0.084	11.87%
2-Way Interactions	3	0.4587	0.4587	0.1529	0.99	0.611	0.62%
IAL*B	1	0.2877	0.2877	0.2877	1.87	0.402	0.39%
IAL*W	1	0.0010	0.0010	0.0010	0.01	0.949	0.00%
B*W	1	0.1700	0.1700	0.1700	1.10	0.484	0.23%
Error	1	0.1541	0.1541	0.1541			0.21%
Total	7	74.2098					100.00%
Model equation	MRR = 34.40 - 0.36 IAL - 3.266 B + 0.22 W + 0.190 IAL*B + 0.011 IAL*W - 0.146 B*W						
Model summary							
S	**R-sq**	**R-sq (adj)**	**PRESS**	**R-sq (pred)**			
0.392615	99.79%	98.55%	9.86536	86.71%			

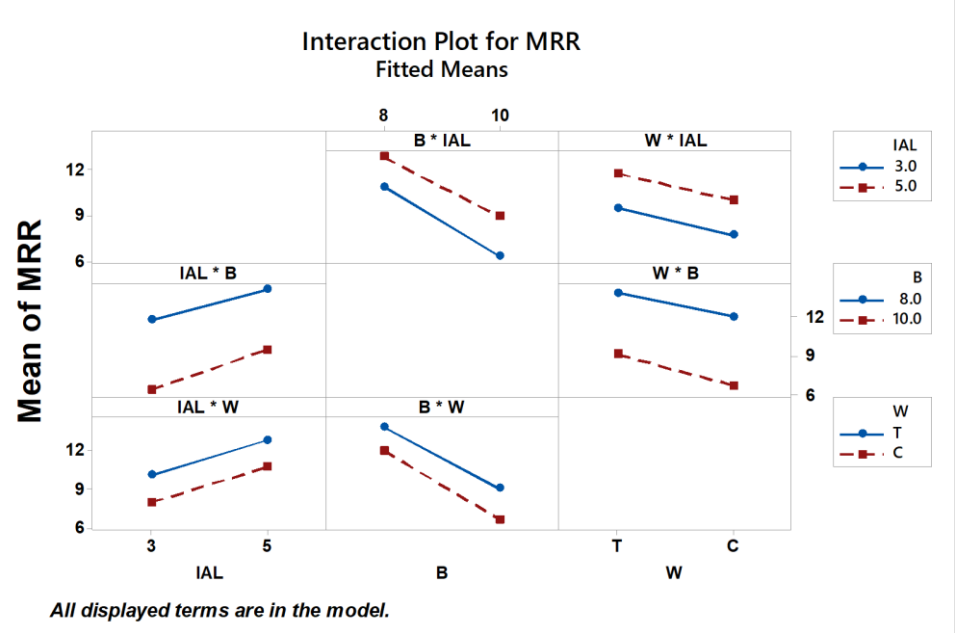


Figure 4.64: Interaction plot matrix for MRR following machining of multidirectional CFRP.

4.8.2 Kerf width

Figure 4.65 displays the average kerf widths (Wa) obtained in each of the tests for both wire electrodes. The kerf widths varied between ~333 to ~347 µm when using the Topas wire and from ~334 up to 374 µm for the Compeed wire. When machining at the low pulse off time level, the kerfs were somewhat wider when using the Compeed wire, which also corresponded to conditions for higher MRR, most likely caused by the greater discharge energies. The main effects plot in Figure 4.66 indicated that Wa typically increased when employing higher current, lower pulse off time and the Compeed wire. Increasing pulse off time generally raises the cooling/flushing time whilst reducing the sparking/machining period, resulting in a narrower kerf.

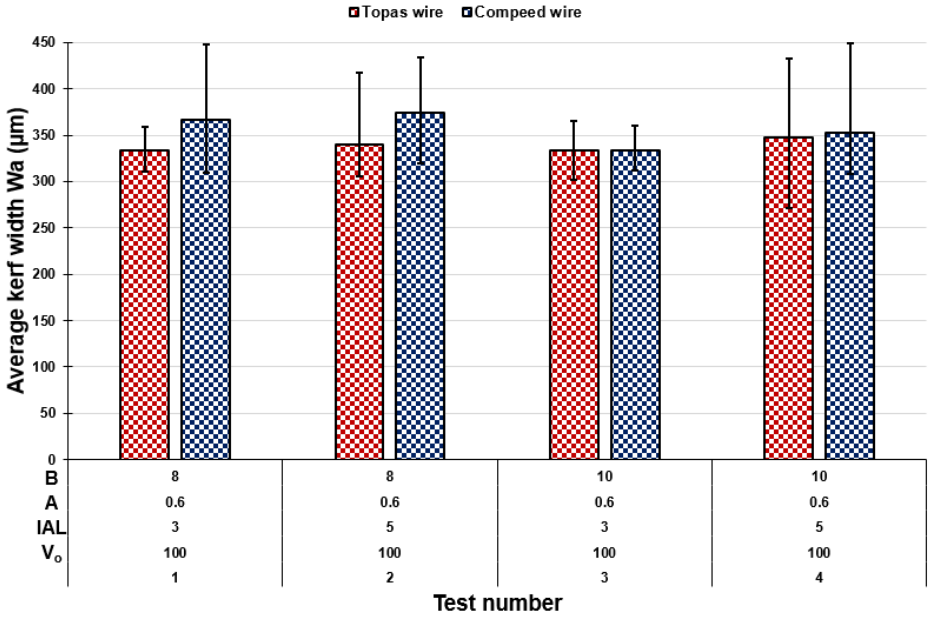


Figure 4.65: Average kerf width following machining of multidirectional CFRP with Topas and Compeed wire electrodes.

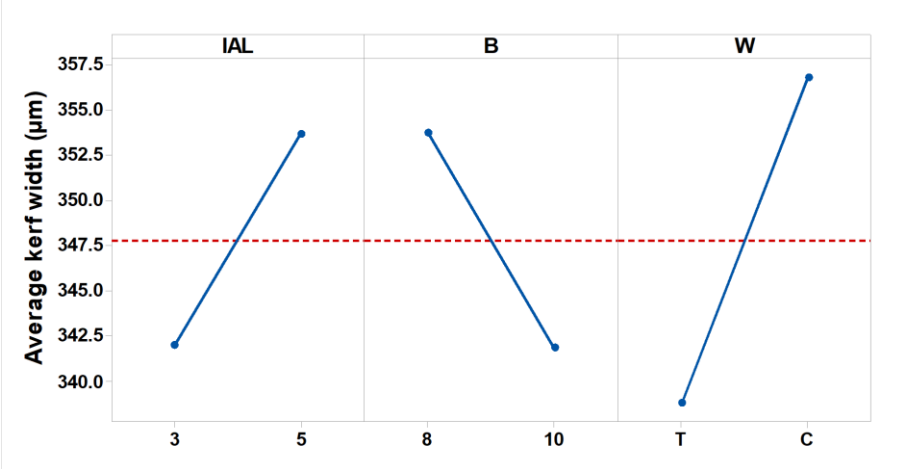


Figure 4.66: Main effects plot for average kerf width following machining of multidirectional CFRP.

According to the ANOVA, none of the parameters had a significant effect on Wa, however the wire electrode showed the highest PCR of 37.69% followed by pulse off time and current as detailed in Table 4.23. Based on the R^2 value of 70.18%, the linear regression model provided moderate agreement with the experimental data, while the relatively low R^2adj of 47.81% suggests that the model had not considered all relevant factors. By including the effect of interactions in the ANOVA, it was observed that the model R^2 and R^2adj values increased considerably to 99.88% and 99.14% respectively, as outlined in Table 4.24. Here, the wire type and the interaction between pulse off time and wire type were found to be statistically significant factors affecting the average kerf width. The interaction between wire type and pulse off time was further illustrated by the interaction plot in Figure 4.67.

Table 4.23: ANOVA for average kerf width considering linear factors.

Source	DF	Seq SS	Adj SS	Adj MS	F-Value	P-Value	PCR
Model	3	1195.8	1195.8	398.6	3.14	0.149	70.18%
Linear	3	1195.8	1195.8	398.6	3.14	0.149	70.18%
IAL	1	272.4	272.4	272.4	2.14	0.217	15.99%
B	1	281.1	281.1	281.1	2.21	0.211	16.50%
W	1	642.2	642.2	642.2	5.06	0.088	37.69%
Error	4	508.2	508.2	127.0			29.82%
Total	7	1704.0					100.00%
Model equation	Wa= 377.8 + 5.84 IAL - 5.93 B + 8.96 W						
Model summary							
S	**R-sq**	**R-sq(adj)**	**PRESS**	**R-sq(pred)**			
11.2714	70.18%	47.81%	2032.70	0.00%			

Table 4.24: ANOVA for average kerf width including interactions.

Source	DF	Seq SS	Adj SS	Adj MS	F-Value	P-Value	PCR
Model	6	1701.86	1701.86	283.643	135.34	0.066	99.88%
Linear	3	1195.78	1195.78	398.592	190.19	0.053	70.18%
IAL	1	272.42	272.42	272.422	129.99	0.056	15.99%
B	1	281.11	281.11	281.111	134.13	0.055	16.50%
W	1	642.24	642.24	642.244	306.45	0.036*	37.69%
2-Way Interactions	3	506.08	506.08	168.693	80.49	0.082	29.70%
IAL*B	1	34.33	34.33	34.332	16.38	0.154	2.01%
IAL*W	1	5.08	5.08	5.084	2.43	0.363	0.30%
B*W	1	466.66	466.66	466.664	222.67	0.043*	27.39%
Error	1	2.10	2.10	2.096			0.12%
Total	7	1703.95					100.00%
Model equation	Wa = 452.4 - 12.81 IAL - 14.21 B + 74.51 W + 2.072 IAL*B + 0.797 IAL*W - 7.638 B*W						
Model summary							
S	**R-sq**	**R-sq(adj)**	**PRESS**	**R-sq(pred)**			
1.44767	99.88%	99.14%	134.129	92.13%			

* significant at the 5% level

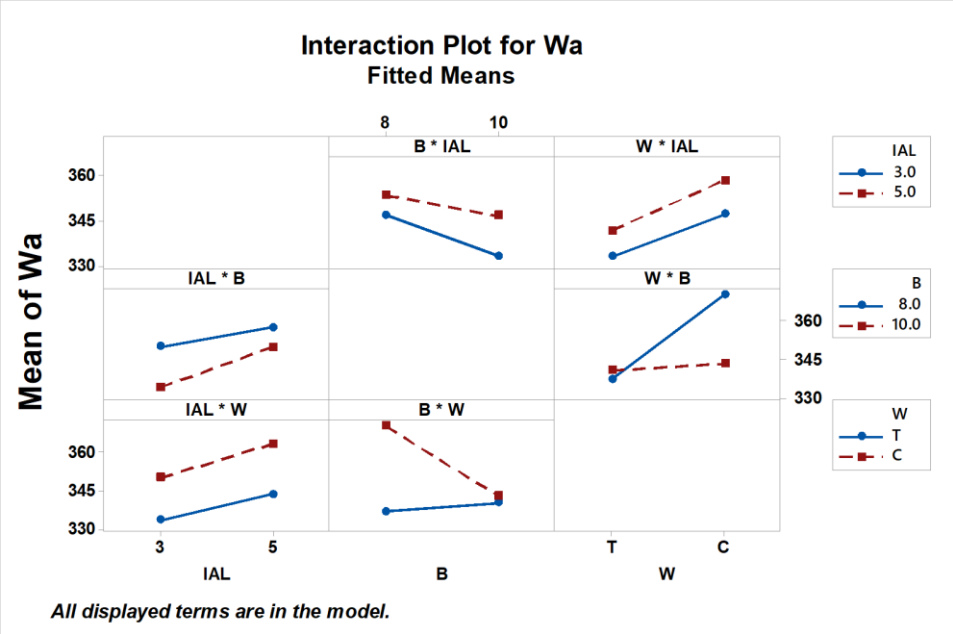


Figure 4.67: Interaction matrix plot for average kerf width.

4.8.3 Surface roughness

The areal roughness results showed similar trends to the average kerf width (Wa) as shown in Figure 4.68, where the Compeed wire produced rougher surfaces compared to the Topas wire, with the exception of Test 3, possibly due to variation in spark stability. The higher surface roughness obtained when machining with the Compeed wire was attributed to the increased energy/heat generated in the machining gap, which produced deeper craters and considerable adhered debris on the surface, see Figure 4.69. For more details of the roughness measurements, see Appendix E. Similarly, the main effects plot in Figure 4.70 for areal roughness showed that high current and low pulse off time levels together with the Compeed wire led to rougher surfaces. However, the associated ANOVA indicated that none of variables had a significant influence on surface roughness, although the ignition current showed a moderately high PCR of 41.62%, see Table 4.25.

.

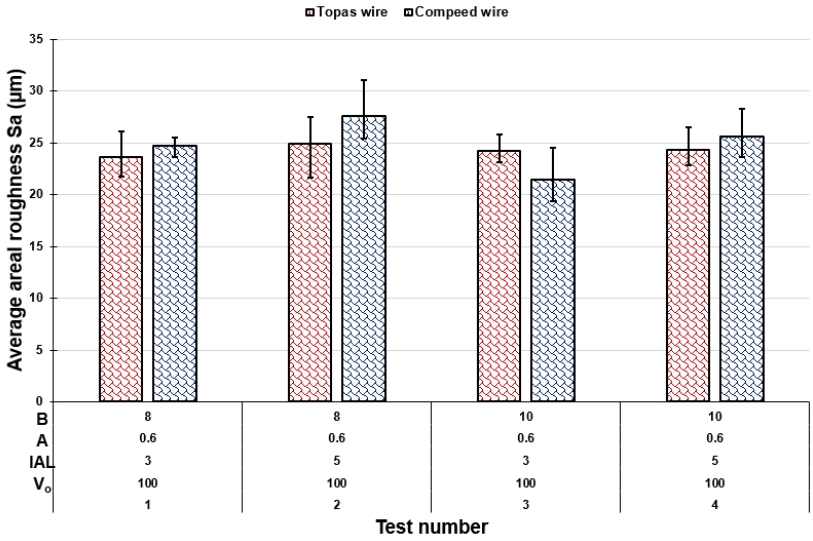


Figure 4.68: Average areal surface roughness following machining of multidirectional CFRP using Topas and Compeed wire electrodes.

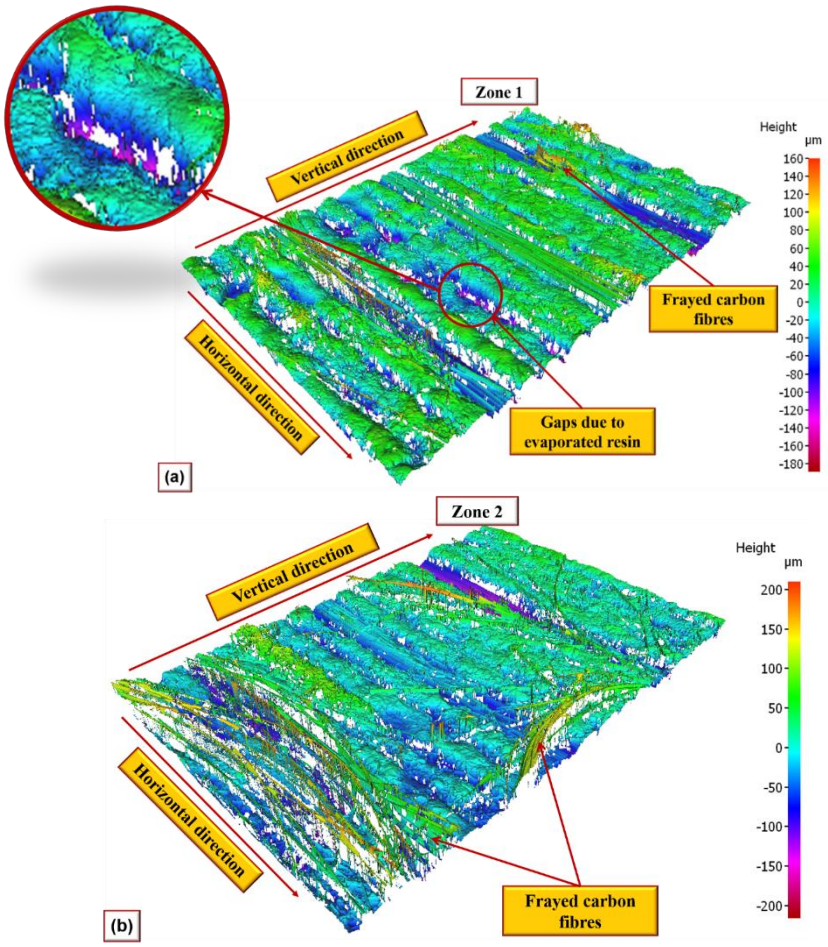


Figure 4.69: Surface topographical map of machined workpiece from Test 2 (highest Sa / MRR) (a) Topas and (b) Compeed.

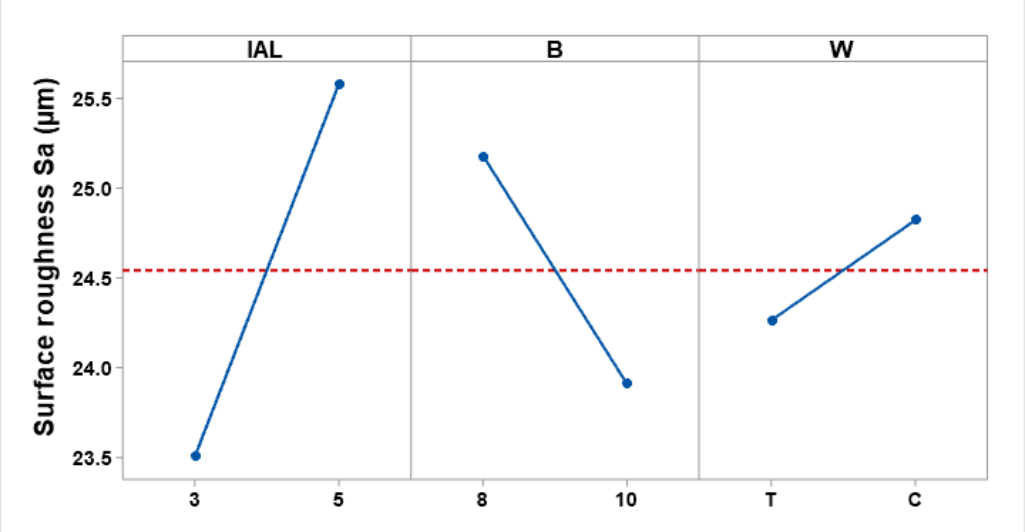


Figure 4.70: Main effects plot for average surface roughness.

Table 4.25: ANOVA for average areal roughness.

Source	DF	Seq SS	Adj SS	Adj MS	F-Value	P-Value	PCR
Model	3	12.4798	12.4798	4.1599	2.01	0.255	60.09%
Linear	3	12.4798	12.4798	4.1599	2.01	0.255	60.09%
IAL	1	8.6433	8.6433	8.6433	4.17	0.111	41.62%
B	1	3.2123	3.2123	3.2123	1.55	0.281	15.47%
W	1	0.6242	0.6242	0.6242	0.30	0.612	3.01%
Error	4	8.2881	8.2881	2.0720			39.91%
Total	7	20.7679					100.00%
Model Equation	Sa= 26.09+ 1.039 IAL – 0.634 B + 0.279 W						
Model summary							
S	**R-sq**	**R-sq(adj)**	**PRESS**	**R-sq(pred)**			
1.43945	60.09%	30.16%	33.1524	0.00%			

According to the model summary, the linear model was inadequate based on the R^2adj of 30.16%, in addition to relatively poor data correlation with a R^2 of 60%. By considering interactions in the model, the R^2 increased considerably to 96.24%, indicating good data correlation and a higher R^2adj of 73.96%, although none of the factors or interactions were statistically significant according to the ANOVA in Table 4.26. Despite this, the interaction plot in Figure 4.71 revealed that interactions were present between wire type and current as well as pulse off time.

Table 4.26: ANOVA for average areal roughness including interactions.

Source	DF	Seq SS	Adj SS	Adj MS	F-Value	P-Value	PCR
Model	6	19.9873	19.9873	3.33121	4.27	0.355	96.24%
Linear	3	12.4798	12.4798	4.15992	5.33	0.306	60.09%
IAL	1	8.6433	8.6433	8.64330	11.07	0.186	41.62%
B	1	3.2123	3.2123	3.21231	4.12	0.292	15.47%
W	1	0.6242	0.6242	0.62416	0.80	0.536	3.01%
2-Way Interactions	3	7.5075	7.5075	2.50250	3.21	0.385	36.15%
IAL*B	1	0.0039	0.0039	0.00389	0.00	0.955	0.02%
IAL*W	1	4.0162	4.0162	4.01620	5.14	0.264	19.34%
B*W	1	3.4874	3.4874	3.48740	4.47	0.281	16.79%
Error	1	0.7806	0.7806	0.78060			3.76%
Total	7	20.7679					100.00%

Model equation	Sa = 26.9 + 0.84 IAL - 0.72 B + 3.39 W + 0.022 IAL*B + 0.709 IAL*W - 0.660 B*W

Model summary

S	R-sq	R-sq(adj)	PRESS	R-sq(pred)
0.883518	96.24%	73.69%	49.9587	0.00%

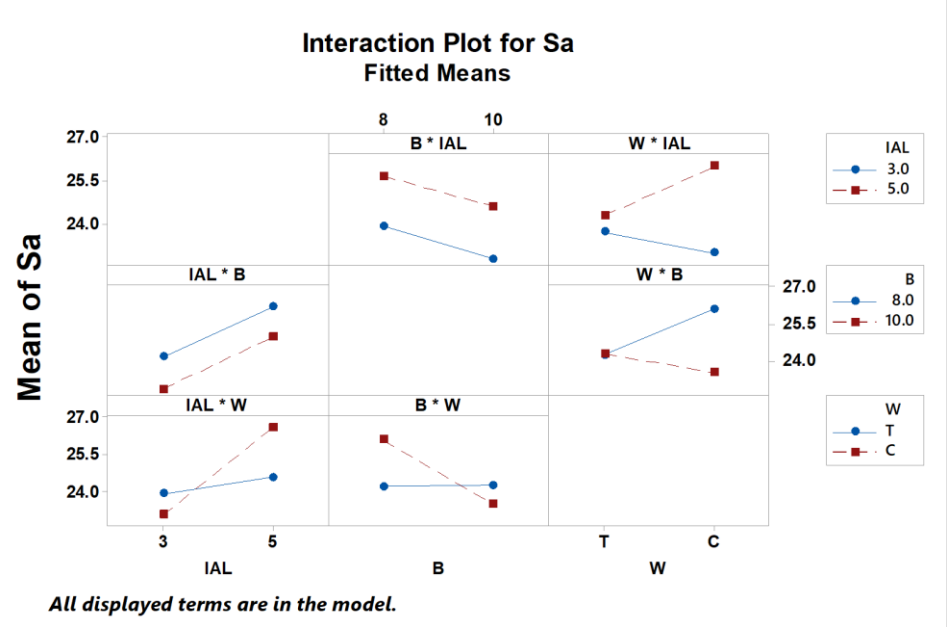


Figure 4.71: Interaction matrix plot for average areal surface roughness.

4.8.4 Surface integrity

Figure 4.72 shows optical micrographs of the kerf on the top and bottom surfaces machined using the Topas wire in Test 2 (highest MRR). The top surface exhibited severe delamination along the kerf edges and at the end of the cut, see Figure 4.72(a). The kerf edges were

irregular/uneven with evidence of adhered debris/contaminants on the surface, with similar damage also found on the bottom surface, albeit to a lesser degree, as shown in Figure 4.72(b). The kerf machined using the Compeed wire at equivalent process parameters also exhibited heavy delamination along the length of kerf edges together with the presence of frayed fibres and bronze coloured debris attached on both the top and bottom surfaces of the workpiece as detailed in Figure 4.73. The damage on the machined kerfs were generally greater in tests using the Compeed wire, probably due to the increased discharge intensity as a result of the higher wire conductivity. Furthermore, the delamination factor of the kerfs machined with the Compeed wire was up to 2.94 as opposed to a maximum of 2.5 when using the Topas wire.

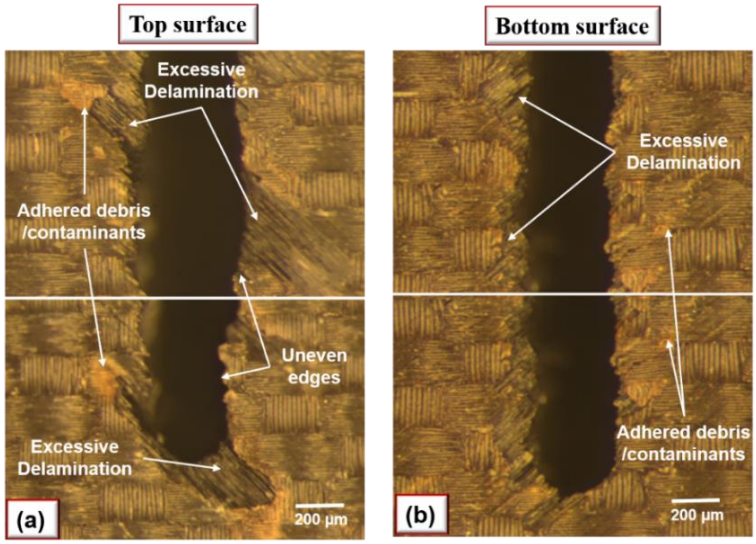


Figure 4.72: Optical micrographs showing the machined kerf in Test 2 (highest MRR) using Topas wire at the (a) top and (b) bottom surface.

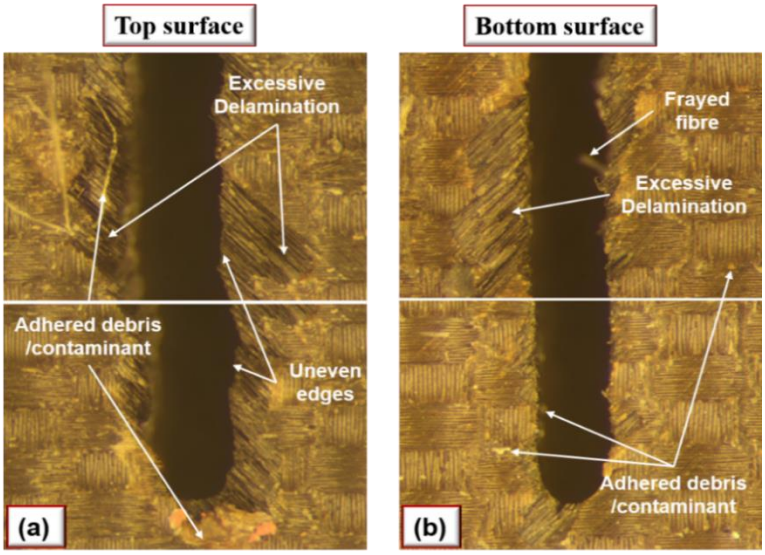


Figure 4.73: Optical micrographs showing the machined kerf in Test 2 (highest MRR) using Compeed wire at the (a) top and (b) bottom surface.

Figure 4.74(a) shows SEM micrographs of the surface machined using the Topas wire from the test with the lowest MRR (7.42 mm^3/min). In addition to significant areas with voids due to fibre/matrix loss, the surface was covered with fragments of broken fibre at different ply orientations together with accumulated re-solidified resin at fibre ends. Conversely, long fibres were predominant in the test achieving the highest MRR (14.82 mm^3/min), together with large cavities and re-solidified resin dispersed over the machined surface. In addition, resin particles were seen on the ends of some fibres at the 45°/135° ply orientation as shown in Figure 4.74(b).

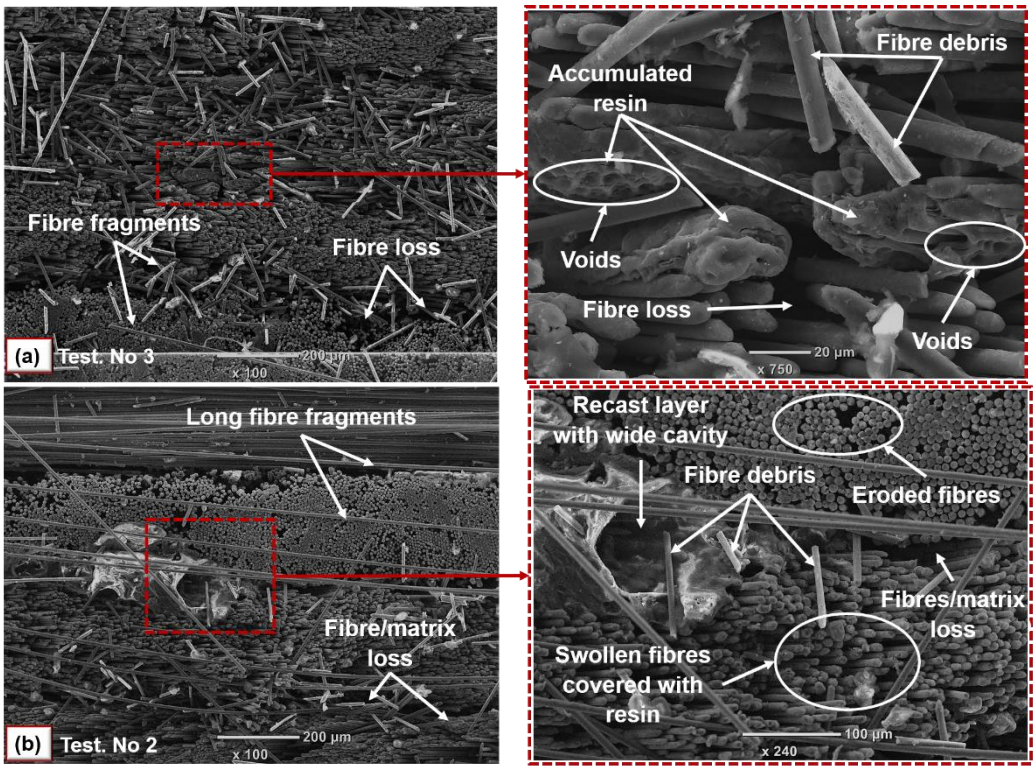


Figure 4.74: Sample SEM micrographs of machined surfaces using Topas wire in (a) Test 3 – lowest MRR and (b) Test 2 – highest MRR.

The damage on the surface machined with the Compeed wire at the lowest MRR comprised substantial matrix/fibre loss particularly at the region between plies as well as fibre fragments and bulk re-solidified resin over the swollen ends of fibres, see Figure 4.75(a). The surface condition further deteriorated in tests achieving higher MRR, with larger zones of accumulated re-solidified material as shown in Figure 4.75(b).

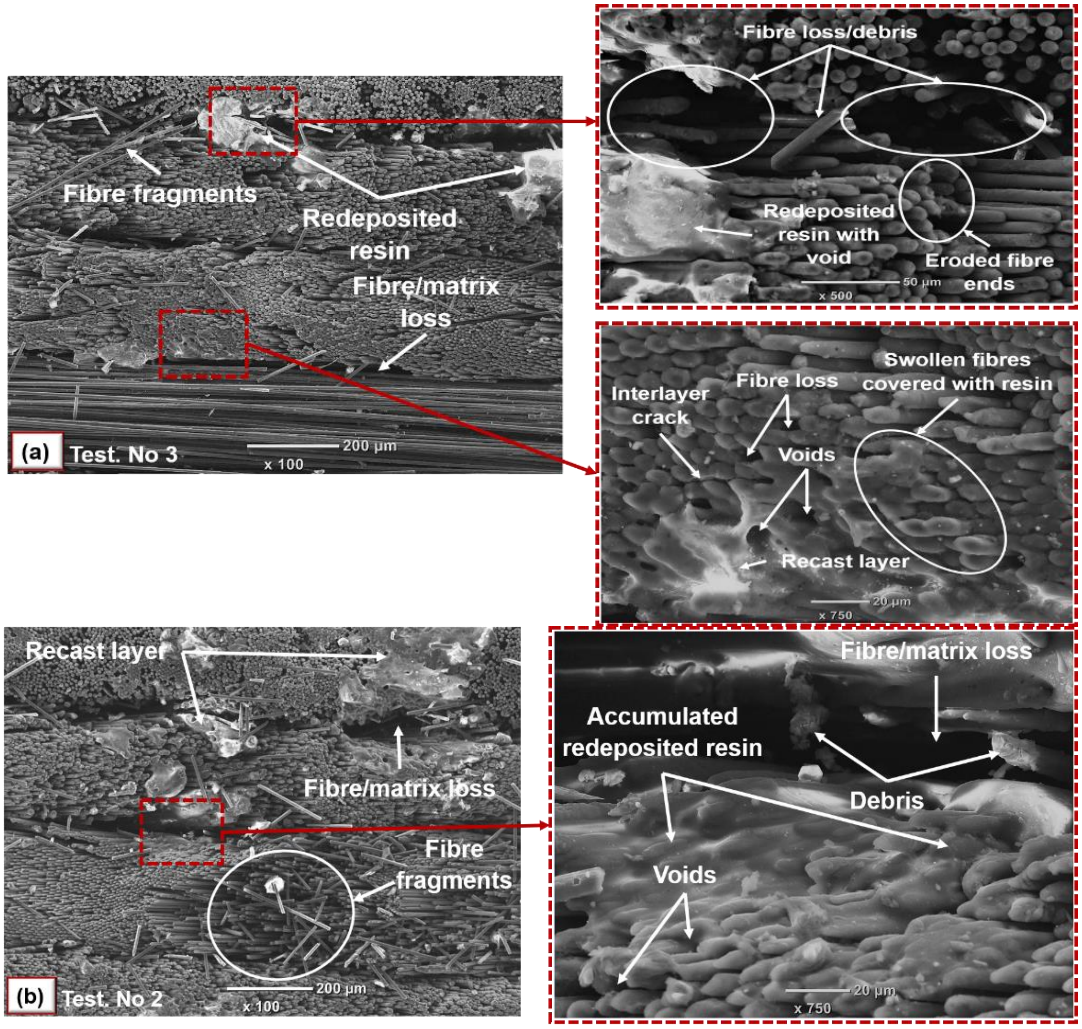


Figure 4.75: Sample SEM micrographs of machined surfaces using Compeed wire in (a) Test 3 – lowest MRR and (b) Test 2 – highest MRR.

4.9 Summary

When cutting UD-CFRP workpieces, it was observed that machining parallel to fibre orientation revealed higher MRR, Wa and Sa compared to results when cutting perpendicular to the fibre direction, particularly when utilising the Compeed wire, see Figure 4.76. However, severe damage in terms of delamination was observed when cutting perpendicular to fibre orientation due to fibre breakage. Stacking with copper plates improved MRR for both wires compared to plain CFRP, in particular when using Topas plus D due to enhancement of workpiece electrical conductivity and flow of current. Excessive damage in terms of frayed fibres and resolidified copper was however observed when machining the stacked configuration. Cutting multidirectional CFRP revealed the highest MRR, Wa and Sa amongst all phases due to the lower electrical resistivity of the workpiece material compared with other samples. Compeed wire showed higher Wa and Sa however lower MRR, due to unstable

discharges caused by greater flow of decomposed resin and fibre fragments into the machining gap.

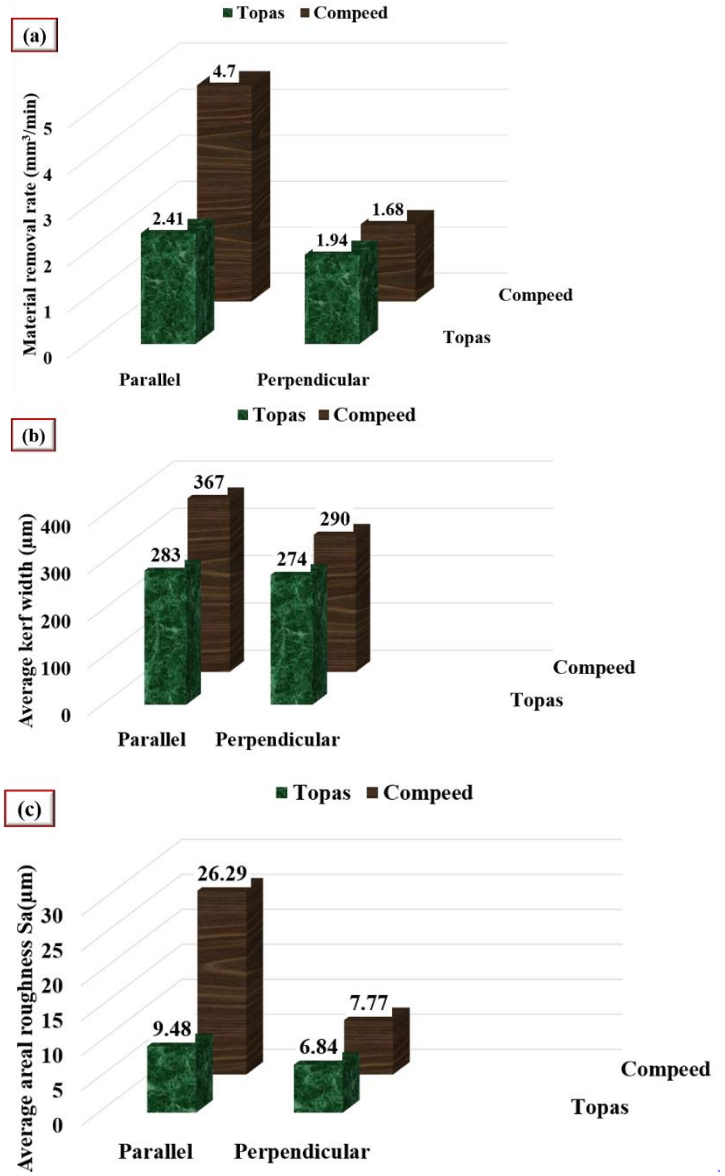


Figure 4.76: Bar chart showing (a) MRR (b) Wa and (c) Sa for each wire type when cutting UD-CFRP.

5 CONCLUSIONS

5.1 Literature review

Based on the detailed literature review, a number of non-conventional machining processes have been evaluated as potential alternatives for the machining of CFRP in order to overcome the drawbacks associated with traditional processes such as drilling and milling. Although high cutting rates and the absence of heat affected zones (HAZ) were observed with abrasive water jet machining, delamination, uncut fibres and hole tapering when drilling were key problems. Similarly, laser beam machining induced considerable surface damage including HAZ and delamination due to the thermal based material removal mechanism as well as tapering and poor roundness particularly for small diameter holes. Hybrid machining processes such as ultrasonic assisted drilling (UAD) and rotary ultrasonic machining (RUM) have been shown to improve cutting performance compared to conventional drilling and milling respectively, by reducing cutting forces and surface damage, however chipping, delamination and uncut fibres have not been completely avoided. Despite the relatively low electrical conductivity of CFRP, the feasibility of die-sink electrical discharge machining (EDM) for macro/micro drilling operations has been demonstrated by a number of researchers. Conversely, extremely limited research was available regarding the use of wire-EDM (WEDM) configuration for cutting of CFRP and was therefore the focus of the work presented in this thesis.

5.2 Experimental work

5.2.1 Phase 1A: Effect operating parameters when cutting UD-CFRP parallel to fibre direction using zinc coated brass core wire

- A maximum MRR of 2.41 mm^3/min was achieved at low open voltage (120 V)/pulse off time (4 µs) together with high current (5A)/pulse on time (1 µs) parameter combination over a cut length of 12 mm. Both current and pulse off time had a significant effect on material removal rate with PCRs of 48.47% and 24.27% respectively. Furthermore, no signs of major damage were observed along the kerf edges, although traces of bronze coloured contaminants were evidence on the bottom surface of the workpiece.
- The machined surface topography was characterised by broken fibres with swollen ends, re-solidified matrix layers comprising voids and cavities due to matrix/fibre loss, which deteriorated further with increasing discharge energy.

- According to the ANOVA, none of the cutting parameters were significant statistically significant with respect to average kerf width, which varied between ~260 and ~283 µm.
- Areal surface roughness measurements were found to be more representative of the machined surface topography compared to linear roughness for CFRP. This varied between 4.53 and 9.48 µm Sa, although none of the variables were significant at the 5% level.

5.2.2 Phase 1B: Effect of operating parameters when cutting UD-CFRP perpendicular to fibre direction using zinc coated brass core wire

- The MRR when cutting perpendicular to the fibre direction was between 0.69 and 1.94 mm^3/min, which increased to 2.08 mm^3/min in the confirmation test employing the preferred operating parameter combination. The ANOVA revealed that all of the factors had a significant influence on MRR, except for pulse on time. Ignition current recorded the highest PCR of 43.28% followed by pulse off time and open gap voltage of 18.56% and 16.56% respectively. Considerable delamination extending along the kerf edges was observed in the test exhibiting the highest MRR, with a delamination factor of up to 1.97. Signs of bronze coloured contaminants adhering on the top surface of the workpiece was apparent, probably caused by debris within the machine or deionised water dielectric.
- Scanning electron micrographs of the machined surface topography indicated the presence of voids/cavities due to fibre pull out/matrix decomposition with the formation of re-solidified resin having craters/cracks and hexagonal shaped swollen fibres becoming more severe at tests with higher MRR.
- Uniform kerf widths ranging between 268 and ~274 µm were obtained, with the small variation attributed to due to the lower workpiece electrical conductivity when machining perpendicular to the fibre direction in addition to the re-solidified resin layer on the machined surface acting as an insulator preventing the current/heat flow along the fibre axis. The corresponding ANOVA showed that none of the factors were significant with respect to kerf width, with the PCR not exceeding 20% for any of the variables.

- Workpiece surface roughness obtained was between 3.3 and 6.84 µm Sa. The open gap voltage was the sole parameter that demonstrated a significant influence on surface roughness with a PCR of 26.97%.

5.2.3 Phase 2A: Effect of operating parameters when cutting UD-CFRP parallel to fibre orientation using copper/brass coated steel core wire

- The highest MRR achieved was 4.7 mm^3/min, which was primarily attributed to the higher electrical conductivity of the brass coated steel core wire. In addition, Joule heating caused by short-circuiting with frayed fibres also resulted in increasing MRR. The associated ANOVA showed that both ignition current and pulse off time had a significant influence on MRR with PCR of 45.93% and 25.13% respectively.
- Large bundles of frayed fibres were observed on the top surface of the kerf machined at the highest MRR due to decomposition/evaporation of the matrix with minor delamination found at the end of the kerf. In contrast, the bottom surface exhibited uneven kerf edges with adhered debris/frayed fibres. Corresponding SEM micrographs revealed swollen fibre ends covered in re-solidified resin with voids due to entrapped gases, which were more pronounced at higher MRR.
- Greater variation in kerf widths was recorded from ~288 to ~367 µm over the range of parameters tested due to the higher discharge efficiency resulting from the increased wire conductivity. However, the ANOVA indicated that none of the factors were statistically significant with regard to average kerf width.
- Relatively high workpiece surface roughness levels were recorded ranging from 9.27 to 26.29 µm Sa. This was attributed to considerable amounts of frayed carbon fibres adhered to the machined surface. Pulse off time was found to be the sole significant factor affecting roughness with a PCR of 40.55%.

5.2.4 Phase 2B: Effect of operating parameters when cutting UD-CFRP perpendicular to fibre orientation using copper/brass coated steel core wire

- The highest MRR when cutting perpendicular to the fibre direction was 1.68 mm^3/min with uniform/even kerf edges on the top and bottom surfaces of the workpiece. Delamination however was observed in the vicinity of the kerf due to breakage of exposed fibres caused by flushing/gaseous jets, with delamination factors of up to ~2.05 recorded. Analysis of variance indicated that all of the factors had a significant influence

on MRR except for pulse off time, with ignition current showing the highest PCR of 54.71%.

- The SEM micrographs of machined surfaces showed regions with fibre loss, cratering and accumulated re-solidified matrix with voids and adhered fibre fragments.
- Average kerf width varied between ~272 and ~290 µm, with none of the variables found to have a significant effect on kerf width, although ignition current had a moderate PCR of 32.89%.
- Workpiece surface roughness when machining perpendicular to fibre direction was between 4.36 and 7.77 µm Sa. Based on the ANOVA, all of the factors were not statistically significant in relation to surface roughness.

5.2.5 Phase 3A: Preliminary investigation on cutting UD-CFRP/Cu stacks using zinc coated brass and copper/brass coated steel core wires

- Stacking the UD-CFRP with copper plates improved the bulk electrical conductivity of the material resulting in elevated MRR of 6.5 and 6.11 mm^3/min when machining with the Topas and Compeed wires respectively.
- At low current (3A) and high pulse off time (8 µs), the Compeed wire exhibited higher MRR however increasing current to 5A resulted in superior MRR when utilising the Topas wire due to better spark/discharge stability.

5.2.6 Phase 3B: Influence of operating parameters and wire electrode material when cutting UD-CFRP-metallic stacks

- Sandwiching the CFRP with Cu plates resulted in MRR of 5.89 mm^3/min when machining with the Topas wire at lower voltage (100V) and pulse on time (0.5 µs) together with higher range of pulse off times (8 and 10 µs) compared to cutting plain CFRP. At equivalent conditions, the Compeed wire achieved marginally lower MRR of 5.35 mm^3/min, possibly due to spark instability caused by the presence of increased debris in the machining gap generated at high discharge energy.
- All of the variable factors had a significant effect on MRR with pulse off time showing the highest PCR of 22.11% followed by wire electrode at 16.11%. Strong correlation was observed between the modelled and experimental results for MRR with a R^2 of 93.29%. The contour and surface plots indicated that high current (5 A) and low pulse off time (8 µs) led to the highest MRR for both wire electrodes.

- Considerable damage in terms of extensive delamination along the kerf, uneven edges and substantial frayed fibres were observed on the top and bottom surfaces of the workpieces machined using both wires. Re-solidified copper particles were also seen attached on the top/bottom surfaces of the workpiece machined with the Compeed wire. Furthermore, SEM micrographs of surfaces machined with the Topas wire revealed the presence of swollen fibre ends with re-solidified resin, fibre breakage and voids/cracks, with damage becoming more severe in tests with higher MRR. Similar conditions were observed on surfaces machined with the Compeed wire, but with adhered fibre fragments evident even on surfaces cut at the lowest MRR.
- Workpiece surface roughness was typically higher when machining with the Topas wire and ranged up to 16.48 µm Sa. The corresponding ANOVA showed that none of the factors had a significant influence on surface roughness, with the response surface model exhibiting poor correlation to the experimental data with R^2 of 47.68%.
- Based on a multi-objective optimisation procedure, intermediate current (4 A) and low pulse off time (8 µs) together with the Topas wire was recommended for minimising Sa and maximising MRR. Results from the confirmation tests showed low relative errors of 3.82% and 8.16% for MRR and Sa respectively.

5.2.7 Phase 3C: Influence of wire electrode material and operating conditions on cutting performance of multidirectional CFRP laminates

- Tests involving the WEDM of 8.75 mm thick multidirectional CFRP workpieces resulted in material removal rates ranging from 7.42 to 14.82 mm^3/min when using the Topas wire, whilst marginally lower MRR of 5.29 to 13.31 mm^3/min was obtained with the Compeed wire. Pulse off time was the sole significant factor affecting MRR with a PCR of 67.76%. The regression model showed strong correlation with experimental results with a coefficient of determination of 99.79%.
- High levels of delamination was evident on the top and bottom surfaces of the workpiece in tests at the highest MRR for both wires. A delamination factor of up to 2.94 was obtained when machining with the Compeed wire, which was somewhat lower at 2.5 when using the Topas wire.
- The SEM micrographs showed significant fibre fragments as well as accumulated re-solidified resin and cavities on surfaces machined with the Topas wire. In corresponding

tests involving the Compeed wire, large cavities were also observed between the plies due to resin vaporisation.

- The Compeed wire produced wider kerfs ranging between ~334 to 374.38 µm compared to the Topas wire (333.66 to 347.15 µm). Wire type was the sole significant factor affecting average kerf width with a PCR of 37.69%. The regression model showed strong correlation with experimental results based on a R^2 value of 99.88%.
- High workpiece surface roughness levels of up to 24.86 µm and 27.53 µm Sa were recorded when machining with the Topas and Compeed wires respectively. However, none of the parameters were statistically significant at the 5% level with respect to surface roughness, despite ignition current showing a moderately high PCR of 41.62%. The associated regression model revealed a strong correlation with a R^2 of 96.24%.

5.3 Overall conclusions and recommended cutting conditions

5.3.1 Comparison between Phase 1 and 2 experiments

- When cutting parallel to fibre orientation, the MRR achieved by the Compeed wire (4.7 mm^3/min) was up to ~95% higher compared to the Topas wire (2.41 mm^3/min), albeit with up to ~30% wider kerfs and ~177% higher surface roughness levels. Following optimisation of process conditions, the MRR when cutting with the Compeed wire (5.79 mm^3/min) was only marginally higher than the Topas wire (5.54 mm^3/min).
- When machining UD-CFRP perpendicular to the fibre direction, the Topas wire exhibited ~15.5% higher MRR compared to the Compeed wire, despite the latter showing larger kerf widths and areal surface roughness of up to 6% and ~13.5%. Furthermore, lower cutting rates were approximately ~20% lower compared to tests carried out parallel to the fibre direction.
- Based on statistical analysis of the experimental results, the preferred operating parameter levels for maximising MRR and minimising kerf width and surface roughness for Phase 1 and 2 tests are detailed in Table 5.1.

Table 5.1: Preferred cutting conditions for machining of UD-CFRP.

	Optimal levels	Response	V_o (V)	IAL (A)	A (µs)	B (µs)
Phase 1A	$V_1I_3A_3B_1$	MRR	120	5	1	4
	$V_1I_2A_1B_3$	Wa	120	4	0.8	8
	$V_1I_2A_1B_3$	Sa	120	4	0.8	8
Phase 1B	$V_1I_3A_1B_1$	MRR	120	5	0.8	4
	$V_2I_2A_1B_3$	Wa	140	4	0.8	8
	$V_2I_1A_3B_3$	Sa	140	3	1	8
Phase 2A	$V_1I_3A_3B_1$	MRR	120	5	1	4
	$V_2I_1A_3B_3$	Wa	140	3	1	8
	$V_2I_1A_3B_3$	Sa	140	3	1	8
Phase 2B	$V_1I_3A_1B_1$	MRR	120	5	0.8	4
	$V_1I_2A_1B_3$	Wa	120	4	0.8	8
	$V_2I_1A_3B_2$	Sa	140	3	1	6

5.3.2 Phase 3A and 3B: Cutting of CFRP/Cu stacks

- Preliminary tests involving the WEDM of CFRP/Cu stacks resulted in higher MRR of up to ~26% even when utilising lower pulse on time of 0.6 µs compared to cutting plain UD-CFRP.
- The MRR achieved using the Topas wire was ~10% higher compared to the Compeed wire. While the stacking configuration increased MRR, workpiece surface damage was generally severe with high levels of delamination, uneven kerf edges and large bundles of frayed fibres.

5.3.3 Phase 3C: Cutting of multidirectional CFRP

- Tests using the Topas wire showed ~11% higher MRR together with lower Wa (~7%) and Sa (~10%) compared to corresponding results utilising the Compeed wire. Pulse off time and wire type were statistically significant factors with respect to MRR and Wa respectively, while none of parameters were found to influence surface roughness.
- Machining UD-CFRP parallel to the fibre direction using the Compeed wire produced lower MRR (65%) together with marginally smaller average kerf widths (2%) and surface roughness (4.5%) in comparison to cutting multidirectional CFRP. Similarly, machining with the Topas wire also resulted in lower MRR of 84%, as well as reduced kerf widths and surface roughness of 18% and 62% respectively. This was attributed to the lower electrical resistivity (55% - 86%) of the multidirectional laminates compared to the UD-CFRP, as well as variation in standoff distances between flushing nozzles and workpiece material.

- Table 5.2 details the preferred operating parameter levels for each response when machining multidirectional CFRP based on statistical analysis of the experimental results.

Table 5.2: Preferred cutting conditions for machining of multidirectional CFRP.

	Optimal levels	Response	IAL (A)	B (µs)	W
Phase 3C	**$I_2B_1W_1$**	MRR	5	8	T
	$I_1B_2W_1$	Wa	3	10	T
	$I_1B_2W_1$	Sa	3	10	T

5.4 Summary

The feasibility of WEDM for cutting thick CFRP composites with various fibre orientations including unidirectional and multidirectional arrangements was demonstrated. The use of Compeed composite wire machining parallel to fibre direction at high current/pulse on time levels together with low pulse off time is recommended to achieve high productivity. Conversely, the Topas wire is preferred for cutting UD-CFRP/Cu stacks and multidirectional workpiece due to more stable spark discharges. Reducing pulse on time while increasing pulse off time is recommended when machining UD-CFRP/Cu stacks and multidirectional CFRP to avoid wire breakage. Furthermore, the results highlight the appropriate operating parameter levels to enable machining without wire failure/breakage.

6 RECOMMENDATIONS FOR FUTURE WORK

Based on the results of the current research, several areas have been identified that warrant further investigation. These include:

- Evaluating the influence of different WEDM generators and a wider range of cutting conditions such as servo voltage, wire speed, frequency and flushing pressure on MRR, heat affected zone (HAZ), average kerf width and surface integrity.
- Investigating the feasibility of cutting thick CFRP stacked with Ti-6Al-4V due to its increasingly widespread use in the aerospace industry.
- Investigating the feasibility of WEDM for deburring of pre-drilled holes in CFRP.
- Investigating the feasibility of improving electrical conductivity of CFRP by addition of carbon content and its subsequent cutting performance using WEDM.
- Further in-depth study of discharge characteristics in WEDM of using high speed camera.
- Direct measurement of discharge energy during WEDM of CFRP and investigate the influence of pulse shape on machining performance.
- Assessing and optimising energy consumption in WEDM of CFRP.
- Modelling of simulation of WEDM of CFRP composites.

REFERENCES

[1] J. P. Jose, S. Thomas, J. Kuruvilla, S. Malhotra, K. Goda, and M. S. Sreekala, "Advances in polymer composites: Macro-and microcomposites—State of the art, new challenges, and opportunities," *Polymer Composites; Wiley: Weinheim, Germany*, vol. 1, pp. 3-16, 2012.

[2] F. M. Orr, "2015 Quadrennial technology review," in *Proceedings of the International Conference for High Performance Computing, Networking, Storage and Analysis*, 2015.

[3] D. Gay, S. V. Hoa, and S. W. Tsai, *Composite Materials: Design and Applications*. CRC Press, 2003.

[4] K. K. Chawla, *Composite Materials: Science and Engineering*, 3rd ed. Springer Science and Business Media, 2012.

[5] F. C. Campbell, *Structural Composite Materials*. ASM international, 2010.

[6] S. Rana and R. Fangueiro, *Advanced Composite Materials for Aerospace Engineering: Processing, Properties and Applications*. Woodhead Publishing, 2016.

[7] W. D. Callister and D. G. Rethwisch, *Materials Science and Engineering: An Introduction*, Eighth ed. John Wiley and Sons New York, 2010.

[8] S. Kalpakjian and S. R. Schmid, *Manufacturing Engineering and Technology*, 6th ed. Prentice Hall, 2010.

[9] J. Y. Sheikh-Ahmad, *Machining of Polymer Composites*. Springer, 2009.

[10] S. Mazumdar, *Composites Manufacturing: Materials, Product, and Process Engineering*. CRC Press, 2002.

[11] FAA, *Aviation Maintenance Technician Handbook—Airframe*. Federal Aviation Administration Oklahoma City, OK, 2012.

[12] M. A. Masuelli, "Introduction of fibre-reinforced polymers− Polymers and composites: Concepts, properties and processes," in *Fiber Reinforced Polymers-The Technology Applied for Concrete Repair*: IntechOpen, 2013.

[13] "Hexply prepreg technology," Available: https://www.hexcel.com/user_area/content_media/raw/Prepreg_Technology.pdf

[14] P. K. Mallick, *Fiber-Reinforced Composites: Materials, Manufacturing, and Design*. CRC Press, 2007.

[15] Umeco. Introduction to advanced composites and prepreg technology. Available: https://www.yumpu.com/en/document/view/9334619/introduction-to-advanced-composites-and-prepreg-technology

[16] P. Irving and C. Soutis, *Polymer Composites in the Aerospace Industry* (no. 50). Elsevier, 2014.

[17] D. Hull and T. W. Clyne, *An Introduction to Composite Materials*. Cambridge University Press, 1996.

[18] A. Ramadhan, A. A. Talib, A. M. Rafie, and R. Zahari, "High velocity impact response of Kevlar-29/epoxy and 6061-T6 aluminum laminated panels," *Materials and Design*, vol. 43, pp. 307-321, 2013.

[19] M. F. Ismail, M. T. H. Sultan, A. Hamdan, and A. U. M. Shah, "A study on the low velocity impact response of hybrid kenaf-kevlar composite laminates through drop test rig technique," *BioResources*, vol. 13, no. 2, pp. 3045-3060, 2018.

[20] P. Bajpai, *Update on Carbon Fibre*. Smithers Rapra, 2013.

[21] S. T. Peters, *Handbook of Composites*, 2nd ed. Springer, 1998.

[22] D. D. Chung, *Carbon Fiber Composites*. Butterworth-Heinemann, 1994.

[23] M. Lumpkin and M. Williams, *Toxicological Profile for Boron*. US Department of Health and Human Services, Public Health Service, Agency, 2010.
[24] S. Coromant, "Machining carbon fibre materials: user's guide," *Composite Solution*, pp. 1-63, 2010.
[25] M. A. Karataş and H. Gökkaya, "A review on machinability of carbon fiber reinforced polymer (CFRP) and glass fiber reinforced polymer (GFRP) composite materials," *Defence Technology*, vol. 14, no. 4, pp. 318-326, 2018.
[26] C. Soutis, "Fibre reinforced composites in aircraft construction," *Progress in Aerospace Sciences*, vol. 41, no. 2, pp. 143-151, 2005.
[27] P. Morgan, *Carbon Fibers and their Composites*. CRC Press, 2005.
[28] M. H. El-Hofy, "Milling/Routing of carbon fibre reinforced plastics (CFRP) composites," PhD, University of Birmingham, 2014.
[29] A. Bhatnagar, D. S. Cordova, and L. C. Lin, "Extended shelf life prepreg article and method," United States, 1992.
[30] V. K. Choo, *Fundamentals of Composite Materials*. Knowen Academic Press, 1990.
[31] *Composite Materials Handbook* (Volume 2. Polymer Matrix Composites Materials Properties). USA, Department of Defense, 2002.
[32] P. Joyce, "Common lay-up terms and conditions," *United States Naval Academy*, 2003.
[33] F. Vatankhahan, M. Mahmoudi, and M. R. Dorali, "Vibrational analysis of perforated composite plate with 3-layered galss, boron and graphite fibre/expoxy," in *3rd International Conference on Recent Innovations in Industrial Engineering and Mechanical Engineering*, 2016, pp. 1-11.
[34] F. M. Mohee, A. Al-Mayah, and A. Plumtree, "Anchors for CFRP plates: State-of-the-art review and future potential," *Composites Part B: Engineering*, vol. 90, pp. 432-442, 2016.
[35] Y. Akematsu, K. Kageyama, and H. Murayama, "Basic characteristics of electrical discharge on CFRP by using thermal camera," *Procedia CIRP*, vol. 42, pp. 197-200, 2016.
[36] I. Shyha, S. L. Soo, D. K. Aspinwall, S. Bradley, S. Dawson, and C. J. Pretorius, "Drilling of titanium/CFRP/aluminium stacks," in *Key Engineering Materials*, 2010, vol. 447, pp. 624-633: Trans Tech Publ.
[37] I. Shyha, D. Aspinwall, S. L. Soo, and S. Bradley, "Drill geometry and operating effects when cutting small diameter holes in CFRP," *International Journal of Machine Tools and Manufacture*, vol. 49, no. 12-13, pp. 1008-1014, 2009.
[38] S. C. Sekaran, H. J. Yap, K. E. Liew, H. Kamaruzzaman, C. H. Tan, and R. S. Rajab, "Haptic-based virtual reality system to enhance actual aerospace composite panel drilling training," in *Structural Health Monitoring of Biocomposites, Fibre-Reinforced Composites and Hybrid Composites*: Elsevier, 2019, pp. 113-128.
[39] P. Jerome, "Composite materials in the Airbus A380-from history to future," in *Beijing: Proceedings 13th International Conference on Composite Materials (ICCM-13)*, 2001, pp. 1-10.
[40] S. V. Hoa, *Principles of the Manufacturing of Composite Materials*. DEStech Publications, Inc, 2009.
[41] D. Kumar and K. Singh, "An approach towards damage free machining of CFRP and GFRP composite material: a review," *Advanced Composite Materials*, vol. 24, no. sup1, pp. 49-63, 2015.

[42] D. Kim, A. Beal, and P. Kwon, "Effect of tool wear on hole quality in drilling of carbon fiber reinforced plastic–titanium alloy stacks using tungsten carbide and polycrystalline diamond tools," *Journal of Manufacturing Science and Engineering,* vol. 138, no. 3, pp. 031006 (1-11), 2016.

[43] J. Y. Sheikh-Ahmad and S. R. Shinde, "Machinability of carbon/epoxy composites by electrical discharge machining," *International Journal of Machining and Machinability of Materials,* vol. 18, no. 1-2, pp. 3-17, 2016.

[44] D. Liu, Y. Tang, and W. Cong, "A review of mechanical drilling for composite laminates," *Composite Structures,* vol. 94, no. 4, pp. 1265-1279, 2012.

[45] M.-B. Lazar and P. Xirouchakis, "Experimental analysis of drilling fiber reinforced composites," *International Journal of Machine Tools and Manufacture,* vol. 51, no. 12, pp. 937-946, 2011.

[46] W.-C. Chen, "Some experimental investigations in the drilling of carbon fiber-reinforced plastic (CFRP) composite laminates," *International Journal of Machine Tools and Manufacture,* vol. 37, no. 8, pp. 1097-1108, 1997.

[47] C. Tsao and H. Hocheng, "Taguchi analysis of delamination associated with various drill bits in drilling of composite material," *International Journal of Machine Tools and Manufacture,* vol. 44, no. 10, pp. 1085-1090, 2004.

[48] L. M. P. Durão, D. J. Gonçalves, J. M. R. Tavares, V. H. C. de Albuquerque, A. A. Vieira, and A. T. Marques, "Drilling tool geometry evaluation for reinforced composite laminates," *Composite Structures,* vol. 92, no. 7, pp. 1545-1550, 2010.

[49] J. P. Davim and P. Reis, "Damage and dimensional precision on milling carbon fiber-reinforced plastics using design experiments," *Journal of Materials Processing Technology,* vol. 160, no. 2, pp. 160-167, 2005.

[50] S.-C. Lee, S.-T. Jeong, J.-N. Park, S.-J. Kim, and G.-J. Cho, "Study on drilling characteristics and mechanical properties of CFRP composites," *Acta Mechanica Solida Sinica,* vol. 21, no. 4, pp. 364-368, 2008.

[51] I. Shyha, S. L. Soo, D. Aspinwall, and S. Bradley, "Effect of laminate configuration and feed rate on cutting performance when drilling holes in carbon fibre reinforced plastic composites," *Journal of Materials Processing Technology,* vol. 210, no. 8, pp. 1023-1034, 2010.

[52] J. P. Davim, J. C. Rubio, and A. Abrao, "A novel approach based on digital image analysis to evaluate the delamination factor after drilling composite laminates," *Composites Science and Technology,* vol. 67, no. 9, pp. 1939-1945, 2007.

[53] D. Kim and M. Ramulu, "Drilling process optimization for graphite/bismaleimide–titanium alloy stacks," *Composite Structures,* vol. 63, no. 1, pp. 101-114, 2004.

[54] R. Zitoune, V. Krishnaraj, and F. Collombet, "Study of drilling of composite material and aluminium stack," *Composite Structures,* vol. 92, no. 5, pp. 1246-1255, 2010.

[55] C. Tsao and H. Hocheng, "Parametric study on thrust force of core drill," *Journal of Materials Processing Technology,* vol. 192, pp. 37-40, 2007.

[56] X. Qiu, P. Li, C. Li, Q. Niu, A. Chen, P. Ouyang, and T. J. Ko, "Study on chisel edge drilling behavior and step drill structure on delamination in drilling CFRP," *Composite Structures,* vol. 203, pp. 404-413, 2018.

[57] S. Joshi, K. Rawat, and A. Balan, "A novel approach to predict the delamination factor for dry and cryogenic drilling of CFRP," *Journal of Materials Processing Technology,* vol. 262, pp. 521-531, 2018.

[58] C. Tsao and H. Hocheng, "Computerized tomography and C-Scan for measuring delamination in the drilling of composite materials using various drills," *International Journal of Machine Tools and Manufacture,* vol. 45, no. 11, pp. 1282-1287, 2005.

[59] R. Stone and K. Krishnamurthy, "A neural network thrust force controller to minimize delamination during drilling of graphite-epoxy laminates," *International Journal of Machine Tools and Manufacture,* vol. 36, no. 9, pp. 985-1003, 1996.

[60] E. U. Enemuoh, A. S. El-Gizawy, and A. C. Okafor, "An approach for development of damage-free drilling of carbon fiber reinforced thermosets," *International Journal of Machine Tools and Manufacture,* vol. 41, no. 12, pp. 1795-1814, 2001.

[61] C. C. Tsao and H. Hocheng, "The effect of chisel length and associated pilot hole on delamination when drilling composite materials," *International Journal of Machine Tools and Manufacture,* vol. 43, no. 11, pp. 1087-1092, 2003.

[62] F. Su, L. Zheng, F. Sun, Z. Wang, Z. Deng, and X. Qiu, "Novel drill bit based on the step-control scheme for reducing the CFRP delamination," *Journal of Materials Processing Technology,* vol. 262, pp. 157-167, 2018.

[63] M. Durante, L. Boccarusso, D. De Fazio, and A. Langella, "Circular cutting strategy for drilling of carbon fiber-reinforced plastics (CFRPs)," *Materials and Manufacturing Processes,* vol. 34, no. 5, pp. 554-566, 2019.

[64] F. Klocke, W. Koenig, S. Rummenhoeller, and C. Wuertz, "Milling of advanced composites," *Manufacturing Engineering and Materials Processing,* vol. 53, pp. 249-266, 1999.

[65] O. Çolak and T. Sunar, "Cutting forces and 3D surface analysis of CFRP milling with PCD cutting tools," *Procedia CIRP,* vol. 45, pp. 75-78, 2016.

[66] O. Pecat, R. Rentsch, and E. Brinksmeier, "Influence of milling process parameters on the surface integrity of CFRP," *Procedia CIRP,* vol. 1, pp. 466-470, 2012.

[67] M. N. Khairusshima and I. Sharifah, "Study on tool wear during milling CFRP under dry and chilled air machining," *Procedia Engineering,* vol. 184, pp. 78-89, 2017.

[68] K. Szallies, N. Siebert, and J. P. Bergmann, "Low frequency oscillated milling of carbon fiber-reinforced plastics," *Procedia CIRP,* vol. 66, pp. 153-158, 2017.

[69] W. Hintze and F. Brügmann, "Influence of spatial tool inclination on delamination when milling CFRP," *Journal of Materials Processing Technology,* vol. 252, pp. 830-837, 2018.

[70] M. El-Hofy, S. Soo, D. Aspinwall, W. Sim, D. Pearson, and P. Harden, "Factors affecting workpiece surface integrity in slotting of CFRP," *Procedia Engineering,* vol. 19, pp. 94-99, 2011.

[71] H. Sasahara, Y. Sukegawa, and Y. Yamada, "CFRP machining capability by a circular saw," *Precision Engineering,* vol. 52, pp. 291-299, 2018.

[72] T. Grilo, R. Paulo, C. Silva, and J. Davim, "Experimental delamination analyses of CFRPs using different drill geometries," *Composites Part B: Engineering,* vol. 45, no. 1, pp. 1344-1350, 2013.

[73] A. Hassan and R. Kovacevic. Effect of cutting parameters on vertical force in AWJ cutting [Online]. Available: https://www.researchgate.net/profile/Ashraf_Hassan7/publication/282735448_Effect_of_Cutting_Parameters_on_Vertical_Force_in_AWJ_Cutting/links/56e5fce808aedb4cc8ae9287.pdf

[74] H. A. Youssef and H. El-Hofy, *Machining Technology: Machine Tools and Operations*. CRC Press, 2008.

[75] A. A. Khan and M. Y. Ali, "Application of silicon carbide in abrasive water jet machining," in *Silicon Carbide-Materials, Processing and Applications in Electronic Devices*: IntechOpen, 2011.

[76] K. Thongkaew, J. Wang, and W. Li, "An investigation of the hole machining processes on woven carbon-fiber reinforced polymers (CFRPs) using abrasive waterjets," *Machining Science and Technology,* vol. 23, no. 1, pp. 19-38, 2019.

[77] H. N. Dhakal, S. O. Ismail, S. O. Ojo, M. Paggi, and J. R. Smith, "Abrasive water jet drilling of advanced sustainable bio-fibre-reinforced polymer/hybrid composites: a comprehensive analysis of machining-induced damage responses," *The International Journal of Advanced Manufacturing Technology,* vol. 99, no. 9-12, pp. 2833-2847, 2018.

[78] M. Li, M. Huang, X. Yang, S. Li, and K. Wei, "Experimental study on hole quality and its impact on tensile behavior following pure and abrasive waterjet cutting of plain woven CFRP laminates," *The International Journal of Advanced Manufacturing Technology,* vol. 99, no. 9-12, pp. 2481-2490, 2018.

[79] G. A. Escobar-Palafox, K. K. Wika, R. S. Gault, and K. Ridgway, "Characterisation of abrasive water-jet process for drilling titanium and carbon fibre reinforced polymer stacks," *Surfaces,* vol. 13, p. 14.

[80] R. Ruiz-Garcia, P. Mayuet Ares, J. Vazquez-Martinez, and J. Salguero Gómez, "Influence of abrasive waterjet parameters on the cutting and drilling of CFRP/UNS A97075 and UNS A97075/CFRP stacks," *Materials,* vol. 12, no. 1, pp. 1-18, 2019.

[81] H. Hocheng, H. Tsai, J. Shiue, and B. Wang, "Feasibility study of abrasive-waterjet milling of fiber-reinforced plastics," *Transactions-American Society of Mechanical Engineers Journal of Manufacturing Science and Engineering,* vol. 119, pp. 133-142, 1997.

[82] P. Mayuet, F. Girot, A. Lamíkiz, S. Fernández-Vidal, J. Salguero, and M. Marcos, "SOM/SEM based characterization of internal delaminations of CFRP samples machined by AWJM," *Procedia Engineering,* vol. 132, pp. 693-700, 2015.

[83] D. Shanmugam, T. Nguyen, and J. Wang, "A study of delamination on graphite/epoxy composites in abrasive waterjet machining," *Composites Part A: Applied Science and Manufacturing,* vol. 39, no. 6, pp. 923-929, 2008.

[84] A. Alberdi, T. Artaza, A. Suárez, A. Rivero, and F. Girot, "An experimental study on abrasive waterjet cutting of CFRP/Ti6Al4V stacks for drilling operations," *The International Journal of Advanced Manufacturing Technology,* vol. 86, no. 1-4, pp. 691-704, 2016.

[85] R. Pahuja and M. Ramulu, "Abrasive water jet machining of Titanium (Ti6Al4V)–CFRP stacks–A semi-analytical modeling approach in the prediction of kerf geometry," *Journal of Manufacturing Processes,* vol. 39, pp. 327-337, 2019.

[86] A. K. Dubey and V. Yadava, "Laser beam machining—a review," *International Journal of Machine Tools and Manufacture,* vol. 48, no. 6, pp. 609-628, 2008.

[87] S. C. Singh, H. Zeng, C. Guo, and W. Cai, "Lasers: fundamentals, types, and operations," *Nanomaterials: Processing and Characterization with Lasers,* pp. 1-34, 2012.

[88] H. El-Hofy, *Advanced Machining Processes: Nontraditional and Hybrid Machining Processes*. McGraw Hill Professional, 2005.

[89] H. Xu and J. Hu, "Modeling of the material removal and heat affected zone formation in CFRP short pulsed laser processing," *Applied Mathematical Modelling,* vol. 46, pp. 354-364, 2017.

[90] S. Genna, F. Tagliaferri, I. Papa, C. Leone, and B. Palumbo, "Multi-response optimization of CFRP laser milling process based on response surface methodology," *Polymer Engineering and Science,* vol. 57, no. 6, pp. 595-605, 2017.
[91] P. Gautam and K. Singh, "Experimental investigation and modeling of heat affected zone and surface roughness in erbium-doped fiber laser cutting of CFRP composite," *Materials Today: Proceedings,* vol. 5, no. 11, pp. 24466-24475, 2018.
[92] M. Li, S. Li, X. Yang, Y. Zhang, and Z. Liang, "Fiber laser cutting of CFRP laminates with single-and multi-pass strategy: A feasibility study," *Optics and Laser Technology,* vol. 107, pp. 443-453, 2018.
[93] C. Leone and S. Genna, "Heat affected zone extension in pulsed Nd: YAG laser cutting of CFRP," *Composites Part B: Engineering,* vol. 140, pp. 174-182, 2018.
[94] J. Hu and D. Zhu, "Investigation of carbon fiber reinforced plastics machining using 355 nm picosecond pulsed laser," *Applied Composite Materials,* vol. 25, no. 3, pp. 589-600, 2018.
[95] S. Oh, I. Lee, Y.-B. Park, and H. Ki, "Investigation of cut quality in fiber laser cutting of CFRP," *Optics and Laser Technology,* vol. 113, pp. 129-140, 2019.
[96] M. S. Raza, S. Datta, B. Bule, and P. Saha, "Parametric study of laser cutting of carbon fibre reinforced polymer (CFRP) and the effect of fibre orientation on cutting quality," *Advances in Materials and Processing Technologies,* vol. 5, no. 2, pp. 202-212, 2019.
[97] J. Finger, M. Weinand, and D. Wortmann, "Ablation and cutting of carbon-fiber reinforced plastics using picosecond pulsed laser radiation with high average power," *Journal of Laser Applications,* vol. 25, no. 4, pp. 042007 (1-5), 2013.
[98] C. Leone, S. Genna, and V. Tagliaferri, "Fibre laser cutting of CFRP thin sheets by multi-passes scan technique," *Optics and Lasers in Engineering,* vol. 53, pp. 43-50, 2014.
[99] A. Salama, L. Li, P. Mativenga, and A. Sabli, "High-power picosecond laser drilling/machining of carbon fibre-reinforced polymer (CFRP) composites," *Applied Physics A: Material Science and Processing,* vol. 122, no. 73, pp. 1-11, 2016.
[100] A. Wolynski, T. Herrmann, P. Mucha, H. Haloui, and J. L'huillier, "Laser ablation of CFRP using picosecond laser pulses at different wavelengths from UV to IR," *Physics Procedia,* vol. 12, pp. 292-301, 2011.
[101] H. Niino and R. Kurosaki, "Laser cutting of carbon fiber reinforced plastics (CFRP) by UV pulsed laser ablation," in *SPIE LASE,* 2011, pp. 792019(1-5): International Society for Optics and Photonics.
[102] J. Mathew, G. Goswami, N. Ramakrishnan, and N. Naik, "Parametric studies on pulsed Nd: YAG laser cutting of carbon fibre reinforced plastic composites," *Journal of Materials Processing Technology,* vol. 89, pp. 198-203, 1999.
[103] Z. Li, H. Zheng, G. Lim, P. Chu, and L. Li, "Study on UV laser machining quality of carbon fibre reinforced composites," *Composites Part A: Applied Science and Manufacturing,* vol. 41, no. 10, pp. 1403-1408, 2010.
[104] K.-W. Jung, Y. Kawahito, and S. Katayama, "Ultra-high speed disk laser cutting of carbon fiber reinforced plastics," *Journal of Laser Applications,* vol. 24, no. 1, pp. 012007(1-8), 2012.
[105] R. Negarestani, L. Li, H. Sezer, D. Whitehead, and J. Methven, "Nano-second pulsed DPSS Nd: YAG laser cutting of CFRP composites with mixed reactive and inert gases," *The International Journal of Advanced Manufacturing Technology,* vol. 49, no. 5, pp. 553-566, 2010.

[106] S. Genna, F. Tagliaferri, I. Papa, C. Leone, and B. Palumbo, "Experimental investigation on CFRP milling by low power Q-switched Yb: YAG laser source," in *AIP Conference Proceedings*, 2016, vol. 1736, no. 1, pp. 020159(1-4): AIP Publishing.

[107] D. Herzog, M. Schmidt-Lehr, M. Canisius, M. Oberlander, J.-P. Tasche, and C. Emmelmann, "Laser cutting of carbon fiber reinforced plastic using a 30 kW fiber laser," *Journal of Laser Applications*, vol. 27, no. S2, pp. S28001(1-7), 2015.

[108] A. Salama, Y. Yan, L. Li, P. Mativenga, D. Whitehead, and A. Sabli, "Understanding the self-limiting effect in picosecond laser single and multiple parallel pass drilling/machining of CFRP composite and mild steel," *Materials and Design*, vol. 107, pp. 461-469, 2016.

[109] C.-W. Wu, X.-Q. Wu, and C.-G. Huang, "Ablation behaviors of carbon reinforced polymer composites by laser of different operation modes," *Optics and Laser Technology*, vol. 73, pp. 23-28, 2015.

[110] R. Staehr, S. Bastick, S. Bluemel, P. Jaeschke, O. Suttmann, J.-P. Negel, V. Angrick, C. Stolzenburg, S. Kaierle, and L. Overmeyer, "High precision laser macrodrilling of carbon fiber reinforced plastics with a new nanosecond pulsed laser—optimized toward industrial needs," *Journal of Laser Applications*, vol. 31, no. 2, pp. 022207(1-11), 2019.

[111] I. Shyha, "An investigation into CO_2 laser trimming of CFRP and GFRP composites," *Procedia Engineering*, vol. 63, pp. 931-937, 2013.

[112] A. Salama, L. Li, P. Mativenga, and D. Whitehead, "TEA CO_2 laser machining of CFRP composite," *Applied Physics A*, vol. 122, no. 5, pp. 1-19, 2016.

[113] C. Leone, I. Papa, F. Tagliaferri, and V. Lopresto, "Investigation of CFRP laser milling using a 30W Q-switched Yb: YAG fiber laser: Effect of process parameters on removal mechanisms and HAZ formation," *Composites Part A: Applied Science and Manufacturing*, vol. 55, pp. 129-142, 2013.

[114] V. Jain, "Advanced (non-traditional) machining processes," in *Machining Fundamentals and Recent Advances*: Springer, 2008, pp. 299-327.

[115] T. Thoe, D. Aspinwall, and M. Wise, "Review on ultrasonic machining," *International Journal of Machine Tools and Manufacture*, vol. 38, no. 4, pp. 239-255, 1998.

[116] F. Ning, H. Wang, W. Cong, and P. Fernando, "A mechanistic ultrasonic vibration amplitude model during rotary ultrasonic machining of CFRP composites," *Ultrasonics*, vol. 76, pp. 44-51, 2017.

[117] F. Ning, W. Cong, Z. Pei, and C. Treadwell, "Rotary ultrasonic machining of CFRP: A comparison with grinding," *Ultrasonics*, vol. 66, pp. 125-132, 2016.

[118] W. Cong, Z. Pei, X. Sun, and C. Zhang, "Rotary ultrasonic machining of CFRP: A mechanistic predictive model for cutting force," *Ultrasonics*, vol. 54, no. 2, pp. 663-675, 2014.

[119] Q. Feng, W. Cong, Z. J. Pei, and C. Ren, "Rotary ultrasonic machining of carbon fiber-reinforced polymer: feasibility study," *Machining Science and Technology*, vol. 16, no. 3, pp. 380-398, 2012.

[120] A. Slimane, S. Slimane, S. Kebdani, M. Chaib, S. Dahmane, B. Bouchouicha, N. Sardi, and S. Adjim, "Parameters effects analysis of rotary ultrasonic machining on carbon fiber reinforced plastic (CFRP) composite using an interactive RSM method," *International Journal on Interactive Design and Manufacturing (IJIDeM)*, vol. 13, no. 2, pp. 521-529, 2019.

[121] W. Cong, Q. Feng, Z. Pei, T. Deines, and C. Treadwell, "Dry machining of carbon fiber reinforced plastic composite by rotary ultrasonic machining: effects of machining variables," in *Proceedings of the ASME 2011 International Manufacturing Science and Engineering Conference (MSEC), Corvallis, OR, USA, June*, 2011, pp. 13-17.

[122] W. Cong, Q. Feng, Z. J. Pei, T. W. Deines, and C. Treadwell, "Rotary ultrasonic machining of carbon fiber-reinforced plastic composites: using cutting fluid vs. cold air as coolant," *Journal of Composite Materials*, vol. 46, no. 14, pp. 1745-1753, 2012.

[123] W. Cong, Z. J. Pei, T. W. Deines, D. Liu, and C. Treadwell, "Rotary ultrasonic machining of CFRP/Ti stacks using variable feedrate," *Composites Part B: Engineering*, vol. 52, pp. 303-310, 2013.

[124] P. K. Fernando, Z. Pei, M. P. Zhang, and X. Song, "Rotary ultrasonic drilling of CFRP: effect of process parameters on delamination," in *ASME 2016 11th International Manufacturing Science and Engineering Conference*, 2016, pp. 1-6: American Society of Mechanical Engineers.

[125] A. Sanda, I. Arriola, V. G. Navas, I. Bengoetxea, and O. Gonzalo, "Ultrasonically assisted drilling of carbon fibre reinforced plastics and Ti6Al4V," *Journal of Manufacturing Processes*, vol. 22, pp. 169-176, 2016.

[126] V. A. Phadnis, F. Makhdum, A. Roy, and V. V. Silberschmidt, "Experimental and numerical investigations in conventional and ultrasonically assisted drilling of CFRP laminate," *Procedia CIRP*, vol. 1, pp. 455-459, 2012.

[127] F. Makhdum, L. T. Jennings, A. Roy, and V. V. Silberschmidt, "Cutting forces in ultrasonically assisted drilling of carbon fibre-reinforced plastics," in *Journal of Physics: Conference Series*, 2012, vol. 382, no. 1, pp. 012019 (1-6): IOP Publishing.

[128] V. A. Phadnis, F. Makhdum, A. Roy, and V. V. Silberschmidt, "Ultrasonically assisted drilling: machining towards improved structural integrity in carbon/epoxy composites," in *Key Engineering Materials*, 2013, vol. 569, pp. 49-55: Trans Tech Publ.

[129] J. Liu, D. Zhang, L. Qin, and L. Yan, "Feasibility study of the rotary ultrasonic elliptical machining of carbon fiber reinforced plastics (CFRP)," *International Journal of Machine Tools and Manufacture*, vol. 53, no. 1, pp. 141-150, 2012.

[130] D. Geng, D. Zhang, Y. Xu, F. He, and F. Liu, "Comparison of drill wear mechanism between rotary ultrasonic elliptical machining and conventional drilling of CFRP," *Journal of Reinforced Plastics and Composites*, vol. 33, no. 9, pp. 797-809, 2014.

[131] Z. Li, D. Zhang, W. Qin, and D. Geng, "Removal analyses of chip and rod in rotary ultrasonic-assisted drilling of carbon fiber-reinforced plastics using core drill," *Journal of Reinforced Plastics and Composites*, vol. 35, no. 15, pp. 1173-1190, 2016.

[132] H. Wang, F. Ning, Y. Hu, Y. Li, X. Wang, and W. Cong, "Edge trimming of carbon fiber-reinforced plastic composites using rotary ultrasonic machining: effects of tool orientations," *The International Journal of Advanced Manufacturing Technology*, vol. 98, no. 5-8, pp. 1641-1653, 2018.

[133] S. Yuan, G. Zhu, and C. Zhang, "Modeling of tool blockage condition in cutting tool design for rotary ultrasonic machining of composites," *The International Journal of Advanced Manufacturing Technology*, pp. 1-10, 2017.

[134] H. Wang, F. Ning, Y. Li, Y. Hu, and W. Cong, "Scratching-induced surface characteristics and material removal mechanisms in rotary ultrasonic surface machining of CFRP," *Ultrasonics*, vol. 97, pp. 19-28, 2019.

[135] D. Geng, D. Zhang, Y. Xu, X. Jiang, Z. Lu, and D. Lu, "Effect of speed ratio in edge routing of carbon fiber-reinforced plastics by rotary ultrasonic elliptical machining," *Journal of Reinforced Plastics and Composites*, vol. 34, no. 21, pp. 1779-1790, 2015.

[136] Z. D. Li, X. B. Wang, and B. Zhao, "An experiment study on milling forces in the ultrasonic milling of CFRP," in *Advanced Materials Research*, 2012, vol. 472, pp. 1028-1031: Trans Tech Publ.

[137] N. F. H. A. Halim, H. Ascroft, and S. Barnes, "Analysis of tool wear, cutting force, surface roughness and machining temperature during finishing operation of ultrasonic assisted milling (UAM) of carbon fibre reinforced plastic (CFRP)," *Procedia Engineering*, vol. 184, pp. 185-191, 2017.

[138] A. N. F. Huda, H. Ascroft, and S. Barnes, "Machinability study of ultrasonic assisted machining (UAM) of carbon fibre reinforced plastic (CFRP) with multifaceted tool," *Procedia CIRP*, vol. 46, pp. 488-491, 2016.

[139] M. Kuruc, M. Necpal, T. Vopát, V. Šimna, and J. Peterka, "Influence of ultrasonic assistance on delamination during machining of CFRP composite," in *International Conference on Advanced Manufacturing Engineering and Technologies*, 2017, pp. 443-450: Springer.

[140] S. Kuriakose and M. Shunmugam, "Characteristics of wire-electro discharge machined Ti6Al4V surface," *Materials Letters*, vol. 58, no. 17, pp. 2231-2237, 2004.

[141] M. Tiwari, K. Mausam, K. Sharma, and R. P. Singh, "Experimental analysis of electro-discharge machining parameters for minimum tool wear rate on machinability of carbon fiber/epoxy composites using Taguchi method," in *International Journal of Engineering Research and Technology*, 2013, vol. 2, no. 10: IJERT.

[142] H. Wang, S. Habib, A. Okada, and U. Uno, "EDM characteristics of carbon fiber reinforced plastic," *Proceedings 16th International Symposium of Electromachining*, vol. 65, 2010.

[143] S. K. Saha, "Experimental investigation of the dry electric discharge machining (Dry EDM) process," Master of Technology, Indian Institute of Technology Kanpur, 2008.

[144] A. M. Patel and V. Achwal, "Optimization of parameters for WEDM machine for productivity improvement," *IOSR Journal of Mechanical and Civil Engineering (IOSR-JMCE) e-ISSN*, vol. 9, no. 5, pp. 10-14, 2013.

[145] W. Lau, M. Wang, and W. Lee, "Electrical discharge machining of carbon fibre composite materials," *International Journal of Machine Tools and Manufacture*, vol. 30, no. 2, pp. 297-308, 1990.

[146] S. Habib and A. Okada, "Influence of electrical discharge machining parameters on cutting parameters of carbon fiber-reinforced plastic," *Machining Science and Technology*, vol. 20, no. 1, pp. 99-114, 2016.

[147] J. Sheikh-Ahmad and S. Shinde, "Drilling of carbon/epoxy composites by electrical discharge machining," in *Proceedings of the 1st International Conference on Industrial, Systems and Manufacturing Engineering (ISME'14)*, 2014.

[148] K. Gourgouletis, N. M. Vaxevanidis, N. I. Galanis, and D. E. Manolakos, "Electrical discharge drilling of carbon fibre reinforced composite materials," *International Journal of Machining and Machinability of Materials*, vol. 10, no. 3, pp. 187-201, 2011.

[149] B. K. Lodhi, D. Verma, and R. Shukla, "Optimization of machining parameters in EDM of CFRP composite using Taguchi technique," *Journal Impact Factor*, vol. 5, no. 10, pp. 70-77, 2014.

[150] A. Itoh, S. Hayakawa, F. Itoigawa, and T. Nakamura, "Feasibility study on electrical discharge machining of carbon fiber reinforced plastics and observation of machining phenomena," *Journal of the Japan Society for Precision Engineering,* vol. 77, pp. 1140-1145, 2010.

[151] S. Habib, A. Okada, and S. Ichii, "Effect of cutting direction on machining of carbon fibre reinforced plastic by electrical discharge machining process," *International Journal of Machining and Machinability of Materials,* vol. 13, no. 4, pp. 414-427, 2013.

[152] S. Ichii, A. Okada, Y. Okamoto, and Y. Uno, "Influence of carbon fiber direction on EDM characteristics of CFRP," in *6th International Conference on Leading Edge Manufacturing in 21st Century, LEM 2011*, 2011, pp. 1-4.

[153] S. Marui, "Research on the EDM characteristics of carbon fiber reinforced plastics," in *Proceedings of Spring Meeting of the Japan Society for Precision Engineering, 2011*, 2011, pp. 11-12.

[154] J. Y. Sheikh-Ahmad, "Hole quality and damage in drilling carbon/epoxy composites by electrical discharge machining," *Materials and Manufacturing Processes*, vol. 31, no. 7, pp. 941-950, 2016.

[155] X. Yue, X. Yang, J. Tian, Z. He, and Y. Fan, "Thermal, mechanical and chemical material removal mechanism of carbon fiber reinforced polymers in electrical discharge machining," *International Journal of Machine Tools and Manufacture,* vol. 133, pp. 4-17, 2018.

[156] A. Ito, S. Hayakawa, F. Itoigawa, and T. Nakamura, "Effect of short-circuiting in electrical discharge machining of carbon fiber reinforced plastics," *Journal of Advanced Mechanical Design, Systems, and Manufacturing*, vol. 6, no. 6, pp. 808-814, 2012.

[157] S. Hayakawa, K. Tominaga, A. Ito, F. Itoigawa, and T. Nakamura, "Effect of carbon fiber orientation on machining phenomena in electrical discharge machining of carbon fiber reinforced plastics," *International Journal of Electrical Machining,* vol. 17, pp. 29-34, 2012.

[158] A. Korlos, D. Tzetzis, and G. Mansour, "Investigation of the electro-discharge open-hole machining on the structural behavior of carbon fiber reinforced polymers," in *Applied Mechanics and Materials*, 2014, vol. 657, pp. 321-325: Trans Tech Publ.

[159] W. Lau and W. Lee, "A comparison between EDM wire-cut and laser cutting of carbon fibre composite materials," *Material and Manufacturing Process,* vol. 6, no. 2, pp. 331-342, 1991.

[160] R. Abdallah, S. L. Soo, and R. Hood, "A feasibility study on wire electrical discharge machining of carbon fibre reinforced plastic composites," *Procedia CIRP,* vol. 77, pp. 195-198, 2018.

[161] H. Dutta, K. Debnath, and D. K. Sarma, "A Study of wire electrical discharge machining of carbon fibre reinforced plastic," in *Advances in Unconventional Machining and Composites*: Springer, 2020, pp. 451-460.

[162] I. Maher, A. A. Sarhan, and M. Hamdi, "Review of improvements in wire electrode properties for longer working time and utilization in wire EDM machining," *The International Journal of Advanced Manufacturing Technology,* vol. 76, no. 1-4, pp. 329-351, 2015.

[163] A. Kumar, V. Kumar, and J. Kumar, "A state of art in development of wire electrodes for high performance wire cut EDM," in *International Conference on Advancements*

and Futuristic Trends in Mechanical and Materials Engineering. Punjab Technical University, Jalandhar, 2012, pp. 5-7.

[164] R. kern. (2008) EDM wire selection. *International Technology Professionals-EDM Today*. 5. Available: http://www.gedms.com/technicalArticles/TechTipsM-A-8.pdf

[165] R. kern. (2007) EDM wire primer. *EDM Today*. Available: http://www.edmtodaymagazine.com/2015/archives/techtips/2007_jan_feb_tech_tip/

[166] J. Kapoor, S. Singh, and J. S. Khamba, "High-performance wire electrodes for wire electrical-discharge machining–a review," *Proceedings of the Institution of Mechanical Engineers, Part B: Journal of Engineering Manufacture*, vol. 226, no. 11, pp. 1757-1773, 2012.

[167] F. Alloys, "Molybdenum - Datasheet," Available: http://futurealloys.co.uk/molybdenum-data-sheet/

[168] J. Kapoor, S. Singh, and J. S. Khamba, "Recent developments in wire electrodes for high performance WEDM," in *Proceedings of the World Congress on Engineering*, 2010, vol. 2, pp. 1-4.

[169] J. Kapoor, S. Singh, and J. S. Khamba, "Current research trends on wire electrodes for wire electrical discharge machining," *An International Journal of Engineering Sciences* vol. 1, pp. 168-175, 2011.

[170] I. Cabanes, E. Portillo, M. Marcos, and J. Sánchez, "An industrial application for on-line detection of instability and wire breakage in wire EDM," *Journal of Materials Processing Technology*, vol. 195, no. 1-3, pp. 101-109, 2008.

[171] Y. Luo, "Rupture failure and mechanical strength of the electrode wire used in wire EDM," *Journal of Materials Processing Technology*, vol. 94, no. 2-3, pp. 208-215, 1999.

[172] B. Schacht, J.-P. Kruth, B. Lauwers, and P. Vanherck, "The skin-effect in ferromagnetic electrodes for wire-EDM," *The International Journal of Advanced Manufacturing Technology*, vol. 23, no. 11-12, pp. 794-799, 2004.

[173] A. B. McKenzie, "Characterization of electrical conductivity of carbon fiber/epoxy composites with conductive AFM and scanning microwave impedance microscopy," Master of Science in Aerospace Engineering, University of Illinois at Urbana-Champaign, 2015.

[174] R. Abid, "Electrical characterisation of aerospace grade carbon-fibre-reinforced polymers," PhD, Cardiff University, 2015.

[175] A. L. Neyestanak, S. A. Nazari, N. Sadeghbeigi, and A. Karimzadeh, "Electrical behaviour of glass/carbon-phenolic conductive hybrid composite woven used in electrostatics precipitator filter," *International Journal Electrochemical Science*, vol. 9, pp. 6416-6430, 2014.

[176] S. Rebouillat and M. E. Lyons, "Measuring the electrical conductivity of single fibres," *International Journal of Electrochemical Science*, vol. 6, pp. 5731-5740, 2011.

[177] Y. C. Shin, E. Novin, and H. Kim, "Electrical and thermal conductivities of carbon fiber composites with high concentrations of carbon nanotubes," *International Journal of Precision Engineering and Manufacturing*, vol. 16, no. 3, pp. 465-470, 2015.

[178] X. Wang, Y. Wang, and Z. Jin, "Electrical conductivity characterization and variation of carbon fiber reinforced cement composite," *Journal of Materials Science*, vol. 37, no. 1, pp. 223-227, 2002.

[179] L. Guadagno, U. Vietri, M. Raimondo, L. Vertuccio, G. Barra, B. De Vivo, P. Lamberti, G. Spinelli, V. Tucci, and F. De Nicola, "Correlation between electrical

conductivity and manufacturing processes of nanofilled carbon fiber reinforced composites," *Composites Part B: Engineering*, vol. 80, pp. 7-14, 2015.

[180] M. L. Clingerman, "Development and modelling of electrically conductive composite materials," PhD, Michigan Technological University 2001.

[181] A. Piche, I. Revel, and G. Peres, "Experimental and numerical methods to characterize electrical behaviour of carbon fiber composites used in aeronautic industry," in *Advances in Composite Materials-Analysis of Natural and Man-Made Materials*: IntechOpen, 2011.

[182] J. González, J. E. Ortiz, and E. Baggio-Saitovitch, "Influence of the anisotropy in the c-axis resistivity measurements of high-Tc superconductors," *Physica C: Superconductivity*, vol. 315, no. 3-4, pp. 271-277, 1999.

[183] X. Wang and D. Chung, "Real-time monitoring of fatigue damage and dynamic strain in carbon fiber polymer-matrix composite by electrical resistance measurement," *Smart Materials and Structures*, vol. 6, no. 4, pp. 504-508, 1997.

[184] C.-L. Kuo, "Drilling of Ti/CFRP/Al multilayer stack materials," PhD, University of Birmingham, 2014.

[185] I. Shyha, "Drilling of carbon fibre reinforced plastic composites " PhD, University of Birmingham, 2010.

[186] G. M. Solutions, "Customer services consumables," Available: https://www.gfms.com/content/dam/gfac_country_CH/PDF/Consumable-Sales-Menu/EN/Consumables%20Catalogue-RES-EN-V1.2_low.pdf

[187] G. AgieCharmilles, "Solutions to boost your applications," Available: https://www.gfms.com/content/dam/gfac/proddb/customer-services/en/certified-wire_en.pdf

[188] B. I. Wire, "Topas® Plus- The high performance wires for grater cutting performance and precision.," Available: http://www.bedra.hk/UploadImage/edit/files/topasplusflyer_GB.pdf

[189] HIG, "Compeed (TM) datasheet," Available: https://www.hig.at/en/client/datasheets/Compeed_ProdBl_engl.pdf

[190] AgieCharmilles, "Fl 240 CC Fl 440 CC Fl 640 CC- GF machining solutions," Available: https://www.gfms.com/content/dam/gfac/PDF-Documents/sales/USA/Literature/EDM-Literature/FI240%20440%20640%20cc%20Brochure.pdf

[191] Charmilles, "Robofil 240/440/640 CC," Available: http://cfsusa.net/detail/shop/Shop-Capacity/CNC/ROBOFIL%20X40%20CC%20US.pdf

[192] O. I. I. Measurement, "InfiniteFocus G5 brochure," Available: https://optimaxonline.com/non-contact-metrology-3d-surface-characterisation/37/alicona-infinitefocus-g5

[193] JOEL, "JCM-6000Plus-Nikon Metrology," Available: https://www.nikonmetrology.com/images/brochures/jcm-6000-plus-neoscope-en.pdf

[194] Y.-C. Lin, Y.-F. Chen, D.-A. Wang, and H.-S. Lee, "Optimization of machining parameters in magnetic force assisted EDM based on Taguchi method," *Journal of Materials Processing Technology*, vol. 209, no. 7, pp. 3374-3383, 2009.

[195] R. Teimouri, S. Amini, and N. Mohagheghian, "Experimental study and empirical analysis on effect of ultrasonic vibration during rotary turning of aluminum 7075 aerospace alloy," *Journal of Manufacturing Processes*, vol. 26, pp. 1-12, 2017.

[196] L. V. Candioti, M. M. De Zan, M. S. Camara, and H. C. Goicoechea, "Experimental design and multiple response optimization. Using the desirability function in analytical methods development," *Talanta*, vol. 124, pp. 123-138, 2014.

APPENDICES

Appendix-A: Carbon fibre data sheet

TECHNICAL DATA SHEET
No. CFA-019

TORAYCA®

T800S DATA SHEET

Intermediate modulus, high tensile strength fiber, developed as a cost effective alternative to T800H. This never twisted fiber has excellent tensile composite properties and is specifically designed to meet the weight saving demand of aircraft and high performance recreational products.

FIBER PROPERTIES

		English	Metric	Test Method
Tensile Strength		850 ksi	5,880 MPa	TY-030B-01
Tensile Modulus		42.7 Msi	294 GPa	TY-030B-01
Strain		2.0 %	2.0 %	TY-030B-01
Density		0.065 lbs/in^3	1.80 g/cm^3	TY-030B-02
Filament Diameter		2.0E-04 in.	5 µm	
Yield	24K	1,446 ft/lbs	1,030 g/1000m	TY-030B-03
Sizing Type & Amount	10E	0.5 %		TY-030B-05
	Twist	Never twisted		

PRELIMINARY COMPOSITE PROPERTIES*

Tensile Strength (RT)	430 ksi	2,950 MPa
Tensile Strength (-75°F)	415 ksi	2,860 MPa
Tensile Modulus (RT)	22.5 Msi	154 GPa
Open Hole Tensile Strength	70.5 ksi	487 MPa
Open Hole Compressive Strength (RT)	42.0 ksi	291 MPa
Open Hole Compressive Strength (180°F/wet)	33.0 ksi	229 MPa
CAI	43.5 ksi	300 MPa
CILS	12.5 ksi	85 MPa

* Toray 350°F Toughened Epoxy Resin. Normalized to 60% fiber volume.

See Section 4 for Safety & Handling information. The above properties do not constitute any warranty or guarantee of values. These values are for material selection purposes only. For applications requiring guaranteed values, contact our sales and technical team to establish a material specification document.

TORAY CARBON FIBERS AMERICA, INC.

Appendix-B: Safety data sheet of carbon fibre prepreg

SOFICAR	MATERIAL SAFETY DATA SHEET (ISO DIS 11014)	No.	AQ.999
	TORAYCA® CARBON FIBRE PREPREG	Date	Sept. 2005

1. Chemical Product and Company Identification.

Product name: **TORAYCA CARBON FIBRE PREPREG 180° Cure**
(Group 6 Resin #3910, #3911)
Manufacturer name: **TORAY Industries, Inc.**
Address: 2-1 Nihonbashi-Muromachi 2-Chome, CHUO-KU
TOKYO 103 JAPAN

Contacts:

- in Europe: **Société des Fibres de Carbone S.A. - SOFICAR**
  Technical Customer Support
  Telephone N°: +33 145 111 280
- in Japan: **ACM Technology Dept.**
  Gal Manager of ACM Technology Dept.
  Telephone N°: +81 332 455 762

2. Composition/Information on ingredients

Chemical name: **TORAYCA CARBON FIBRE PREPREG 180° Cure**
(Resin #3910, #3911)
Common chemical name: Prepreg
Substance/mixture: Mixture

Hazardous Components	*WT%*
Fiber or woven fabric Carbon fiber (PAN based)	50 – 70
Thermoplastic resin	5 – 15
Bisphenol F type epoxy resin, CAS N°: 58421-55-9, R36 R38 R43	2 - 10
Hardener	15 - 25
Polymer additive	5 - 15

3. Hazards Identification

Main Routes of Entry: Dermal contact, ingestion
Carcinogenicity inds: NA

Adverse human health effects:

- Irritating to eyes
- Irritating to skin
- May cause sensitization by skin contact.

Environmental effects:

- The dust of hardened prepreg or carbon fiber fuzz may cause short circuit when contacted to electrical apparatus.

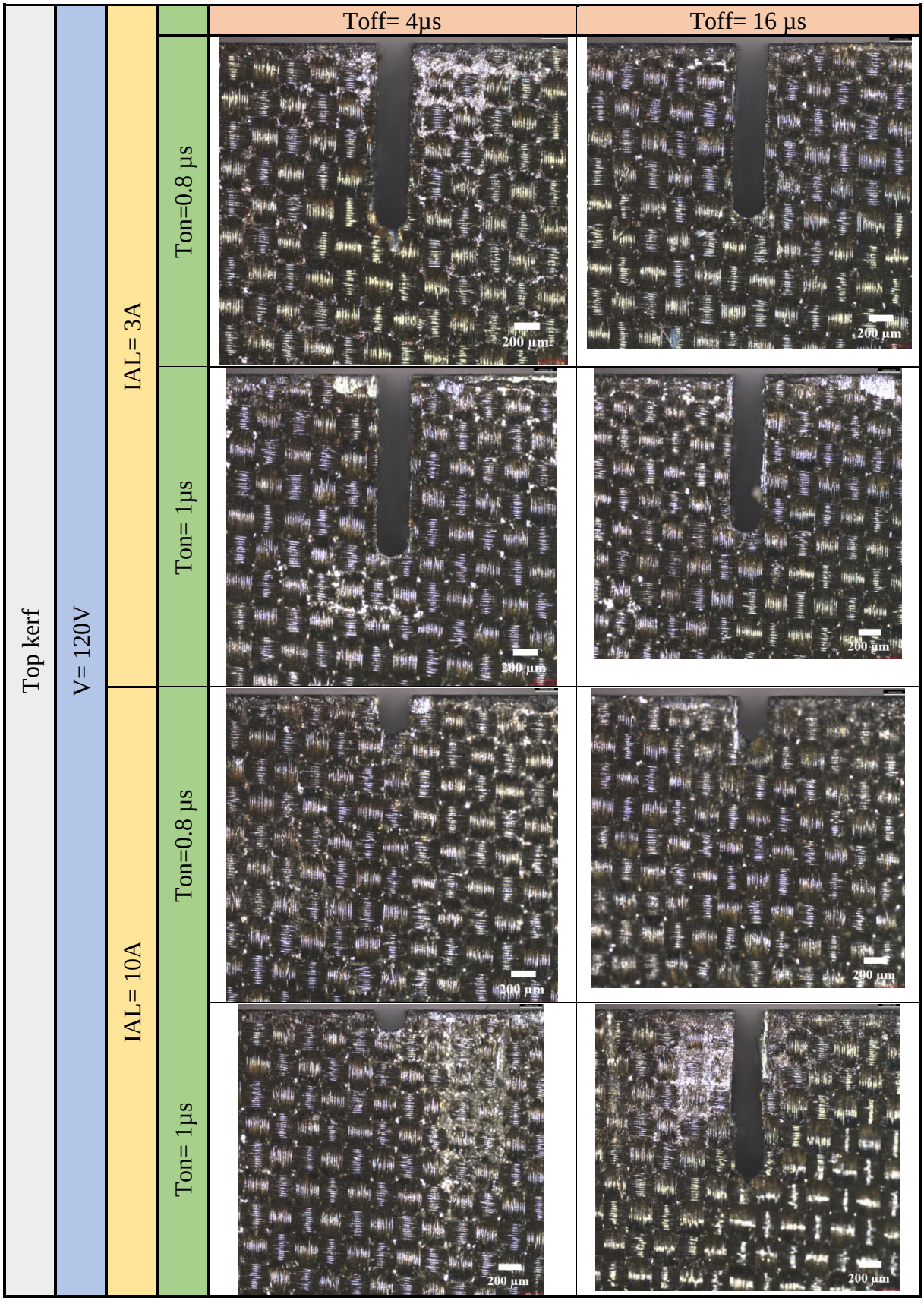
Appendix-C: Resistivity measurements for CFRP samples

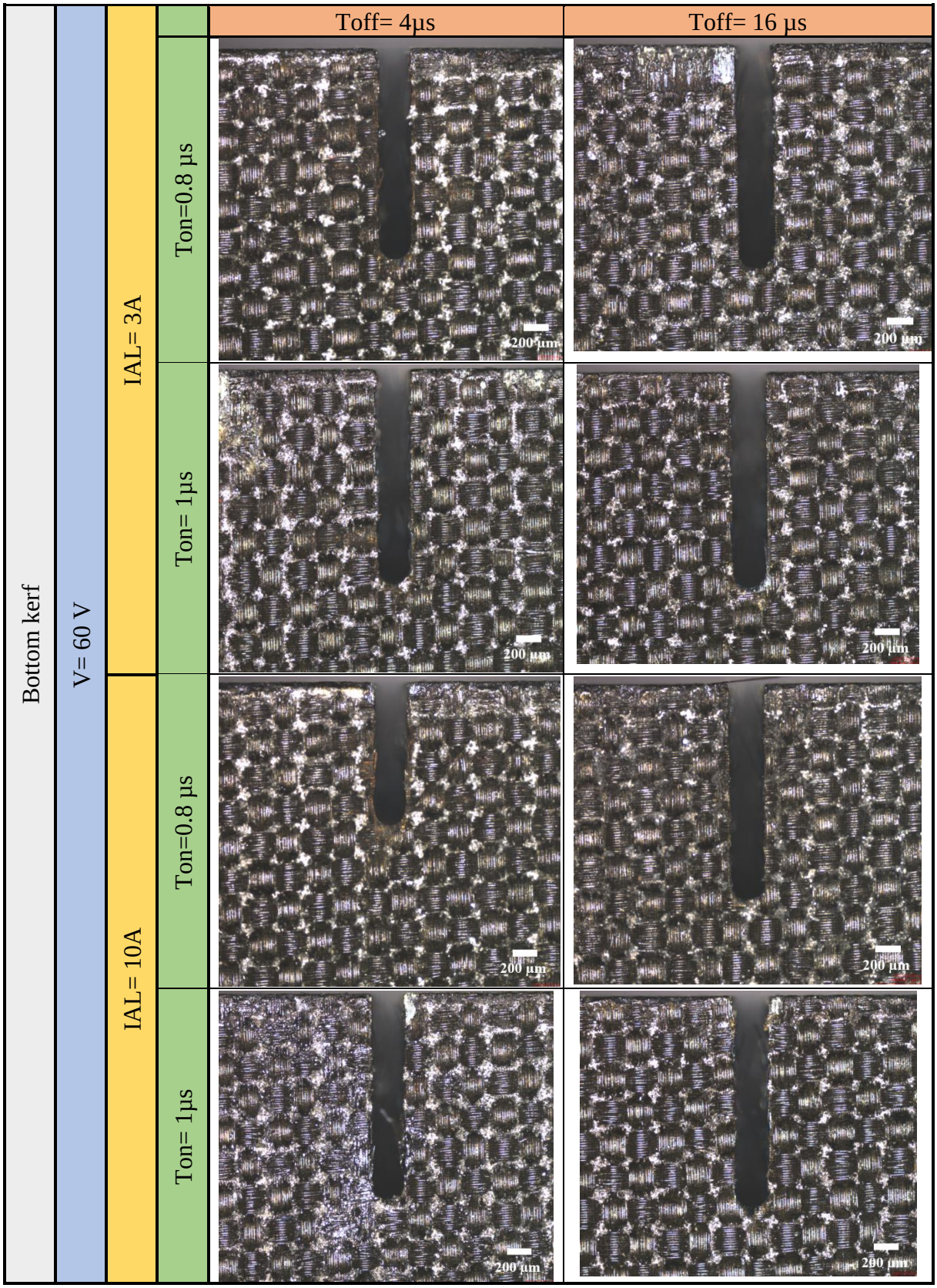
Sample no	Weight (g)	Multi-meter resistance reading (Ω)			Sample dimensions (mm)			Resistivity calculation (Ω.cm)			Sample density (g/mm^3)	Resistivity Normalization (Ω/mm)
		Parallel	Perpendi-cular	Vertical	Length	Width	Thick ness	Parallel	Perpendi cular	Vertical		
11491 (1)	129.7	0.2	8.5	24.4	100.5	100.2	8.2	0.1634	6.994	2995.0	0.0015719251	3.0
11491(17)	130.1	0.1	8.4	36.6	100.2	100.5	8.37	0.0840	7.006	4401.2	0.0015444101	4.4
11491(12)	131.3	0.1	8.7	68.78	100.0	100.4	8.19	0.0822	7.098	8435.8	0.0015964769	8.4
11491(10)	131.6	0.2	8.7	121.36	99.9	100.5	8.3	0.1663	7.154	14734.8	0.0015850231	14.7
11491(23)	129.2	0.1	8.9	198	100.1	100.4	8.02	0.0805	7.113	24814.3	0.001603165	24.7
Multi-directional	208.2	0.1	0.1	20.78	93.62	89.08	8.752	0.0833	0.092	1980.1	0.001588023	2.4

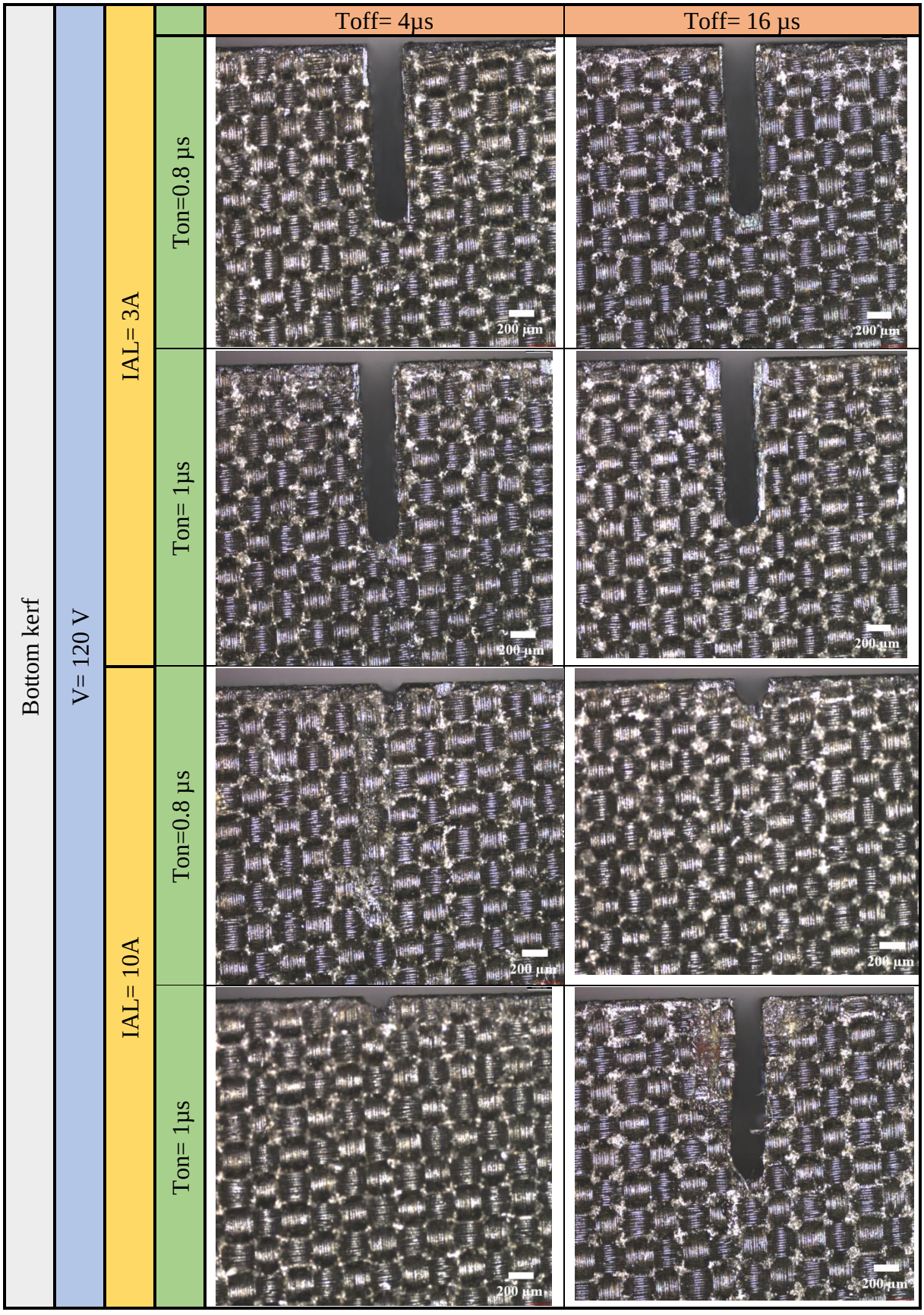
- Sample 11491 (1) used in preliminary experiments, phase 3A & 3B.
- Sample 11491(17) &11491 (12) used in phase 1A&1B (Taguchi experiments) using Topas plus D wire.
- Sample 11491(10) &11491(23) used in phase 2A&2B (Taguchi experiments) using Compeed wire.
- Multi-directional sample used in phase 3C.

Appendix-D: Micrographs of machined kerf for preliminary tests



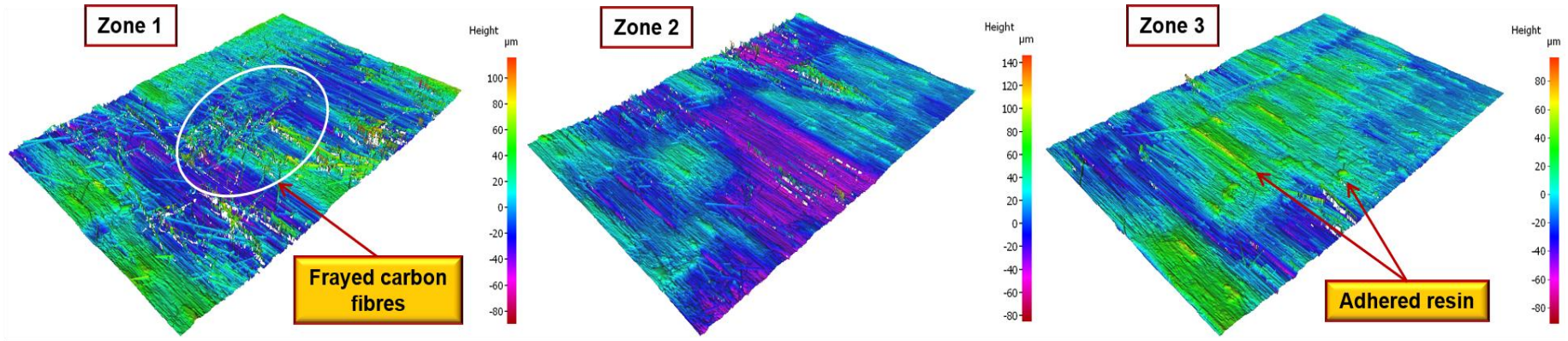

Top kerf
V= 120V
IAL= 3A
IAL= 10A
Ton=0.8 µs
Ton= 1µs
Ton=0.8 µs
Ton= 1µs
Toff= 4µs
Toff= 16 µs
200 µm


Bottom kerf
V= 60 V
IAL= 3A
IAL= 10A
Ton=0.8 µs
Ton= 1µs
Ton=0.8 µs
Ton= 1µs
Toff= 4µs
Toff= 16 µs
200 µm
200 µm
200 µm
200 µm
200 µm
200 µm
200 µm
200 µm

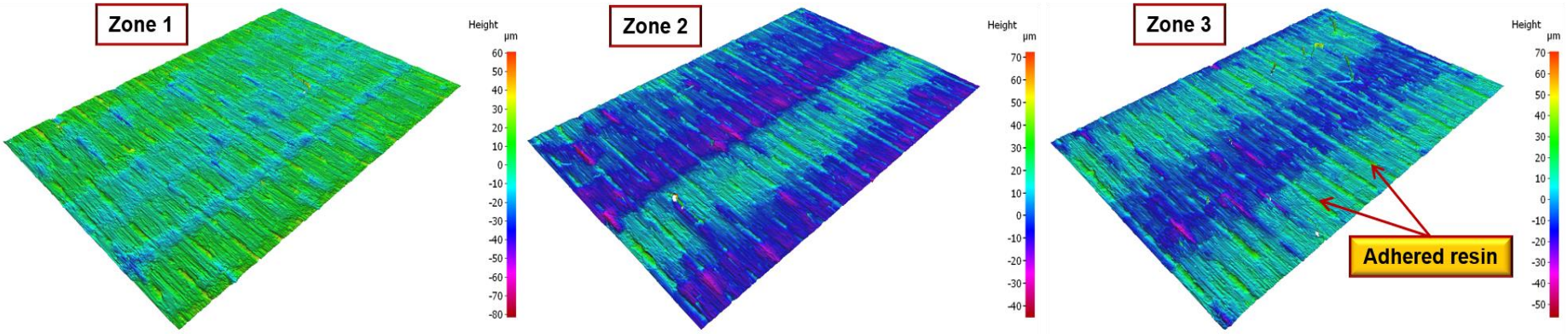

Bottom kerf
V= 120 V
IAL= 3A
IAL= 10A
Ton=0.8 µs
Ton= 1µs
Ton=0.8 µs
Ton= 1µs
Toff= 4µs
Toff= 16 µs
200 µm

Appendix-E: Surface topographical maps for areal roughness measurements

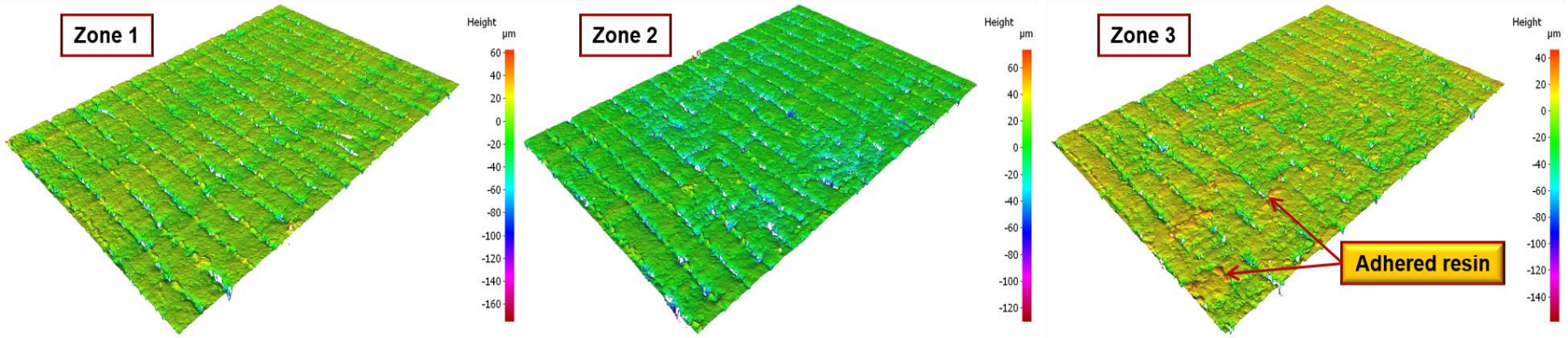
Surface topographical maps for Test 9 (highest roughness/MRR) in Phase 1A



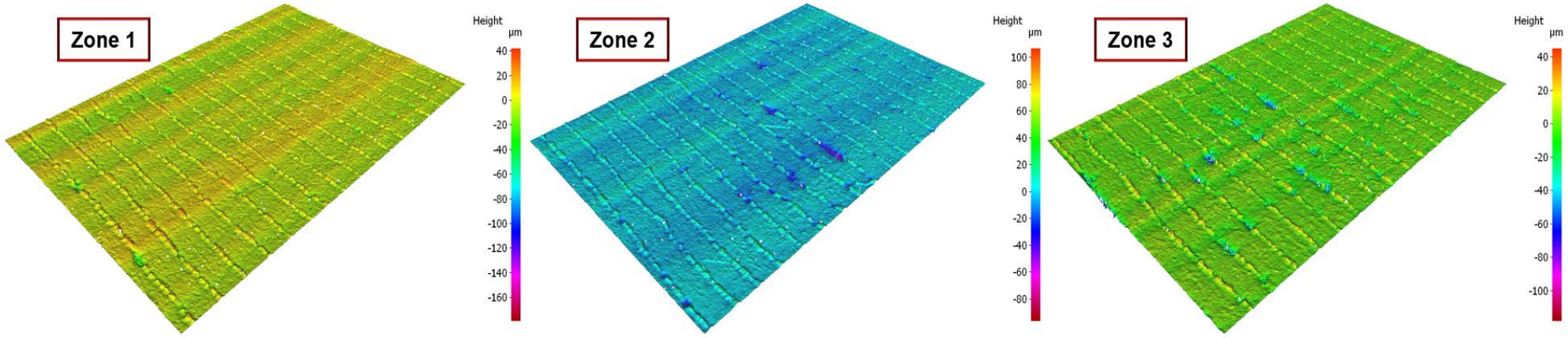
Surface topographical maps for Test 4 (lowest roughness) in Phase 1A



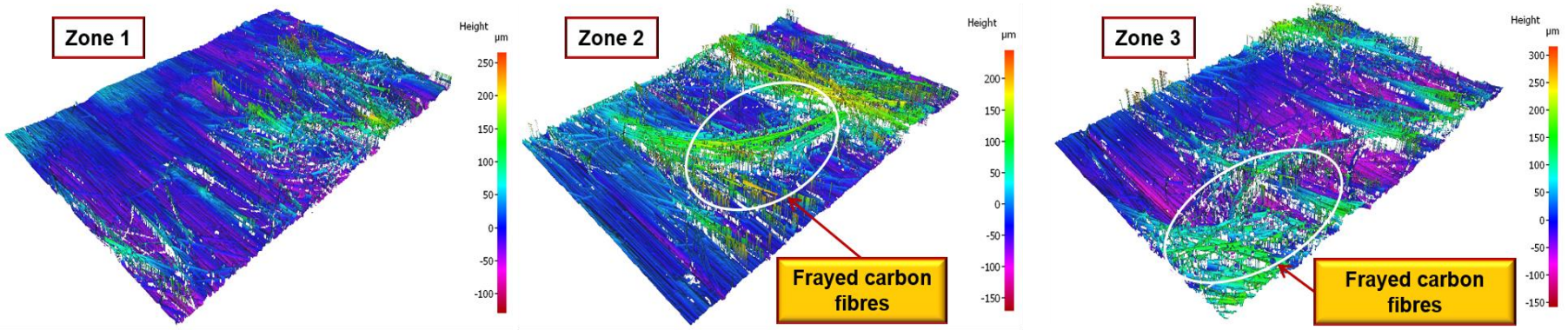
Surface topographical maps for Test 1 (highest roughness) in Phase 1B



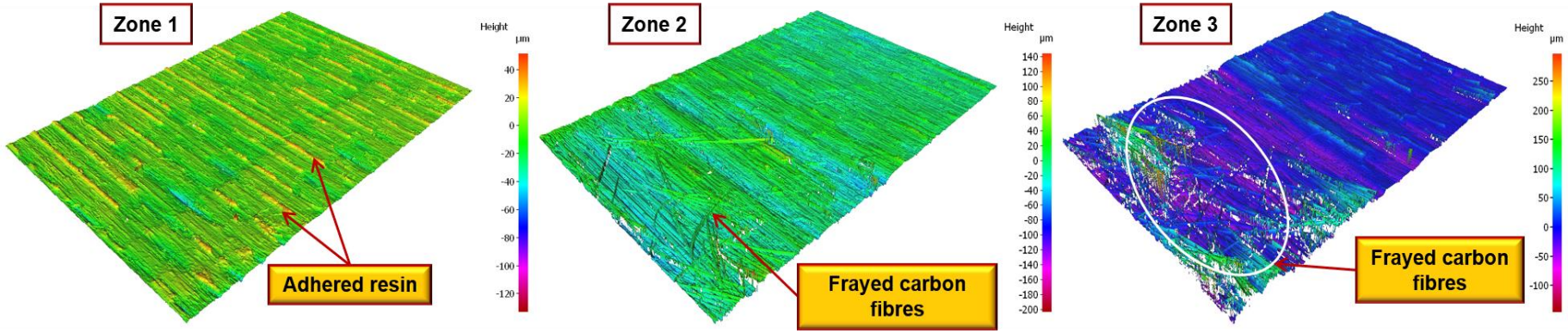
Surface topographical maps for Test 12 (lowest roughness) in Phase 1B



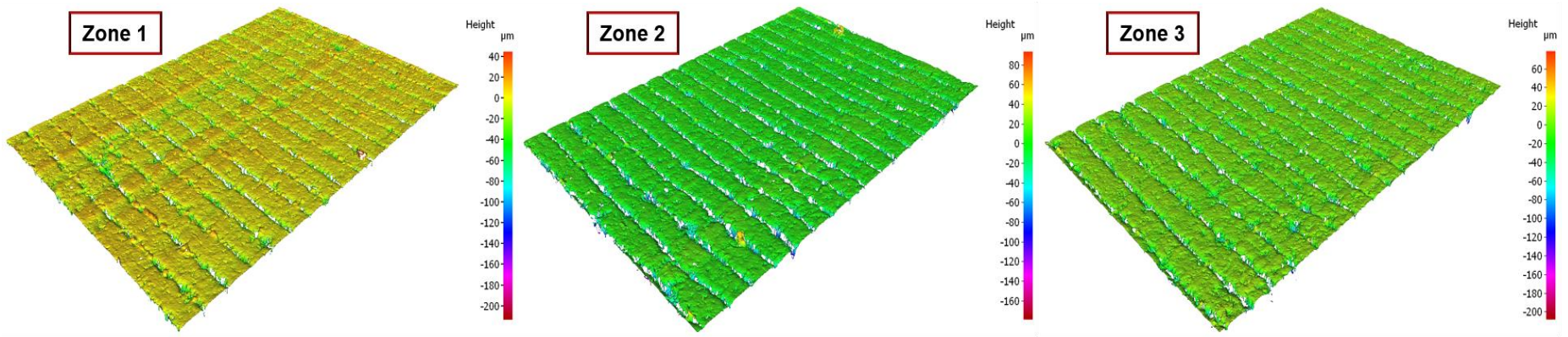
Surface topographical maps for Test 4 (highest roughness) in Phase 2A



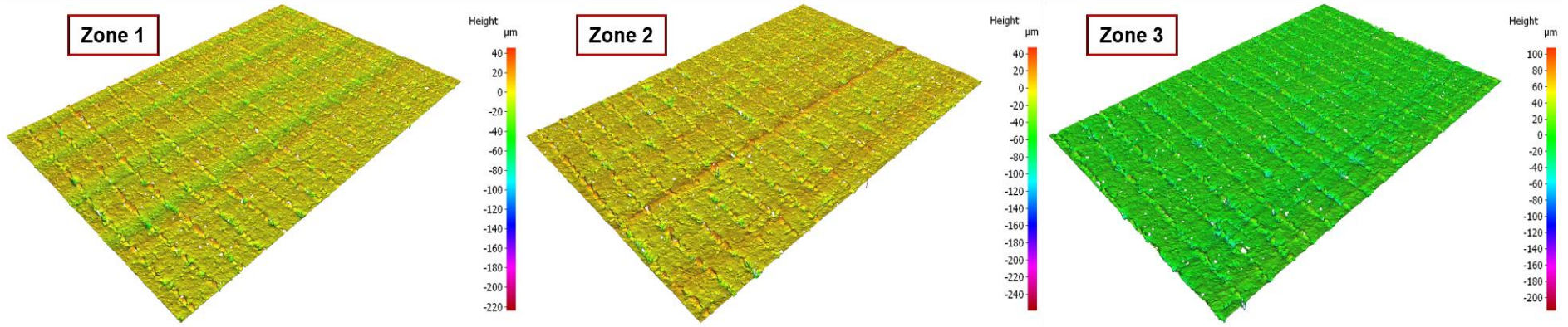
Surface topographical maps for Test 3 (lowest roughness) in Phase 2A



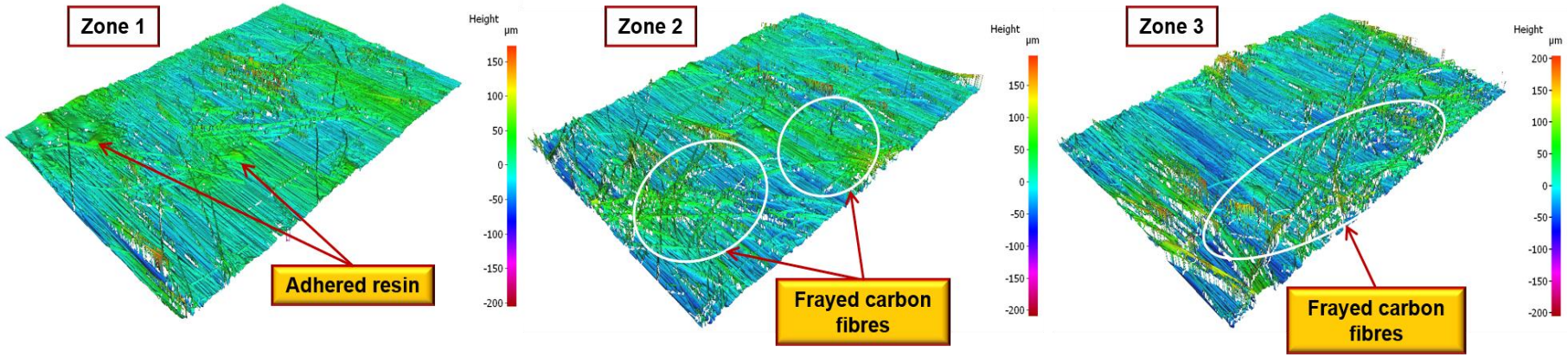
Surface topographical maps for Test 11 (highest roughness) in Phase 2B



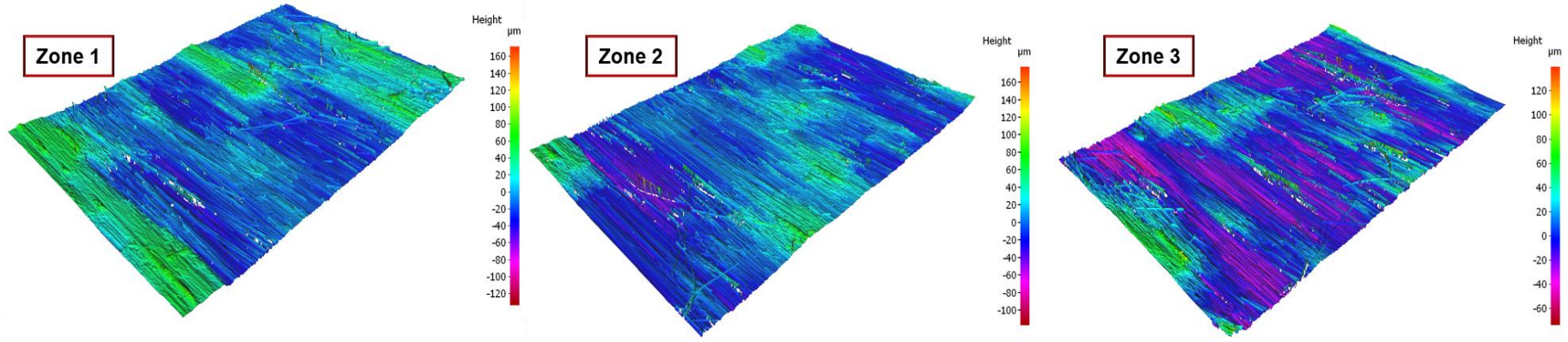
Surface topographical maps for Test 10 (lowest roughness) in Phase 2B



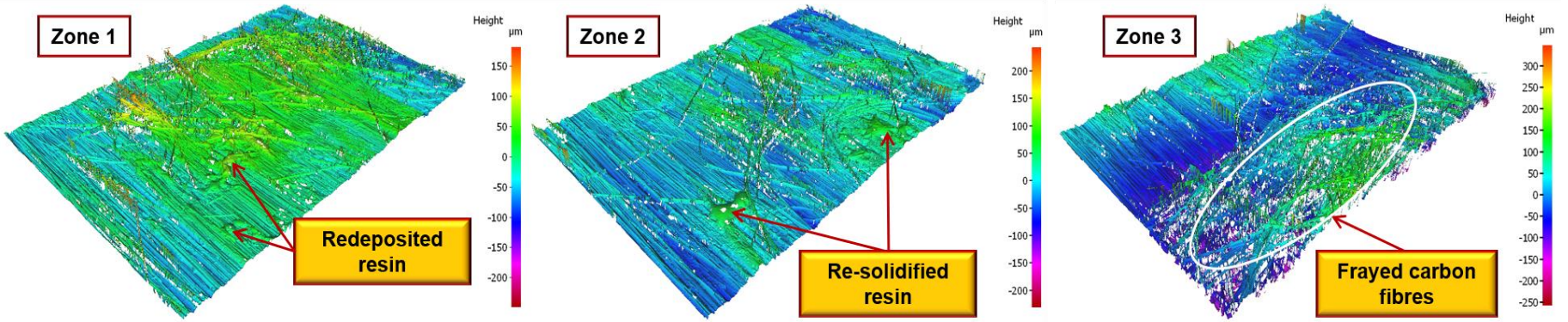
Surface topographical maps for Test 2 (highest roughness/MRR) in Phase 3B using Topas wire



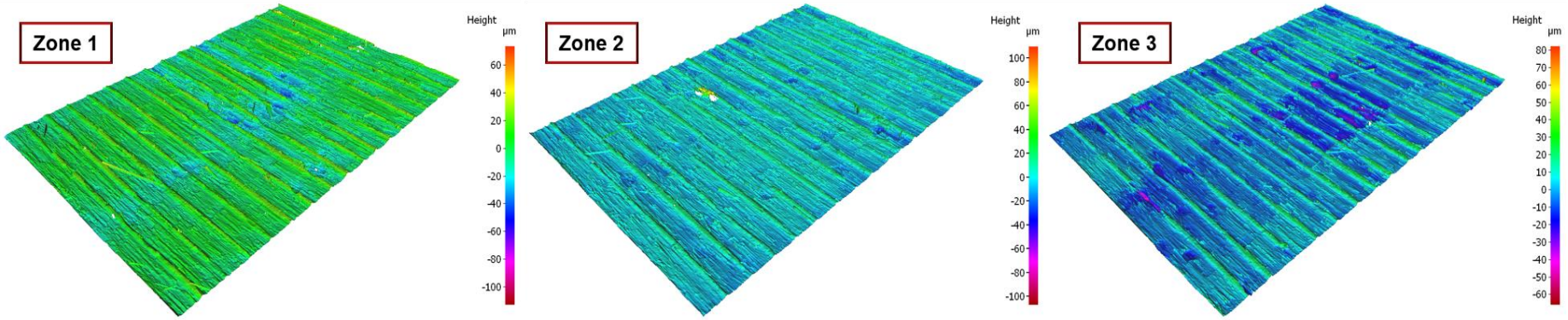
Surface topographical maps for Test 9 (lowest roughness) in Phase 3B using Topas wire



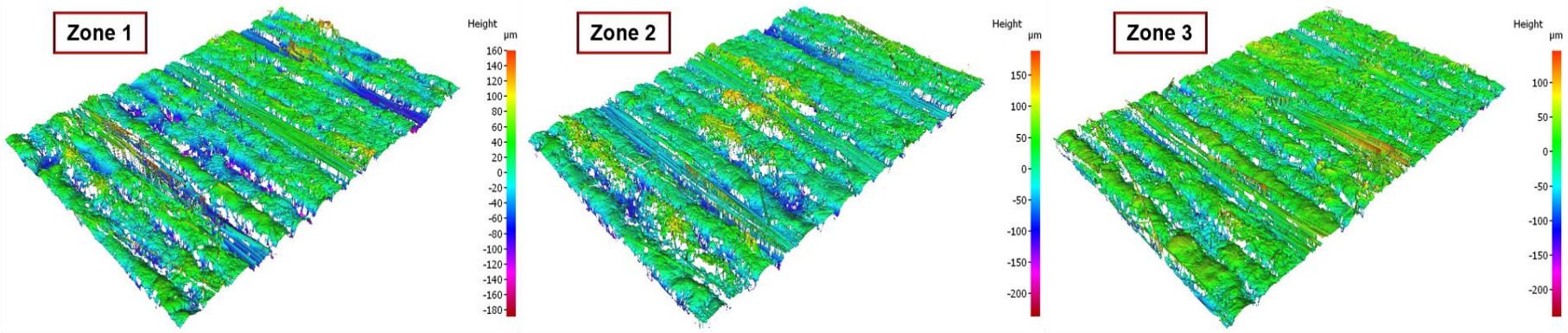
Surface topographical maps for Test 15 (highest roughness/MRR) in Phase 3B using Compeed wire



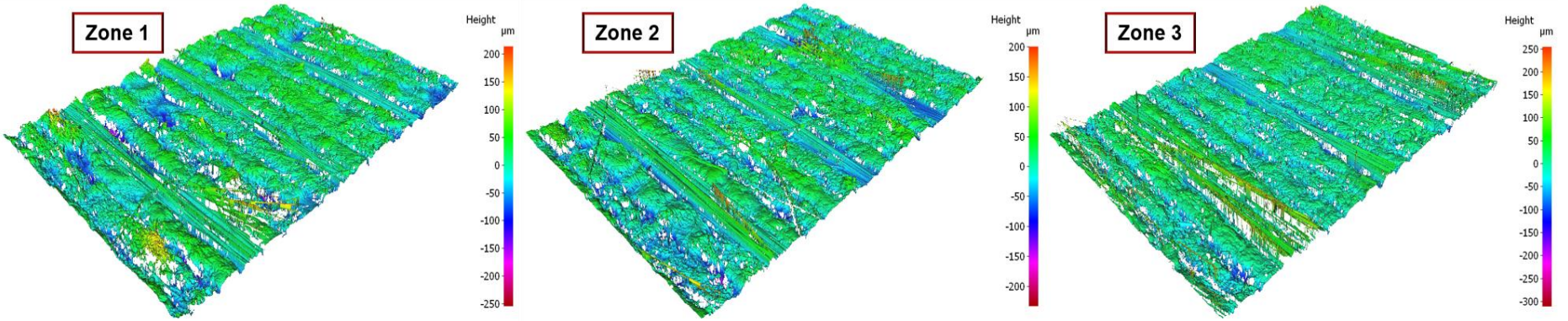
Surface topographical maps for Test 25 (lowest roughness) in Phase 3B using Compeed wire



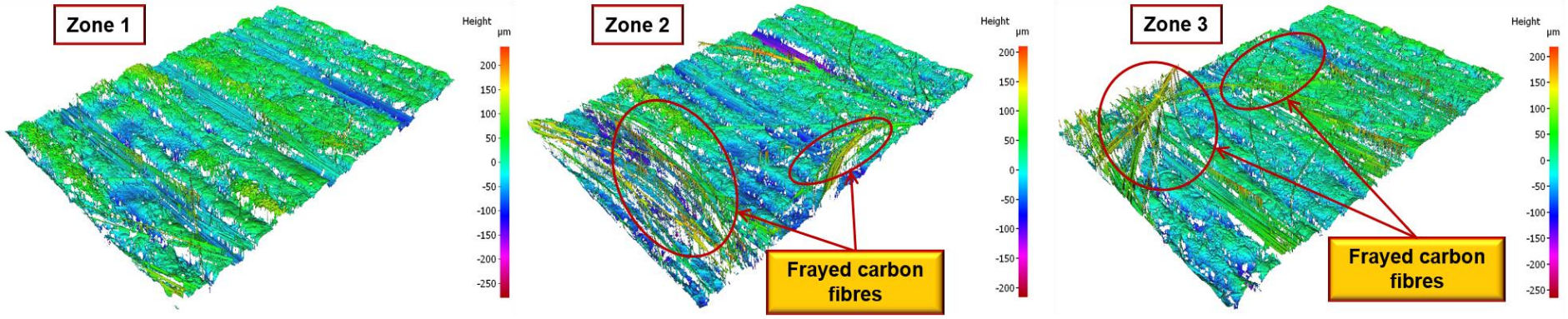
Surface topographical maps for Test 2 (highest roughness/MRR) in Phase 3C using Topas wire



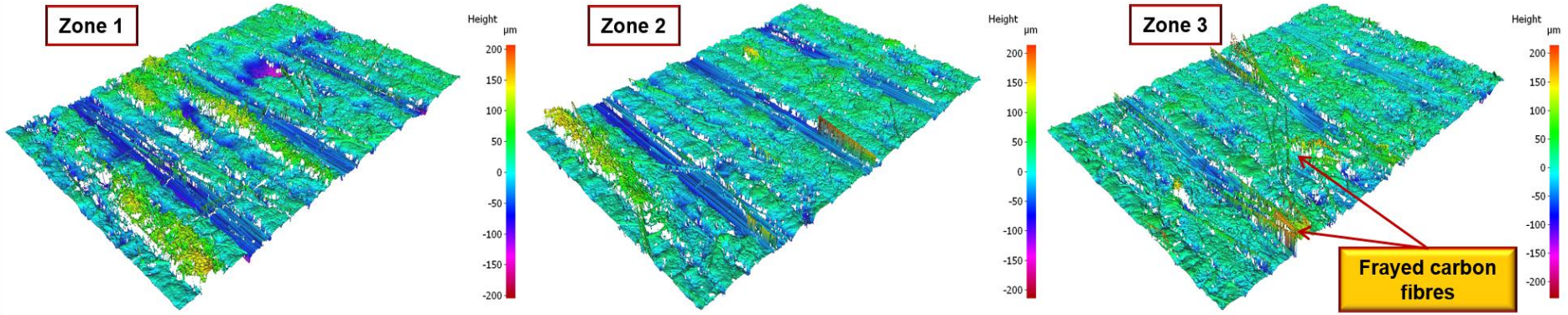
Surface topographical maps for Test 1 (lowest roughness) in Phase 3C using Topas wire



Surface topographical maps for Test 6 (highest roughness/MRR) in Phase 3C using Compeed wire



Surface topographical maps for Test 7 (lowest roughness) in Phase 3C using Compeed wire



Appendix-F: Data tables for experimental phases

Phase 1: parallel and perpendicular cutting to fibre orientation using Topas wire electrode

Trial no.	V	IAL	A	B	Parallel cutting			Perpendicular cutting		
	Volt	Amp	µs	µs	MRR (mm^3/min)	Wa (µm)	Sa (µm)	MRR (mm^3/min)	Wa (µm)	Sa (µm)
1	120	3	0.8	4	0.96	270.59	5.42	1.40	269.49	6.84
2	120	3	0.9	6	0.43	269.91	5.43	0.84	270.96	6.24
3	120	3	1.0	8	0.72	261.46	5.07	1.14	268.66	4.95
4	120	4	0.8	4	1.41	263.88	4.53	1.94	271.12	6.21
5	120	4	0.9	6	1.40	266.95	4.73	1.50	272.00	5.76
6	120	4	1.0	8	1.17	273.98	4.93	1.32	270.89	4.78
7	120	5	0.8	6	1.68	267.21	5.55	1.90	272.43	4.91
8	120	5	0.9	8	1.23	260.30	5.12	1.41	270.01	4.60
9	120	5	1.0	4	2.41	272.78	9.48	1.57	271.13	4.79
10	140	3	0.8	8	0.70	271.29	5.93	0.76	271.67	3.78
11	140	3	0.9	4	0.93	283.15	6.96	0.79	273.33	3.95
12	140	3	1.0	6	0.52	271.90	5.11	0.82	271.51	3.30
13	140	4	0.8	6	0.92	269.32	5.45	1.20	268.30	5.31
14	140	4	0.9	8	0.54	262.82	5.42	0.69	270.20	4.53
15	140	4	1.0	4	1.22	269.34	4.76	1.50	270.41	5.50
16	140	5	0.8	8	0.73	267.89	5.01	1.22	268.00	4.69
17	140	5	0.9	4	1.77	269.10	5.88	1.75	273.90	5.31
18	140	5	1.0	6	1.58	271.02	5.71	1.51	268.99	4.58

Phase 2: Parallel and perpendicular cutting to fibre orientation using Compeed wire electrode

Trial no.	V	IAL	A	B	Parallel cutting			Perpendicular cutting		
	Volt	Amp	µs	µs	MRR (mm3/min)	Wa (µm)	Sa (µm)	MRR (mm3/min)	Wa (µm)	Sa (µm)
1	120	3	0.8	4	1.78	308.24	19.92	1.33	276.86	6.41
2	120	3	0.9	6	1.51	304.38	14.15	0.87	273.17	5.23
3	120	3	1.0	8	1.17	287.69	9.27	0.73	272.46	5.61
4	120	4	0.8	4	2.36	305.79	26.29	1.23	274.17	6.64
5	120	4	0.9	6	2.65	344.78	20.27	1.37	275.30	6.57
6	120	4	1.0	8	1.58	300.75	12.62	0.83	275.57	6.27
7	120	5	0.8	6	4.31	347.23	19.45	1.68	276.66	6.25
8	120	5	0.9	8	2.93	338.66	22.60	1.13	278.08	6.83
9	120	5	1.0	4	4.70	366.55	20.38	1.53	275.27	6.56
10	140	3	0.8	8	1.81	306.94	15.01	0.65	280.62	4.36
11	140	3	0.9	4	2.03	325.47	19.29	0.62	277.47	7.77
12	140	3	1.0	6	1.95	297.36	18.45	0.59	275.63	4.72
13	140	4	0.8	6	2.22	306.10	12.64	1.01	275.57	6.49
14	140	4	0.9	8	1.28	291.56	11.46	0.74	273.42	5.88
15	140	4	1.0	4	3.19	317.94	17.49	1.03	273.41	6.87
16	140	5	0.8	8	1.82	292.81	15.75	1.50	277.08	6.45
17	140	5	0.9	4	3.64	308.26	24.84	1.19	285.44	5.67
18	140	5	1.0	6	2.37	298.24	18.14	1.34	290.38	5.31

Phase 3A: Material removal rate for stacked UD-CFRP with copper plates

Trial no	Wire	V	IAL	A	B	MRR (mm^3/min)
1	Topas	120	5	0.6	4	6.50
2		120	3	0.6	8	1.81
3	Compeed	120	5	0.6	4	6.11
4		120	3	0.6	8	2.45

Phase 3B: Material removal rate and areal roughness gained via stacking with CU sheets

Trial no	IAL	B	W	Coded levels		MRR (mm^3/min)	Sa (µm)
1	3	8	T	-1	-1	5.58	15.14
2	5	8	T	1	-1	5.89	16.48
3	3	10	T	-1	1	3.37	13.22
4	5	10	T	1	1	3.87	15.40
5	3	9	T	-1	0	3.12	15.44
6	5	9	T	1	0	3.53	13.52
7	4	8	T	0	-1	5.08	12.70
8	4	10	T	0	1	3.52	11.44
9	4	9	T	0	0	3.11	9.08
10	4	9	T	0	0	3.09	10.38
11	4	9	T	0	0	3.01	12.78
12	4	9	T	0	0	2.89	11.95
13	4	9	T	0	0	3.00	12.76
14	3	8	C	-1	-1	3.51	13.77
15	5	8	C	1	-1	5.35	15.22
16	3	10	C	-1	1	3.12	14.23
17	5	10	C	1	1	3.85	14.59
18	3	9	C	-1	0	2.65	12.85
19	5	9	C	1	0	2.77	10.61
20	4	8	C	0	-1	3.32	12.35
21	4	10	C	0	1	2.40	13.33
22	4	9	C	0	0	2.18	11.34
23	4	9	C	0	0	2.75	14.63
24	4	9	C	0	0	2.27	11.01
25	4	9	C	0	0	1.82	6.42
26	4	9	C	0	0	2.27	12.88

Phase 3C: Material removal rate, average kerf width and areal roughness for multidirectional CFRP

Trial no	Wire	IAL	B	MRR (mm^3/min)	Wa (µm)	Sa (µm)
1	Topas	3	8	12.80	333.66	23.62
2		5	8	14.82	340.62	24.86
3		3	10	7.42	333.96	24.25
4		5	10	10.75	347.15	24.33
5	Compeed	3	8	10.70	366.28	24.70
6		5	8	13.31	374.38	27.53
7		3	10	5.29	333.99	21.45
8		5	10	8.11	352.42	25.61

Appendix-G: List of publications

Published papers

[1] R. Abdallah, S. L. Soo, and R. Hood, "A feasibility study on wire electrical discharge machining of carbon fibre reinforced plastic composites," Procedia CIRP, vol. 77, pp. 195-198, 2018.

[2] R. Abdallah, S. L. Soo, and R. Hood, "The influence of cut direction and process parameters in wire electrical discharge machining (WEDM) of carbon fibre reinforced plastic composites," 2020. (submitted)

Papers under preparation

[1] R. Abdallah, S. L. Soo, and R. Hood, "A Review on non-conventional machining for carbon fibre reinforced plastics (CFRP) composites,", 2016. (draft completed)

[2] R. Abdallah, S. L. Soo, and R. Hood, "An investigation of composite wire on cutting performance of carbon fibre reinforced plastic (CFRP) using Wire-EDM process, ", 2019. (draft completed)

[3] R. Abdallah, S. L. Soo, and R. Hood, "A comparative study on machining performance gained at different cut directions using high performance wire electrodes in wire electrical discharge machining (WEDM) of carbon fibre reinforced plastic composites.

[4] R. Abdallah, S. L. Soo, and R. Hood, "A feasibility study on stacked UD-CFRP with Cu plates using wire electrical discharge machining (WEDM)".

[5] R. Abdallah, S. L. Soo, and R. Hood, "Effect of process parameters in wire electrical discharge machining (WEDM) on cutting performance of multi-directional CFRP composites ".